Molecular Nanomagnets of Fe(III)

Ian Andrew Gass

A Thesis Submitted for the degree of
Doctor of Philosophy

School of Chemistry

Faculty of Science and Engineering

University of Edinburgh

August 2008

Abstract

Two routes for preparing polymetallic clusters of iron have been investigated: the first strategy is to make molecular analogues of naturally occurring magnetic oxides using controlled hydrolysis and the second involves investigation of the coordination chemistry of salicylaldoxime ($saoH_2$) and its derivatives R-$saoH_2$ (where R=Me, Et, Ph). In total seventeen new complexes are reported. These are a family of heptadecametallic iron structures (**1-6**): $Hpy[Fe_{17}O_{16}(OH)_{12}(py)_{12}Br_4]Br_4{\cdot}8py{\cdot}MeCN$ (**1**), $(HPy)_{0.5}[Fe_{17}O_{16}(OH)_{12}(py)_{12}Br_4]Br_{3.5}$ (**2**), $Hpy[Fe_{17}O_{16}(OH)_{12}(py)_{12}Br_4]Br_4{\cdot}2(C_3H_6O){\cdot}1/2py{\cdot}2H_2O$ (**3**), $[Fe_{17}O_{16}(OH)_{12}(iso\text{-}quin)_{12}Br_3(H_2O)_3]Br_4{\cdot}6(iso\text{-}quin){\cdot}3(H_2O)$ (**4**), $[Fe_{17}O_{16}(OH)_{12}(3,5\text{-}lut))_{12}Br_4]Br_3{\cdot}H_2O$ (**5**), $[Fe_{17}O_{16}(OH)_{12}(\beta\text{-}pic)_{12}Br_4]Br_3$ (**6**); dimetallic to octametallic cages stabilised with R-sao^{2-} ligands: $[HNEt_3][Fe_2(OMe)(Ph\text{-}sao)_2(Ph\text{-}saoH)_2]{\cdot}5MeOH$ (**7**), $[Fe_3O(Et\text{-}sao)(O_2CPh)_5(MeOH)_2]{\cdot}3MeOH$ (**8**), $[Fe_4(Me\text{-}sao)_4(Me\text{-}saoH)_4]{\cdot}MeOH$ (**9**), $[HNEt_3]_2[Fe_6O_2(Me\text{-}sao)_4(SO_4)_2(OMe)_4(MeOH)_2]$ (**10**), $[Fe_8O_3(Me\text{-}sao)_3(tea)(teaH)_3(O_2CMe)_3]{\cdot}3MeOH$ (**11**), $[Fe_8O_3(Et\text{-}sao)_3(tea)(teaH)_3(O_2CMe)_3]{\cdot}3MeOH$ (**12**), $[Fe_8O_3(Ph\text{-}sao)_3(tea)(teaH)_3(O_2CMe)_3]{\cdot}4MeOH$ (**13**), $[Fe_6O_2(OH)_2(Et\text{-}sao)_2(Et\text{-}saoH)_2(O_2CPh)_6].NEt_3$ (**14**), $[HNEt_3]_2[Fe_6O_2(OH)_2(O_2CPh(Me)_2)_6(Et\text{-}sao)_6]{\cdot}2MeCN$ (**15**); a coordination polymer stablised with Me-sao^{2-}: $([Fe_6Na_3O(OH)_4(Me\text{-}sao)_6(OMe)_3(H_2O)_3(MeOH)_6]{\cdot}MeOH)_n$ (**16**); a dodecamatallic cage stabilised with sao^{2-}: $[HNEt_3]_2[Fe_{12}Na_4O_2(OH)_8(sao)_{12}(OMe)_6(MeOH)_{10}]$ (**17**); the first polymetallic transition metal cluster to be synthesised using microwave heating - an unusual octametallic cluster using $saoH_2$, $[Fe_8O_4(sao)_8(py)_4]$ (**18**). Studies of the magnetic properties of **1-18** show that **1-6** are high spin clusters with S=35/2, which can show long range magnetic order (LRMO) or super-paramagnetic blocking depending on their crystal symmetry; **7-17** exhibit spin ground states between S=0 and S=4; while **18** has a spin ground state of S=0 and represents an ideal Heisenberg antiferromagnet.

Acknowledgements

I would like to thank Dr. Euan. Brechin or "the boss" for taking me on and being a great supervisor who has encouraged and guided me through it all. It`s fair to say I wouldn't have acheived a tenth of the results or publications that I have without his guidance and incidentally Euan sorry about that 5 iron. (I wonder where that went?)

I would also like to thank the esteemed Dr. Costas. Milios for all his help and getting me started in the lab before he got whisked off to defend his proud nation! I particularly enjoyed those awesome burgers in Vancouver and that wee pub opposite.

Also in the mix recently has been been Dr. Leigh. Jones who has helped me loads the last year and has infinite patience for stupid or odd questions. Always good to meet another mighty pool fan as well! Giorgos Karotsis, a Greek patriot, has to be thanked for his constant good banter and attempts to get me fit, 10K nailed! I would like to thank Ross Inglis as well for supporting Cowdenbeath, some quality chat and for keeping me up to date on all the film news! Also thanks goes out to Maria Manoli and Alessandro Prescimone for being great colleagues.

I would like to particularly like thank Prof. Simon. Parsons and his group (past and present) : Dr Ana Collins, Dr Stephen Moggach, Dr Francesca Fabbiani, Dr. Peter Wood, Frazer White, Alessandro Prescimone, Russel Johnstone and Laura Budd for solving all my structures!

I also need to thank all the scientists who have worked with me and/or helped analyse my samples: Dr. Marco Evangelisti for the specific heat measurements; Prof. Wolfgang Wernsdorfer for the single crystal hysteresis; Dr. Mark Murrie for magnetic measurements; Prof. Marshall Luban, Dr. Ruslan Prozorov, Dr. Matthew. Vanette and Dr. Larry. Engelhardt for the MAGPACK calculations; Dr. Oscar Moze, Prof. Dominic Ryan and coworkers for neutron diffraction; Prof. Hiroyuki Nojiri for high field measurements and Sylvia Williamson for elemental analysis.

I would also like to thank all my family, Ma, Pa, Mikee and G for understanding my wishes to be a student again and keeping me in good supply of

tennents and chat! I would also like to thank Phillip, Jackie and David Snelle for being so supportive throughout this whole venture.

Lastly I would like to thank the one and only Rachael. We both jumped straight in to this, although there was some motivation (moving from Prestonpans to Melbourne!) and she has seen me through it all. Thanks!

Declaration

I hereby declare that except where specific reference is made to other sources, the work contained in this thesis is the original work of the author. It has been composed by the candidate and has not been submitted, in whole or in part, for any other degree, diploma, or other qualification.

Ian Andrew Gass

9th September 2008

Contents

*** A cd with all the CIF files and appendices (bond lengths and angles tables, BVS calculations) can be found in a case at the end of the thesis.** **cd**

Abbreviations

ac	Alternating current
BVS	Bond Valence Sum
D	Zero Field Splitting Parameter
dc	Direct current
DFT	Density Functional Theory
ENDOR	Electron nuclear double resonance
EPR	Electron Paramagnetic Resonance
EXAFS	Extended X-RayAbsorption Fine Structure
HF EPR	High Field Electron Paramagnetic Resonance
INS	Inelastic Neutron Scattering
ITO	Irreducible Tensor Approach
LRMO	Long Range Molecular Order
MCE	Magnetocaloric Effect
MMO	Methane monooxygenase
NMR	Nuclear Magnetic Resonance
PAP	Purple Acid Phosphates
PND	Polarised Neutron Diffraction
py	Pyridine
QTM	Quantum Tunnelling of the Magnetisation
RNR	Ribonucleotide reductase
s.e	Symmetry equivalent
SMMs	Single Molecule Magnets
ZFS	Zero field splitting

Chapter 1
Introduction

This thesis describes the strategies for synthesising polynuclear iron complexes and particular attention is focused on their magnetic properties. An introduction to the significance of iron clusters is described including relevant bioinorganic iron chemistry, the phenomenon of single-molecule magnetism and the magnetocaloric effect. In addition to this the strategies used for the syntheses of these complexes are described.

Bioinorganic Iron Chemistry

The interest in polynuclear complexes of Fe stems, at least in part, to the studies of the mechanism of Fe hydrolysis in aqueous solution. The hydrolysis of the hexa-aqua $[Fe(H_2O)_6]^{3+}$ ion would give rise firstly to an insoluble iron hydroxide which then may transform itself into an oxy-hydroxide (e.g. goethite; α-Fe-O(OH)) phase and perhaps eventually to a thermodynamically stable oxide (e.g. haematite; Fe_2O_3). These hydrolytic products, found naturally, can be related to synthetic Fe-oxo clusters which may give some important insights into the mechanism of Fe hydrolysis.[1]

			pK_a
$Fe^{3+} + H_2O$	⟶	$Fe(OH)^{2+} + H^+$	2.2
$2Fe^{3+} + 2H_2O$	⟶	$Fe_2(OH)_2^{4+} + 2H^+$	2.9
$Fe(OH)^{2+} + H_2O$	⟶	$Fe(OH)_2^{+} + H^+$	3.5
$Fe(OH)_2^{+} + H_2O$	⟶	$Fe(OH)_3 + H^+$	6
$Fe(OH)_3 + H_2O$	⟶	$Fe(OH)_4^{-} + H^+$	10

Fig. 1. Hydrolysis reactions of Fe^{III} at 25ºC.

The same mechanistic processes can be found in biomineralisation,[2,3] which involves the selective extraction of elements such as Fe from the local surroundings, and

their inclusion in various biological environments, even at an intracellular level. Biomineralisation processes are dominated by Fe with its ease of hydrolysis in aqueous solution, its affinity for O, OH and S-containing ligands and redox behaviour contributing to the large variety of iron oxide biominerals found naturally (See **Table. 1**).

Table. 1 Types and functions of iron oxide biominerals

Formula	Mineral	Location	Organism	Function
Fe_3O_4	Magnetite	Intracelluar	Bacteria	Magnetoaxis
		Teeth	Chitons	Mechanical Strength
		Head	Tuna / Salmon	Magnetic Navigation
α-FeOOH	Goethite	Teeth	Limpets	Mechanical Strength
γ-FeOOH	Lepidocrocite	Filaments	Sponges	Unknown
		Teeth	Chitons	Mechanical Strength
$Fe_2O_3{\cdot}nH_2O$	Ferrihydrite	Ferritin	Plants	Storage Protein
		Teeth	Chitons	Precursor Phase
		Tooth surface	Beaver	Mechanical Strength

One of the most interesting examples shown in **Table. 1** are magnetotactic bacteria (Fig. 3) which produce intracellular magnetite (Fe_3O_4) in a chain of discrete crystals which aids navigation in the ambient geomagnetic field. The organism *Aquaspirillum magnetotacticum* contains 2% iron by weight and the presence of octahedral high spin Fe^{III} and both tetrahedral and octahedral high spin Fe^{II} has been identified via Mössbauer spectroscopy, which is consistent with the known inverse spinel structure of magnetite. Species in the northern hemisphere have a north seeking biological compass `needle`, while similar species in the southern hemisphere have an identical arrangement of magnetite crystals, with the opposite polarity (south seeking).[4,5] Bulk magnetite is ferrimagnetic due to the presence of both Fe^{3+} and Fe^{2+} ions whose non equivalent opposing magnetic moments contribute to the spontaneous magnetization. However in the case of the magnetism of individual crystals of magnetite, size and shape is of paramount importance. In crystals less than 5nm in size

the energy required to change the direction of the magnetic moment becomes comparable to the available thermal energy and hence leads to the loss of any permanent magnetic moment. This arises from the large surface-area to volume ratio which gives rise to a large number of Fe ions in unstable surface sites. Decreasing the surface-area to volume ratio by increasing the size of the crystals to 10 nm in size results in any single magnetic domain splitting internally into separate antiparallel domains. Magnetotactic bacteria produce crystals of magnetite in a critical region between 5-10 nm, whose narrow size region result in the greatest magnetization per unit volume, leading to a permanent single magnetic domain.[2] (Fig. 2)

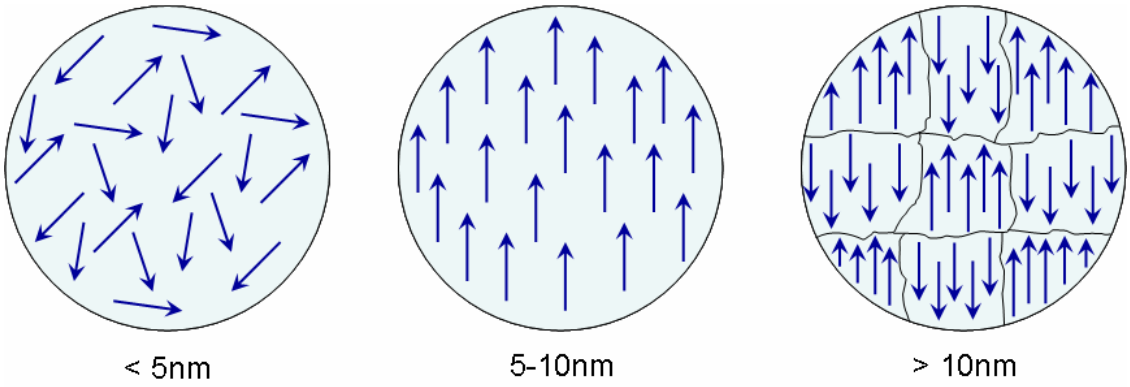

Fig. 2 Magnetic domains of magnetite.

Another interesting example of an oxo bridged poly Fe^{III} centre found in biological systems is the iron storage protein ferritin. The early evolution of organisms had a strong dependence on Fe, however the advent of photosynthesis about 2.5 billion years ago created a problem. H_2O was now used as a source of hydrogen and one of the main by-products of photosynthesis was O_2, which over the course of 300 million years led to what is known as the oxygen catastrophe. O_2 was toxic to all the anaerobic organisms at the time so what we take for granted as an essential precursor for life, was

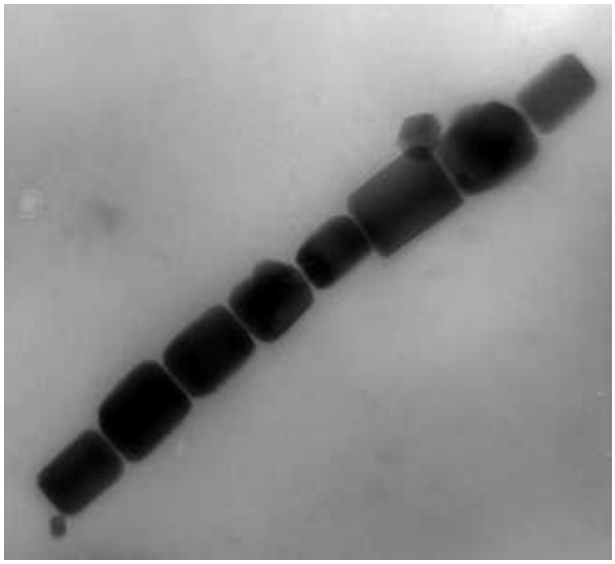

Fig. 3 TEM image of magnetotactic bacteria

initially a major ecological crisis. The environment was initially reducing with only 1% O_2 in the atmosphere rising to its current level of 21%, producing Fe^{III} *en mass* by oxidising the available Fe^{II}. The solubility of Fe^{III} is 10^{-9} times less than that for Fe^{II} so this caused a dilemma for all organisms dependant on iron. They could either move to environments devoid of oxygen or adapt and accommodate the low solubility of Fe^{III}. They `*chose*` to adapt with the protein ferritin able to store up to 4500 Fe^{III} ions in a soluble form which could then be used in oxygen transfer, electron transfer, nitrogen fixation, and DNA synthesis.[6]

The protein consists of a spherical protein coat called apoferritin which consists of 24 polypeptide subunits which can encapsulate an iron oxyhydroxide core containing up to 4500 Fe ions. Knowledge of the structure of the protein coat of ferritin, apoferritin (Fig. 4), is based on the X-ray crystallography of horse spleen apoferritin[7,8] which shows eight hydrophilic and six hydrophobic channels thought to be responsible for the entry and release of the Fe.[9,10] The Fe^{III} core of ferritin is thought to be formed by Fe^{II} oxidation on specific ferroxidase sites[11] or directly on the core surface[12], the structure of

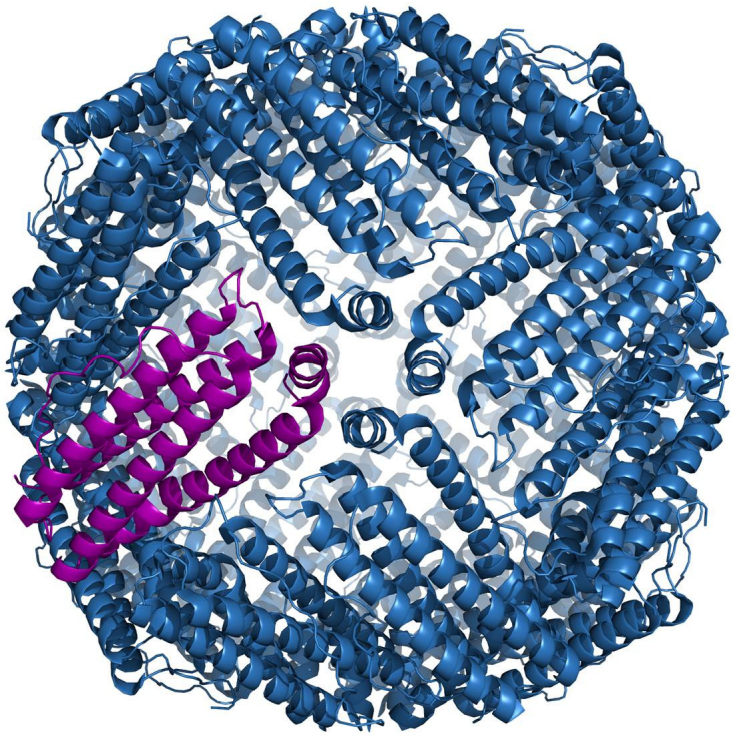

Fig. 4 Structure of apoferritin

which resembles ferrihydrite[13] (Fig. 5) with varying amounts of phosphate present affecting the crystallinity of the core.[14]

Mössbauer studies showed that ferritin is superparamagnetic below its Néel temperature of 240K, i.e it acts as a single magnetic domain.[15] Magnetic measurements show a correlation between the ferritin particle size and the quantum tunneling rate[16] which had been predicted by theory[17,18] and also reveal a spin flop transition at high fields associated with such antiferromagnetic systems.[16]

There has been a long standing interest in the function of certain proteins containing di-nuclear Fe centres in biological systems and with good reason: methane monooxygenase (MMO) can oxidise methane to methanol; hemerythrin is responsible

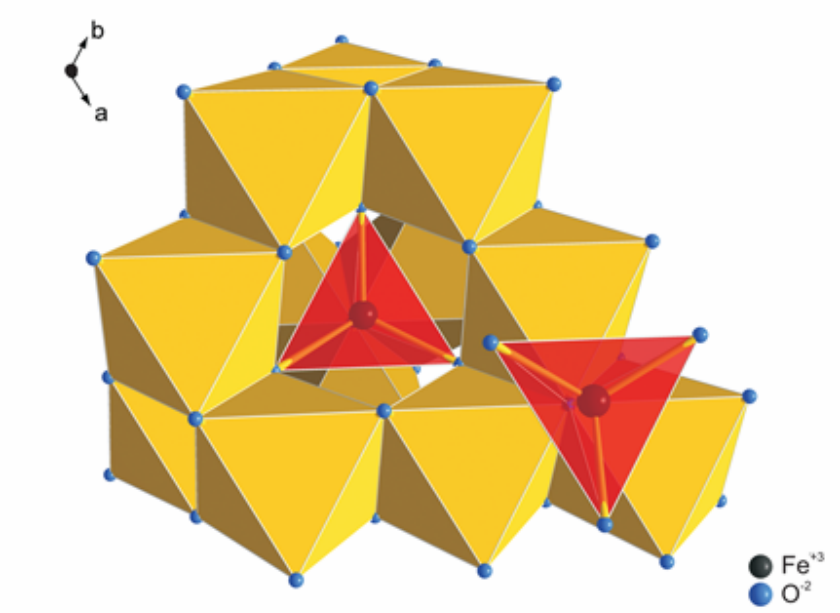

Fig. 5 Ideal ferrihydrite structure.

for O_2 transportation; ribonucleotide reductase catalyzes the conversion of ribonucleotides to deoxyribonucleotides and purple acid phosphatase catalzyes the dephosphorylation of phosphino proteins.

The catalytic cycle in MMO is known and understood to consist of four intermediates whose active site consists of a dinuclear iron centre capable of accessing the redox states [Fe^{II}, Fe^{II}], [Fe^{III}, Fe^{III}] and [Fe^{IV}, Fe^{IV}] (Fig. 6). Reduction of H_{ox}, an $Fe^{III}Fe^{III}$ state, leads to H_{red} in the $Fe^{II}Fe^{II}$ form which reacts with O_2 to form the intermediate species H_{peroxo}.[19-25] This subsequently decays to form Q which is a high-valent $Fe^{IV}Fe^{IV}$ species with a diamond $Fe^{IV}{}_2(\mu\text{-}O)_2$ core, which is directly responsible for the activation of the C-H bonds in the catalytic oxidation of methane to methanol.[26-34]

Several marine invertebrates contain oxygen transport metalloproteins called hemerythrins (Hr),[35] whose structure, determined by X-ray diffraction, identifies a dinuclear Fe centre at the active site of the protein.[36] The deoxygenated (deoxyHr) form

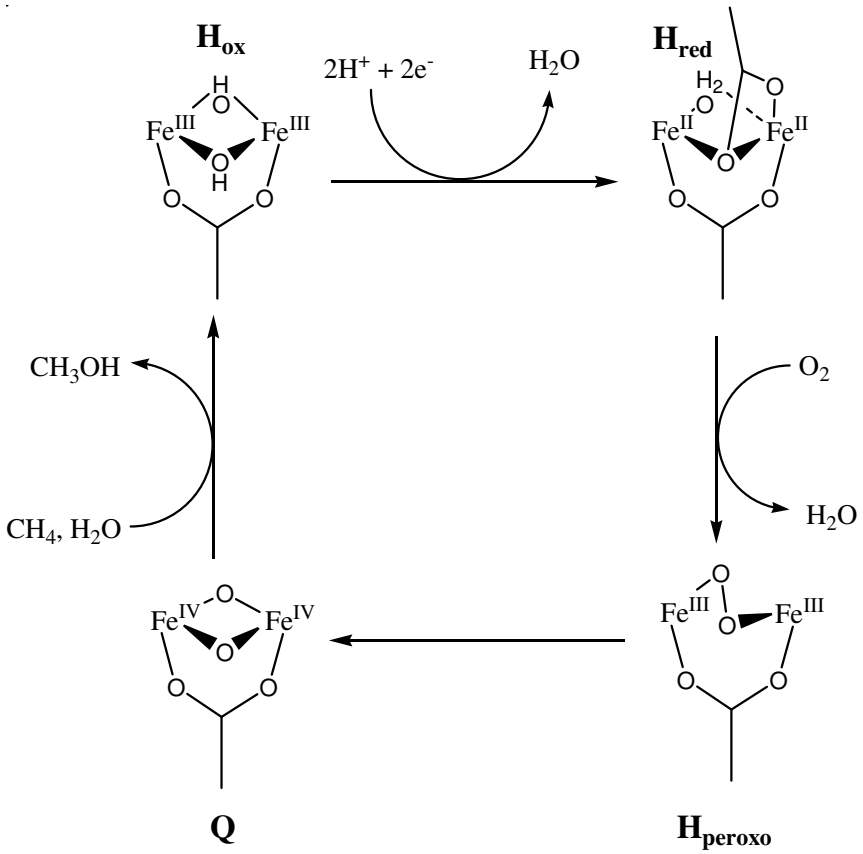

Fig. 6 The MMO catalytic cycle.

contains one six coordinate octahedral Fe^{II} connected to a five coordinate trigonal bipyramidal Fe^{II} via the carboxylate groups of glutamate, aspartate and one hydroxide group.[37-41] Binding of O_2 then sets up a reversible process where the bipyramidal Fe^{II} geometry changes to an octahedral Fe^{III} environment by terminal addition of a hydroperoxide[42] and the Fe-O bond distances shorten. This suggests the formation of an oxo bridge which is then hydrogen bonded to the hydroperoxide producing the oxygenated form (oxyHr) (Fig. 7). Due to the reversible nature of this process it is clear that the free energies of deoxyHr and oxyHr must be similar, indeed experimental values suggest that the oxyHr form is 7.3 kcal mol^{-1} lower than the deoxy form[35] which has been confirmed by quantum mechanical / molecular mechanical calculations.[43]

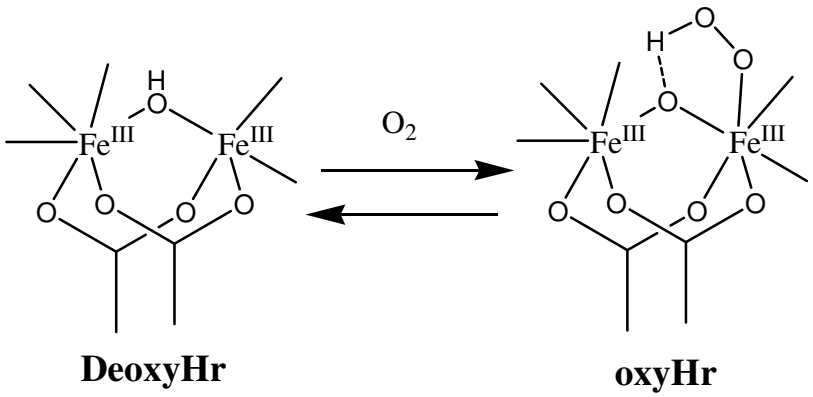

Fig. 7 Structures of deoxyHr and oxyHr

The dinuclear Fe centre in the class I protein ribonucleotide reductase (RNR) oxidises the amino acid tyrosine into a tyrosine radical which then converts ribonucleotides into deoxy ribonucleotides, which are the precursors to DNA[44-46] and have also been shown to catalyze hydroxylation reactions, specifically a tyrosine residue into 3,4 dihydroxyphenylalanine.[47] The intermediate, X, thought to be responsible for the catalytic oxidation has an $Fe^{III}Fe^{IV}(\mu\text{-}O)_2$ core as determined by ENDOR and Mössbauer spectoscopy. (Fig. 8)[45,48]

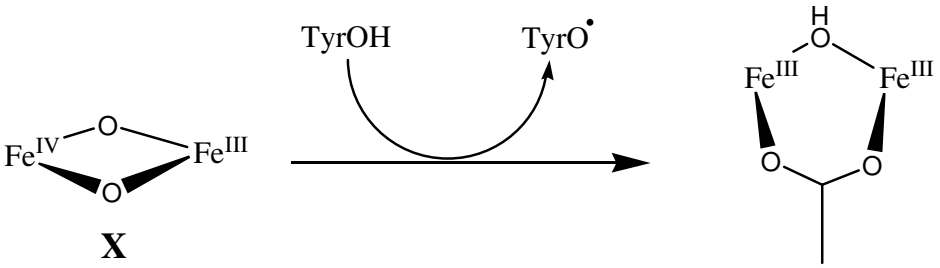

Fig. 8 RNR oxidation of tyrosine.

Mammalian purple acid phosphatases (PAP) such as uteroferrin and beef spleen PAP (bsPAP) catalyse the hydrolysis of activated phosphoric acid esters and anhdyrides.

The active site is an $Fe^{III}Fe^{II}$ centre as determined by Mössbauer, NMR, EXAFS, EPR, electrochemical and Raman methods.[49] The only crystal structure determination has been carried out on a plant rather than mammalian enzyme, the kidney bean PAP (kbPAP). This is actually an Fe^{III}-Zn^{II} centre although similarities in the local sequence around the metal ligating residues suggests the $Fe^{III}Fe^{II}$ centre has identical ligation, that is the metal centres are bridged via one μ-OH and the carboxylate group of an asparagine (Fig. 9).

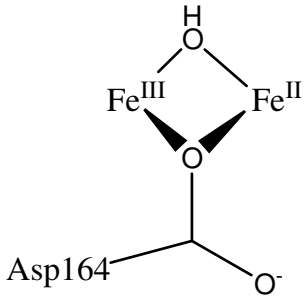

Fig. 9 Proposed structure of active site of mammalian PAPs.

A huge volume of work has been undertaken to model the active sites of such non-heme diiron proteins[50-54] for two reasons. The first is to mimic the function of enzymes such as MMO whose catalytic oxidation of methane could lead to new methods of producing methanol, a potential fuel source - although the effect of the local protein environment on the diiron centres in question would have to be taken into account. Secondly a comparison of the structural, mechanistic, and spectroscopic data of the model compounds with the properties of a protein under investigation could assist in the determination of the structure of the diiron active site.

Magneto-structural correlations

Small dinuclear Fe^{3+} complexes, similar to the diiron active site centres in biological systems (*vide supra*), are of interest from a magnetic viewpoint and were

amongst the first compounds to be studied to examine the relationship between the structure and magnetic properties and amongst the first series of compounds to be examined to develop magneto-structural correlations. The magnetic properties of exchange coupled dinuclear compounds have, for some time, been known to depend on the identity of the metal ions, the nature of the bridging ligands providing the super-exchange pathway and the bridging geometry, *i.e* the angles and distances. There have been a number of magneto-structural correlations published for the Fe-O-Fe moiety, which have attempted to describe the relationship between the strength of interaction (*J*) and the Fe···Fe distance, the Fe···O distance, and the Fe-O-Fe bridging angle. As yet, none have appeared universally correct.

For example Gerloch and Towl suggested a rapid decrease in J with decreasing Fe-O-Fe angle, with the maximum value expected for a bridging angle of 180º.[55] Gorun and Lippard suggested an approach which includes only one structural parameter P, which has units of distance (Å) and defined as half the shortest superexchange pathway between two Fe^{III} ions. Magnetic data from 36 dinuclear iron centres, which are all bridged by a ligand oxygen atom (oxo, hydroxo, alkoxo etc) and at least one other bridging ligand (carboxylate, sulphate etc), suggests there is a correlation between P and J, the exchange coupling constant, which is represented by an equation of the form:

$$-J = 8.763 \times 10^{11} \exp(-12.663P) \quad (\mathbf{1})$$

where *J* is in cm^{-1}, *P* in Å, and the exchange Hamiltonian is of the form $H = JS_1 \cdot S_2$. This correlation depends only on the average Fe-(μ-O) distance and is not valid for singly bridged dinuclear Fe^{3+} species. Attempts to correlate *J* with other structural parameters such as the Fe-(μ-O)-Fe angle were unsuccessful and as such the correlation shows no angular dependance.[56] Weihe and Güdel suggested that the physical meaning of the purely empirical parameters in **Eqn. 1** is obscure and propose the use of an

angular and radial overlap model to account for the dependency of *J* on both the Fe-(μ-O) distance and the Fe-(μ-O)-Fe angle yielding the equation:

$$J = 1.337 \times 10^{8}(3.536+2.488 \cos ø + \cos^{2} ø) \times \exp(-7.909r) \quad (\mathbf{2})$$

where ø is the Fe-(μ-O)-Fe angle (in degrees) and *r* is the mean bond Fe-(μ-O) bond length (in Å).[57] The angular dependence is less pronounced for larger *r* values and an increase of J with decreasing bridging angle ø is in direct contrast to that proposed in ref 55.

The only attempted magneto-structural correlation for alkoxide-bridged diiron(III) species was published by Caneschi and co-workers in 1997 who investigated molecules of the type $[Fe_2(OR)_2 L_4]$ where L is a β-diketonate ligand.[58] Based on their experimental evidence they suggested a linear dependence of *J* with the Fe–O–Fe bridging angle (*a*), expressed as $J = 1.48a - 135$, with the switch from antiferromagnetic to ferromagnetic occurring at $a = 91^{\circ}$. DFT calculations later refined the expression to $J = 5.0(1)a - 450(10)$.[59]

All of the magneto-structural correlations above are derived from data on dimeric systems and applying such correlations to larger systems, like high spin clusters and high nuclearity single-molecule magnets (SMM), is made difficult by the large number of magnetic orbitals and exchange interactions present in such systems.

Single Molecule Magnets (SMMs)

In 1980 Lis[60] described the synthesis of the mixed valence cluster $[Mn_{12}O_{12}(O_2CMe)_{16}(H_2O)_4]$, $[Mn_{12}OAc]$, via the oxidation of $Mn(OAc)_2{\cdot}4H_2O$ with MnO_4^- in an acetic acid / water mixture (Fig. 10). Although characterised structurally it took over a decade before it was shown that the eight outer Mn^{III} ions (S=2) and the four inner Mn^{IV} ions (S=3/2) were antiferromagnetically coupled to give a bistable S=10

ground state. This property was uncovered through high field magnetization, electron paramagnetic resonance (EPR) and ac susceptibility measurements. The out-of-phase component of the susceptibility (χ'') exhibited frequency-dependent peaks indicating slow relaxation of the magnetization and superparamagnetic-like behaviour. The presence of an energy barrier (ΔE) to the (thermally activated) reorientation of the magnetization (from "spin up" to "spin down") gave rise to hysteresis effects of purely molecular origin (similar to that found in bulk magnets) when the sample was cooled to around 2K and magnetization versus field measurements taken.[61-63] Clusters which behave in this manner, like [$Mn_{12}OAc$], are called Single-Molecule Magnets (SMMs).

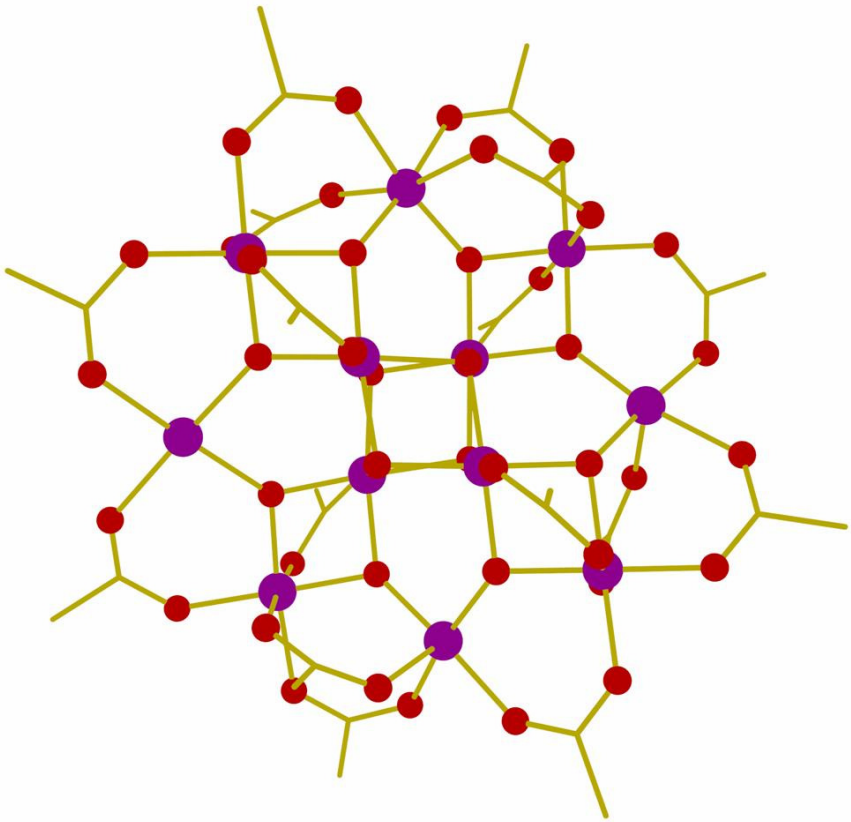

Fig. 10 Structure of [$Mn_{12}OAc$]. H atoms and H_2O`s omitted for clarity. Purple, Mn; Red, O.

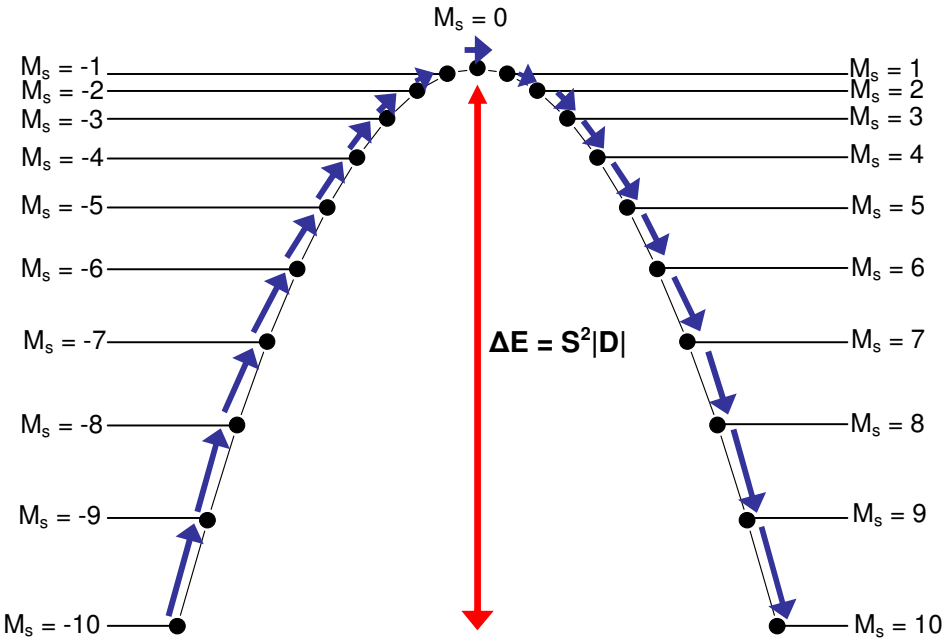

Fig. 11 Energy diagram showing the relative positons of the zero field split M_S levels of an $S_T = 10$ system as in $[Mn_{12}OAc]$, and the energy barrier ΔE.

The most striking feature of SMMs is that they straddle the quantum / classical interface with slow relaxation of their magnetization, displaying both quantum tunneling[64,65] and quantum phase interference.[66] SMMs also show promise in a number of potential applications[67-70] including as qubits for quantum computation where the required arbitrary superposition of quantum states with opposite projections of spin are produced by quantum tunnelling of the magnetisation (QTM), intermolecular exchange and/or multifrequency EPR pulses; and as high density information storage devices where the magnetization of an individual molecule is used as a bit of information. The full electronic and magnetic structure of several SMMs has been studied by a battery of techniques including magnetic circular dichroism,[71] solid state ^{55}Mn NMR,[72,73] ^{1}H

NMR[74] and ^{13}C NMR,[75] inelastic neutron scattering[76,77] and high field EPR.[78-81] Theoretical techniques including Density Functional Theory (DFT),[82-84] Monte Carlo[85] and *ab initio*[86] calculations in tandem with experimental techniques, have also provided some invaluable insights into the properties of SMMs.

In order for any SMM to function in real applications the blocking temperature, that is the temperature below which the sample can retain its magnetization in the absence of a magnetic field, must be raised. After the discovery of $[Mn_{12}OAc]$ many research groups have tried to increase the blocking temperature of SMMs. It became clear that to achieve this you must build molecules with the highest possible spin ground state, S_T. Any SMM properties associated with this spin ground state will be observed at (low) temperatures where only the spin ground state is populated. At higher temperatures thermal population of excited states destroys SMM behaviour. In addition a large, easy-axis (Ising) type anisotropy characterized by the negative axial zero field splitting (ZFS) parameter D, is required. The energy barrier (Fig. 11) thus occurs because the components $M_s = \pm S_T$ lie lowest in energy for a system with spin S_T; with the upper limits of the energy barrier equal to S_T^2 |D| (integer spins) and (S_T^2-1/4) |D| (non integer spins) (Fig. 12).

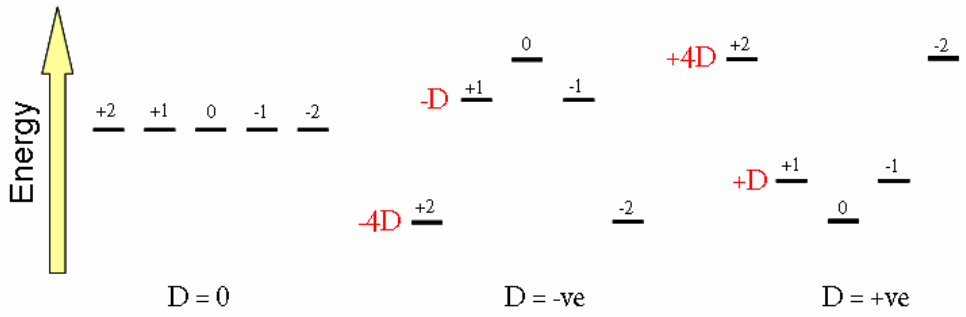

Fig. 12 Zero field splitting of the 5 M_s states +2,+1,0,-1,-2 of an S=2 system where $E(M_s) = M_s^2D$.

Beyond the many derivatives of $[Mn_{12}OAc]$ a substantial number of other manganese complexes have been shown to behave as SMMs. A far smaller number have been characterized using other 3d metals such as vanadium, cobalt, nickel and iron and mixed-metal combinations of 3d with 4d, 5d and 4f.[87] A significant breakthrough was the discovery that the mononuclear lanthanide complex (NBu_2) $[Pc_2Ln]^-$ TBA^+ (Ln=Tb,Dy) showed slow relaxation of the magnetization which was probed by multidimensional minimisation analysis of the magnetic susceptibility and ^1H NMR.[88,89] The origin of the superparamagnetism in the mononuclear lanthanide complexes originates from both the orbital and spin angular momentum and so the mechanism of the relaxation is different to that in transition metal SMMs. The long magnetization relaxation times are still a matter of debate but are thought to be caused by the energy required to equilibrate the spin-orbit ground state $\pm J_z$ upon removal of the applied external magnetic field - the *J* sublevels being separated by several hundred cm^{-1}.

There are essentially two synthetic methodologies in the construction of coordination compounds that exhibit SMM properties. The first is serendipitous self-assembly where a (flexible) ligand (one which has a large number of coordination modes) and a metal salt are mixed in a solvent leading to products that are rarely, if ever, predicted. Winpenny[90] and others argue that this serendipitous approach is a very useful one that, importantly, is not limited by the imagination of the scientist who prefers a more controlled or "designed" approach. The vast majority of SMMs have been made in such a serendipitous manner and we only need to briefly scan through the annals of chemistry to remind us of the role serendipity has had; the nobel prize in chemistry in 2000 was shared jointly by Alan J. Heeger, Alan G. MacDiarmid and Hideki Shirakawa for the development of conductive polymers[91] which was discovered when a foreign researcher mistranslated instructions and added a starting material a thousand times more concentrated than required; the discovery of *cis*-platin, $Pt(NH_3)_2Cl_2$, came about during the study of an electric field on the *Escherichia coli* bacteria[92] and Aspartame (Nutrasweet) was accidentally ingested by James Schlatter who was trying to develop a

test for an anti-ulcer drug.[93] A far less dramatic example is of course the discovery of $[Mn_{12}OAc]$ as the unexpected product of the reaction of Mn^{2+} and MnO_4^- in the presence of acetic acid. The desire to have full control over your product formation leads to a second approach that is labelled `rational molecular design`. Here the building blocks offer a much lower degree of flexibility and as such the geometry and properties of the products of such systems can often (though not always) be predicted. A well know example is in the use of polycyanometalates such as hexacyanochromate (III) where the central metal ion is surrounded by six CN^- groups in an octahedral environment which can then bind to six more metal ions to form a cluster which has the shape of an octahedron with chromium at the centre.[94] Here the linear CN^- bridge offers strong magnetic exchange interactions and the sign of these interactions is easily predicted. These are molecular analogues of 3D Prussian Blues.

Whether one relies on serendipitous self-assembly or rational design (or somewhere in between), the choice of metal ion is paramount when building coordination compounds capable of displaying SMM behaviour. One necessary goal is to achieve a large (or at least non-zero) spin ground state. Assembling single ions with large spin states is an obvious and intuitive step. This is why ions such as high spin Mn^{III}, Fe^{II} (S=2) and Fe^{III} (S=5/2) are routinely used. If we assume ferromagnetic interactions then we can assemble a large molecular spin ground state from a relatively small number of metal ions. In addition Ferritin has been shown to display superparamagnetism and has more recently been investigated for quantum tunneling of the magnetisation (*vide supra*).

Synthetic Methodologies

The final product of the hydrolysis of Fe^{III} in water is ferrihydrite, Fe_2O_3, due to the inability of Fe^{III} to stabilise the terminal oxo ligands - a situation true for all systems containing only oxo, hydroxo or aqua ligands. In the presence of additional ligands the

situation is different and solutions of Fe^{III} ions in the presence of carboxylates have been known for over a century to form stable trinuclear complexes of the form $[Fe_3O(O_2CR)_6(H_2O)_3]X$ (where X= Cl, ClO_4^-, NO_3^- etc) (Fig. 13).[95] Alkoxides may also be used to block the growth of the ferrihydrite particles. For instance a methanolic solution of Fe^{III} in the presence of sodium methoxide produces $Na_2[OFe_6(OMe)_6](MeOH)_6$.[96] By blocking core growth and carefully controlling the pH in aqueous media one can avoid precipitation of the insoluble Fe_2O_3 and trap discrete polynuclear oxy/hydroxide iron clusters with an organic sheath. The variety of organic ligands used to block the oxide growth is essentially limitless and many, much more complicated, ligands have been employed. In addition one need not restrict the solvent to H_2O.

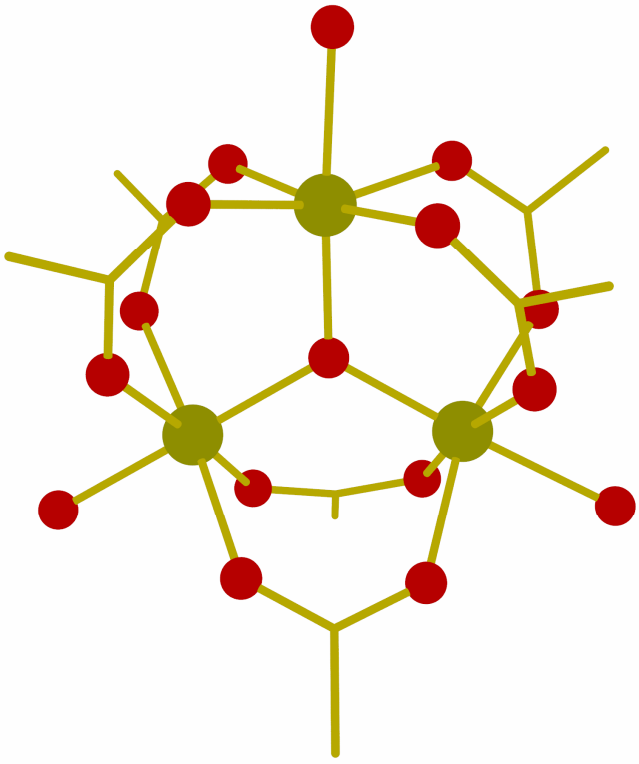

Fig. 13 The molecular structure of $[Fe_3O(O_2CMe)_6(H_2O)_3]Cl$. Colour code: Fe = green; O = red; C = gold. H atoms and Cl^- anion omitted for clarity.

For example, the product $[Fe_8O_2(OH)_{12}(tacn)_6]Br_8$ (tacn = 1,4,7-triazacyclononane) (Fig. 14) ([Fe_8Br]), is obtained via the reaction of $[Fe(tacn)Cl_3]$ with NaBr in H_2O and pyridine, which, as with $[Mn_{12}OAc]$, was discovered almost a decade before its SMM properties were revealed.[97] At the time this was claimed to be the first oxo/hydroxo bridged Fe^{III} cluster with a nuclearity greater than three. The structure (Fig. 14) comprises four Fe^{III} ions linked via two μ_3-O^{2-} ligands to form a "butterfly" structure, which is then bridged to a further four Fe^{III} ions via twelve hydroxide bridges. These along with the wings of the butterfly are then capped by the six tridentate tacn ligands. The use of an irreducible tensor approach (ITO) in the calculation of the Hamiltonian matrix along with magnetic susceptibility studies made it possible to identify an S=10 spin ground state.[98] Mössbauer, AC magnetic susceptibility,[99] HF EPR,[99,100] polarised neutron diffraction (PND)[101], inelastic neutron scattering (INS)[102] and far infrared measurements[103] confirmed the superparamagnetic behaviour and full electronic structure of [Fe_8Br]. [Fe_8Br] was the second compound, after $[Mn_{12}OAc]$, to show hysteresis of molecular origin,[104] and was the first compound in which detailed physics of the QTM were developed, elucidating in detail the mechanisms involved in such processes.[105-107]

The discovery and subsequent magnetic characterisation of [Fe_8Br] stimulated the pursuit of other polynuclear iron compounds that would show similar properties. Notable Fe^{III} SMMs discovered since then include: $[Fe_{19}(metheidi)_{10}(OH)_4O_6(H_2O)_{12}](NO_3)$ (H_3metheidi = N-(1-Hydroxy-2-methylethyl) aminodiacetic acid), the largest nuclearity and spin iron SMM[108-109]; a family of Fe_4 stars, $[Fe_4(OMe)_6(dpm)_6]$ (Hdpm = dipivaloylmethane)[110-112], $[Fe_4(thme)_2(dpm)_6]$ (H_3thme = 1,1,1-tris(hydroxymethyl)-ethane)[113] and $[Fe_4(thme)_2(CH_3CH_2CH_2OH)]$,[114]; $[Fe_{10}Na_2O_6(OH)_4(O_2CPh)_{10}(chp)_6(H_2O)_2(Me_2\ CO)_2]$ (Hchp = 6-chloro-2-pyridinol)[115-116]; $(NEt_4)[Fe_{11}O_4(O_2CPh)_{10}(thme)_4(dmhp)_2Cl_4]$ (Hdmhp = 4,6-dimethylhydroxy-

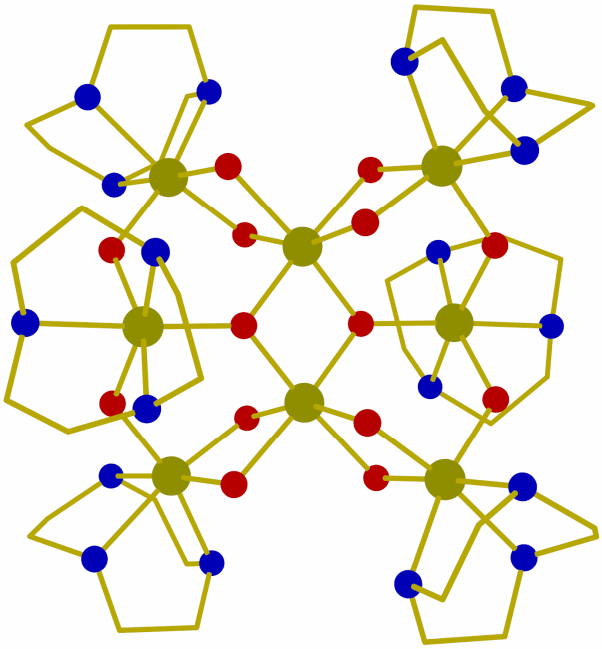

Fig. 14 The molecular structure of $[Fe_8O_2(OH)_{12}(tacn)_6]Br_8$. Colour code: Fe = green; O = red; N = blue; C = gold. H atoms and Br anions omitted for clarity.

pyrimidine),[117] and $[Fe_9O_4(OH)_5(heia)_6(Hheia)_2]$ (Hheia = N-(1-Hydroxyethyl)aminoaceticacid).[118] Two Fe^{II} SMM`s discovered include $[Fe_4(sae)_4(MeOH)_4]$ (H_2sae = Salicylidene-2-ethanolamine)[119] and $[Fe_9(N_3)_2(O_2CMe)_8(pdol)_4]$ (H_2pdol = Dipyridyldiol),[120] synthesised by replacing two μ_4-OH^- ligands with two μ_4-N_3^- on an analogous compound $[Fe_9(OH)_2(O_2CMe)_8(pdol)_4]$. It is clear that there are still only a handful of iron based SMMs compared to the examples based on managanese (> 100). This is due to the isotropic nature of the high spin Fe^{III} ion (the ground term for the free ion is the orbital singlet ^6S) and difficulty in synthesising polynuclear Fe^{II} and/or mixed-valence $Fe^{II/III}$ compounds.

Despite all the advances in the field and hundred of papers published on the subject, until recently the SMM with the highest blocking temperature was still the

prototype SMM [$Mn_{12}OAc$] (T_B ~3K). In 2006, however the Christou group derivatised [$Mn_{12}OAc$] where each of the O_2CMe groups was replaced by a O_2CH_2Br group to give [$Mn_{12}BrAc$] with a blocking temperature, T_B, of 3.6K which corresponds to an effective energy barrier to the reorientation of the magnetization, U_{eff}, value of 74.4K.[121] This higher symmetry derivative had a larger U_{eff} value than [$Mn_{12}OAc$] (60-64K) and at the time represented the only improvement in terms of effective energy barrier on the original [$Mn_{12}OAc$]. However in 2007 Brechin and co-workers synthesised a hexametallic Mn cluster, [$Mn^{III}_6O_2$(Et-sao)$_6$(O_2CPh(Me)$_2$)(EtOH)$_6$], which exhibits an effective energy barrier, U_{eff} = 86.4K (12K above [$Mn_{12}BrAc$]) and a blocking temperature of 5K (1.4 K above [$Mn_{12}BrAc$]).[122] This shows that progress is being made in the field and as such the search for new first row transition metal SMMs still remains an intensive area of research with the molecular magnetism community.

The Magnetocaloric Effect (MCE)

Molecules with a large spin ground state and negligible or zero ZFS do not behave as SMMs although the isotropic nature of the large spin can lead to an enhanced magnetocaloric effect (MCE) and hence to the possibility of acting as magnetic refrigerants. The MCE is the change of the magnetic entropy S_m upon application and removal of an applied field in an adiabatic system which leads to a decrease in temperature. Debye and Giaugue suggested this fundamental principle and proposed that the MCE could be used for refrigeration in adiabatic demagnetisation processes.[123-124] This is shown in Fig. 15 as the curves of S_m vs T for a paramagnet of spin S.

Ignoring any ZFS effects a spin ground state *S* has 2S+1 degenerate M_s levels, and the total magnetic entropy S_m = R ln(2S+1) (where R is the gas constant.) Applying a magnetic field induces Zeeman splitting and therefore the ordering of the 2S+1 M_s levels, with a concomitant decrease of S_m. If we start at point A at temperature T_i and at field H_i (H=0) and we isothermally magnetise the sample from A to B(T_i, H_f) we get a

decrease in magnetic entropy (ΔS_m). If we then thermally isolate the sample and remove the field we can perform an adiabatic demagnetisation from B to C(T_f, H_i). Under such conditions the total entropy of the system must remain constant so the increase in the magnetic entropy ΔS_m must be compensated

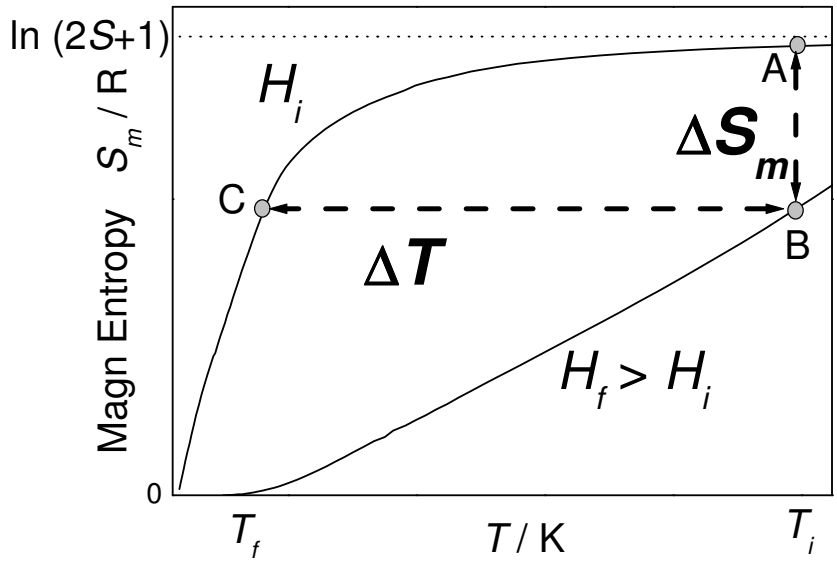

Fig. 15 Magnetic entropy S_m as a function of temperature T, for two different applied magnetic fields H_i and H_f where $H_i < H_f$. A → B: isothermal magnetization with entropy change ΔS_m; B → C: adiabatic demagnetization with resulting temperature change $\Delta T = T_f - T_i$.

by an equal but opposite change in the entropy associated with the lattice which results in a decrease in temperature (ΔT_{ad}) of the sample. Clusters with large magnetic moments could therefore potentially offer very large changes of S_m at low temperature (where only the ground state is populated) and such materials could compete favourably[125-130] with the existing intermetallic and lanthanide compounds currently employed as magnetic refrigerant materials. The large moments can provide large magnetic entropy changes by being easily polarisable via application of an applied field. making them

very attractive in terms of MCE. However the magnetic anisotropy associated with SMMs, which determines the blocking temperature, is a drawback in the efficiency of the MCE. The increased anisotropy lowers ΔT_{ad} and ΔS_m by shifting them towards higher temperatures which results in lower magnetic entropies and therefore lower MCE parameters (ΔS_m and ΔT_{ad} are the characteristic parameters associated with the MCE). For example the prototype SMMs $[Mn_{12}OAc]$ and $[Fe_8Br]$ were the first molecular materials to be studied in terms of MCE by Tejada and co-workers[125-126] and they found that the ΔS_m values were limited to 11 and 12.5 J kg^{-1} K^{-1} respectively although these were very difficult to observe because of the large anisotropies present in both systems. Preferred molecules would therefore be clusters with a large spin ground state (S) and small or zero anisotropy. The tetradecametallic cluster $[Fe_{14}(bta)_6O_6(OMe)_{18}Cl_6]$ possesses a very large spin ground state, S=25 while the ZFS of the ground state is negligible (D ~ 0 cm^{-1}). This results in huge MCE at low temperatures with ΔS_m = 17.6±2.8 J kg^{-1} K^{-1} at 6K for ΔH = (7-0)T as determined from variable temperature, variable field specific heat and magnetization experiments.[131-132] A similar study on the decametallic mixed valent cluster $[Mn_{10}O_4Br_4(amp)_6(ampH_2)(HampH_2)]Br_3$ revealed a ferromagnetic S=22 spin ground state with a D value of 0 cm^{-1}.[130] Subsequent specific heat measurements revealed a ΔS_m value of 13.0 J kg^{-1} at around 2.2K for ΔH = (7-0) T amongst the highest values ever reported for this temperature range.[128] This suggests such species to be excellent candidate for use in an adiabatic demagnetisation refrigerator which would permit cooling to below 0.1K - such micro-refrigeration having potential application in astrophysics in ultra sensitive X-ray detectors.[133-134]

Project Aims

The project is focused on the synthesis and magnetic characterisation of polynuclear iron clusters using derivatised salicylaldoxime ligands and a controlled hydrolysis approach.

Physical Methods

Elemental analyses (C, H, N) were performed by the EaStCHEM microanalysis service. IR spectra were recorded as KBr pellets in the 4000-400 cm^{-1} range on a JASCO FT/IR-410 spectrometer. Variable temperature magnetic susceptibility (dc and ac) measurements were made on a Quantum Design MPMS-XL SQUID magnetometer equipped with a 7T magnet. Data were collected on powdered samples restrained in eicosane to prevent torquing. Diamagnetic corrections were applied using Pascal's constants. Magnetic studies below 1.8 K were carried out on single crystals using a micro-SQUID apparatus operating down to 40 mK[135] and using a magnetometer consisting of a micro hall bar. Specific heat measurements were carried out in a Quantum Design physical property measurement system PPMS setup for the $0<H<7$ T magnetic field range.

X-ray Crystallography

Diffraction data were collected at 150 K on a Bruker Smart Apex CCD diffractometer equipped with an Oxford Cryosystems LT device, using Mo radiation The structures were solved by Paterson methods (DIRDIF for **1**,**7**,**9** and **11**),[136] direct methods (SIR92 for **2**, **8**, **10** and **14**-**17,** SHELXS-97 for **4** and **6**, SHELXS86 for **3**, **5**, **12**, **13**, **18**) and refined by full-matrix least squares against F^2 (SHELXL-97 for **1,** **4**, **6-9**, **11**, **12**, CRYSTALS for **2**, **3**, **5**, **10**, **13**-**18**).[137-138] Crystallographic data and structure refinement details are listed in Tables 2.1-2.2, for complexes **1-6**; Tables 3.2 - 3.5, for complexes **7-17** and Table 4.1 for complex **18**.

Supporting Information

Selected bond lengths (Å) and angles (deg), BVS calculations and CIF files for complexes **1-18** can be found in the attached CD.

References

1. W. Schneider, *Chimia*, 1988, **42**, 9.
2. *Biomineralization Principles and Concepts in Bioinorganic Materials Chemistry*, S. Mann, 2001, Oxford University Press.
3. *Biomineralization: Chemical and Biochemical Perspectives*, ed.S. Mann, J.Webb and R. J. P.Williams, 1988,VCH, NewYork;
4 R. P. Blakemore, *Annu. Rev. Microbiol*, 1982, **36**, 217.
5 R. B. Frankel, G. C. Papaefthymiou, R. P. Blakemore, W. O`Brien, *Biochim. Biophys. Acta*, 1983, **763**, 147.
6 *The Evolution of the Atmosphere*, J. C. G. Walker, 1977, Macmillan, New York.
7 J. L. Smith, J. M. A. Smith, P. M. Harrsion, *Adv. Inorg. Biochem.*, 1983, **5**, 39.
8 S. H. Banyard, D. K. Stammers, P. M. Harrison, *Nature*, 1980, **288**, 298.
9 P. M. Harrison, A. Treffry, T. H. Lilley, *J. Inorg. Biochem.* 1986, **27**, 287.
10 J. G. Wardeska, B. Vigilone, N. D. Chasteen, *J. Biol. Chem.* 1986, **261**, 6677.
11 R. R. Crichton, F. Roman, *J. Mol. Cat*, 1978, **4**, 75.
12 I. G. Macara, T. G. Hoy, P. M. Harrison, *Biochem. J*., 1972, **126**, 151.
13 P. M. Harrison, F. A. Fischback, T. G. Hoy, G. H. Harris, *Nature*, 1967, **216**, 1188.
14 S. Mann, J. V. Bannsiter, R. J. P. Williams, *J. Mol. Biol*., 1986, **188**, 225.
15 T. G. St. Pierre, D. H. Jones, D. P. E. Dickson, *J. Magn. Magn. Mat.,* 1987, **69**, 276.

16 S. Gider, D. D. Awschalom, T. Douglas, S. Mann, M. Chaparala., *Science*, 1995, **268**, 77.

17 B. Barbara, E. M. Chudnovsky, *Phys. Lett. A*, 1990, **145**, 205.

18 I. V. Krive, O. B. Zaslavskii, *J. Phys. Condens. Matter,* 1990, **2**, 9457.

19 A.C. Rosenzweig, P. Nordlund, P.M. Takahara, C.A. Frederick, S.J. Lippard, *Chem. Biol*. 1995, **2**, 409.

20 A.C. Rosenzweig, C.A. Frederick, S.J. Lippard, P. Nordlund, *Nature.*, 1993, **366,** 537.

21 A.C. Rosenzweig, S.J. Lippard, *Acc. Chem. Res.,* 1994, **27**, 229.

22 D.A. Whittington, S.J. Lippard, *J. Am. Chem. Soc.*, 2001, **123**, 827.

23 J.G. Dewitt, J.G. Bentsen, A.C. Rosenzweig, B. Hedman, J. Green, S. Pilkington, G.C. Papaefthymiou, H. Dalton, K.O. Hodgson, S.J. Lippard, *J. Am .Chem .Soc.*, 1991, **113**, 9219.

24 B.G. Fox, K.K. Surerus, E. Mu¨nck, J.D. Lipscomb*, J. Biol. Chem*., 1988, **263**, 10553.

25 N. Elango, R. Radhakrishnan, W.A. Froland, B.J. Wallar, C.A. Earhart, J.D. Lipscomb, D.H. Ohlendorf, *Protein Sci.,* 1997, **6**, 556.

26 K.E. Liu, D.L. Wang, B.H. Huynh, D.E. Edmondson, A. Salifoglou, S.J. Lippard, *J. Am. Chem. Soc*., 1994, **116**, 7465.

27 K.E. Liu, A.M. Valentine, D.L. Wang, B.H. Huynh, D.E. Edmondson, A. Salifoglou, S.J. Lippard, *J. Am. Chem. Soc*., 1995, **117**, 10174.

28 S.K. Lee, J.C. Nesheim, J.D. Lipscomb, *J. Biol. Chem*., 1993, **268**, 21569.

29 L.J. Shu, J.C. Nesheim, K. Kauffmann, E. Münck, J. D. Lipscomb, L. Que, *Science*., 1997, **275**, 515.

30 A.M. Valentine, S.S. Stahl, S.J. Lippard, *J. Am. Chem. Soc*., 1999, **121**, 3876.

31 J.D. Lipscomb, L. Que, *J. Biol. Inorg. Chem*., 1998, **3**, 331.

32 S.-K. Lee, B.G. Fox, W.A. Froland, J.D. Lipscomb, E. Münck, *J. Am. Chem. Soc*., 1993, **115**, 6450.

33 K.E. Liu, A.M. Valentine, D. Wang, B.H. Huynh, D.E. Edmondson, A. Salifoglou, S.J. Lippard, *J. Am. Chem. Soc*., 1995, **117**, 10174.

34 H.-H.T. Nguyen, A.K. Shiemke, S.J. Jacobs, B.J. Hales, M.E. Lidstrom, S.I. Chan, *J. Biol. Chem*., 1994, **269**, 14995.

35 R.E. Stenkamp, *Chem. Rev*., 1994, **94**, 715.

36 M.A. Holmes, I. Letrong, S. Turley, L.C. Sieker, R.E. Stenkamp, *J. Mol. Biol*., 1991, **218**, 583.

37 J.L. York, A.J. Bearden, *Biochemistry*., 1970, **9**, 4549.

38 K. Garbett, D.W. Darnall, I.M. Klotz, R.J. Williams, *Arch. Biochem. Biophys*., 1969, **135**, 419.

39 T.C. Brunold, E.I. Solomon, *J. Am. Chem. Soc*., 1999, **121**, 8277.

40 K. Zhang, E.A. Stern, F. Ellis, J. Sandersloehr, A.K. Shiemke, *Biochemistry*., 1988, **27**, 7470.

41 A.K. Shiemke, T.M. Loehr, J. Sandersloehr, *J. Am. Chem. Soc*., 1984, **106**, 4951.

42 R.E. Stenkamp, L.C. Sieker, L.H. Jensen, J.D. Mccallum, J. Sandersloehr, *Proc. Natl. Acad. Sci. USA*., 1985, **82**, 713.

43 M. Wirstam, S. J. Lippard, R. A. Friesner, *J. Am. Chem. Soc.,* 2003, **125**, 3980.

44 M. Fontecave, P. Nordlund, H. Eklund, P. Reichard, *Adv. Enzym.*, 1992, **65** 147.

45 B.E. Sturgeon, D. Burdi, S. Chen, B.-H. Huynh, D.E. Edmondson, J. Stubbe, B.M. Hoffman, *J. Am. Chem. Soc*., 1996, **118**, 7551.

46 W.H. Tong, S. Chen, S.G. Lloyd, D.E. Edmondson, B.H. Huynh, J. Stubbe, *J. Am. Chem. Soc*., 1996, **118** 2107.

47 A. Åberg, M. Ormö , P. Nordlund, B.-M. Sjöberg, *Biochemistry*., 1993, **32**. 9845.

48 D. Burdi, B.E. Sturgeon, W.H. Tong, J. Stubbe, B.M. Hoffman, *J. Am. Chem. Soc.*, 1996, **118**, 281.

49 R. Than, A. A. Feldmann, B. Krebs, *Coord. Chem. Rev.*, 1999, **182**, 211 and references therin.

50 K. S. Murray, *Coord. Chem. Rev.*, 1974, **12**, 1.

51 D. M. Kurtz, Jr, *Chem. Rev.*, 1990, **90**, 585.

52 P. Nordlund, H. Eklund, *Curr. Opin. Struct. Biol.*, 1995, **5**, 758.

53 L. Que, Jr, *J. Chem. Soc., Dalton Trans.,* 1997, 3933.

54 M. Fontecave, S. Ménage, C. Duboc-Toia, *Coord. Chem. Rev.*, 1998, **178-180**, 1555.

55 M. Gerloch, E. D. McKenzie, A. D. C. Towl, *J. Chem. Soc. (A).*, 1969, 2850.

56 S. M. Gorun, S. J. Lippard, *Inorg. Chem.*, 1991, **30**, 1625.

57 H. Weihe, H. U. Güdel, *J. Am. Chem. Soc.*, 1997, **119**, 6539.

58 F. Le Gall, F. Fabrizi. de Biani, A. Caneschi, P. Cinelli, A. Cornia, A. C. Fabretti, D. Gatteschi, *Inorganica. Chimica. Acta.*, 1997, **262**, 123.

59 A. Caneschi, F.Fabrizi de Biani, L. Kloo, P.Zanello, *Int. J. Quantum Chem.*, 1999, **72**, 61.

60 T. Lis, *Acta. Crystallogr. Sect. B.*, 1980, **36**, 2042.

61 A. Caneschi, D. Gatteschi, R. Sessoli, *J. Am. Chem. Soc.*, 1991, **131**, 5873.

62 R. Sessoli, H. R. Tsai, A. R. Schake, S. Wang, J. B. Vincent, K. Folting, D. Gatteschi, G. Christou, D. N. Hendrickson, *J. Am. Chem. Soc.*, 1993, **115**, 1804.

63 R. Sessoli, D. Gatteschi, A. Caneschi, M. A. Novak, *Nature.*, 1993, **365**, 141.

64 J. R. Friedman, M. P. Sarachik, J. Tejada, R. Ziolo, *Phys. Rev. Lett.*, 1996, **76**, 3830

65 L. Thomas, F. Lionti, R. Ballou, D. Gatteschi, R. Sessoli, B. Barbara, *Nature.,* 1996, **383**, 145.

66 W. Wernsdorfer, R, Sessoli, *Science.*, 1996, **383**, 145.

67 M. N. Leuenberger, D. Loss, *Science.*, 1999, **284**, 133.

68 W. Wernsdorfer, N. Aliaga-Acalde, D. N. Hendrickson, G. Christou, *Nature.*, 2002, **416**, 406.

69 S. Hill, R. S. Edwards, N. Aliaga-Acalde, G. Christou, *Science.,* 2003, **302**, 1015

70 J. Tejada, E. M. Chudnovsky, E. del Barco, J. M. Hernandez, T. P. Spiller,

Nanotechnology., 2001, **12**, 181.

71 E. J. L. McInnes, E. Pidcock, V. S. Oganesyan, M. R. Cheesman, A. K. Powell, A. J. Thomson, *J. Am. Chem. Soc.*, 2002, **124**, 9219.

72 A. Morello, O. N. Bakharev, H. B. Brom, L. J. de Jongh, *J. Magn. Magn. Mater.*, 2004, **272-276**, 1015.

73 A. Morello, O. N. Bakharev, H. B. Brom, L. J. de Jongh, *Polyhedron.,* 2003, **22**, 1745.

74 D. Procissi, B. J. Suh, A. Lascialfari, F. Borsa, A. Caneshi, A. Cornia, *J. Appl. Phys.*, 2002, **91**, 7173.

75 R. M. Achey, P. L. Kuhns, W. G. Moulton, A. P. Reyes, N. S. Dalal, *Polyhedron.,* 2001, **20**, 1745.

76 S. Carreta, E. Liviotti, G. Amoretti, R. Caciuffo, A. Caneschi, D. Gatteschi, *Phys. Rev. B.*, 2002, **65**, 052411.

77 H. Andres, R. Basler, H. U. Gudel, G. Aromi, G. Christou, H. Buttner, B. Ruffle, *J. Am. Chem. Soc.*, **122**, 12469.

78 A. L. Barra, D. Gatteschi, R. Sessoli, *Chem-Eur. J.*, 2000*,* **6**, 1608.

79 A. L. Barra, *Appl. Magn. Reson.*, 2001, **21**, 619.

80 A. Bouwen, A. Caneschi, D. Gatteschi, E. Goovaerts, D. Schoemaker, L. Sorace, M. Stefan, *J. Phys. Chem. B.*, 2001, **105**, 2658.

81 D. Zipse, J. M. North, N. S. Dalal, S. Hill, R. S. Edwards, *Phys. Rev. B.*, 2003, **68**, 184408.

82 T. Baruah, M. R. Pederson, *Int. J. Quantum. Chem.*, 2003, **93**, 324.

83 J. Kortus, M. R. Pederson, T. Baruah, N. Bernstein, C. S. Hellberg, *Polyhedron.*, **22**, 1871.

84 K. Park, M. R. Pederson, S. L. Richardson, N. Aliaga-Alcade, G. Christou, *Phys. Rev. B.*, 2003, **68**, 020405.

85 C. Benelli, J. Cano, Y. Journaux, R. Sessoli, G. A. Solan, R. E. P. Winpenny, *Inorg. Chem.*, 2001, **40**, 188.

86 A. E. Clark, E. R. Davidson, *J. Chem. Phys.*, 2001, **115**, 7382.

87 G. Aromi, E. K. Brechin, *Synthesis of 3d Metallic Single-Molecule Magnets,* Structure & Bonding, Springer Berlin / Heidelberg, Volume 122/2006.

88 N. Ishikawa, M. Sugita, T. Ishikawa, S. Koshihara, Y. Kaizu, *J. Am. Chem. Soc.*, 2003, **125**, 8694.

89 N. Ishikawa, M. Sugita, T. Ishikawa, S. Koshihara, Y. Kaizu, *J. Phys. Chem. B.*, 2004, **108**, 11265.

90 R. E. P. Winpenny, *J. Chem. Soc., Dalton Trans.,* 2002, 1.

91 H. Shirakawa, E. J. Louis, A. G. MacDiarmid, C. K. Chiang, A. J. Heeger, *J. Chem. Soc., Chem. Commun.*, 1977, 578.

92 B. Rosemberg, L. Van Camp., J. E. Trosko, V. H. Mansour, *Nature.*, 1969, **222**, 385.

93 G. D. Searle and Co, United States patent 3,492,131.

94 V. Marvaud, C. Decroix, A. Scuiller, C. Guyard-Duhayon, J. Vaisserman, F. Gonnet, M. Verdaguer, *Chem. Eur. J.*, 2003, **9**, 1677.

95 R. Weinland, *Einführung in die Chemie der Komplex-Verbindungen,* Verlag von Ferdinand Enke, Stuttgart, 1919, 345 and references therein.

96 K. Hegetschweiler, H. Schmalle, H. M. Streit, W. Schneider, *Inorg. Chem.*, 1990, **29**, 3625.

97 K. Weighardt, K. Pohl, I. Jibril, G. Huttner, *Angew. Chem. Int. Ed. Engl.*, 1984, **23**, 77.

98 C. Delfs, D. Gatteschi, L. Pardi, R. Sessoli, K. Wieghardt, D. Hanke, *Inorg. Chem.*, 1993, 32, 3099.

99 A. L. Barra, P. Debrunner, D. Gatteschi, C. E. Schulz, R. Sessoli, *Europhys, Lett.*, 1996, **35**, 133.

100 A. L. Barra, D. Gatteschi, R. Sessoli, *Chem. Eur. J.*, 2000, **6**, 1608.

101 Y. Pontillion, A. Caneschi, D. Gatteschi, R. Sessoli, E. Ressouche, J. Schweizer, E. Lelievre-Berna, *J. Am. Chem. Soc.*, 1999, **121**, 5342.

102 R. Cacuiffo, G. Amoretti, A. Murani, R. Sessoli, A. Caneschi, D. Gatteschi, *Phys. Rev. Lett.*, 1998, **81**, 4744.

103 A. A. Mukhin, V. D. Travkin, A. K. Zvezdin, S. P. Lebedev, A. Caneschi, D. Gatteschi, *Europhys. Lett.*, 1998, **44**, 778.

104 C. Sangregorio, T. Ohm, C. Paulsen, R. Sessoli, D. Gatteschi, *Phys. Rev. Lett.*, 1997, **78**, 4645.

105 T. Ohm, C. Sangregorio, C. Paulsen, *Eur. Phys. J.*, 1998, **6**, 195.

106 T. Ohm, C. Sangregorio, C. Paulsen, *J. Low. Temp. Phys.*, 1998, **113**, 1141.

107 W. Wernsdorfer, T. Ohm, C. Sangregorio, R. Sessoli, D. Mailly, C. Paulsen, *Phys. Rev. Lett.*, 1999, **82**, 3903.

108 D. J. Price, F. Lionti, R. Ballou, P. T. Wood, A. K. Powell, *Philos. Trans. R. Soc. Lond. Ser. A-Math. Phys. Eng. Sci.*, 1999, **357**, 3099.

109 J. C. Goodwin, R. Sessoli, D. Gatteschi, W. Wernsdorfer, A. K. Powell, S. L. Heath, *J. Chem. Soc. Dalton Trans.*, 2000, 1835.

110 A. Caneschi, A. Cornia, A. C. Fabretti, S. Foner, D. Gatteschi, R. Grandi, L. Schenetti, *Chem-Eur. J.*, 1996, **2**, 1379.

111 G. L. Abbati, A. Cornia, A. C. Fabretti, S. Foner, D. Gatteschi, R. Grandi, L. Schenetti, *Inorg. Chem.*, 1997, **36**, 6443.

112 A. L. Barra, A. Caneschi, A. Cornia, F. F. de Biani, D. Gatteschi, C. Sangregorio, R. Sessoli, L. Sorace, *J. Am. Chem. Soc.*, 1999, **121**, 5302.

113 A. Cornia, A. C. Fabretti, P. Garrisi, C. Mortalo, D. Bonacchi, D. Gatteschi, R. Sessoli, L. Sorace, W. Wernsdorfer, A. L. Barra, *Angew. Chem. Int. Ed.*, 2004, **43**, 1136.

114 M. Moragues-Canovas, P. Riviere, L. Ricard, C. Paulsen, W. Wernsdorfer, G. Rajaraman, E. K. Brechin, T. Mallah, *Adv. Mater.*, 2004, **16**, 1101.

115 C. Benelli, S. Parsons, G. A. Solan, R. E. P. Winpenny, *Angew. Chem. Int. Ed. Engl.*, 1996, **35**, 1825.

116 C. Benelli, J. Cano, Y. Journax, R. Sessoli, G. A. Solan, R. E. P. Winpenny,

Inorg. Chem., 2001, **40**, 188.

117 L. F. Jones, E. K. Brechin, D. Collison, M. Helliwell, T. Mallah, S. Piligkos, G. Rajaraman, W. Wernsdorfer, *Inorg. Chem.*, 2003, **42**, 6601.

118 G. W. Powell, H. N. Lancashire, E. K. Brechin, D. Collison, S. L. Heath, T. Mallah, W. Wernsdorfer, *Angew. Chem. Int. Ed.*, 2004, **43**, 5772.

119 H. Oshio, N. Hoshino, T. Ito, *J. Am. Chem. Soc.*, 2000, **122**, 12602.

120 A. K. Boudalis, B. Donnadieu, V. Nastopoulos, J. J-C. Modesto, A. Mari, Y. Sanakis, J-P. Tuchages, S. P. Perlepes, *Angew. Chem. Int. Ed.*, 2004, **43**, 2266.

121 N. E. Chakov, S.-C. Lee, A. G. Harter, P. L. Kuhns, A. P. Reyes, S. O. Hill, N. S. Dalal, W. Wernsdorfer, K. A. Abboud, G. Christou, *J. Am. Chem. Soc.*, 2006, **128**, 6975.

122 C. J. Milios, A. Vinslava, W. Wernsdorfer, S. Moggach, S. Parsons, S. P. Perlepes, G. Christou, E. K. Brechin, *J. Am. Chem. Soc.*, 2007, **129**, 2754.

123 P. Debye, *Ann. Phys.*, 1926, **81**, 1154;

124 W.F. Giauque, *J. Am. Chem. Soc.,* 1927, **49**, 1864.

125 F. Torres, J. M. Herna´ndez, X. Bohigas and J. Tejada, *Appl. Phys. Lett.*, 2000, **77**, 3248.

126 F. Torres, X. Bohigas, J. M. Herna´ndez and J. Tejada, *J. Phys.: Condens. Matter,* 2003, **15**, L119.

127 M. Affronte, A. Ghirri, S. Carretta, G. Amoretti, S. Piligkos,G. A. Timco and R. E. P. Winpenny, *Appl. Phys. Lett.*, 2004, **84**, 3468.

128 M. Evangelisti, A. Candini, A. Ghirri, M. Affronte, E. K. Brechin and E. J. L. McInnes, *Appl. Phys. Lett.*, 2005, **87**, 072504.

129 M. Evangelisti, A. Candini, A. Ghirri, M. Affronte, S. Piligkos, E. K. Brechin, E. J. L. McInnes, *Polyhedron.*, 2005, **24**, 2573.

130 M. Manoli, R. D. L. Johnstone, S. Parsons, M. Murrie, M. Affronte, M. Evangelisti, E. K. Brechin, *Angew. Chem. Int. Ed.*, 2007, **46**, 4456.

131 D. Low, L. F. Jones, A. Bell, E. K. Brechin, T. Mallah, E. Riviére, S. J. Teat, E.

J. L. McInnes, *Angew. Chem. Int. Ed.*, 2003, **42**, 3781.

132 R. Shaw, R. H. Laye, L. F. Jones, D. M. Low, C. Talbot-Eeckelaers, Q. Wei, C. J. Milios, S. Teat, M. Helliwell, J. Raftery, M. Evangelisti, M. Affronte, D. Collison, E. K. Brechin, E. J. L. McInnes, *Inorg. Chem.*, 2007, **46**, 4968.

133 D. A. Wollman, K. D. Irwin, G. C. Hilton, L. L. Dulcie, D. E. Newbury, J. M. Martins, *J. Microscopy*, 1997, **188**, 196.

134 F. Giazotto, T. T. Heikkila, A. Luukanen, A. M. Savin, J. P. Pekola, *Rev. Mod. Phys.*, 2006, **78,** 217.

135 W. Wernsdorfer, *Adv. Chem. Phys*., 2001, **118**, 99.

136 P. W. Betteridge, J. R. Carruthers, R. I. Cooper, K. Prout, D. J. Watkin, *J. Appl. Crystallogr*., 2003, **36**, 1487.

137 P. T. Beurskens, G. Beurskens, W. P. Bosman, R. E. Gelder, S. Garcia-Granda, R. O. Gould, R. Israel, J. M. M. Smits, *The DIRDIF96 Program System,* Technical Report of the Crystallography Laboratory, University of Nijmegen, The Netherland, 1996.

138 G. M. Sheldrick, *SHELXL-97, Program for refinement of crystal structures*, University of Gottingen, Germany, 1997.

Chapter 2
Simple Synthetic Routes to Molecular Magnetite

Introduction

The magnetic properties of large polymetallic cluster compounds have attracted much attention in the last decade or so since the discovery that the magnetisation of a dodecametallic manganese cluster relaxes so slowly that the molecule can be considered to be a zero-dimensional 'magnet'.[1] Such complexes have enormous potential, since their possible applications include high density information storage in which each bit of information is stored as the magnetisation orientation of an individual molecule, and as qubits for quantum computation where the required arbitrary superposition of quantum states with opposite projections of spin could be produced by either quantum tunneling of the magnetisation (QTM), inter-molecular exchange, or multi-frequency EPR pulses.[2] There are now several species displaying such behaviour – and several successful synthetic strategies have been employed, ranging from the self-assembly of manganese carboxylate clusters,[3] to molecular Prussian Blue analogues[4], to heterometallic 3d-4f complexes,[5] and recently to 'simple' 4f monometallic species.[6] Molecular nanomagnets in which the high spin ground state is *isotropic* in nature cannot function as SMMs, but are ideal candidates to act as low temperature magnetic refrigerants. Enhanced magnetocaloric effects (MCE) have previously been demonstrated for the isotropic high spin molecules $[Fe_{14}]$[7] and $[Mn_{10}]$[8] with values for $[Fe_{14}]$ the largest known for any material below 10K, competing favourably with intermetallic and lanthanide compounds typically used as magnetic refrigerant materials.[9]

An extremely attractive alternative synthetic strategy is to try to make molecular analogues of naturally occurring magnetic oxides. The 'traditional' way to achieve this is to perform *'controlled'* hydrolysis in which a metal salt (e.g. $Fe(NO_3)_3{\cdot}9H_2O$) is dissolved in water and the pH of the solution raised by

addition of base in order to form, in this case, an iron hydroxide or oxy-hydroxide core whose growth is then stopped or capped by the addition of a polydentate chelating ligand. Without the addition of the capping ligand, it would be expected that the hydrolysis of original hexa-aqua $[Fe(H_2O)_6]^{3+}$ ion would give rise firstly to an insoluble iron hydroxide which then may transform itself into an oxy-hydroxide (e.g. goethite; α-Fe-O(OH)) phase and perhaps eventually to a thermodynamically stable oxide (e.g. haemitite; Fe_2O_3). Unfortunately there exists few such examples in the literature with, perhaps, the most interesting still being the prototype complex $[Fe_{19}O_6(OH)_{10}(metheidi)_{10}(H_2O)_2]^+$ (and its analogues) first characterised in 1992.[10] Here, iron nitrate is dissolved in H_2O and the pH of the solution raised to approximately 3.5 through the addition of pyridine. Addition of the polydentate 'H_3metheidi' (N-(1-Hydroxymethylethyl)iminodiacetic acid; $\{N(CH_2CO_2H)_2(CH(CH_3)CH_2OH)\}$) ligand then crystallises the product within one day in yields up to a maximum of approximately 40%. The structure of this complex is related to the $Mg(OH)_2$ brucite lattice. We have discovered, and herein report, heptadecametallic iron clusters that are all-ferric pieces of molecular magnetite, that can be made by simply dissolving $FeBr_3$ in pyridine or an analogous base which acts simultaneously as solvent, base and ligand.

Experimental Section

All manipulations were performed under aerobic conditions using chemicals as received, unless otherwise stated.

Synthetic Procedures

$Hpy[Fe_{17}O_{16}(OH)_{12}(py)_{12}Br_4]Br_4\cdot 8py\cdot MeCN$ (**1**·8py·MeCN).

$FeBr_3$ (0.691 g, 2.34 mmol) was added to pyridine (25 ml) and stirred for 60 minutes. 25ml MeCN was then added and the solution stirred for 90 minutes. The

solution was then filtered and allowed to evaporate slowly, producing complex **1** in 3 days in approximately 10% yield. The dried complex analysed as solvent free. Found (calc.%): $C_{65}H_{78}Fe_{17}O_{28}N_{13}Br_8$; C, 25.74 (25.46), H, 2.45 (2.17), N, 5.86 (5.94). IR data (KBr pellet; cm^{-1}): 1633m, 1604s, 1484m, 1445s, 1216m, 1071m, 1040m, 1013m, 915m, 758m, 698m, 512m, 463m, 411m.

$(HPy)_{0.5}[Fe_{17}O_{16}(OH)_{12}(py)_{12}Br_4]Br_{3.5}$ (2).

$FeBr_3$ (0.5g, 1.69 mmol) was added to pyridine (30 ml) and stirred for 30 minutes. The solution was filtered and layered with IPA (isopropyl alcohol) producing complex **1** in 3 days in approximately 40% yield. The dried complex analysed as solvent free. Found (calc.%): $C_{62.5}H_{75}Fe_{17}O_{28}N_{12.5}Br_{7.5}$; C, 24.52 (25.04), H, 2.57 (2.52), N, 5.78 (5.84). IR data (KBr pellet; cm^{-1}): 1636s, 1539vs, 1482s, 1414m, 1359w, 1223w, 1112m, 1049vs, 943s, 583m.

$Hpy[Fe_{17}O_{16}(OH)_{12}(py)_{12}Br_4]Br_4 \cdot Me_2CO \cdot 0.5py \cdot 2H_2O$

(**3**·Me_2CO·0.5py·$2H_2O$).

$FeBr_3$ (0.691 g, 2.34 mmol) was added to pyridine (25 ml) and stirred for 60 minutes. The solution was filtered and layered with acetone, producing complex **1** in 3 days in approximately 10% yield. The dried complex analysed as solvent free. Found (calc.%): $C_{65}H_{78}Fe_{17}O_{28}N_{13}Br_8$; C, 25.86 (25.46), H, 2.35 (2.17), N, 5.74 (5.94). IR data (KBr pellet; cm^{-1}): 1634m, 1604s, 1538m, 1485s, 1445s, 1216s, 1152m, 1073m, 1040m, 1013m, 922m, 759m, 699m, 511m, 466m, 415m.

$[Fe_{17}O_{16}(OH)_{12}(iso\text{-}quin)_{12}Br_3(H_2O)_3]Br_4 \cdot 6iso\text{-}quin \cdot 3H_2O$

(4·6isoquin·$3H_2O$**).**

$FeBr_3$ (1 g, 3.38 mmol) was added to iso-quinoline (20 ml) and stirred for 30 minutes. The solution was filtered and layered with acetone producing complex **4** in 3 days in approximately 25% yield. The dried sample analysed as **4**·6 (iso-quin). Found (calc.%): $C_{162}H_{144}Fe_{17}O_{31}N_{18}Br_7$; C, 45.40 (44.75), H, 3.14 (3.34), N, 5.66 (5.80). IR data (KBr pellet; cm^{-1}): 1631s, 1594s, 1499m, 1459m, 1385s,

1277m, 1212m, 1045m, 1013m, 909m, 822s, 745m, 635s, 509m, 482m, 418m.

$[Fe_{17}O_{16}(OH)_{12}(3,5\text{-lut})_{12}Br_4]Br_3 \cdot H_2O$ (**5**·H_2O).

$FeBr_3$ (1 g, 3.38 mmol) was added to 3,5 lutidine (20 ml) and stirred for 30 minutes. The solution was filtered producing complex **5** in 3 days in approximately 15% yield. The dried sample analysed as **5**·H_2O. Found (calc.%): $C_{84}H_{122}Fe_{17}O_{29}N_{12}Br_7$; C, 30.68 (30.83), H, 3.82 (3.76), N, 5.16 (5.14). IR data (KBr pellet; cm^{-1}): 1634s, 1537vs, 1486m, 1446s, 1212s, 1075m, 1040m, 1013m, 916m, 585m.

$[Fe_{17}O_{16}(OH)_{12}(\beta\text{-pic})_{12}Br_4]Br_3$ (**6**).

$FeBr_3$ (0.834g, 2.82 mmol) was added to β-picoline (20 ml) and stirred for 30 minutes. The solution was filtered and layered with acetone producing complex **6** in 3 days in approximately 40% yield. The dried sample analysed as solvent free. Found (calc.%): $C_{72}H_{96}Fe_{17}O_{28}N_{12}Br_7$; C, 27.86 (28.02), H, 3.20 (3.14), N, 5.58 (5.45). IR data (KBr pellet; cm^{-1}): 1637s, 1539vs, 1486m, 1459s, 1215s, 1075m, 1040m, 1013m, 920m, 585m.

Results and Discussion

Synthesis

Dissolution of $FeBr_3$ in pyridine, followed by approximately thirty minutes of stirring produces a dark red solution, which, after filtration and slow evaporation, produces complex **1** in three days. The yield is improved by layering the solution with a co-solvent such as diethyl-ether, hexanes, MeCN or THF etc. In all cases the complex produced crystallises in the trigonal space group *R*-3. However, if the co-solvent is an alcohol, such as isopropyl alcohol (IPA) the $[Fe_{17}]$ cluster (**2**) crystallises in the cubic space group *P*a-3. Layering a pyridine solution of $FeBr_3$ with acetone results in a $[Fe_{17}]$ cluster which crystallises in the

triclinic space group *P*-1 (**3**). The resultant change in the packing of the molecules within the crystal has important consequences for the observed (low temperature) magnetic properties (*vide infra*). Simply substituting the pyridine with a 'similar' base allows us to produce a family of analogous complexes. For example, dissolving $FeBr_3$ in iso-quinoline produces the complex $[Fe_{17}O_{16}(OH)_{12}(iso\text{-}quin)_{12}Br_3(H_2O)_3]Br_4$ (**4**) which again crystallises in the trigonal space group *R*-3; whilst dissolving $FeBr_3$ in 3,5-lutidine produces the complex $[Fe_{17}O_{16}(OH)_{12}(3,5\text{-}lut)_{12}Br_4]Br_3$ (**5**) which crystallises in the tetragonal space group *I*41/*a*. In addition dissolving $FeBr_3$ in β–picoline affords the complex $[Fe_{17}O_{16}(OH)_{12}(\beta\text{-}pic)_{12}Br_4]Br_3$ (**6**) which crystallises in the monoclinic space group $P2_1/c$. Thus, by simply changing base and co-solvent, a whole family of $[Fe_{17}]$ clusters has been isolated from an extremely simple reaction - and therefore there potentially exists a plethora of new compounds that could be made in a similar manner. In each case the source of the oxide and hydroxide ions is clearly the base (solvent), as reactions performed in dried (water-free) solvents do not produce the heptadecametallic clusters **1**-**6**.

As all 6 complexes are essentially the same, both structurally and magnetically, in what follows we will limit our discussion, in general, to complex **1** (Fig. 2.1) except where there are significant differences in the observed properties.

Description of Structures

$Hpy[Fe_{17}O_{16}(OH)_{12}(py)_{12}Br_4]Br_4$ (1) Selected bond lengths and angles are given in Table 2.3. Complex **1** (Fig. 2.1) contains a central tetrahedral Fe^{III} ion linked *via* μ_4-oxo bridges to twelve outer octahedral Fe^{III} ions - forming a truncated tetrahedron (Fig. 2.2). The faces of this tetrahedron are capped by four further Fe^{III} ions linked *via* a combination of μ_3-oxo and μ_2-hydroxo ligands. The inner Fe^{III} ion and the four outer Fe^{III} ions sit in the tetrahedral sites of the lattice with the others occupying the octahedral sites. The four bromide ions cap the outer tetrahedral Fe^{III} ions with the pyridine molecules capping the octahedral

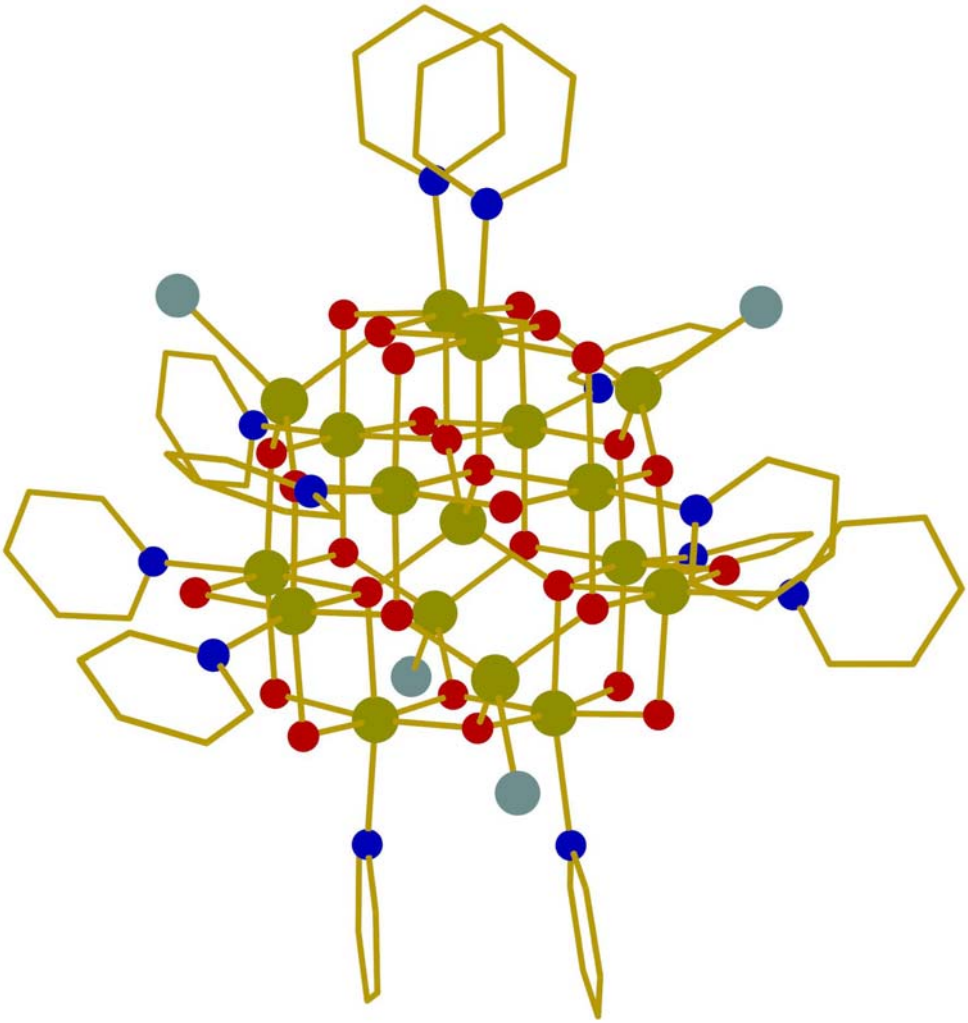

Fig. 2.1. The molecular structure of complexes **1-3**; colour scheme, Fe = green, O = red, N = blue; Br = green, C = gold

Fe^{III} ions (Fig. 2.1). The Fe-O-Fe bridges fall into two clear categories (Table 2.2):those that connect the tetrahedral Fe^{III} ions to the octahedral Fe^{III} ions are all characterised by angles in the range 122 - 126º, whilst those that bridge solely between octahedral Fe^{III} ions are characterised by angles in the range 94 - 98º. All the Fe centres (both tetrahedral and octahedral) are Fe^{III} ions, as confirmed by bond length and charge balance considerations, and Bond Valence Sum (BVS)

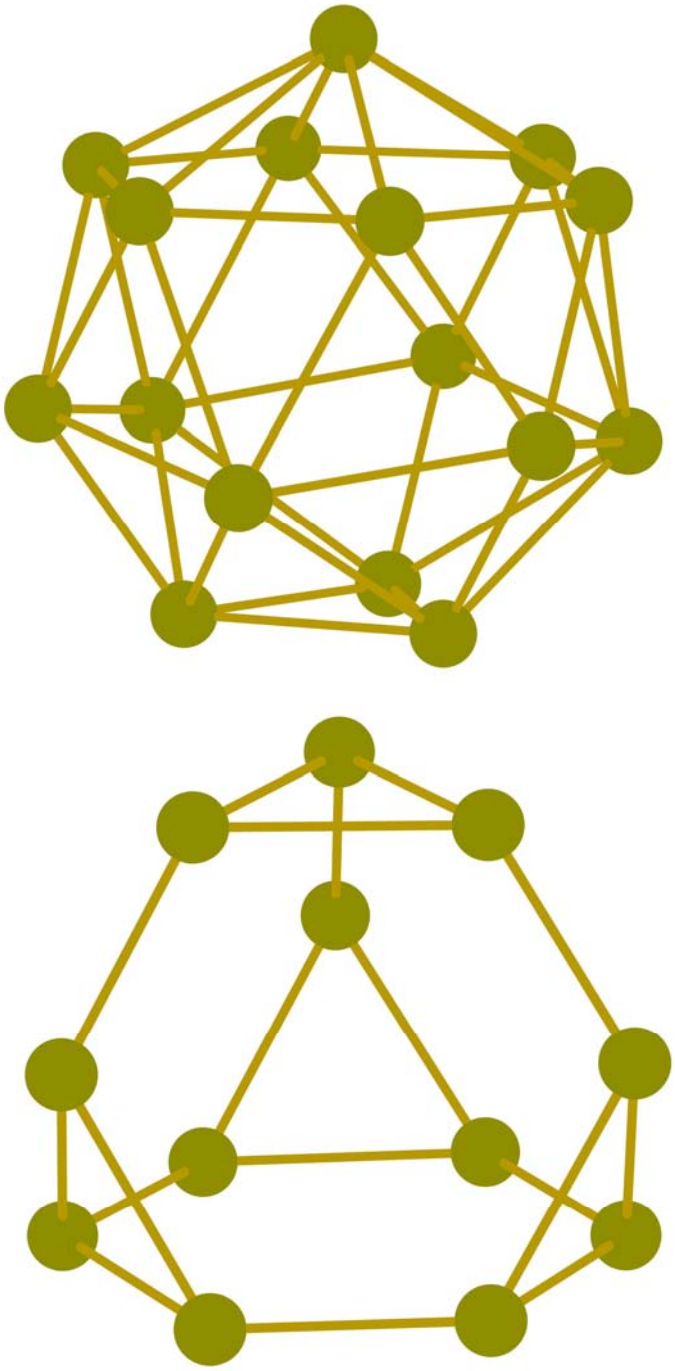

Fig. 2.2. The metallic core common to complexes **1-6** (top); the central unit is a hexagonal antiprism capped on the upper face by a single Fe ion, and on the lower face by three Fe ions (top). The truncated tetrahedron formed by the octahedral Fe ions (bottom). The central octahedral Fe ion has been excluded for clarity.

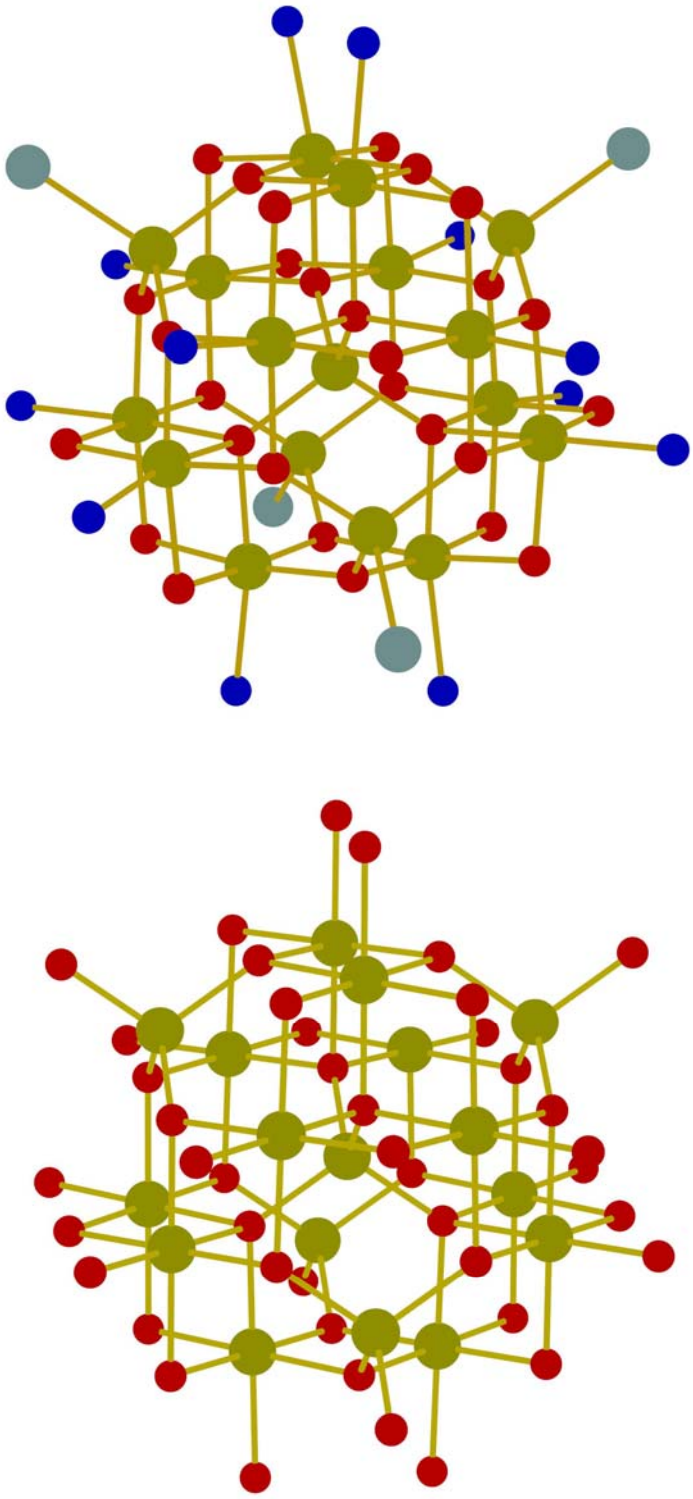

Fig. 2.3. A comparison of the central core of **1-6** (top) to magnetite (bottom).

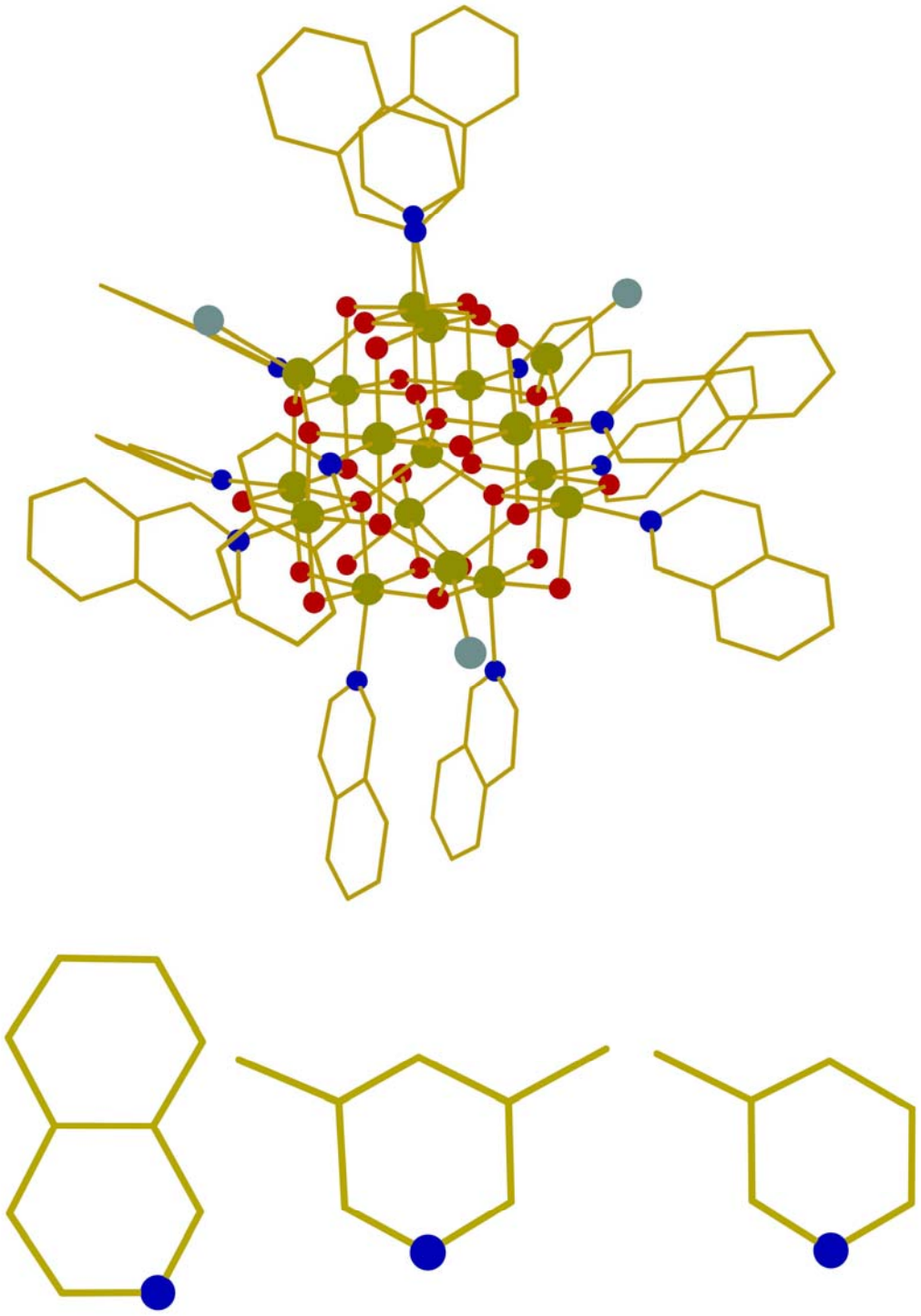

Fig. 2.4. The structure of complex **4** (top); colour scheme, Fe = green, O = red, N = blue; Br = green, C = gray. Structure of isoquinoline (bottom left), 3,5 lutidine (bottom middle) and β-picoline (bottom right).

calculations. This is in contrast to the situation in magnetite where half the octahedral sites in the lattice are occupied by Fe^{II} ions. The assignment of OH^- *vs* O^{2-} was also achieved on the basis of geometry and BVS calculations (Table A.2.2). A closer inspection of the core of **1** reveals that it is a fragment of the iron and oxygen positions defined by the magnetite lattice as shown in the comparison of **1** to the corresponding fragment of magnetite in Fig. 2.3. The coordination spheres of the 'outer' tetrahedral Fe^{III} centres are completed by terminal bromide ions while the 'outer' octahedral metal sites contain terminal pyridines. For complexes **2-6,** the structures remain essentially the same with the iso-quinoline, 3,5 lutidine and β-picoline ligands occupying the pyridine sites (**4**, **5** and **6**)**.** In **4** three H_2O molecules are terminally coordinated to an octahedral Fe^{III} ion in contrast to the situation in **1-3** and **5-6** where the equivalent Fe^{III} site is tetrahedral completed by a terminal bromide ion. (Fig. 2.4).

The packing diagrams for **1-6** are shown in Figs 2.5-2.10. In the crystal lattice of **1** there are OH···Br^- hydrogen bonds between three μ_2-hydroxy groups and lattice Br^- anions (O···Br^{--}, 3.288(2)Å, 3.339(2)Å, 3.379(2)Å) with each of these four lattice Br^- anions sitting in the four hydrogen bond 'cavities` created by the twelve μ_2-hydroxy groups (Fig. 2.5). The same is true for **2** (O···Br^-, 3.343(2)Å, 3.318(2)Å, 3.350(2)Å) but with the fourth Br^- also hydrogen bonded to three μ_2-hydroxy groups (O···Br^-, 3.282(2)Å) on a neighbouring molecule, effectively creating hydrogen bonded pairs of $[Fe_{17}]$ clusters (Fig. 2.6) - leading to the difference in the packing in the crystal between **1** and **2**. . In **3** there also exists four hydrogen bond interactions between the three μ_2 hydroxy groups and the four lattice Br^- anions (O···Br^-, 3.345(2)Å, 3.364(2)Å, 3.299(2)Å, 3.350(2)Å, 3.355(2)Å, 3.285(2)Å,3.336(2)Å, 3.347(2)Å, 3.326(2)Å, 3.374(2)Å, 3.406(2)Å, 3.266(2)Å), with chains of **3** lying parallel to the ab plane, formed via interactions between a pyridine and a terminal Br^- (C···Br^-, 3.600(2)Å) and a pyridine with a lattice Br^- anion (C···Br^-, 3.818(2)Å). These rows are then hydrogen bonded to each other via a terminal Br^- ion and a pyridine (C···Br^-, 3.580(2)Å) and between

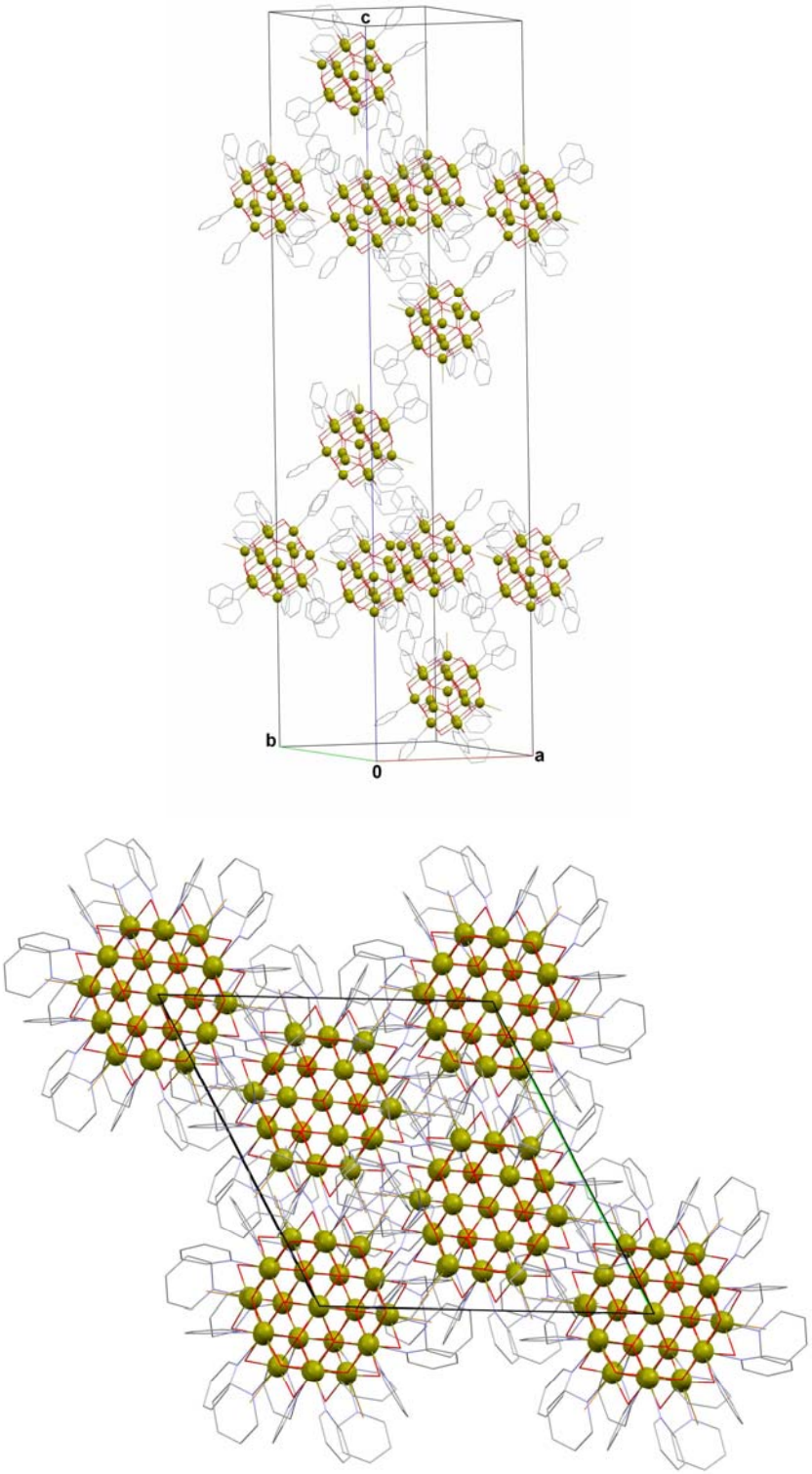

Fig. 2.5 The packing of molecules of **1** in the unit cell (top) and viewed along the c-axis (bottom).

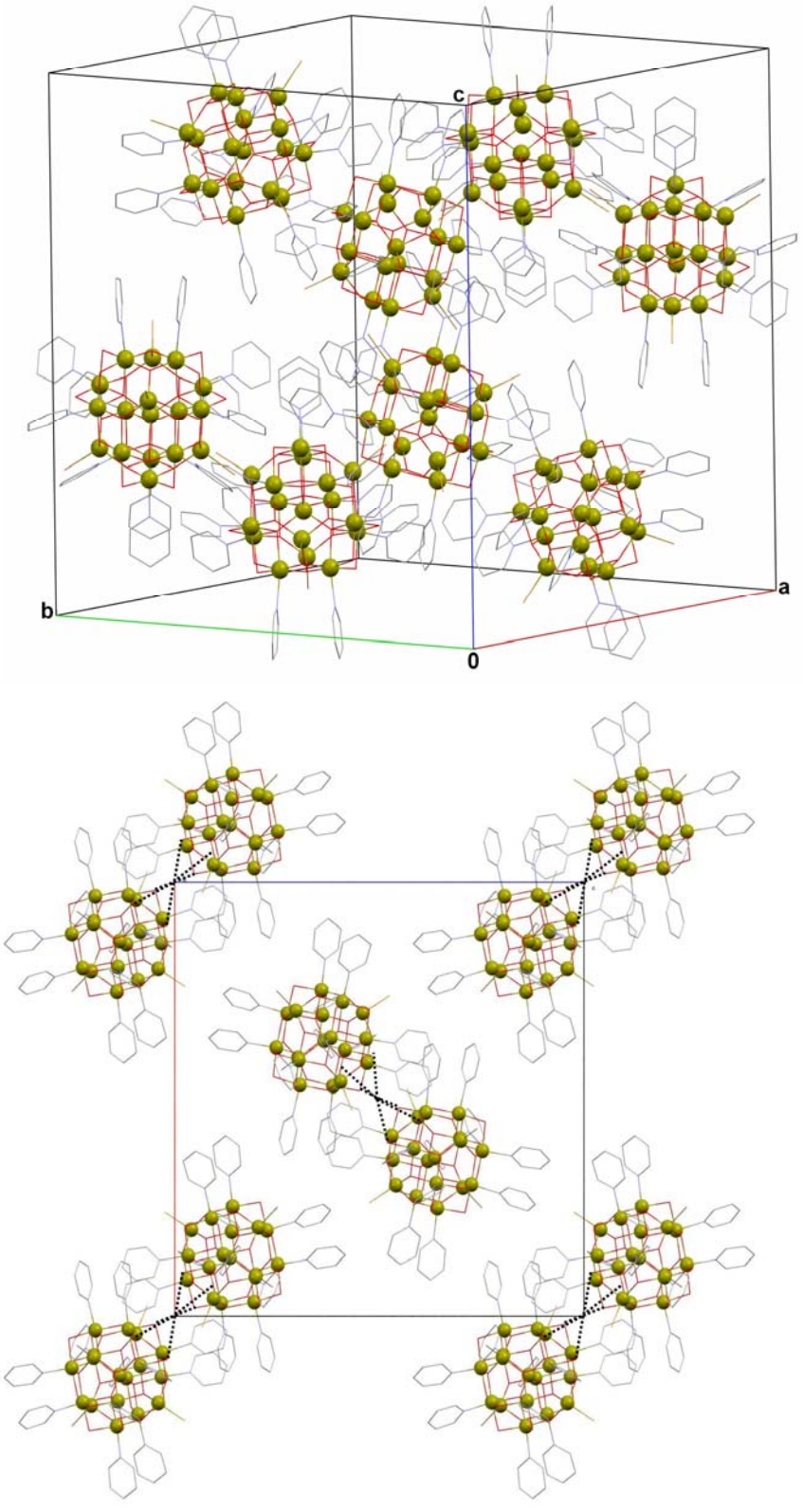

Fig. 2.6 The packing of molecules of **2** in the unit cell (top) and viewed along the b-axis (bottom). H-bonding shown as dashed line.

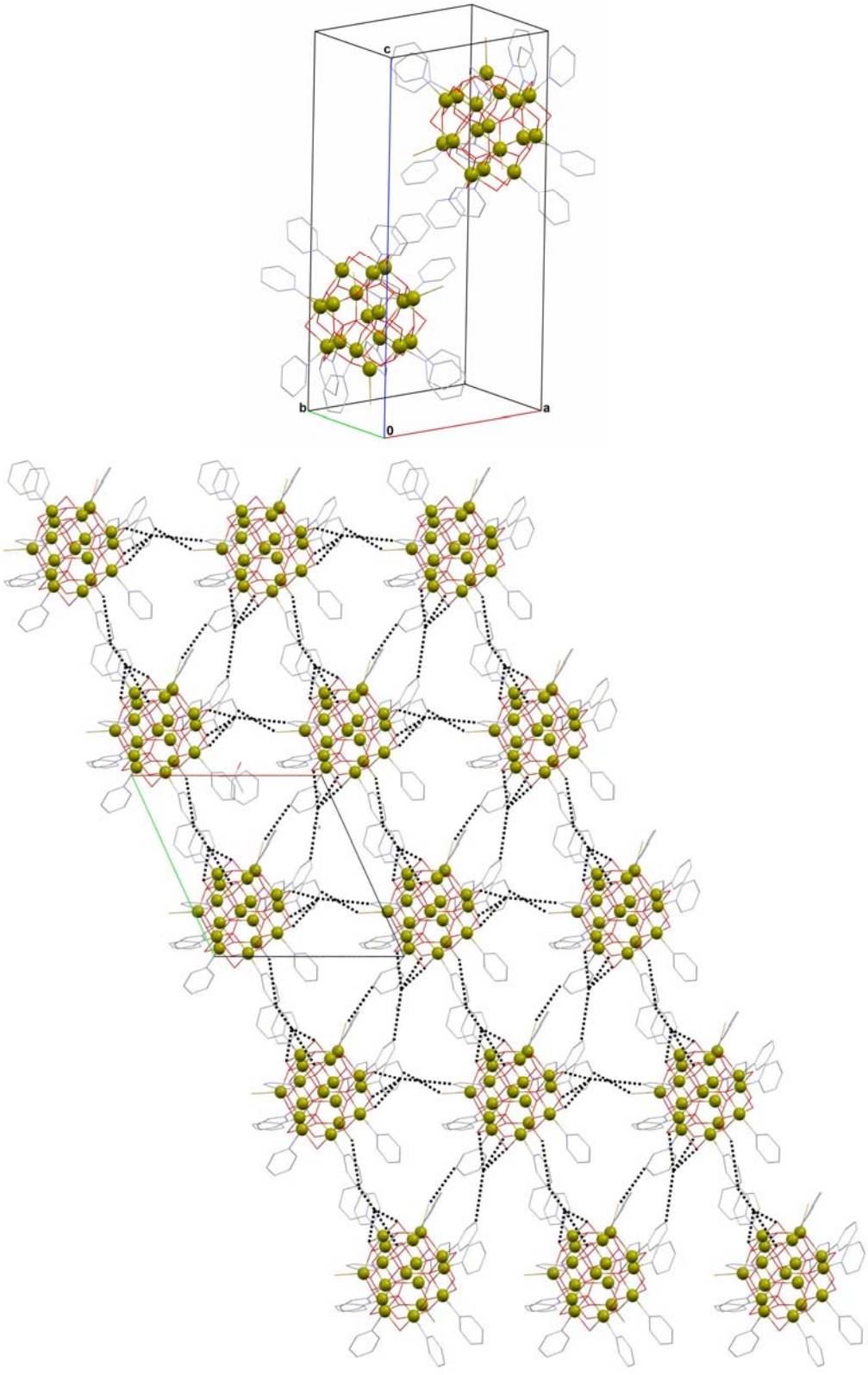

Fig. 2.7 The packing of molecules of **3** in the unit cell (top) and viewed along the c-axis (bottom). H-bonding shown as dashed line.

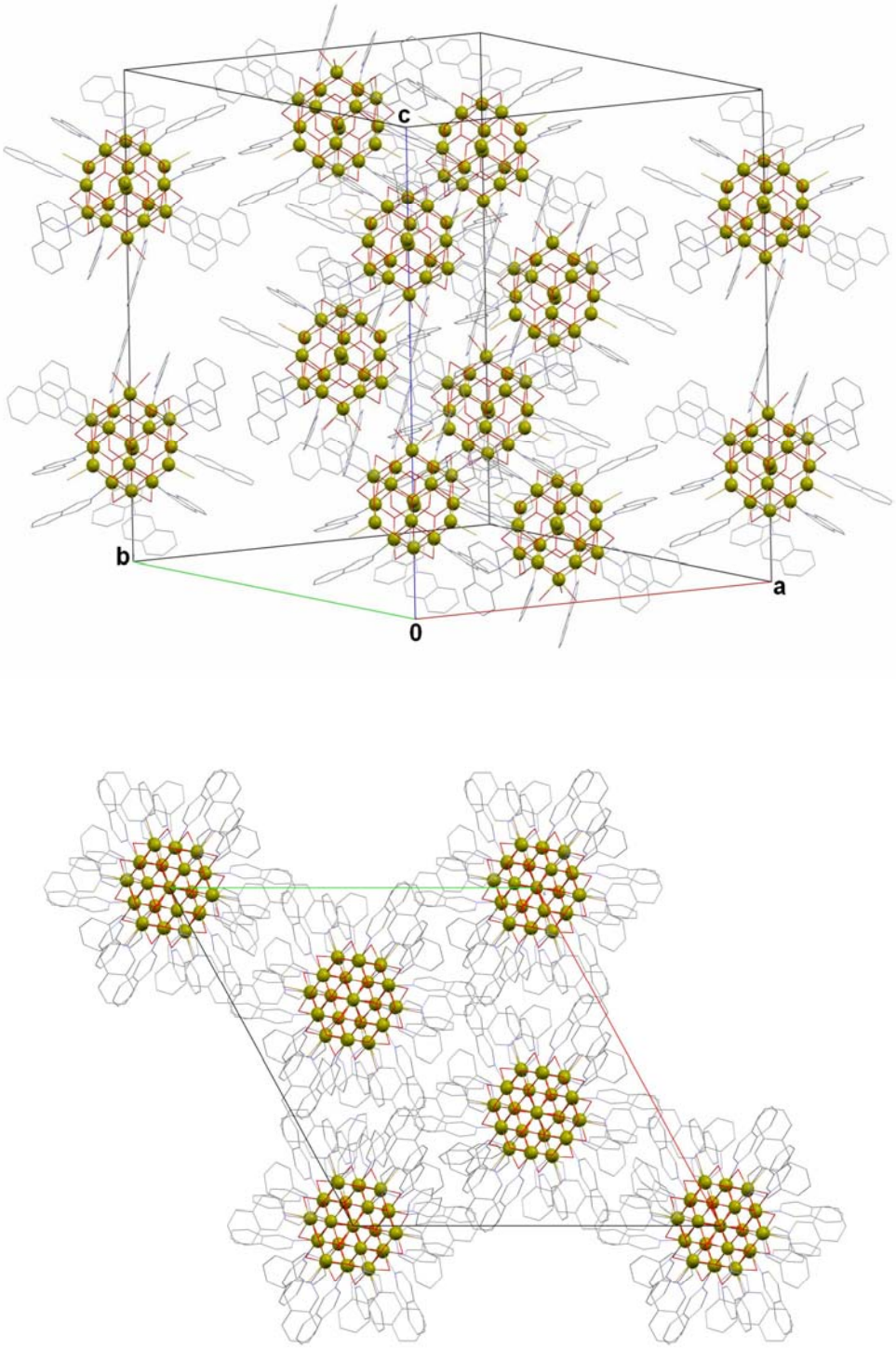

Fig. 2.8 The packing of molecules of **4** in the unit cell (top) and viewed along the c-axis (bottom).

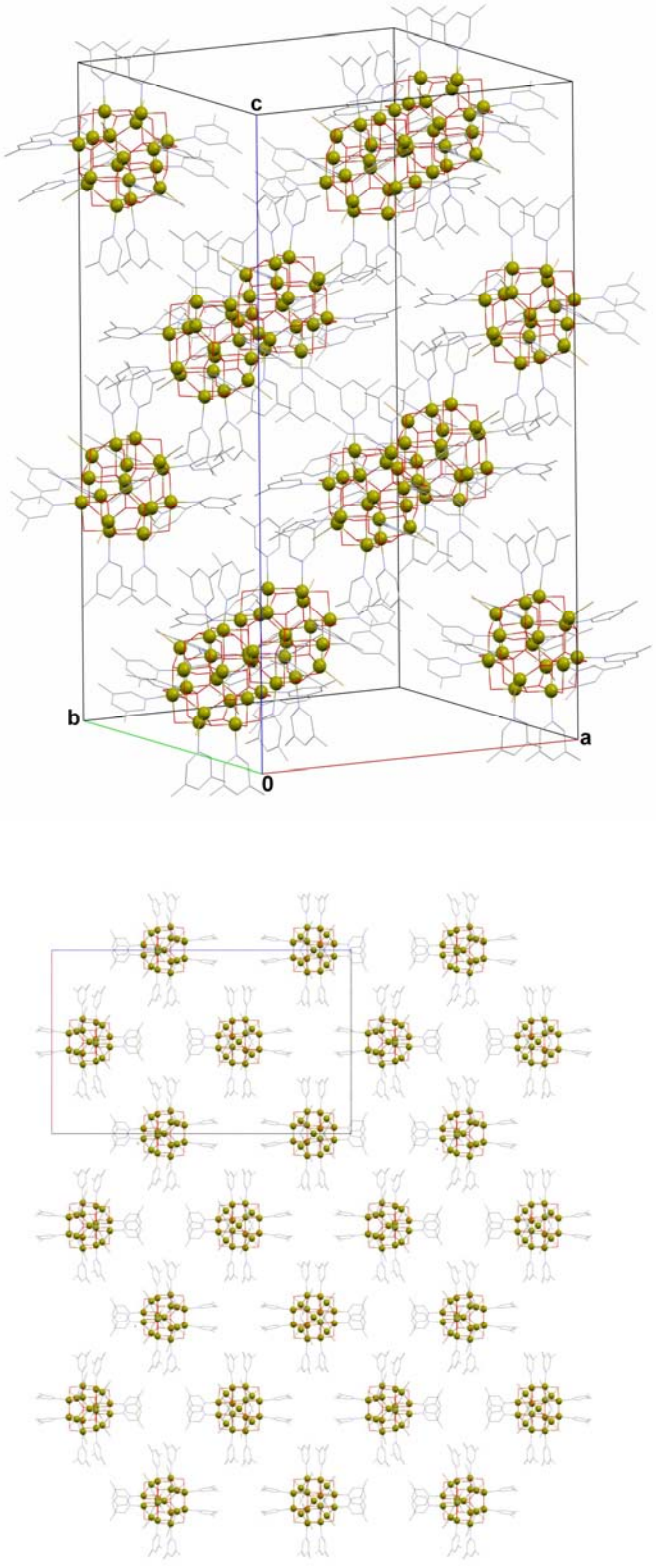

Fig. 2.9 The packing of molecules of **5** in the unit cell (top) and viewed along the b-axis (bottom).

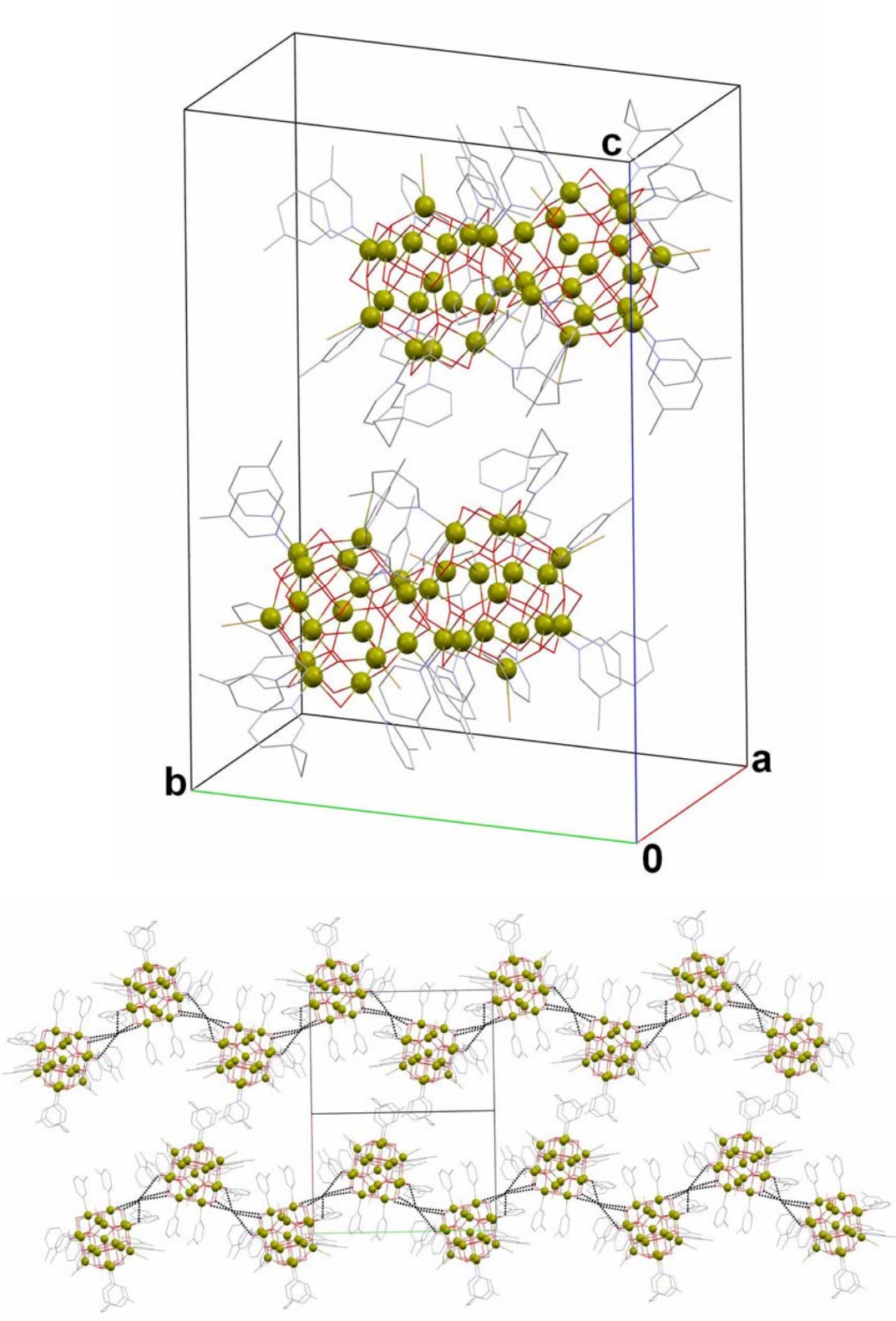

Fig. 2.10 The packing of molecules of **6** in the unit cell (top) and viewed along the c-axis (bottom). H-bonding shown as dashed line.

a pyridine and a lattice Br^- anion (C···Br^-, 3.580(2)Å) to form 2D sheets in the *ab* plane (Fig. 2.7). These sheets are then hydrogen bonded to each other via a terminal Br^- ion and three pyridines (C···Br^-, 3.526(2)Å, 3.439(2)Å, 3.479(2)Å,); a lattice Br^- anion and three pyridines (C···Br^-, 3.760(2)Å, 3.693(2)Å, 3.686(2)Å,) and a terminal Br and a pyridine (C···Br^-, 3.580(2)Å). In **4** as before there exists four hydrogen bond interactions between the three μ_2 hydroxy groups and four lattice Br^- anions (O···Br^-, 3.416(2)Å, 3.416(2)Å, 3.417(2)Å, 3.290(2)Å, 3.356(2)Å, 3.336(2)Å) with Br4 half occupied. Three terminal H_2O molecules have replaced the terminal bromides seen in **1-3** leading to hydrogen bonding interactions between each of the terminal H_2O molecules to a lattice H_2O (O···O, 2.701(2)Å), and the lattice H_2O molecules and isoquinoline (O···N, 2.802(2)Å) producing similar packing to that found in **1** (Fig. 2.8). In **5** only half the [Fe_{17}] molecules in the crystal lattice exhibit hydrogen bonding between the four lattice Br^- anions and the four hydrogen bond 'cavities' each created by three μ_2 hydroxy groups (O···Br^-, 3.274(2)Å, 3.308(2)Å, 3.351(2)Å). Between each pair consisting of a hydrogen bonded [Fe_{17}] and a non hydrogen bonded [Fe_{17}], two H_2O molecules hydrogen bond to two lattice Br^- anions forming rows of [Fe_{17}] as shown in Fig. 2.9. In **6** two of the hydrogen bond 'cavities' consisting of three μ_2 hydroxy groups each hydrogen bond to two of the lattice Br^- anions (O···Br^-, 3.282(2)Å, 3.345(2)Å, 3.337(2)Å) as seen previously, however the third lattice Br^- anion hydrogen bonds to two μ_2 hydroxy groups (O···Br^-, 3.252(2)Å, 3.273(2)Å, 3.284(2)Å, 3.247(2)Å) on each of two neighbouring clusters forming serpentine like hydrogen bonded chains of [Fe_{17}] as seen in Fig 2.10. The closest intermolecular separations deduced from the measurement of the centroid-centroid distances are 15.179 Å for **1** (trigonal), slightly longer at 16.095 Å for complex **2** (cubic), 14.882 Å for complex **3** (triclinic), 17.241 Å (n=4) for complex **4**, 17.786 Å for complex **5** and 13.569 Å for **6**.

Table 2.1 Crystallographic details for complexes **1**-**3**.

	1·8py·MeCN	**2**	**3**·Me_2CO·0.5py·$2H_2O$
M, $gmol^{-1}$	3752.32	5915.5	6323.4
crystal system	Trigonal	Cubic	Triclinic
space group	*R*-3	*P*a-3	*P*-1
a, Å	16.2552	29.2854(3)	16.1739(3)
b, Å	16.2552	29.2854(3)	16.3192(3)
c , Å	71.9185	29.2854(3)	25.4267(5)
α, deg	90	90	71.4450(10)
β, deg	90	90	73.1330(10)
γ, deg	120	90	60.7690(10)
V , $Å^3$	16457.3(14)	25116.2(4)	5478.04(19)
Z	6	4	2
$\rho_{, calc}$ [g cm^{-3}]	2.272	1.564	1.95
T , K	150(2)	150	150
λ (Å)	0.71073	0.71073	0.71073
μ, [mm^{-1}]	5.176	4.339	5.165
Measd/independant (R_{int})	53332/7986(0.0673)	313281/3857(0.070)	74584/22288(0.048)
Obsd reflns [I>2σ (*I*)]	5792	3857	15748
$R1^b$	0.0660	0.0924	0.0442
$wR2^c$	0.1916	0.1407	0.0948
GOF on F^2	1.086	0.8595	0.8418
Δ $\rho_{max,min,}$ e $Å^{-3}$	1.364, -1.380	0.44, -0.33	2.40, --2.46

[a] $R1 = \Sigma(|Fo| - |Fc|)/\Sigma(|Fo|)$ for observed reflections. [b] $wR_2 = \{\Sigma[w(F_{o2} - F_{c2})_2]/\Sigma[w(F_{o\,2})_2]\}_{1/2}$ for all data.

Table 2.2 Crystallographic details for complexes **4**-**6**.

	4·6iso-quin·3H_2O	**5**·H_2O	**6**
M, gmol^{-1}	4401.82	3254.67	3086.34
crystal system	Trigonal	Tetragonal	Monoclinic
space group	*R*-3	*I*41/*a*	*P*21/*c*
a, Å	28.4520(3)	26.9509(3)	16.732(3)
b, Å	28.4520(3)	26.9509(3)	22.675(3)
c , Å	36.0903(9)	46.5362(12)	33.140(5)
α, deg	90	90	90
β, deg	90	90	98.013(3)
γ, deg	120	90	90
V , Å^3	25301.5(7)	33688.8(10)	12450.0
Z	6	16	4
ρ, calc [g cm^{-3}]	1.733	1.280	N/A[c]
T , K	150(2)	150	150
λ (Å)	0.71073	0.71073	0.71073
μ, [mm^{-1}]	3.148	3.360	N/A[c]
Measd/independant (R_{int})	58115/9938 (0.0628)	14841/9113	N/A[c]
Obsd reflns [I>2σ (*I*)]	7228	9113	N/A[c]
R1[a]	0.0443	0.1253	N/A[c]
wR2[b]	0.1217	0.1398	N/A[c]
GOF on F^2	1.034	0.8422	N/A[c]
Δ $\rho_{max,min,}$ e Å^{-3}	1.926, -1.058	5.48, -4.42	N/A[c]

[a]$R1$) $\sum(|F_o| - |F_c|)/\sum(|F_o|)$ for observed reflections. [b] wR_2) $\{\sum[w(F_{o2} - F_{c2})_2]/\sum[w(F_{o\,2})_2]\}_{1/2}$ for all data.[c] complex **6** partial cif used for connectivity.

Table 2.3 Selected Bond Lengths (Å) and Angles (deg) for complexes **1 - 5.**

	1	**2**	**3**
Fe-OH	1.987(1)-2.041(1)	1.98(1)-2.0683(1)	1.979(3)-2.055(3)
Fe-O	1.8528(1)-2.0852(1)	1.8386(0-) 2.0816(1)	1.854(3)-2.094(3)
Fe-N	2.145(1)-2.1573(1)	2.094(1)–2.211(1)	2.142(6)-2.189(4)
Fe-Br	2.319(1)-2.35691)	2.3601(0)-2.3711(1)	2.356(1)-2.421(3)
Fe-OH-Fe	97.246(3) – 97.71(3)	95.882(1)-98.614(2)	97.08(16)-99.15(13)
Fe-O-Fe	93.583(3) – 125.86(3)	92.571(2)-127.329(2)	93.52(13)-127.70(17)
Fe_{oct} – O - Fe_{oct}	93.58(3) – 94.989(2)	92.571(2)-98.614(20)	93.52(13)-99.15(13)
Fe_{oct} – O - Fe_{tet}	122.74(3) – 126.128(6)	122.49(1)-127.33(2)	121.72(17)-127.70(17)
	4	**5**	
Fe-OH	1.983(5)-2.037(5)	1.999(1)-2.025(1)	
Fe-O	1.852(5)-2.091(5)	1.802(1)-2.070(1)	
Fe-N	2.098(14)-2.160(7)	2.144(1)-2.171(1)	
Fe-Br	2.3612(16)-2.3732(14)	2.311(0)-2.311(0)	
Fe-OH-Fe	93.64(19) – 98.7(2)	97.3(1)-100.0(1)	
Fe-O-Fe	93.8(2) – 125.8(3)	90.94(1)-127.3(1)	
Fe_{oct} – O - Fe_{oct}	93.64(19)-98.7(2)	90.94(1)-98.62(1)	
Fe_{oct} – O - Fe_{tet}	121.3(2) – 126.4(3)	120.05(1)-127.22(1)	

Magnetic Studies

DC and AC Magnetic Studies

Variable temperature magnetic susceptibility data were collected on **1** in the temperature range 300-5 K in an applied field of 1 kG (Fig. 2.11). The room temperature $\chi_M T$ value of approximately 120 cm^3 K mol^{-1} rises constantly as temperature is decreased to a maximum value of approximately 180 cm^3 K mol^{-1} at 5 K. The spin only (g = 2) value for a $[Fe^{III}_{17}]$ unit is approximately 74 cm^3 K mol^{-1}. This behaviour is indicative of dominant antiferromagnetic exchange between the metal centres with the low temperature (5 K) maximum indicating an S ≈ 18 spin ground state. In order to determine the spin ground state for complex **1**, magnetisation data were collected in the ranges 10 – 70 kG and 2 – 20 K and these are plotted in Fig. 2.11. The data were fitted by a matrix-diagonalisation method to a model that includes only the Zeeman term and axial zero-field splitting. The corresponding Hamiltonian is given by:

$$H = DS_z^{\,2} + g\mu_B \vec{H} \cdot \vec{S}$$

Where D is the zero field splitting parameter, S_z is the easy axis spin operator, g is the Landé g-factor, μ_B is the Bohr magneton and H is the applied field. The best fit gave S = 35/2, g = 2.06(3), and D = -0.03 K. The ground state can be rationalised by assuming an antiferromagnetic interaction between the tetrahedral and octahedral Fe^{III} sites – consistent with the two distinct categories of Fe-O-Fe bridging angles present in the complex. Complexes **2** - **6** show similar behaviour and can be equally well modelled with the same parameters, suggesting that the intra-molecular behaviour for all six complexes is identical.

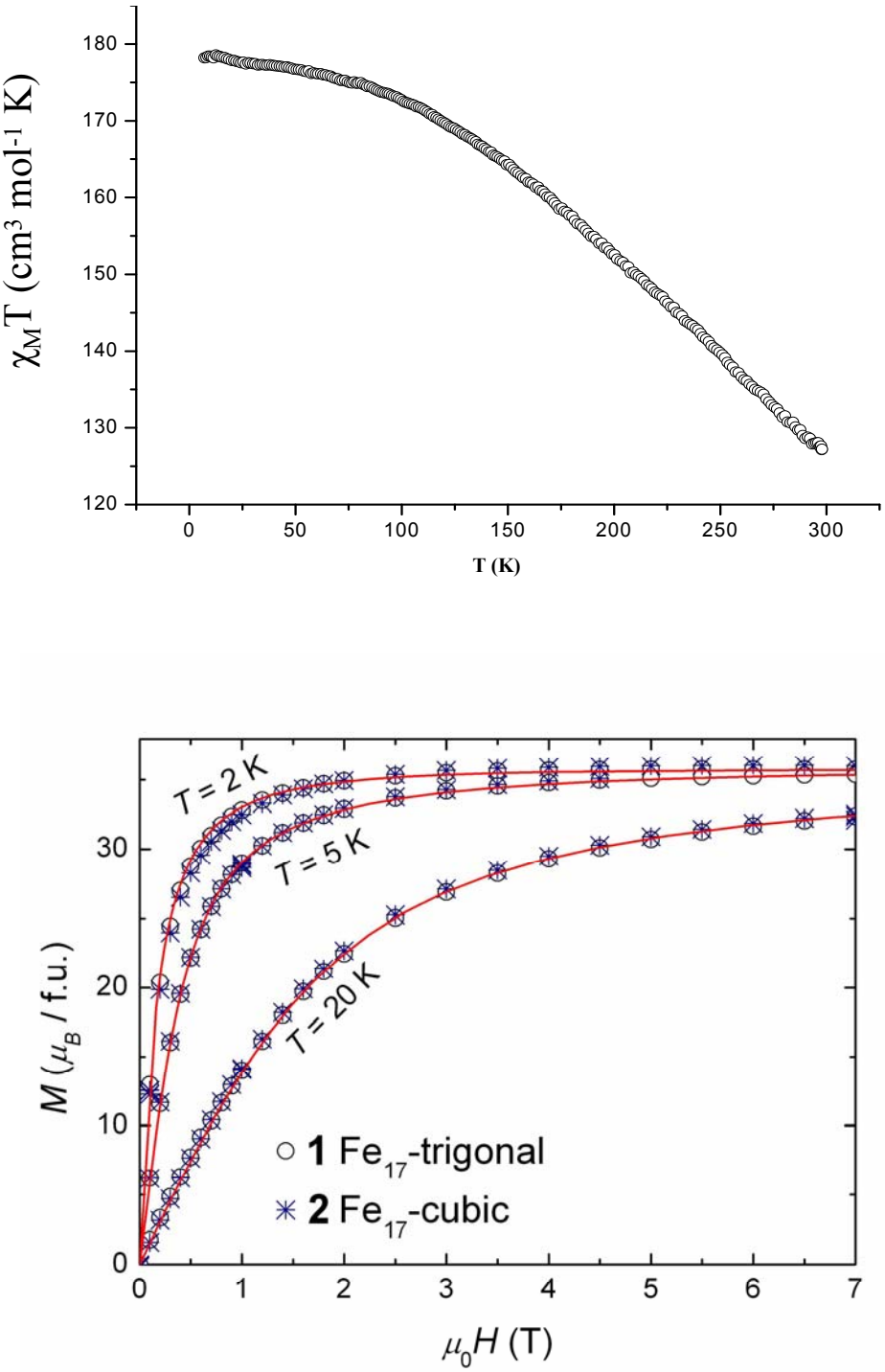

Fig. 2.11 $\chi_M T$ *vs* *T* for complex **1** measured in a field of 0.1 T (top); Magnetisation measurements for **1** and **2** taken in the 1 – 7 T field range (middle) at the indicated temperatures (middle);

Specific Heat Measurements

Fig. 2.12 shows the collected specific heat *C(T , H)* data of **1** and **2** as a function of temperature for several applied fields. At first sight and as for the *M*(*H*) data (Fig. 2.11), the *C(T , H)* of **1** does not differ from that of **2**, at least for $H > 0$. The main difference is in the zero-applied-field data for which a λ-type anomaly centred at $T_C = 0.81$ K is observed for **1** (inset in Fig. 2.12). Anticipating the discussion below, this feature reveals the onset of long range molecular order (LRMO); the magnetic nature is indeed proven by its disappearance upon application of *H*. Clearly, the λ-type anomaly arises on top of a much broader one, which shifts with increasing applied field towards higher temperatures. Because of the small anisotropy ($D \approx -0.03$ K), it is expected that the magnetic contribution to *C(T , H)* for $H \geq 1$ T is due to Schottky-like Zeeman splitting of the otherwise nearly degenerate energy spin states. Indeed, the calculated Schottky curves (solid lines in Fig. 2.12) arising from the field-split levels account very well for the experimental data. The same behaviour is followed by **2** except that no sign of LRMO is apparently observed.

As particularly evident in the low-*T* / high-*H* region in Fig. 2.12, phonon modes of the crystal lattice contribute differently to *C*(*T*) of **1** and **2**. We estimated the lattice contributions (dashed lines in Fig. 2.12) by fitting to a model given by the sum of a Debye term for the acoustic low-energy phonon modes plus an Einstein term that likely arises from intramolecular vibration modes. From the field dependencies of *M*(*T, H)* and *C*(*T, H*), we have already deduced that the individual Fe_{17} molecule remains identical regardless of space group. Therefore, it is not surprising that the fit provides the same Einstein temperature $\theta_E \approx 42$ K for both compounds (Fig. 2.12). Contrary, low-energy phonon modes result in different Debye temperatures whose values are $\theta_D \approx 28$ and 23 K for **1** and **2**, respectively. Because **2** has larger intermolecular distances, softer low-energy modes yielding smaller θ_D are to be expected. The so-obtained lattice contributions allow us to

estimate the entropy changes ΔS by using the relation $\Delta S/R = \int_0^\infty C_m(T) / (RT)dT$, where $C_m(T)$ is the magnetic contribution obtained from $C(T)$ after subtraction of the respective lattice contribution. For both compounds, the obtained ΔS amounts to $3.7R$, which is in good agreement with the entropy expected $R\ln(2S + 1) \approx 3.6R$, given $S = 35/2$. As already anticipated, we can therefore safely attribute $T_C = 0.81$ K to the LRMO temperature of the molecular spins in **1**.

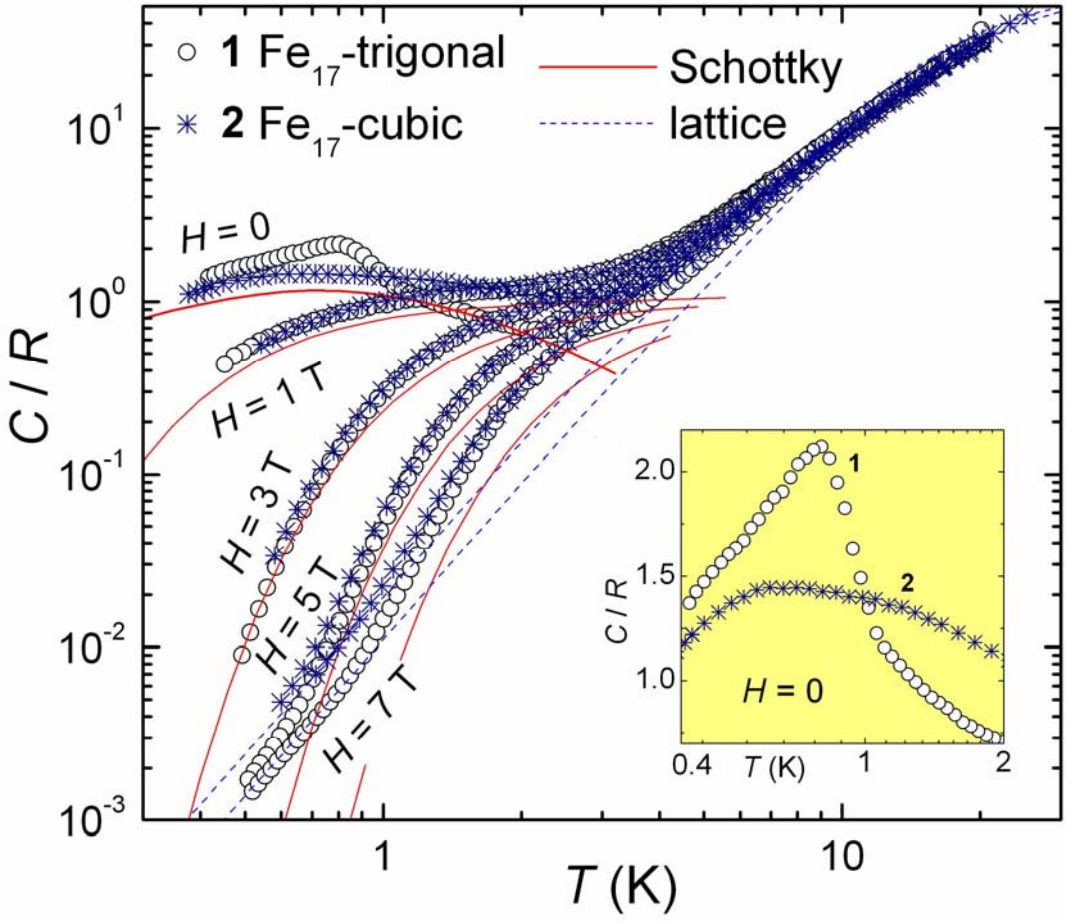

Fig. 2.12 Specific heat of **1** and **2** for several applied fields, as labeled. Drawn curves are explained in the text. Inset: Magnification of the low-*T* / zero-field range showing the different ordering behaviours.

Low Temperature DC and AC Measurements

Although the high temperature behaviour is consistent for each of the six complexes, low temperature susceptibility measurements (Fig. 2.11) reveal sharp anomalies that take place at $T_C \sim 0.8$K for **1**, corroborating the LRMO deduced from specific heat data (LRMO), and at $T_B \sim 0.5$ K for **2**, whose nature is discussed below. For $T > 4$ K, both susceptibilities tend to overlap each other (Fig. 2.11). The observed behaviour in **1** is compatible with a ferromagnetically ordered phase, in which demagnetisation effects become important. The measured susceptibility at T_C is close to the estimated limit for a ferromagnetic grainlike sample, $\chi_N = 1/\rho N \approx 227$ emu mol^{-1}. (see Fig. 2.11), where $\rho = 3.32$ g cm^{-3} is the density of **1**, and $N = 4\pi/3$ is the demagnetising factor of the grainlike sample approximated to a sphere.

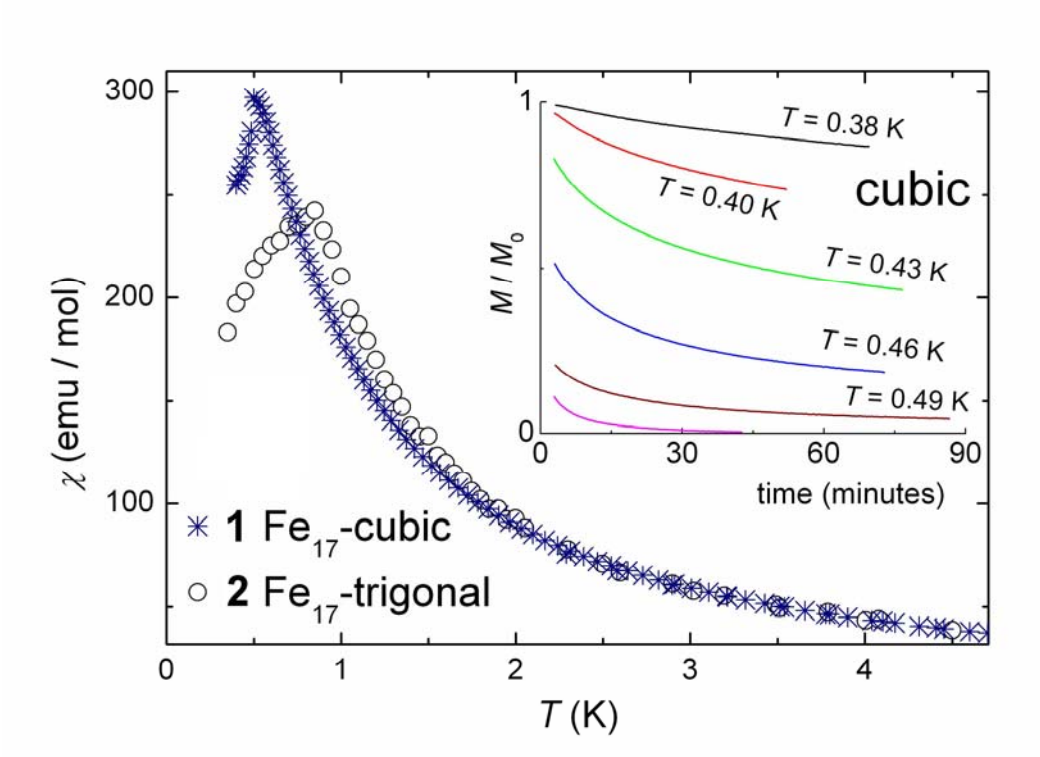

Fig. 2.13 Low temperature susceptibility (χ) measurements for **1** and **2** taken in the 5 – 0.3 K temperature range (bottom) and magnetic relaxation measurements for **2** (inset).

For the 5K ≤ T ≤ 80 K temperature range, the fit to the Curie-Weiss law $\chi = C/(T-\theta)$ for the susceptibility of **1** corrected for the demagnetising field, $\chi = \chi' / (1 - \rho N\chi')$, provides C = 175.4 emu K mol^{-1} and θ = 0.9 K, in agreement with the observed ferromagnetic order at $T_C \approx 0.8$ K (Fig. 2.14). The Curie constant C equals (within error) the expected value of a (super)paramagnet with spin S = 35/2 and g = 2.06, as deduced above from the magnetisation data. This analysis is corroborated by single crystal hysteresis loop measurements on **1** and **2** performed using a micro-SQUID setup[11] with the resulting loops shown in Fig. 2.15. Measurements undertaken on **1** show hysteresis loops whose coercivity increases with increasing temperature, but independent of applied field sweep rate and can be seen to behave as a soft ferromagnet with a coercivity of 60 Oe. We recall that from *M(H)* curves, we estimated the anisotropy D = -0.023 K, which likely causes a pinning of the domain-wall motions responsible therefore for the slow decrease of the experimental susceptibility below T_C (Fig. 2.13).

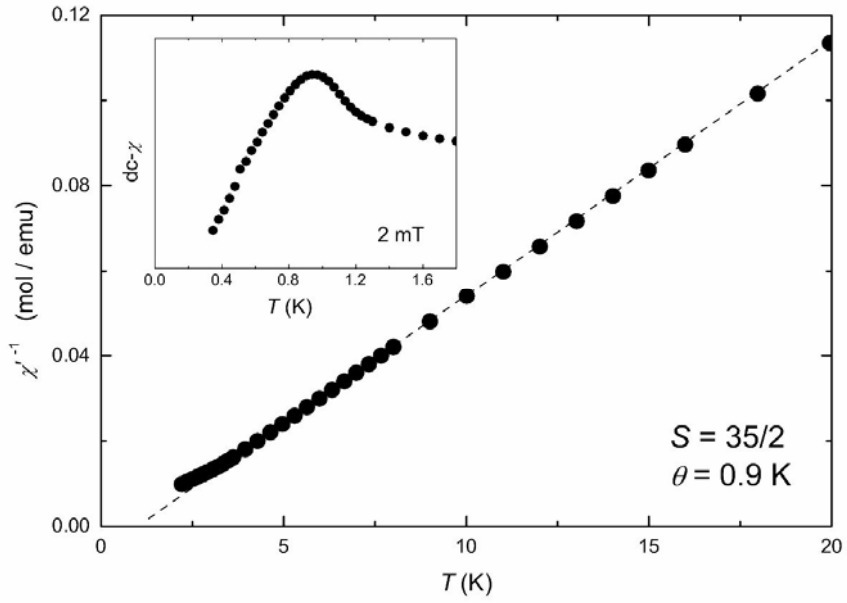

Fig. 2.14 Inverse of the in-phase component of the ac magnetic susceptibility collected for f =1730 Hz together with the fit to the Curie–Weiss law (dashed line). Inset: low temperature behaviour of the susceptibility collected using a Hall microprobe with an applied field of B_0 = 2 mT.

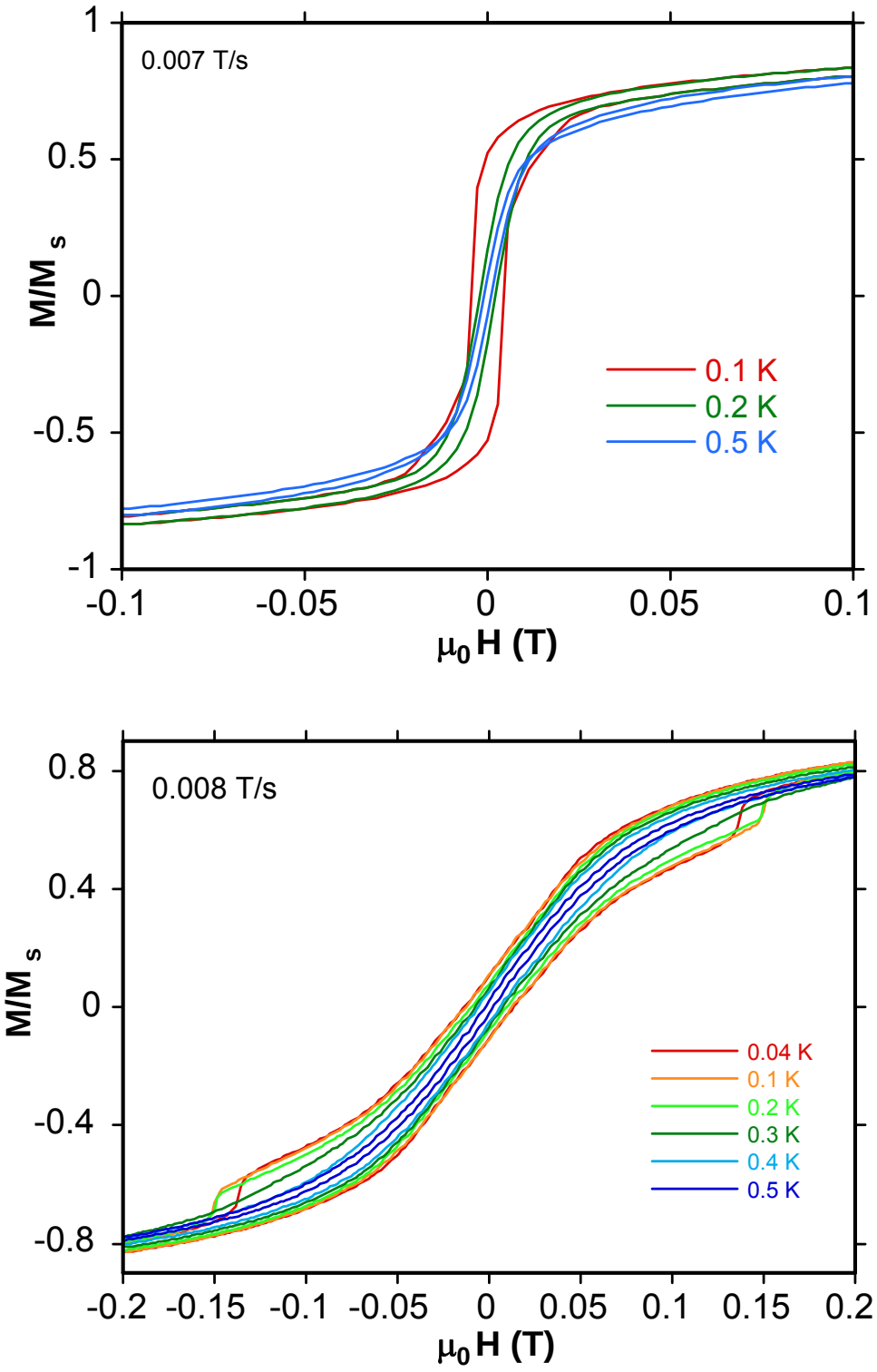

Fig. 2.15 Single crystal hysteresis loop measurements for complexes **1** (top) and **2** (bottom) taken at the indicated temperatures and field sweep rates. M is normalised to its saturation value.

The occurrence of a sharp peak at $T_B \approx 0.5$ K in the susceptibility of **2** (Fig. 2.13) has apparently no counterpart in the specific heat (inset in Fig. 2.12). We therefore exclude LRMO as a possible source. We recall that intermolecular distances for **2** are slightly larger than that of **1** (*vide supra*). It is then reasonable to assume that in **2** the intermolecular coupling is weaker and that the molecular anisotropy is the predominant energy. This would lead to superparamagnetic blocking at T_B of the molecular spins along preferred directions dictated by the anisotropy and indeed single crystal hysteresis loop measurements on **2** show hysteresis loops below 0.5 K whose coercivities increase with decreasing temperature and increasing field sweep rate, as expected for the superparamagnetic-like behaviour of a SMM (Fig. 2.15). To better elucidate this point, we performed magnetic relaxation experiments on **2** at temperatures below T_B. We first applied a field necessary to saturate the magnetisation of the sample at 2 K. We then cooled down to a given temperature below T_B, and, upon removing the field, we followed the relaxation of the Fe_{17} molecules to thermal equilibrium by collecting the time decay of the magnetisation. Results are shown in the inset in Fig. 2.13, where it is seen that the decay neatly slows down below T_B, as expected for a superparamagnet. Magnetisation data are well described by a stretched exponential decay $M/M_0 = \exp(-t/\tau)^{\beta}$ where M_0 is the initial magnetisation, β the stretched parameter, and τ the characteristic decay time. The T dependence of τ follows an Arrhenius law providing the activation energy $U = 9.0$ K that, given $S = 35/2$ and $U = -D(S^2 - ¼)$, corresponds to $D \approx -0.03$ K, which is of the same order of that estimated above. We note that U of the Fe_{17} molecule is about 8 times smaller than that of the well-known single-molecule magnet Mn12-ac[1c]. As a result of similar spin dynamics, the same ratio holds for the respective blocking temperatures as well.

Neutron Diffraction

The following neutron diffraction experiments and analysis of the data was performed in its entirety by O. Moze and D. H. Ryan and is included here for

completeness only.

Two sets of neutron diffraction measurements were performed on deuterated samples of **1.** Deuteration was achieved by an identical method to that described for **1** (page 34) with use of deuterated pyridine instead of pyridine. For the neutron diffraction experiments, deuteration of the sample was necessary in order to avoid the enormous incoherent scattering from hydrogen (σ_{inc}= 80.3 barns). This scattering leads to an unacceptably high background signal that dominates even the coherent nuclear scattering and makes it essentially impossible to observe any magnetic scattering. The incoherent background can be reduced to an acceptable level by partial replacement of hydrogen atoms by deuterium, for which σ_{inc} = 2.1 barns. The degree of deuteration of **1** under investigation is estimated at approximately 80%–90%. The first set was performed on the GEM time-of of flight diffractometer, located at the ISIS pulsed

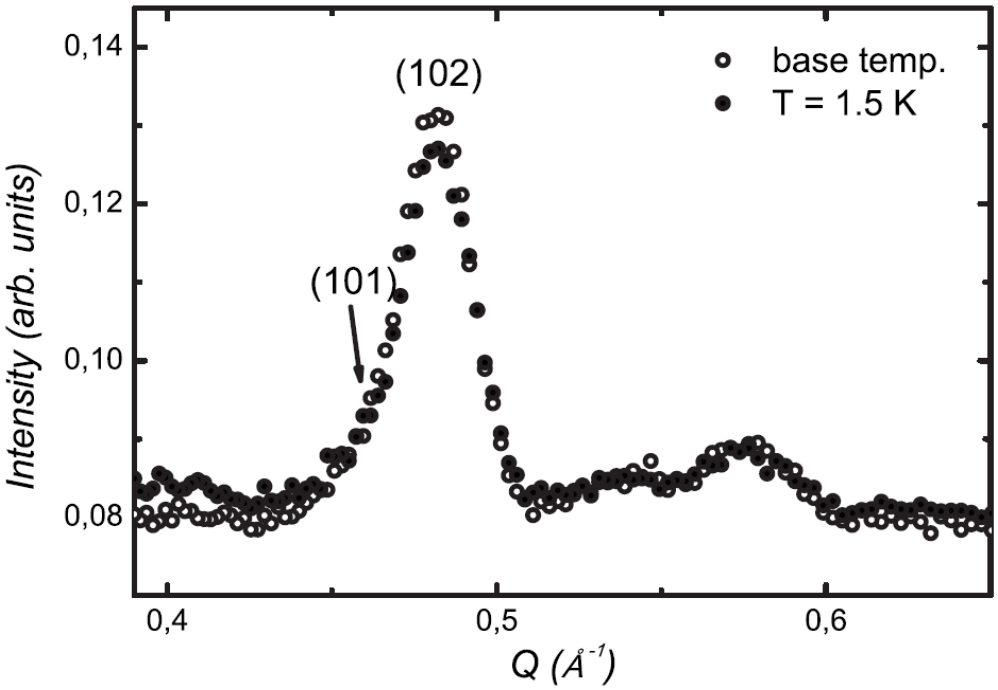

Fig. 2.16. Section at low values of the scattering vector *Q* of the time-of-flight neutron powder diffraction patterns collected on the GEM diffractometer at 1.5 K and the base temperature of the system.

source, Rutherford Appleton Laboratory source, Rutherford Appleton Laboratory, U.K. A sample weighing approximately 2g was inserted in a 6 mm diameter vanadium sample can with a copper "cold finger" inserted from top to bottom for the length of the sample can in order to assist in the thermalisation of the sample.

An "orange-type" cryostat and a ^{3}He closed cycle system were used to cool the sample, and measurements were performed at four different temperatures: the ambient (293 K), an intermediate temperature (50 K), the low T (~1.5 K), and the base temperature of the ^{3}He cryostat. Data were normalised to the wavelength distribution of the incident neutron beam. The most important part of the data is contained in the low-angle banks, which corresponds to the small values of the scattering vector Q, where one can expect magnetic scattering.

No changes were observed in the scattering patterns between 293 and 1.5 K, confirming that the high-spin system remains paramagnetic, with no long-range magnetic order, down to at least 1.5 K. This is consistent with the bulk data, reported

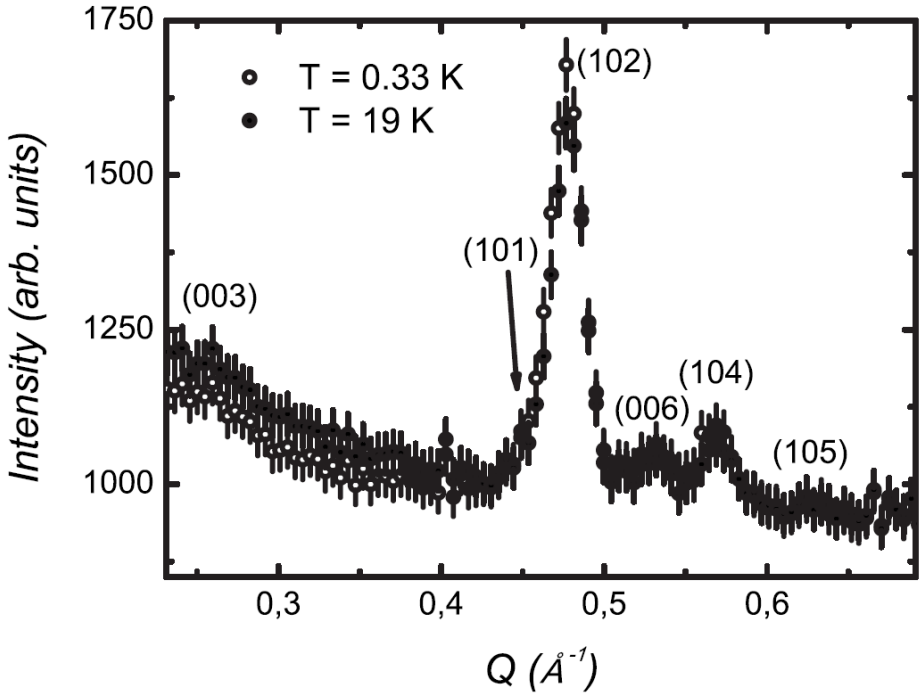

Fig. 2.17 Section at low-scattering vectors of the neutron powder diffraction patterns collected on the DUALSPEC spectrometer at T = 0.33 and 19 K. Note the

loss of paramagnetic scattering for $Q \leq 0.45$ Å^{-1} and the extra intensity at the (102) and (104) positions.

above, which indicate that magnetic correlations are not expected to set in above $T \approx$ 1.2 K. The unchanging nuclear scattering also shows that the material retains its $R\bar{3}$ crystal symmetry on cooling. The first indication of magnetic ordering comes from a suppression of the paramagnetic background scattering for $Q < 0.45$ Å^{-1} on cooling below 1.5 K, as seen in Fig. 2.16. This is typical of a transition from a disordered to an ordered state. The observed Bragg intensities are dominated by the nuclear scattering and any magnetic scattering is expected to be weak. In spite of this limitation, a discernible increase in intensity was noted on cooling from 1.5 K, particularly for $Q \sim 0.48$ Å^{-1}, which corresponds to the overlapping nuclear (101) and (102) reflections (Fig. 2.16). This increase in intensity with decreasing temperature is positive of the presence of magnetic Bragg scattering. Furthermore, as no new reflections were observed, the scattering from the magnetic structure is superimposed on the nuclear scattering, and the ordering wave vector **k** of the magnetic structure is therefore {000}. This corresponds to either a commensurate ferromagnetic or commensurate antiferromagnetic structure. The peak shape is of the expected double-exponential pseudo-Voigt type, commonly obtained on time-of-flight diffraction instruments, so that the ordering can be taken to be three-dimensional in nature.

The second set of neutron diffraction measurements consisted of a more complete and detailed temperature dependent survey of the magnetic signal and was performed on the constant wavelength C2 DualSpec spectrometer (located at the Canadian Neutron Beam Centre, Chalk River, Canada) on the same sample of deuterated Fe_{17}. An incident neutron wavelength of 2.3723 Å was used and a modified Oxford Instruments Heliox ^{3}He cold stage was adapted to fit into an orange cryostat that was mounted on the spectrometer. This system enabled subkelvin temperatures down to 330 mK to be reached with typical holding times of ~48h. Earlier experience with mounting powdered samples on this Heliox system showed

that cooling time constants of several days can be observed unless significant efforts are taken to ensure thermalisation.[12] The following procedure, which has been found to yield thermalisation times of less than 30s, was therefore used. The 1.17g of powder Fe_{17} was mixed with 1.25g of 99.99% pure copper powder and hydraulically pressed into a 6mm inside diameter oxygen-free, high conductivity copper can to form a 26mm long solid rod inside the can. While this packing does not affect the properties of the Fe_{17}, it does add some fcc-Cu reflections, however, the first of these occur at $Q \sim 3$ Å^{-1}, well outside our region of interest. Diffraction patterns were collected at temperatures from 0.33 to 1.4 K to follow the magnetic ordering in detail. In addition, a nonmagnetic reference pattern was taken at 19 K.

Two signatures of magnetic ordering are clearly visible in Fig. 2.17 which shows a comparison of the 19 and 0.33 K diffraction patterns: (i) The background scattering for $Q \leq 0.45$ Å^{-1} is significantly lower, reflecting that the loss of the paramagnetic contribution as a long-ranged magnetic order is established, and (ii) extra intensity is evident at the (102) and (104) reciprocal lattice positions, reflecting the presence of magnetic order.

Fig. 2.18 shows that the temperature dependence of the low-angle background can be used to obtain a preliminary estimate for T_C. There is a striking drop below ~1K as long-ranged magnetic order develops and the incoherent paramagnetic scattering is reduced. This observation is inconsistent with random spin freezing, such as superparamagnetic blocking, and requires that the magnetic transition at T_C to be a long-ranged ordered state. No new reflections are observed in Fig. 2.17, and the weak magnetic scattering is superimposed on much stronger nuclear reflections. Both the (102) and (104) reflection intensities increase on cooling, while the (006) and much weaker (003) reflections show no temperature dependence. The fundamental selection rule for magnetic neutron diffraction is that the neutrons are scattered by the components of the magnetic moment *perpendicular* to the scattering vector; the systematic absence of magnetic peaks of the type (00*l*) is direct evidence that the ordered magnetic moment lies along the *c* axis (the moment direction with respect to the uniaxial direction can be specified even for powder

samples, as is the case here).[13] Fits to the *line shape* show no temperature dependence associated with the onset of magnetic order, indicating that the magnetic peaks have the same width as the underlying nuclear reflections and that the magnetic and crystallographic structures have the same correlation lengths. This supports our conclusion that the ordering at T_C is long ranged in nature.

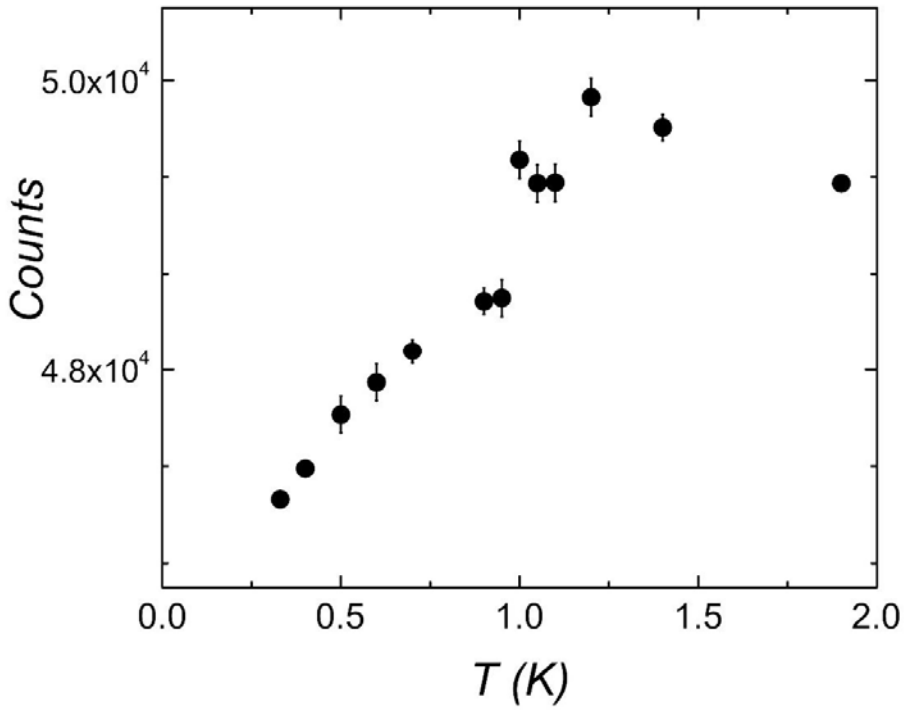

Fig. 2.18 Integrated intensity for 0.2 Å^{-}1 ≤ Q ≤ 0.35 Å^{-1} showing the marked reduction in paramagnetic scattering on cooling through T_C.

The only constraints imposed on the magnetic structure are that all single-ion Fe^{III} spins in the molecule are *nonzero* and equal in magnitude to S=5/2 and that each molecule consists of a well-defined *colinear ferrimagnetic* arrangement of spins. The present neutron data are restricted to a limited range of scattering vector. This implies that a traditional Rietveld refinement of the crystal and magnetic structures is not feasible. With the available neutron data and the above constraints, we have

utilised the theory of irreducible representations[31,32] for magnetic groups to define a magnetic structure compatible with the neutron and bulk macroscopic magnetic data. This theory is particularly valid for second order phase transitions. There are six

Table 2.4 Basis vectors and basis vector components (m_x, m_y, m_z) of the irreducible group representations for the space group $R\bar{3}$ with propagation vector **k** = {000}. The atom notations $6c_1$ and $6c_2$ refer to atom 1 and its symmetry equivalent atom 2 in an *adjacent* molecule.

Irreducible representation	Basis vector	6*c*	18*f*
Γ_1	ψ_1	$(6c_1)$ $00+m_z$	$(18f_1)$ $00+m_z$
		$(6c_2)$ $00+m_z$	$(18f_2)$ $00+m_z$
			$(18f_3)$ $00+m_z$
			$(18f_4)$ $00+m_z$
			$(18f_5)$ $00+m_z$
			$(18f_6)$ $00+m_z$
Γ_2	ψ_2	$(6c_1)$ $00+m_z$	$(18f_1)$ $00+m_z$
		$(6c_2)$ $00-m_z$	$(18f_2)$ $00+m_z$
			$(18f_3)$ $00+m_z$
			$(18f_4)$ $00-m_z$
			$(18f_5)$ $00-m_z$
			$(18f_6)$ $00-m_z$

possible irreducible representations of the space group $R\bar{3}$ for **k** = {000}. For the two types of magnetic sites, 6*c* and 18*f*, which comprise the Fe_{17} molecule, *each* of these six representations occur for *both* sites. The basis vectors of these representations for each of the magnetic sites were calculated using SARA *h*- representational analysis[16]

(downloadable at ftp://ftp.ill.fr/ pub/dif/sarah/). The selected basis vectors belong to two of the six irreducible presentations, Γ_1 and Γ_2, which correspond to the magnetic structures with all moments aligned either parallel or antiparallel to the *c* axis, respectively. The other four, Γ3, Γ4, Γ5, and Γ6, represent various planar configurations. We can discard these latter configurations on the basis of the observed intensities, which clearly point to an axial configuration. Furthermore, some of the basis vectors for Γ_3, Γ_4, Γ_5, and Γ_6 give sites where a magnetic moment is not allowed. Table 2.4 lists the irreducible representations and their corresponding basis vectors for the magnetic structures compatible with our data. Fig. 2.19 displays our simulations of the expected powder diffraction patterns for the two corresponding magnetic structures Γ_1 and Γ2.

The ferromagnetic configuration Γ1 attributes a small intensity to the (101) reflection and a larger assignment of intensity to the (102) reflection. This is in stark contrast to the antiferromagnetic configuration Γ2, for which the intensity ratios of these two peaks are practically inverted. The representations corresponding to the four planar configurations all give intensity at the (003) position. Of the six possible models, only the axial ferromagnet is in accord with our data. We therefore conclude that dipolar interactions do, in fact, favour this configuration. As a further confirmation and anticipating ground state energy calculations (vide infra), dipolar calculations indicate indeed that of the two ground states displayed in Fig. 2.20, the axial ferromagnet has a lower energy than the axial antiferromagnet.

The Fe-O cluster forming the core of the Fe_{17} molecule behaves as a single, exchange-coupled S=35/2 entity. The temperature dependence of the ordered magnetisation below T_C reflects excitations of these giant-spin orderings in the mean field established by intercluster dipolar forces and manifests itself in the intensity of the (102) reflection. This peak intensity is directly proportional to the square of the ordered moment (Fig. 2.21). Fitting the observed magnetic intensity to a S=35/2 Brillouin function, neglecting any effects due to the small anisotropy, yields an ordering temperature of 1.13(2) K in good agreement with values obtained from both susceptibility and heat capacity measurements. We emphasise here that the neutron

diffraction data do more than simply confirm the transition temperature; they unequivocally demonstrate that the magnetic order is long ranged and ferromagnetic in nature, with moments aligned parallel to the *c* axis.

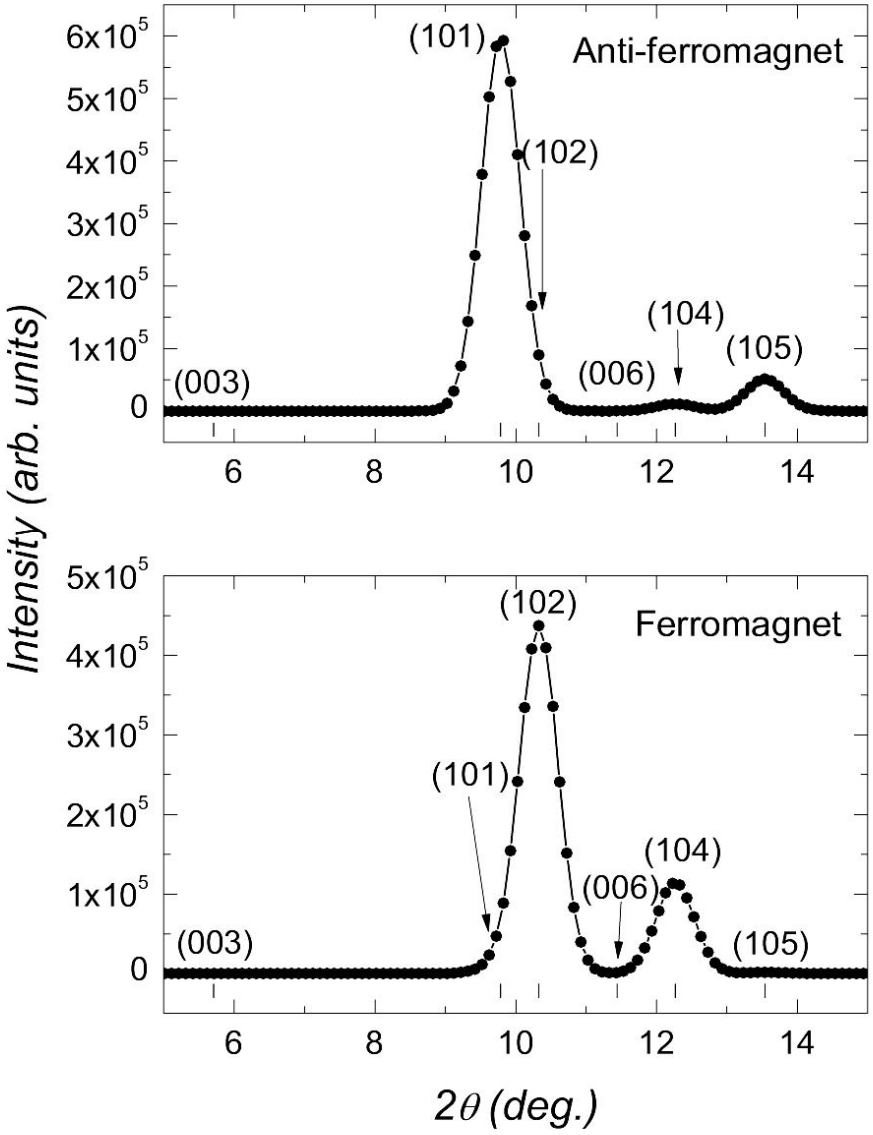

Fig. 2.19 Simulations of the low-Q magnetic diffraction pattern at T=0.33 K for an antiferromagnetic (AF) (top) and ferromagnetic (FE) (bottom) alignment of Fe_{17} molecules along the *c* axis.

Ground State Energy Calculations

We calculated ground-state dipolar energies E_{dip} for the pointlike Heisenberg spins arranged in crystallographic lattice analogs to that of Fe_{17}. In particular, the position of the spins was fixed accordingly to molecular centroids. The molecular

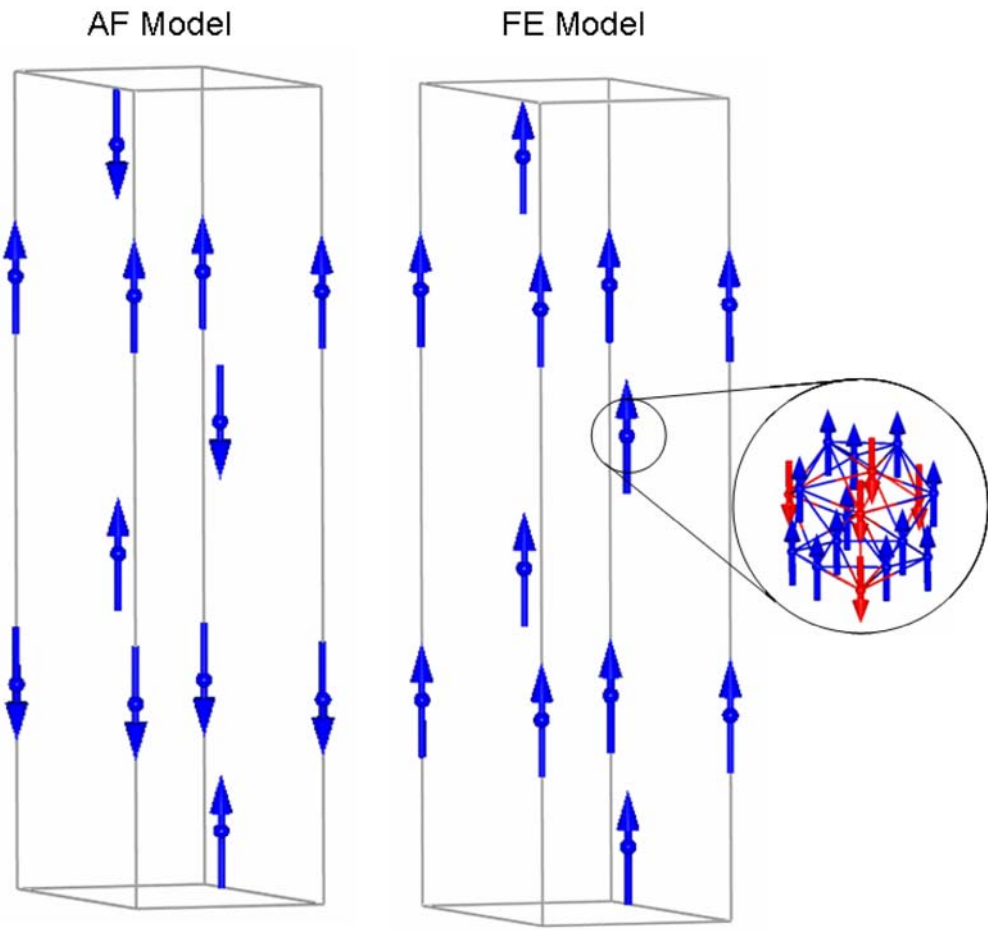

Fig. 2.20 Representation of the axial AF and axial FE structures, as induced by dipolar interactions between the Fe_{17} molecules, indicated by large arrows (blue). Inset: ferromagnetic structure of the Fe17 molecule represented by 12 *up spins* (blue) and 5 *down spins* (red).

symmetry of Fe_{17} is such that the centroid of each individual molecule corresponds to the position of the Fe^{III} ion at the centre of the molecule. The net spin carried by each molecule is represented by a vector $\vec{S}$ of length $S = 35/2$. This classical

approximation is good because of the large value of the spin. Therefore, the molecular magnetic moment is $\vec{\mu} = \mu_B \vec{g} \cdot \vec{S}$ For the sake of simplicity, we assume the isotropic $\vec{g}$ with g=2.

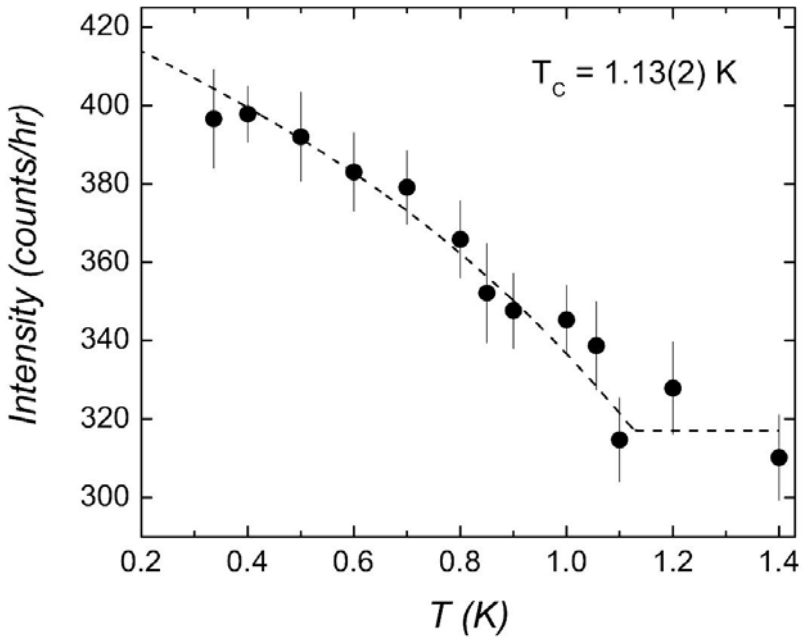

Fig. 2.21 Temperature dependence of (102) peak intensity showing the onset of magnetic order below T_C=1.13(2) K. The underlying nuclear intensity was taken from data recorded at 19 K, while the magnetic intensity was fitted to S=35/2 mean-field behaviour (dotted line; see text).

If the magnetic cell contains m spins, the magnetic structure is given by a set of m magnetic moment vectors $\vec{\mu}_i$. The dipolar energy per ion of an ordered crystal is given by

$$E_{\mathrm{dip}} = \frac{R}{2mk_B} \sum_{i=1}^{m} \vec{\mu}_i \cdot \vec{H}_i,$$

where $\vec{H}_i$ is the molecular field at site i, given by

$$\vec{H}_i = -\sum_{j \neq i}^{N} \left\{ \frac{\vec{\mu}_j}{r_{ij}^3} - 3\frac{(\vec{\mu}_i \cdot \vec{r}_{ij})\vec{r}_{ij}}{r_{ij}^5} \right\}.$$

We evaluate these summations using free boundary conditions for spherical shaped systems, for which all spins inside the sphere are allowed to interact. Slow numerical convergences are usually solved by the summation techniques such as the Ewald method. However, we checked that direct sums for a cut-off radius larger than 200 Å (corresponding roughly to 280 00 spins) provide reproducible E_{dip} results with differences within 2%.

The calculations are carried out for the spin configurations depicted in Fig. 2.20, i.e., the ferromagnetic (FE) and AF spin alignments along the *c* axis. We obtain E_{dip} = 0.2 and 2.0 K for FE and AF, respectively. Since they differ by 1 order of magnitude, we can clearly conclude that the most probable configuration is ferromagnetic, corroborating the neutron diffraction analysis.

Conclusions

Simply dissolving $FeBr_3$ in pyridine produces a heptadecametallic cluster that is an all-ferric piece of molecular magnetite. A family of analogous compounds can be made by simply changing the halide or base – that also acts as the solvent and terminal capping ligand. This is therefore a new, simple and extremely attractive methodology for the synthesis of molecular magnetic oxides. Antiferromagnetic exchange between the octahedral and tetrahedral Fe^{III} ions, as governed by the Fe-O-Fe bridging angles, leads to the stabilisation of an S = 35/2 spin ground state with D ≈ -0.03 K In addition, the synthesis of a molecule with a combination of an extremely large spin ground state and small |D| is very unusual. By changing the co-solvents of crystallisation identical [Fe_{17}] molecules can be crystallised in different crystal systems and packing arrangements. We experimentally demonstrate that Fe_{17}

represents the first molecular system to undergo either LRMO or superparamagnetic blocking of the molecular spins depending on its symmetry. We show that this results from the interplay of the dipolar magnetic coupling between the molecular spins, with respect to the single-molecule magnetic anisotropy. That supramolecular chemistry leads to fascinating ordered arrangements of identical high-spin nanomagnets is no novelty; that these arrangements can be achieved without affecting the magnetic properties of the individual nanomagnets (e.g., keeping unaltered the cluster spin ground state and magnetic anisotropy) is a step forward in the manipulation of the magnetic interactions at the nanometer scale. The Fe_{17} system is, therefore, a test model material for workers interested in the modelisation of phase transitions purely driven by dipolar interactions. In addition The Fe_{17} magnetic molecule represents a unique system, in which neutron scattering techniques can be successfully employed to assess the long-range ferromagnetically ordered structure induced by dipolar interactions. A highly symmetric molecular core and a correspondingly small uniaxial anisotropy combine to support the occurrence of magnetic ordering at accessible temperatures. Neutron diffraction measurements performed on powder samples of Fe_{17} confirm the type of the order and the direction of the ordered magnetic moments with respect to the crystallographic unit cell. A small but clear magnetic signal is observed and successfully tracked in the temperature interval 0.33 K $\leq T \leq$ 1.4 K. The transition temperature T_C=1.13(2) K is in good agreement with susceptibility and specific heat data. Furthermore, unlike most other examples of long-range ordered molecular magnets, it is possible to obtain the relatively large amounts of deuterated Fe_{17} essential for a successful neutron diffraction experiment. Modelling the magnetic structure with a net spin S=35/2 positioned in the molecular centroids shows a good agreement with the experimental data, indicating that the Fe_{17} molecule behaves as an atom with a macrospin given by the sum of the contribution of the constituent Fe^{III} ions. This encouraging result should stimulate neutron powder diffraction experiments in other molecular superparamagnets where long-range order may be active.

References

1 (a) R. Sessoli, D. Gatteschi, D. N. Hendrickson, G. Christou, *MRS Bull*, 2000, **25**, 66; (b) R. Sessoli, H-L. Tsai, A. R. Schake, S. Wang, J. B. Vincent, K. Folting, D. Gatteschi, G. Christou, D. N. Hendrickson, *J. Am. Chem. Soc.*, 1993, **115**, 1804; (c) R. Sessoli, D. Gatteschi, A. Caneschi, M. A. Novak, *Nature*, 1993, **365**, 141; (d) A. Caneschi, D. Gatteschi, R. Sessoli, A. L. Barra, L. C. Brunel, M. Guillot, *J. Am. Chem. Soc.*, 1991, **113**, 5873.

2 (a) M. N. Leuenberger, D. Loss, *Nature*, 2001, **410**, 789; (b) W. Wernsdorfer, N. Aliaga-Acalde, D. N. Hendrickson, G. Christou, *Nature,* 2002, **416**, 406; (c) S. Hill, R. S. Edwards, N. Aliaga-Acalde, G. Christou, *Science*, 2003, **302**, 1015; (d) J. Tejada, E. M. Chudnovsky, E. del Barco, J. M. Hernandez, T. P. Spiller, *Nanotechnology*, 2001, **12**, 181.

3 (a) R. E. P. Winpenny, *Dalton Trans*., 2002, 1; (b) G. Christou, *Polyhderon*, 2005, **24**, 2065;(c) G. Aromı´, E. K. Brechin, *Struct. Bonding*., 2006, **122**, 1.

4 (a) J.-N. Rebilly, T. Mallah, *Struct. Bonding*., 2006, **122**, 103; (b) L. M. C. Beltran, J. R. Long, *Acc. Chem. Res*., 2005, **38**, 325; (c) R. J. Parker, L. Spiccia, K. J. Berry, G. D. Fallon, B. Moubaraki, K. S. Murray, *Chem. Commun*., 2001, 333; (d) V. Marvaud, C. Decroix, A. Scuiller, C. Guyard-Duhayon, J. Vaissermann, F. Gonnet, M. Verdaguer, *Chem. Eur. J*., 2003, **9**, 1677; (e) V. Marvaud, C. Decroix, A. Scuiller, F. Tuyeras, C. Guyard-Duhayon, J. Vaissermann, M. Marrot, F. Gonnet, M. Verdaguer, *Chem. Eur. J*., 2003, **9**, 1692.

5 (a) A. Mishra, W. Wernsdorfer, K. A. Abboud, G. Christou, *J. Am. Chem. Soc*., 2004, **126**, 15648; (b) A. Mishra, W. Wernsdorfer, S. Parsons, G. Christou, E. K. Brechin, *Chem. Commun*., 2005, 2086; (c) C. M. Zaleski, E. C. Depperman, J. W. Kampf, M. L. Kirk, V. Pecoraro, *Angew. Chem., Int. Ed*., 2004, **43**, 3912; (d) J.-P Costes, F. Dahan, W. Wernsdorfer, *Inorg. Chem*., 2006, **45**, 5; (e) F. He, M.-L Tong, X.-M. Chen, *Inorg. Chem*., 2005, **44**, 8285; (f) J.-P Costes, M. Auchel, F. Dahan, V. Peyrou, S. Shova, W. Wernsdorfer, *Inorg. Chem*., 2006, **45**, 1924; (g) S. Ueki, M. Sahlan, T. Ishida, T. Nogami, *Synth. Met*., 2005, **154**, 217; (h) F.

Mori, T. Ishida, T. Nogami, *Polyhedron*, 2005, **24**, 2588; (i) F. Mori, T. Nyui, T. Ishida, T. Nogami, K.-Y Choi, H. Nojiri, *J. Am. Chem. Soc*., 2006, **128**, 1440; (j) C. Aronica, G. Pilet, G. Chastanet, W. Wernsdorfer, J.-P. Jacquot, D. Luneau, *Angew. Chem., Int. Ed*., 2006, **45**, 4659; (k) M. Ferbinteanu, T. Kajiwara, K.-Y. Choi, H. Nojiri, A. Nakamoto, N. Kojima, F. Cimpoesu, Y. Fujimura, S. Takaishi, M. Yamashita, *J. Am. Chem. Soc*., 2006, **128**, 9008; (l) F. Pointillart, K. Bernot, R. Sessoli, D. Gatteschi, *Chem. Eur. J*., 2007, **13**, 1602; (m) J. Tang, I. Hewitt, N. T. Madhu, G. Chastanet, W. Wernsdorfer, C. E. Ansen, C. Benelli, R. Sessoli, A. K. Powell, *Angew. Chem., Int. Ed*., 2006, **45**, 1729. (n) K. Bernot, L. Bogani, A. Caneschi, D. Gatteschi, R. Sessoli, *J. Am. Chem. Soc*., 2006, **128**, 7947. (o) L. Bogani, C. Sangregorio, R. Sessoli, D. Gatteschi, *Angew. Chem., Int. Ed*., 2005, **44**, 5817; (p) T. Hamamatsu, K. Yabe, M. Towatari, S. Osa, N. Matsumoto, N. Re, A. Pochaba, J. Mrozinski, J. Gallani, A. Barla, P. Imperia, C. Paulsen, J. Kappler, *Inorg. Chem*., 2007, **46**, 4458.

6 (a) N. Ishikawa, M. Sugita, W. Wernsdorfer, *J. Am. Chem. Soc*., 2005, **127**, 3650; (b) N. Ishikawa, M. Sugita, N. Tanaka, T. Ishikawa, S. Koshihara, Y. Kaizu, *Inorg. Chem*., 2004, **43**, 5498.

7 (a) M. Evangelsiti, A. Candini, A. Ghirri, M. Affronte, S. Piligkos, E. K. Brechin, E. J. L McInnes, *Polyhedron*, 2005, **24**, 2573; (b) M. Evangelsiti, A. Candini, A. Ghirri, M. Affronte, E. K. Brechin, E. J. L. McInnes, *Appl. Phys. Lett*., 2005, **87**, 072504.

8 M. Manoli, R. D. L. Johnstone, S. Parsons, M. Murrie, M. Affronte, M. Evangelisti, E. K. Brechin, *Angew. Chem. Int. Ed*., 2007, **46**, 4456.

9 M. Evangelsiti, F. Luis, L. J. M. de Jongh, L. J. M. Affronte, J. *Mater. Chem*., 2006, **16**, 2534.

10 S. L. Heath, A. K. Powell, *Angew. Chem., Int. Ed*., 1992, **31**, 191.

11 W. Wernsdorfer, *Adv. Chem. Phys*., 2001, **118**, 99.

12 I. A. Swanson, D. H. Ryan, *private communication*, 2007.

13 G. Shirane, *Acta Crystallogr.*, 1959, **12**, 282.

14 E. F. Bertaut, *J. Appl. Phys*., 1962, **33**, 1138.

15 E. F. Bertaut, in *Treatise on Magnetism*, edited by G. T. Rado and H. Suhl (Academic, New York, 1963), **Vol. III**, 149.

16 S. Wills, Physica B (Amsterdam), 2000, **276-278**, 680.

Chapter 3
Polymetallic clusters of iron(III) with derivatised salicylaldoximes

Introduction

The coordination chemistry of $saoH_2$ (salicylaldoxime) and its derivatives R-$saoH_2$ (Scheme 3.1) have previously been explored in Mn chemistry, a project that has yielded complexes varying in nuclearity from four to eight, exhibiting fascinating magnetic properties.[1] Herein we report our first foray into Fe-R-$saoH_2$ chemistry. It is worth noting that no Fe^{III} complex containing the ligands R-$saoH_2$ has been crystallographically identified to date. The ligand $saoH_2$ and its derivatives belong to the family of phenolic oximes that have found uses not only in academic coordination chemistry, but industrially as metal extractants and as anticorrosives in protective coatings.[2a] The peculiar selectivity for the Cu^{II} ion in particular (and the formation of square planar [Cu(R-$saoH)_2$] complexes) stems from the 'ideal' cavity size and thermodynamic stability created by the two H-bonded R-$saoH^{1-}$ ligands in acidic solutions.[2a] However deprotonation of both the phenolic and oximic oxygen atoms can lead to a large variety of coordination modes resulting in the formation of polynuclear complexes.[2a-c] Indeed **11–13** join a small family of crystallographically identified octanuclear Fe complexes[3] that, along with **17**, are also the largest Fe complexes containing R-$saoH_2$-based ligands.

The coordination chemistry of the sulfate ion, SO_4^{2-}, has recently been explored in Ni cluster chemistry[4] and has been widely used in the preparation of simple Fe monomers and polymers, including Kagome lattices.[5-7] Despite displaying a variety of coordination modes (μ_2–μ_5, Scheme 2),[8-17] its use as a bridging ligand for the formation of polymetallic Fe molecules is surprisingly rare, with the majority of the crystallographically identified compounds being dimeric (Table 3.1). Complex **10** is thus a rare and welcome addition to this small family and suggests much potential.

Experimental Section

All manipulations were performed under aerobic conditions using chemicals as received, unless otherwise stated. Care should be taken when using the potentially explosive perchlorate anion. 2′-Hydroxyacetophenone oxime (Me-saoH$_2$), 2′-hydroxypropiophenone oxime (Et-saoH$_2$) and 2-hydroxybenzophenone oxime (Ph-saoH$_2$) were synthesised *via* the reaction of the appropriate ketone with hydroxylamine and sodium acetate in EtOH, as described in the literature.[18]

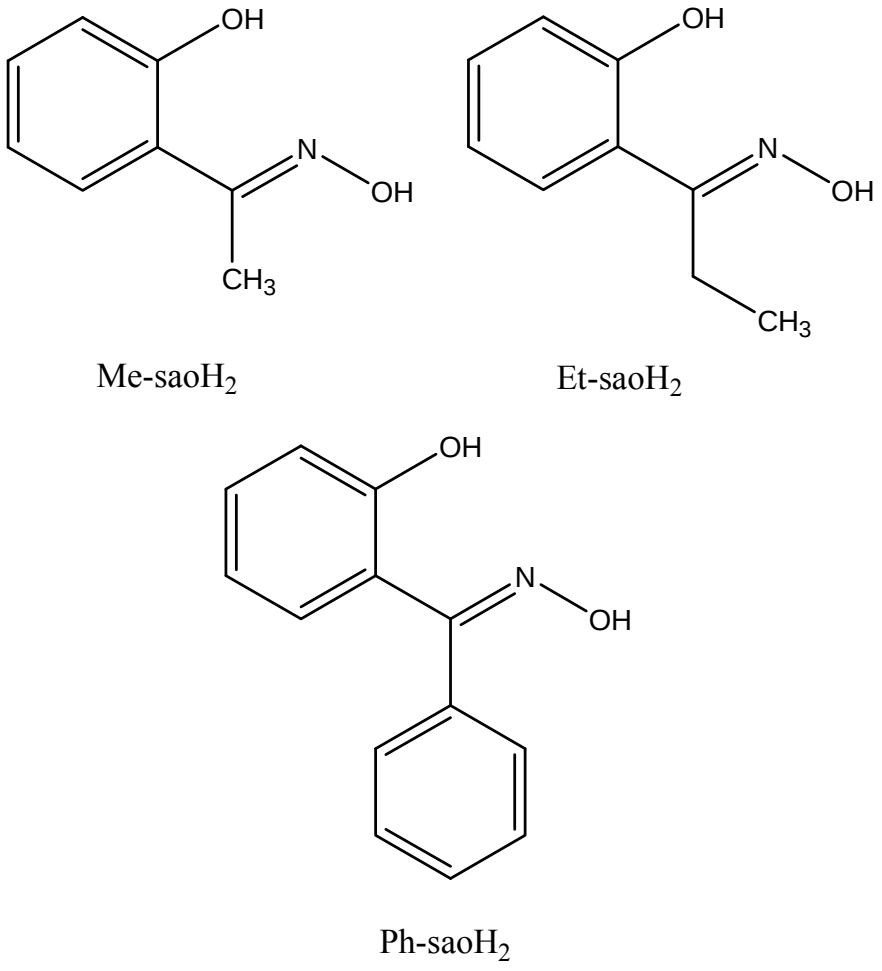

Me-saoH$_2$ Et-saoH$_2$

Ph-saoH$_2$

Scheme 3.1 Structural formulae of the R-saoH$_2$ ligands discussed in the text.

Table 3.1 Crystallographically identified complexes of Fe with coordinated sulfate ions

Formula	Reference
$[(Fe^{III}(TPP))_2SO_4]$	8
$[Fe^{III}_2O(SO_4)_2(phen)]\cdot 8H_2O$	9
$[NH_2(CH_3)_2]_8[Fe^{III}_{12}O_4(SO_4)_{12}(link)_x(py)_{12}]\cdot G$	10
$[Fe^{III}_2O(HL)_4(SO_4)_2]\cdot 2MeOH\cdot 3H_2O$	11
$[NH_4][Fe^{III}_2(bbpmp)(SO_4)_2]$	12
$[Fe^{III}_2(H_2O)_6(bipym)(SO_4)_2]$	13
$\{[Fe^{III}(bispicMe_2en)]_2OSO_4\}[ClO_4]_2\cdot 2H_2O$	14
$[Fe^{II}_2(SO_4)(CO)_4(Cp)_2]$	15
$[Fe^{III}_2O(SO_4)_2(btt)_2]\cdot 3H_2O$	16
$[Fe^{III}_2(SO_4)_2(H_2O)_6(bpp)]\cdot 2H_2O$	17

Abbreviations. TPP, tetraphenylporphyrin; phen, 1,10-phenanthroline; link = (H_2BDC, 1,4-benzenedicarboxylic acid, H_2BPDC, 4,4'-biphenyl carboxylic acid, H_2HPDC, tetrahydropyrene-2,7-dicarboxylic acid, H_2TPDC, 4,4``-terphenyldicarboxylic acid, H_3BTB, 1,3,5-tris(4-carboxyphenyl)-benzene); G, gaseous guests; HL, 3-(2-pyridyl)-pyrazole; bbpmp, anion of 2,6-bis[(2-hydroxy-benzyl)(2-pyridyl-methyl)-amino-methyl]-4-methylphenol; bipym, 2.2` -bipyrimidine; bispicMe_2en, N,N'-bis(2-pyridylmethyl)-N,N'-bis(methyl)-1,2-ethanediamine; Cp, cyclopentadienyl; btt, N,N',N''-trimethyl-1,4,7-triazacyclononane- N,N',N''; bpp, 2,5-bis(2'-pyridyl)pyrazine-N,N',N'',N''''.

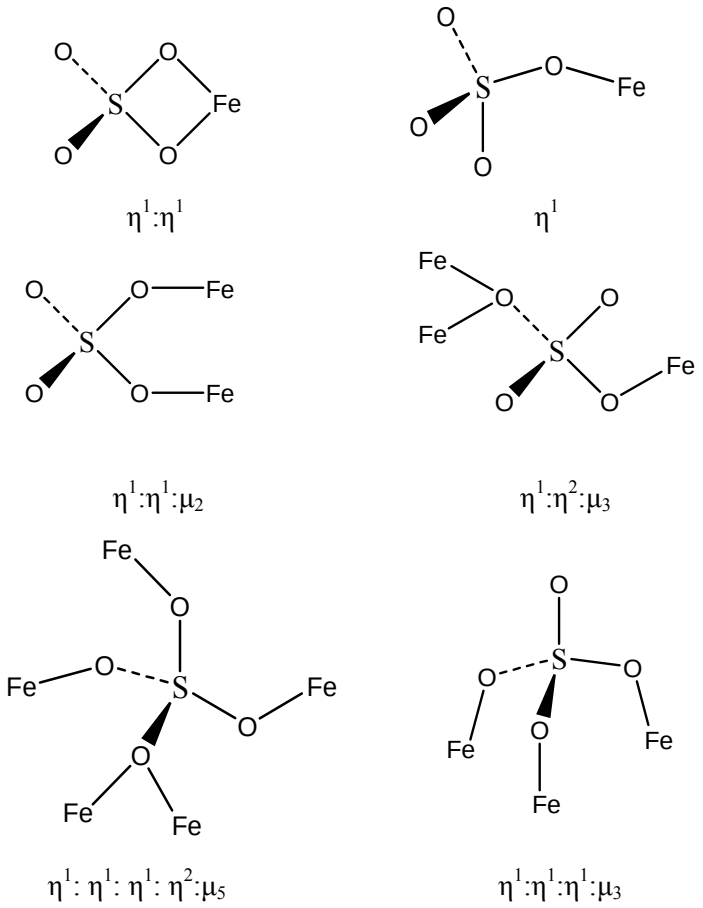

Scheme 3 The crystallographically identified coordination modes of the SO_4^{2-} ion with Fe.

Synthetic Procedures

$[HNEt_3][Fe_2(OMe)(Ph\text{-}sao)_2(Ph\text{-}saoH)_2]\cdot 5MeOH$ (**7**·5MeOH)**.**

$Fe_2(SO_4)_3\cdot 6H_2O$ (730 mg, 1.44 mmol) in MeOH (30 ml) was treated with solid Ph-saoH$_2$ (328 mg, 1.43 mmol) in the presence of NEt_3 (0.5 ml, 4.9 mmol). After 1 h stirring, the resulting dark brown solution was filtered and the dark brown solution left to slowly evaporate at room temperature. X-ray quality black crystals formed during 1 day. The crystals were collected by filtration and dried *in vacuo.* The yield

was approximately 65%. The dried sample analysed as **1**·4MeOH. Found (calc.%): $C_{63}H_{73}Fe_2N_5O_{13}$; C 62.26 (62.02), H 6.38 (6.03), N 5.81 (5.74). IR data (KBr pellet; cm^{-1}): 1637 s, 1617 s, 1591 s, 1560 w, 1542 w, 1531 w, 1490 w, 1468 m, 1436 s, 1385 m, 1310 s, 1255 m, 1147 m, 1041 m, 1026 m, 959 m, 945 m, 917 w, 849 m, 755 s, 700 m, 667 m, 648 m, 611 m, 597 m, 513 w, 474 m.

$[Fe_3O(Et\text{-}sao)(O_2CPh)_5(MeOH)_2]$·3MeOH (**8**·3MeOH)**.**

$Fe(ClO_4)_2$·$6H_2O$ (365 mg, 1.0 mmol) in MeOH (30 ml) was treated with solid Et-$saoH_2$ (165 mg, 1.0 mmol) and NaO_2CPh (144 mg, 1.0 mmol) in the presence of NEt_4OH (0.5 ml, 0.5 mmol). After 1 h stirring, the resulting dark brown solution was filtered and the dark brown solution left to slowly evaporate at room temperature. X-ray quality black crystals formed during 3 days. The crystals were collected by filtration and dried *in vacuo*. The yield was approximately 50%. The dried sample analysed as **8**·MeOH. Found (calc.%): $C_{47}H_{46}Fe_3NO_{16}$; C 53.71 (53.84), H 4.04 (4.42), N 1.51 (1.34). IR data (KBr pellet; cm^{-1}): 1699 w, 1615 m, 1593 s, 1573 m, 1545 m, 1474 s, 1438 s, 1366 m, 1323 s, 1307 s, 1247 s, 1171 w, 1159 w, 1130 m, 1071 w, 1047 m, 1014 s.

$[Fe_4(Me\text{-}sao)_4(Me\text{-}saoH)_4]$·MeOH (**9**)**.**

$Fe(ClO_4)_2$·$6H_2O$ (255 mg, 0.70 mmol) in MeOH (30 ml) was treated with solid Me-$saoH_2$ (755 mg, 5.0 mmol) and NaO_2CCMe_3 (179 mg, 1.44 mmol) in the presence of NEt_4OH (0.5 ml, 0.5 mmol). After 1 h stirring, the resulting dark brown solution was filtered and the dark brown solution left to slowly evaporate at room temperature. X-ray quality black crystals formed during 3 days. The crystals were collected by filtration and dried *in vacuo*. The yield was approximately 55%. The dried sample analysed as solvent free. Found (calc.%): $C_{65}H_{64}Fe_4N_8O_{17}$; C 57.21 (56.74), H 4.45 (4.44), N 8.06 (7.71). IR data (KBr pellet; cm^{-1}): 1595 s, 1576 m, 1552 w, 1531 m, 1471 w, 1435 s, 1367 w, 1335 w, 1311 s, 1294 s, 1242 s, 1159w, 1130 m, 1070w, 1030 m, 1012 m, 945 s, 852 m, 752 s, 652 m, 609 m, 582 w, 563 m, 532 w, 515 m, 476 w, 453 m, 430 w,411 w.

$[HNEt_3]_2[Fe_6O_2(Me\text{-}sao)_4(SO_4)_2(OMe)_4(MeOH)_2]$ (10).

$Fe_2(SO_4)_3 \cdot 6H_2O$ (508 mg, 1.0 mmol) in MeOH (30 ml) was treated with solid Me-saoH_2 (151 mg, 1.0 mmol) in the presence of NEt_3 (404 mg, 4.0 mmol). After 1 h stirring, the resulting solution was filtered and the black solution layered with Et_2O to produce X-ray quality black crystals in 3 days. The crystals were collected by filtration and dried *in vacuo.* The yield was approximately 30%. The dried sample analysed as solvent-free. Found (calc.%): $C_{50}H_{80}Fe_6N_6O_{24}S_2$; C 38.96 (38.78), H 5.10 (5.21), N 5.38 (5.43). IR data (KBr pellet; cm^{-1}): 1593 w, 1562 w, 1518 w, 1475 w, 1433 m, 1319 m, 1255 w, 1228 w, 1176 m, 1161 m, 1130 w, 1039 s, 1003 m, 984 m, 941 m, 856 w, 758 w, 663 m, 627 m, 540 m, 476 m, 426 m.

$[Fe_8O_3(Me\text{-}sao)_3(tea)(teaH)_3(O_2CMe)_3]\cdot 3MeOH$ (11·3MeOH**).**

$Fe(O_2CMe)_2$ (250 mg, 1.44 mmol), Me-saoH_2 (218 mg, 1.44 mmol) and H_3tea (215 mg, 1.44 mmol) were dissolved in MeOH (20 ml) and the mixture stirred for 2 h, then filtered. The solution was then layered with Et_2O to produce X-ray quality crystals in two weeks. The crystals were collected by filtration and dried *in vacuo.* The yield was approximately 15%. The dried sample analysed as solvent free. Found (calc.%): $C_{54}H_{81}Fe_8N_7O_{27}$; C 37.99 (38.00), H 4.93 (4.78), N 5.64 (5.74). IR data (KBr pellet; cm^{-1}): 1636 m, 1575 s, 1437 s, 1308 m, 1248 w, 1109 m, 1099 m, 1076 m, 1052 m, 1027 m, 988 w, 962 w, 908 w, 877 w, 858 w. 755 m, 670 m, 660 m, 597 s, 575 s, 507 m, 472 m, 411 m.

$[Fe_8O_3(Et\text{-}sao)_3(tea)(teaH)_3(O_2CMe)_3]\cdot 3MeOH$ (12·3MeOH**).**

$Fe(O_2CMe)_2$ (250 mg, 1.44 mmol), Et-saoH_2 (218 mg, 1.44 mmol) and H_3tea (215 mg, 1.44 mmol) were dissolved in MeOH (20 ml) and the mixture stirred for 2 h, then filtered. The solution was then layered with Et_2O to produce X-ray quality crystals in two weeks. The crystals were collected by filtration and dried *in vacuo.* The yield was approximately 20%. The dried sample analysed as solvent free. Found (calc.%): $C_{57}H_{87}Fe_8N_7O_{27}$; C 39.22 (39.14), H 5.05 (5.01), N 5.37 (5.61). IR data

(KBr pellet; cm^{-1}): 1635 w, 1574 s, 1559 s, 1473 w, 1434 s, 1384 w, 1347 w, 1314 m, 1262w, 1107 m, 1073 m, 1048 m, 1000 m, 942 m, 910 m, 874 w, 849 w, 758 m, 669 m, 660 m, 578 m, 513 m, 481 w, 442 w, 409 w.

$[Fe_8O_3(Ph\text{-}sao)_3(tea)(teaH)_3(O_2CMe)_3]\cdot 4MeOH$ (**13**·4MeOH)**.**

$Fe(O_2CMe)_2$ (250 mg, 1.44 mmol), Ph-saoH_2 (307 mg, 1.44 mmol) and H_3tea (215 mg, 1.44 mmol) were dissolved in MeOH (20 ml) and the mixture stirred for 2 h, then filtered. The solution was then layered with Et_2O to produce X-ray quality crystals in two weeks. The crystals were collected by filtration and dried *in vacuo.* The yield was approximately 25%. The dried sample analysed as solvent free. Found (calc.%): $C_{70}H_{91}Fe_8N_7O_{28}$; C 43.58 (43.77), H 4.57 (4.63), N 5.17 (5.18). IR data (KBr pellet; cm^{-1}): 1634 w, 1591 m, 1569 s, 1527 m, 1490 w, 1434 s, 1372 w, 1340 w, 1314 s, 1255 m, 1168w, 1147w, 1096 s, 1081 s, 1048 s, 1038 s, 1022 s, 958 m, 926 w, 908 m, 878 w, 849 w, 780 w, 758 m, 739 m, 701 m, 661 s, 580 s, 549 m, 528 m, 502 m, 409 w.

$[Fe_6O_2(OH)_2(Et\text{-}sao)_2(Et\text{-}saoH)_2(O_2CPh)_6]$ (**14**).

$FeCl_3\cdot 6H_2O$ (135 mg, 0.5 mmol), Et-saoH_2 (82.5 mg, 0.5 mmol), NaO_2CPh (216 mg, 1.5 mmol) were dissolved in MeCN in the presence of NEt_3 (0.25 ml, 0.2 mmol) and heated to 50°C. After 90 mins stirring the solution was filtered and then layered with Et_2O to produce X-ray quality crystals in 2 weeks. The crystals were collected by filtration and dried *in vacuo.* The yield was approximately 55%. The dried sample analysed as 14·NEt_3. Found (calc.%): $C_{84}H_{85}Fe_6N_5O_{24}$; C 54.10 (53.56), H 4.72 (4.55), N 3.96 (3.72). IR data (KBr pellet; cm^{-1}): 1599s, 1560s, 1400s, 1313m, 1254m, 1070m, 1016m, 935m, 839m, 752m, 717s, 671m, 638m, 586m, 513m, 467s.

$[HNEt_3]_2[Fe_6O_2(OH)_2(Et\text{-}sao)_4(O_2CPh(Me)_2)_6]\cdot 2MeCN$ (**15**·2MeCN).

$FeCl_3\cdot 6H_2O$ (270 mg, 1.0 mmol), Et-saoH_2 (165 mg, 1.0 mmol), $NaO_2CPh(Me)_2$ (158 mg, 1.0 mmol) were dissolved in MeCN in the presence of NEt_3 (1.0 ml, 8.0

mmol) and heated to 50°C. After 120 mins stirring the solution was filtered and the solution left to slowly evaporate at room temperature. X-ray quality crystals formed in 2 weeks. The crystals were collected by filtration and dried *in vacuo*. The yield was approximately 30%. The dried sample analysed as **2**·MeCN. Found (calc.%): $C_{104}H_{127}Fe_6N_7O_{24}$; C 56.42 (56.93), H 5.81 (5.83), N 4.72 (4.47). IR data (KBr pellet; cm^{-1}): 1568s, 1431s, 1398s, 1309m, 1267m, 1076m, 1053m, 931m, 841m, 789m, 752s, 648m, 598m, 509m, 465s.

$([Fe_6Na_3O(OH)_4(Me\text{-}sao)_6(OMe)_3(H_2O)_3(MeOH)_6]\cdot MeOH)_n$ (**16**·MeOH).

Method 1 $Fe(ClO_4)_2\cdot 6H_2O$ (182.5 mg, 0.5 mmol), Me-saoH_2 (151 mg, 1.0 mmol), NaO_2CHCl_3 (185 mg, 1.0 mmol) were dissolved in MeOH in the presence of NEt_3 (1.0 ml, 8 mmol). After 180 mins stirring the solution was filtered and then left to slowly evaporate producing X-ray quality crystals in 4 days. The crystals were collected by filtration and dried *in vacuo*. The yield was approximately 65%. The dried sample analysed as solvent free. Found (calc. %): $C_{57}H_{84}Fe_6Na_3N_6O_{29}$; CHN; C 37.03 (39.77), H 4.04 (4.92), N 5.18 (4.88). IR data (KBr pellet; cm^{-1}): 1630m, 1593m, 1568m, 1531m, 1473m, 1435s, 1306s, 1250m, 1130m, 1024s, 962m, 856m, 752s, 665s, 611m, 449m, 415m.

Method 2 $Fe(O_2CMe)_2\cdot 6H_2O$ (174 mg, 1.0 mmol), Me-saoH_2 (151 mg, 1.0 mmol), NaOMe (324 mg, 6.0 mmol) were dissolved in MeOH. After 120 mins stirring the solution was filtered and then left to slowly evaporate producing X-ray quality crystals in 3 days. The crystals were collected by filtration and dried *in vacuo*. The yield was approximately 50%. The dried sample analysed satisfactorily as solvent free **16**.

Method 3 $FeCl_3\cdot 6H_2O$ (270 mg, 1.0 mmol), Me-saoH_2 (302 mg, 2.0 mmol), NaOMe (216 mg, 4.0 mmol) were dissolved in MeOH. After 120 mins stirring the solution was filtered and then left to slowly evaporate producing X-ray quality crystals in 4 days. The crystals were collected by filtration and dried *in vacuo*. The yield was approximately 50%. The dried sample analysed satisfactorily as solvent free **16**.

Method 4 $Fe(ClO_4)_2 \cdot 6H_2O$ (182.5 mg, 0.5 mmol), Me-$saoH_2$ (151 mg, 1.0 mmol), NaO_2CHBr_3 (319 mg, 1.0 mmol) were dissolved in MeOH in the presence of NEt_4OH (1.0M in water) (0.125 ml, 0.125 mmol). After 120 mins stirring the solution was filtered and then left to slowly evaporate producing X-ray quality crystals in 3 days. The crystals were collected by filtration and dried *in vacuo*. The yield was approximately 55%. The dried sample analysed satisfactorily as solvent free **16**.

$[HNEt_3]_2[Fe_{12}Na_4O_2(OH)_8(sao)_{12}(OMe)_6(MeOH)_{10}]$ (**17**)

$Fe(ClO_4)_2 \cdot 6H_2O$ (365 mg, 1.0 mmol), $saoH_2$ (137 mg, 1.0 mmol), NaO_2CHBr_3 (319 mg, 1.0 mmol) were dissolved in MeOH in the presence of NEt_3 (0.125 ml, 1 mmol). After 180 mins stirring the solution was filtered and then left to slowly evaporate producing X-ray quality crystals in 3 days. The crystals were collected by filtration and dried *in vacuo*. The yield was approximately 30%. The dried sample analysed as solvent free. Found (calc. %): $C_{112}H_{156}Fe_{12}Na_4N_{14}O_{50}$; CHN; C 40.2 (41.26), H 4.46 (4.82), N 5.83 (6.01). IR data (KBr pellet; cm^{-1}): 1593s, 1543m, 1473m, 1437m, 1321m, 1290s, 1200m, 1153m, 1120m, 1018m, 916s, 818m, 764s, 665m, 607m.

Results and Discussion

Synthesis

In the preparations of **8**,**9** and **11–13** an Fe^{II} to Fe^{III} oxidation occurs. Treatment of $Fe_2(SO_4)_3 \cdot 6H_2O$ with Ph-$saoH_2$ in the presence of NEt_3 in a 1 : 1 molar ratio in MeOH yields the dinuclear complex $[HNEt_3][Fe_2(OMe)(Ph\text{-}sao)_2(Ph\text{-}saoH)_2] \cdot 5MeOH$ (**7**·5MeOH) in high yield. This is likely due to the presence of the bulky Ph-sao^{n-} ligands, which aid rapid crystallisation and thus favour the formation of low nuclearity products. The sulfate ion is not present in **7** either as a bridging ligand or

as counter ion, but repeating the reaction in its absence does not produce **7**, suggesting it must play some role. The same reaction with the less bulky oxime Me-saoH$_2$ affords the hexanuclear complex [HNEt$_3$]$_2$[Fe$_6$O$_2$(Me-sao)$_4$(SO$_4$)$_2$(OMe)$_4$(MeOH)$_2$] (**10**). Thus it appears that a reduction in the bulk of the oxime produces not only a larger cluster, but one that can also incorporate bridging SO_4^{2-} ions. In changing the Fe salt from Fe$_2$(SO$_4$)$_3$·6H$_2$O to Fe(ClO$_4$)$_2$·6H$_2$O we lose the coordinative flexibility of the SO_4^{2-} ligand and so to compensate we incorporated carboxylates into our reaction scheme. Thus treatment of Fe(ClO$_4$)$_2$·6H$_2$O with Et-saoH$_2$ and NaO$_2$CPh in a 1 : 1 : 1 molar ratio in the presence of NEt$_4$OH in MeOH yields the trinuclear complex [Fe$_3$O(Et-sao)(O$_2$CPh)$_5$(MeOH)$_2$]·3MeOH (**8**·3MeOH). This is essentially a direct analogue of the basic Fe^{III} carboxylates of general formula $[Fe_3O(O_2CR)_6L_3]^+$, (L = solvent) where the oxime has directly replaced one of the carboxylates and one of the terminal solvate molecules. This of course suggests that oximes could be used as direct replacements for carboxylates in all known polymetallic Fe carboxylate clusters – a concept with far reaching implications and huge potential. Thus the same reaction was explored using Me-saoH$_2$ with NaO$_2$CCMe$_3$, changing the molar ratio to 3.5 : 1. The resulting tetranuclear complex [Fe$_4$(Me-sao)$_4$(Me-saoH)$_4$] (**9**) now contains no carboxylates, and is the iron derivative of a (ferromagnetic) $[Mn^{III}_4]$ distorted cube recently published.[19]

We also have a long standing interest in the use of polyalkoxides for the formation of cluster compounds[20] and thus also decided to incorporate triethanolamine (H$_3$tea) into these oxime based reaction schemes. Treatment of Fe(O$_2$CMe)$_2$ with R-saoH$_2$ and H$_3$tea yields the octanuclear complexes [Fe$_8$O$_3$(R-sao)$_3$(tea)(teaH)$_3$(MeCO$_2$)$_3$] where R = Me (**11**), Et (**12**) and Ph (**13**). The combined flexibility of incorporating both oximes and tripodal alcohols leads to the isolation of larger Fe clusters than those obtained using only R-saoH$_2$ ligands, and suggests this may be a route to obtaining yet larger clusters.

Synthesis of **14** and **15** under ambient reaction conditions resulted in a dark red solution from which no crystals were obtained. A similar system ,[Fe$_6$O$_2$(O$_2$CPh)$_{10}$(sao)$_2$(H$_2$O)$_2$],[23f] required refluxing for 24 hrs so we decided to try

the synthesis at 50° C from which we obtained our single crystals. It is not clear why this particular system requires heating especially in view of the large number and variety of structures obtained from ambient conditions. **16** can be made in any one of four methods (*vide supra*) all of which simply require an Fe salt, Me-saoH$_2$ and a source of Na which can be the base as in methods 2 and 3, or a sodium carboxylate as in methods 1 and 4. Use of Me-saoH$_2$ in **16** leads to the formation of a (6,3) net of [Fe$_6$] units while simply changing the oxime to saoH$_2$ as in **17** forms an isolated dodecametallic dimer consisting of two [Fe$_6$Na] units (*vide infra*) although it is unclear why the addition of a methyl group has such a profound effect on the final structure.

Description of Structures

[HNEt$_3$][Fe$_2$(OMe)(Ph-sao)$_2$(Ph-saoH)$_2$] (**7**) crystallises in the triclinic space group $P\bar{1}$ with two molecules in the unit cell (Fig. 3.1; selected bond lengths and angles are given in Table A.3.1) The two Fe^{III} ions are linked to each other *via* one μ-OMe$^-$ ion (Fe–O15–Fe, 108.81(30)°) and two fully deprotonated Ph-sao^{2-} ligands bridging in a η^1: η^1: η^1:μ fashion. The coordination geometry of the Fe^{III} ions is completed by two chelating Ph-saoH$^-$ ligands which coordinate through the deprotonated phenolic oxygen and the oximic nitrogen atom, with the oximic oxygen atoms (O91, O93) remaining unbound and protonated, and involved in extensive H-bonding (*vide infra*). Each Fe^{III} ion is in a distorted octahedral geometry (*cis*, 81.8(3)–99.4(3) °; *trans*, 164.8(3)–177.0(3)°) with their oxidation states assigned using charge balance considerations, bond lengths and BVS calculations[21] (Table A.3.2). In the crystal lattice there are a significant number of hydrogen bonds: one between the cation and the phenolate O atom (N· · ·O, 2.757(11) Å); two between the phenolate O-atoms and the MeOH solvate (O· · ·O 2.680(11) Å and 2.816(12) Å); two between the oximato O-atom and the MeOH solvate (O· · ·O 2.667(12) Å and 2.754(13) Å); and between individual solvate

Table 3.2 Crystallographic details for complexes **7**-**9**.

	7·5MeOH	**8**·3MeOH	**9**
M, gmol^{-1}	1252.01	1112.48	1452.65
crystal system	Triclinic	Monclinic	Monoclinic
space group	$P\bar{1}$	*P21/c*	*P21/n*
a, Å	10.1601(8)	21.0901(12)	13.4558(3)
b, Å	15.1676(16)	11.5474(7)	18.4743(5)
c , Å	21.610(3)	20.5990(12)	26.9983(7)
α, deg	106.158(9)	90	90
β, deg	99.287(7)	100.198(4)	102.765(1)
γ, deg	93.760(5)	90	90
V , Å^3	3135.2(6)	4937.3(5)	6545.5(3)
Z	2	4	4
$\rho_{, calc}$ [g cm^{-3}]	1.326	1.497	1.441
T , K	150(2)	150	150
λ (Å)	0.71073	0.71073	0.71073
μ, [mm^{-1}]	0.531	0.946	0.942
Measd/independant (R_{int})	20024/6596 (0.1073)	62527/14827 (0.0298)	97083/19572 (0.068)
Obsd reflns [I>2σ (*I*)]	3894	12120	10934
*R*1[b]	0.0941	0.0391	0.0879
*wR*2[c]	0.2567	0.1097	0.2116
GOF on F^2	1.032	1.051	0.9134
Δ $\rho_{max,min,}$ e Å^{-3}	0.809, -0.627	0.987, -0.572	2.33, -1.63

[a]$R1$) $\sum(|F_o|-|F_c|)/\sum(|F_o|)$ for observed reflections. [b] $_b wR_2$) $\{\sum[w(F_{o2} - F_{c2})_2]/\sum[w(F_{o2})_2]\}_{1/2}$ for all data.

Table 3.3 Crystallographic details for complexes **10**-**12**.

	10	**11**·3MeOH	**12**·3MeOH
M, gmol^{-1}	1548.43	1803.18	1845.26
crystal system	Orthorhombic	Rhombohedral	*Rhombohedral*
space group	*Pbca*	*R3c*	*R3c*
a, Å	19.9693(6)	23.2455(8)	23.3194(7)
b, Å	14.2060(4)	23.2455(8)	23.3194(7)
c , Å	22.7462(7)	23.7519(15)	23.8317(17)
α, deg	90	90	90
β, deg	90	90	90
γ, deg	90	120	120
V , Å^3	6452.7(3)	11114.9(9)	11223.3(9)
Z	4	6	6
$\rho_{, calc}$ [g cm^{-3}]	1.71	1.616	1.638
T , K	150	150(2)	150(2)
λ (Å)	0.71073	0.71073	0.71073
μ, [mm^{-1}]	1.458	1.606	1.592
Measd/independant (R_{int})	149468/9264 (0.046)	68038/7134 (0.0566)	50293/3586 (0.1417)
Obsd reflns [I>2σ (*I*)]	6354	6260	2785
$R1$[b]	0.0323	0.0422	0.0448
$wR2$[c]	0.0732	0.1103	0.1128
GOF on F^2	1.0215	1.082	0.990
Δ $\rho_{max,min,}$ e Å^{-3}	1.71, -0.89	0.805, -0.417	0.702, -0.705

[a]$R1$) $\sum(|F_o|-|F_c|)/\sum(|F_o|)$ for observed reflections. [b] $_b wR_2$) $\{\sum[w(F_{o2} - F_{c2})_2]/\sum[w(F_{o2})_2]\}_{1/2}$ for all data.

Table 3.4 Crystallographic details for complexes **13-15**

	13·4MeOH	**14**	**15**·2MeCN
M, gmol^{-1}	2021.43	1835.66	2235.32
crystal system	Triclinic	Triclinic	Monoclinic
space group	$P\bar{1}$	*P - 1*	$P2_1/c$
a, Å	16.2363(5)	12.8061(8)	14.6892(6)
b, Å	17.6493(6)	13.5584(9)	19.6643(9)
c , Å	18.6823(6)	14.0247(9)	19.2762(9)
α, deg	108.435(2)	71.209(4)	90
β, deg	98.275(2)	78.955(4)	104.153(2)
γ, deg	105.150(2)	78.812(4)	90
V , Å^3	4749.9(3)	2239.6(3)	5399.0(4)
Z	2	1	2
$\rho_{, calc}$ [g cm^{-3}]	1.41	1.322	1.37
T , K	150(2)	150	150
λ (Å)	0.71073	0.71073	0.71073
μ, [mm^{-1}]	1.262	1.015	0.859
Measd/independant (R_{int})	113796/27792 (0.094)	7881/7881(0.065)	58382/ 11075(0.096)
Obsd reflns [I>2σ (*I*)]	9803	4615	6311
$R1$[b]	0.0500	0.0617	0.0536
$wR2$[c]	0.1600	0.1741	0.1660
GOF on F^2	0.6171	0.9039	0.6354
$\Delta \rho_{max,min,}$ e Å^{-3}	1.80, -1.29	1.48, -0.87	0.96, -1.08

[a]$R1$) $\sum(|F_o|-|F_c|)/\sum(|F_o|)$ for observed reflections. [b] $_b wR_2$) $\{\sum[w(F_{o2} - F_{c2})_2]/\sum[w(F_{o2})_2]\}_{1/2}$ for all data.

Table 3.5 Crystallographic details for complexes **13-16**

	16	**17**
M, $gmol^{-1}$	1753.41	3262.67
crystal system	Hexagonal	Monoclinic
space group	*P63/m*	$P2_1/c$
a, Å	12.40610(10)	23.1511(7)
b, Å	12.40610(10)	13.5740(4)
c , Å	28.8478(6)	23.7570(8)
α, deg	90	90
β, deg	90	95.223
γ, deg	120	90
V , $Å^3$	3845.16(9)	7434.7(4)
Z	2	2
$\rho_{, calc}$ [g cm^{-3}]	1.51	1.45
T , K	150	150
λ (Å)	0.71073	0.71073
μ, [mm^{-1}]	1.199	1.227
Measd/independant (R_{int})	46897/2110 (0.066)	15221/15162 (0.157)
Obsd reflns [I>2σ (*I*)]	2110	6186
$R1^b$	0.0297	0.0753
$wR2^c$	0.0322	0.2685
GOF on F^2	0.9647	1.4701
Δ $\rho_{max,min,}$ e $Å^{-3}$	0.71, -0.41	1.83, -1.92

[a]$R1$) $\sum(|F_o|-|F_c|)/\sum(|F_o|)$ for observed reflections. [b] $_bwR_2$) $\{\sum[w(F_{o2} - F_{c2})_2]/\sum[w(F_{o2})_2]\}_{1/2}$ for all data.

MeOH molecules (O· · ·O, 2.717(17) Å). A further hydrogen bonding interaction between the oximato O-atom and a phenyl group on a neighbouring molecule plays a major role in the packing of the molecules in the crystal lattice directing the formation of 1D chains with the cations sitting on alternative sides of neighbouring molecules along the chain (Fig. 3.2). The closest intermolecular Fe· · ·Fe distance is 11.31(3) Å .

$[Fe_3O(Et\text{-}sao)(O_2CPh)_5(MeOH)_2]$ (**8**) crystallises in the monoclinic space group *P*21/*c* with four molecules in the unit cell (Fig. 3.3, 3.4; selected bond lengths and angles are given in Table A.3.3) Its structure is analogous to that of the basic Fe^{III} carboxylates of general formula $[Fe_3O(O_2CR)_6L_3]^+$ with one of the carboxylates replaced with a η^1: η^1: η^1:μ-bridging Et-sao^{2-} ligand along the Fe1–Fe2 edge, and the terminal "L" positions occupied by two methanol molecules and the terminal oximate nitrogen atom (N81) of the Et-sao^{2-} ligand. The Fe· · ·Fe separations and Fe–μ_3-O–Fe angles are unequal (3.2397(4)Å, 3.2611(4) Å, 3.3254(4) Å , 116.44(5)°, 120.65(6)°, 122.65(6)°) and so the triangle is truly scalene rather than isosceles. Each Fe^{III} ion is in a distorted octahedral geometry with *cis* angles in the range 83.04(5)–97.21(5)°, and *trans* angles in the range 167.57(5)–179.67(5)° with their oxidation states assigned using charge balance considerations, bond lengths and BVS calculations (Table A.3.4) In the crystal lattice there are a significant number of strong hydrogen bonds: between the terminally bound MeOH molecules and solvate MeOH; between individual solvate MeOH molecules; and between the phenolate O-atoms and solvate MeOH molecules, all with O· · ·O distances in the range 2.633(2)–2.687(2)Å. The consequence is the formation of 1D chains of H-bonded triangles as shown in Fig. 3.4. The closest intermolecular Fe · · ·Fe distance is 8.2503(5) Å.

$[Fe_4(Me\text{-}sao)_4(Me\text{-}saoH)_4]$ (**9**) crystallises in the monoclinic space group *P*21/*c* with four molecules in the unit cell. (Fig. 3.5, 3.6; selected bond lengths and angles are given in Table A.3.5). The metallic skeleton consists of a tetrahedron of Fe^{III} ions which are linked together by four fully deprotonated Me- sao^{2-}ligands in a η^2: η^1: η^1: μ_3 fashion forming a distorted $[Fe_4(NO)_4]^{8+}$ cube. Four singly deprotonated Me-saoH$^-$ ligands then each chelate one Fe^{III} ion. The metal ions are in distorted

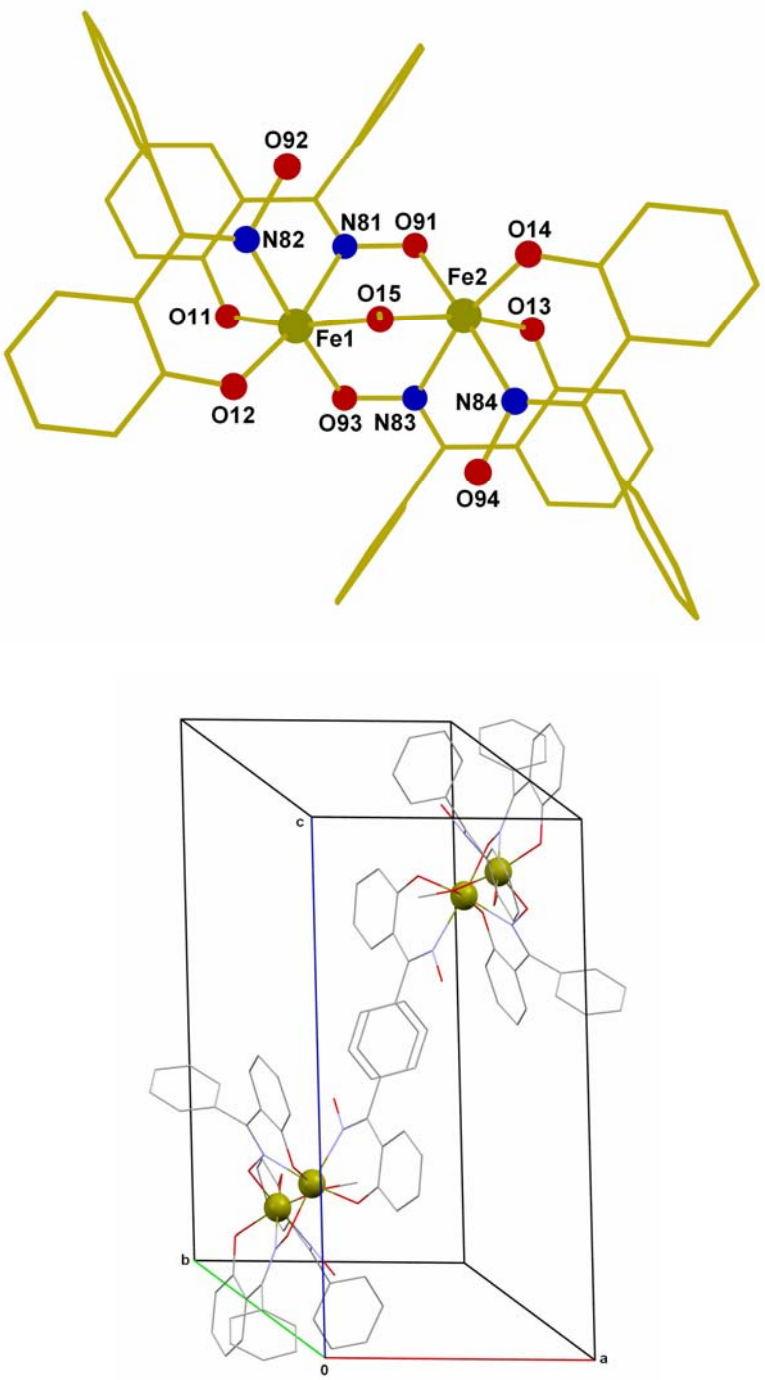

Fig 3.1 Molecular structure of **7** (top) and the packing of molecules of **7** in the unit cell (bottom). Colour code: Fe = green; O = red; N = blue; C = gold.

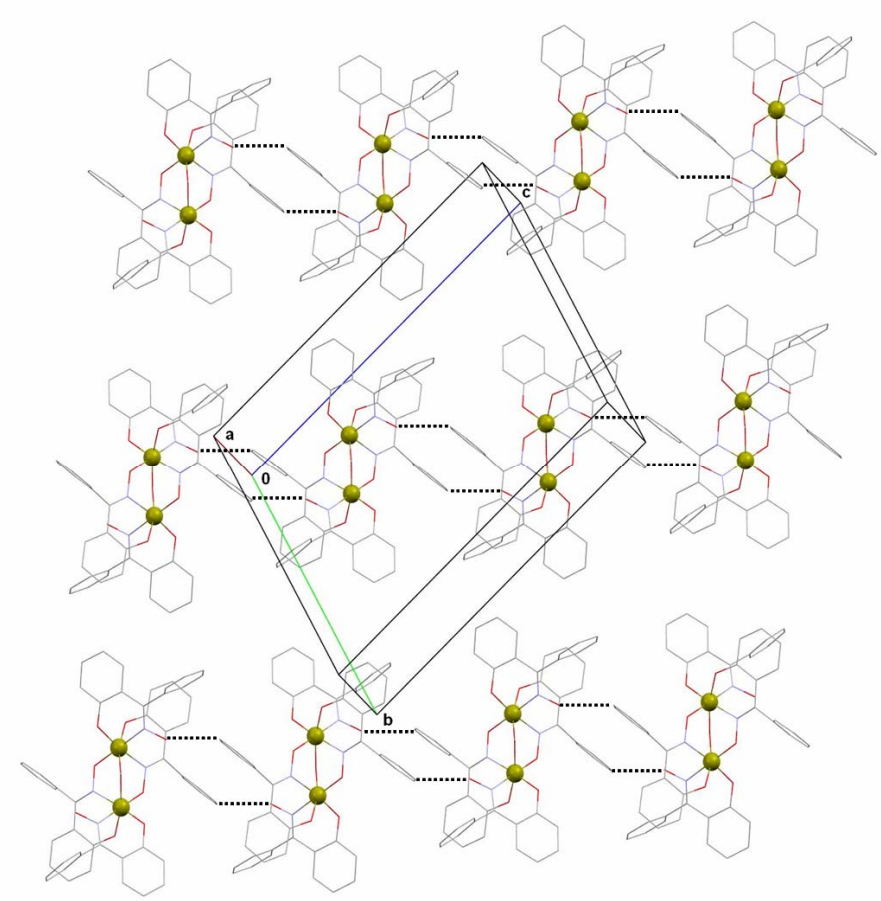

Fig 3.2 The packing of molecules of **7**. H-bonding shown as dashed line.

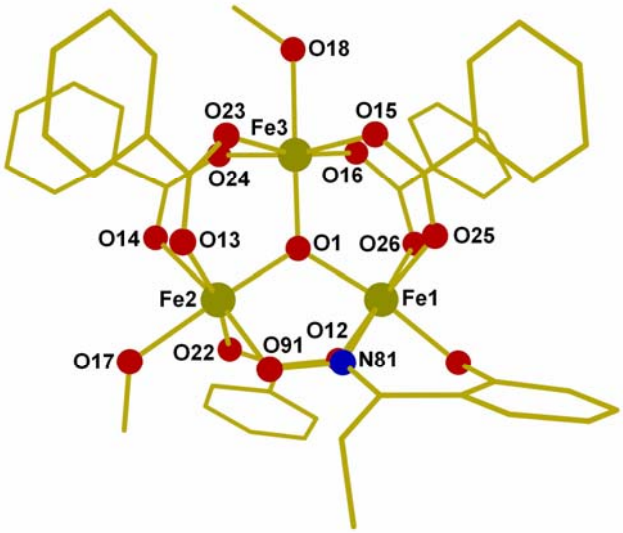

Fig 3.3 The molecular structure of **8**. Colour code: Fe = green; O = red; N = blue; C = gold.

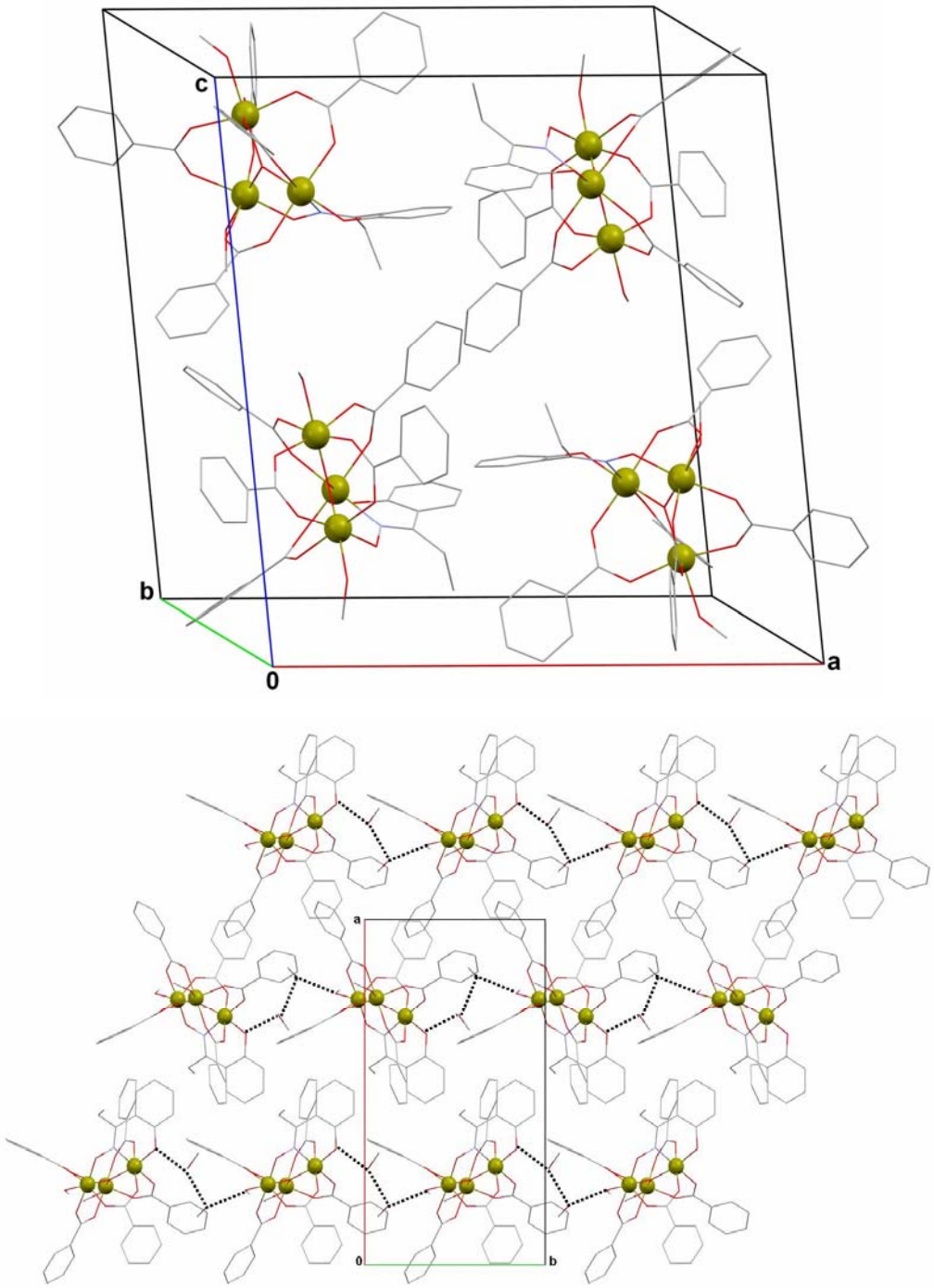

Fig 3.4 The packing of molecules of **8** in the unit cell (top) and viewed along the c-axis (bottom).

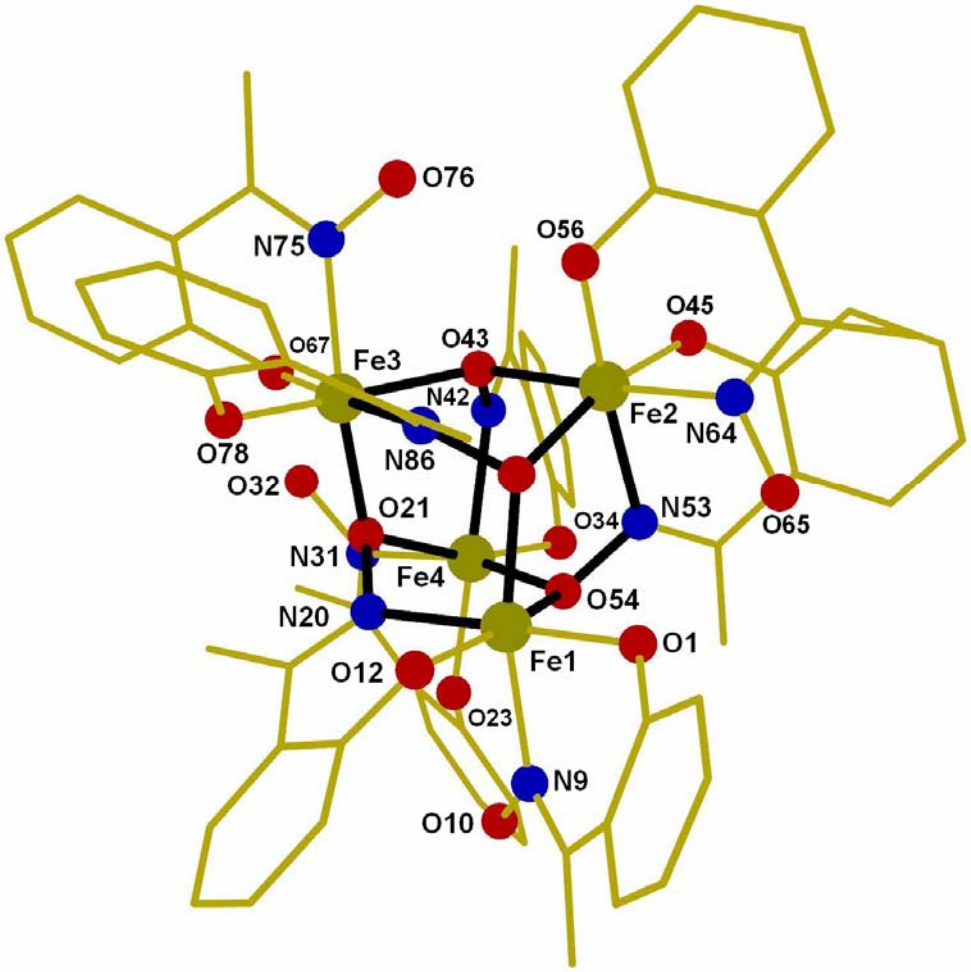

Fig 3.5 The molecular structure of **9**. Colour code: Fe = green; O = red; N = blue; C = gold. The black lines highlight the magnetic core of the molecule.

octahedral geometries (*cis*, 82.36(17)–101.59(15)°; *trans*, 163.84(15)–178.92(16)°) with their oxidation states assigned using charge balance considerations, bond lengths and BVS calculations (Table A.3.6) In the crystal lattice each of the four protonated phenolic O-arms is hydrogen bonded to the oxime oxygen on a neighbouring Fe^{III} ion, resulting in a serpentine like packing arrangement (Fig. 3.6). The closest intermolecular Fe · · ·Fe distance is 8.8797(12) Å.

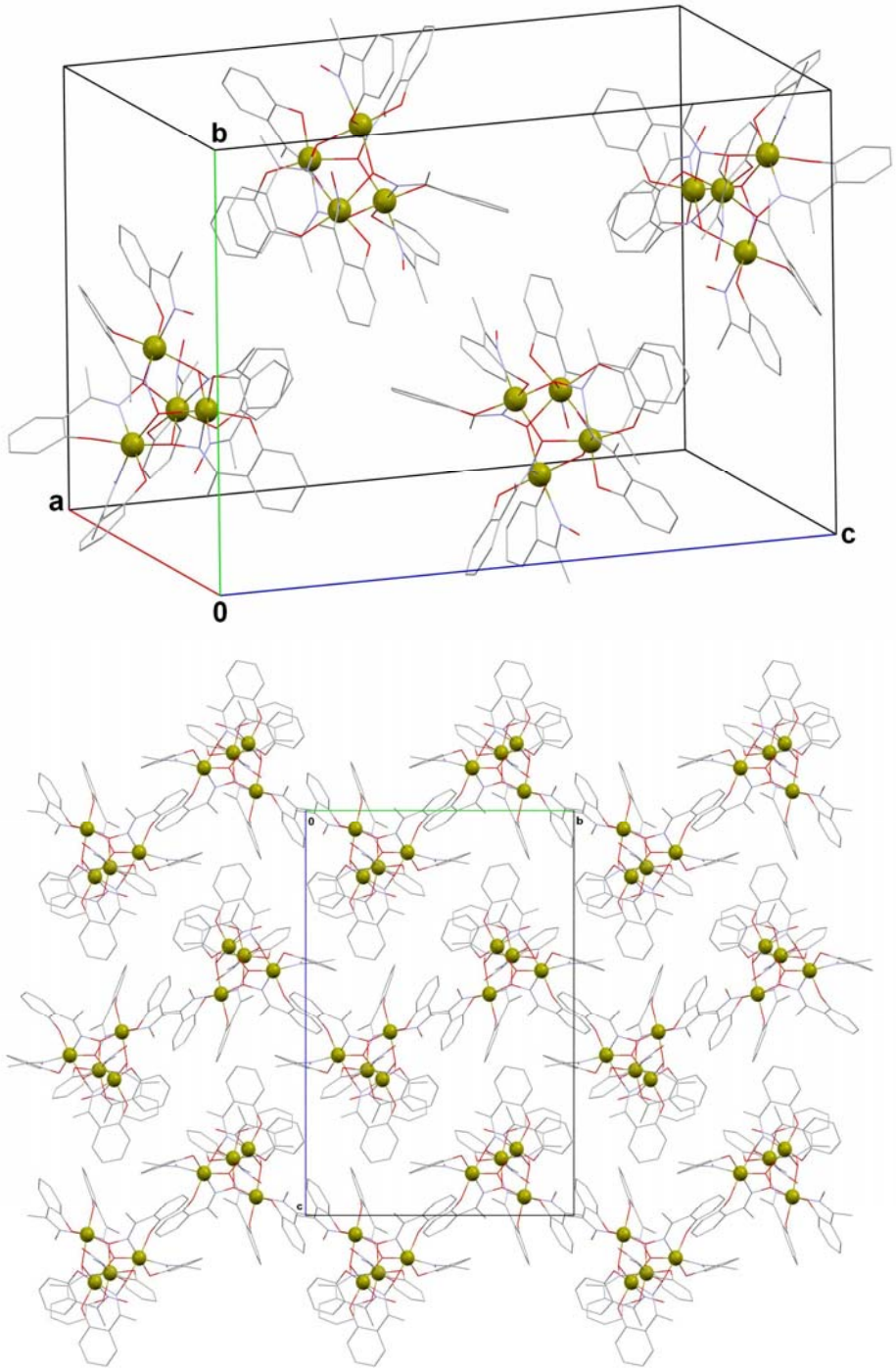

Fig. 3.6 The packing of molecules of **9** in the unit cell (top) and viewed along the a-axis (bottom).

$[HNEt_3]_2[Fe_6O_2(Me\text{-}sao)_4(SO_4)_2(OMe)_4(MeOH)_2]$ (**10**) crystallises in the orthorhombic space group *Pbca* with the unit cell containing four complete [Fe_6] clusters (Fig. 3.7, 3.8; selected bond lengths and angles are given in Table A.3.7). The metallic skeleton of the anion describes two edge sharing (Fe1–Fe1′) Fe^{III}_4 tetrahedra with an inversion centre bisecting the common edge. The Fe^{III} ions are connected *via* a combination of two μ_4-O^{2-} ions (O32 and s.e.) and four μ-MeO^- ions (O26, O30 and s.e.) creating a $[Fe_6O_2(OMe)_4]^{10+}$ core. The Fe1–Fe3 face (and s.e.) is bridged by an η^1: η^1: η^1: μ_3 SO_4^{2-} ligand, while the four η^1: η^1: η^1: μ-Me-sao^{2-} ligands bridge the Fe1–Fe2′ and Fe1–Fe3′ (and s.e.) edges. A terminal MeOH molecule completes the coordination sphere of Fe3 (and s.e.). Each Fe^{III} ion lies in a distorted octahedral geometry (*cis*, 77.05(6)–101.19(8)°; *trans*, 152.53(7)–176.71(7)°) with their oxidation states assigned using charge balance considerations, bond lengths and BVS calculations (Fig. A.3.8) In the crystal lattice there are a significant number of hydrogen bonds: between the SO_4^{2-} ions and the cation (N · · ·O, 2.804(3) Å); between terminally bound MeOH and the bridging OMe^- (O · · ·O, 2.938(2) Å); between a Me-sao^{2-} ligand and the phenolic O-atom (C · · ·O, 3.553(4) Å); and between a Mesao^{2-} ligand and the SO_4^{2-} ion (C· · ·O, 3.302(3) Å). These result in the formation of anionic 1D chains with the cations sitting between the chains (Fig. 3.8). The closest intermolecular Fe · · · Fe distance is 8.4047(5) Å.

$[Fe_8O_3(R\text{-}sao)_3(tea)(teaH)_3(O_2CMe)_3]$ **(**R=Me (**11**)**,** Et (**12**)**,** Ph (**13**)) Complexes **11–13** are isostructural, differing only in the identity of the oxime ligand (and for **13** in the crystal system and space group, *vide infra*) and so here we describe only complex **11** in detail. Complex **11** crystallises in the rhombohedral space group *R*3c with six molecules in the unit cell (Fig. 3.9-3.11; selected bond lengths and angles are given in Table A.3.9). The metallic skeleton (Fig. 3.10) describes a distorted bicapped trigonal antiprism of Fe^{III} ions, connected via three μ_4-O^{2-} ions (O1 and s.e.) to form a $[Fe^{III}_8O_3]^{18+}$ central core (Fig. 3.10). This is then further bridged by three doubly deprotonated η^1: η^2: η^2: μ_3 $Htea^{2-}$ ligands (O43, and s.e). The "upper" triangular face of the prism (as depicted in Fig. 3.10) is capped by the sole tea^{3-} ligand bridging in a η^2: η^2: η^2: μ_4-fashion, thus forming an

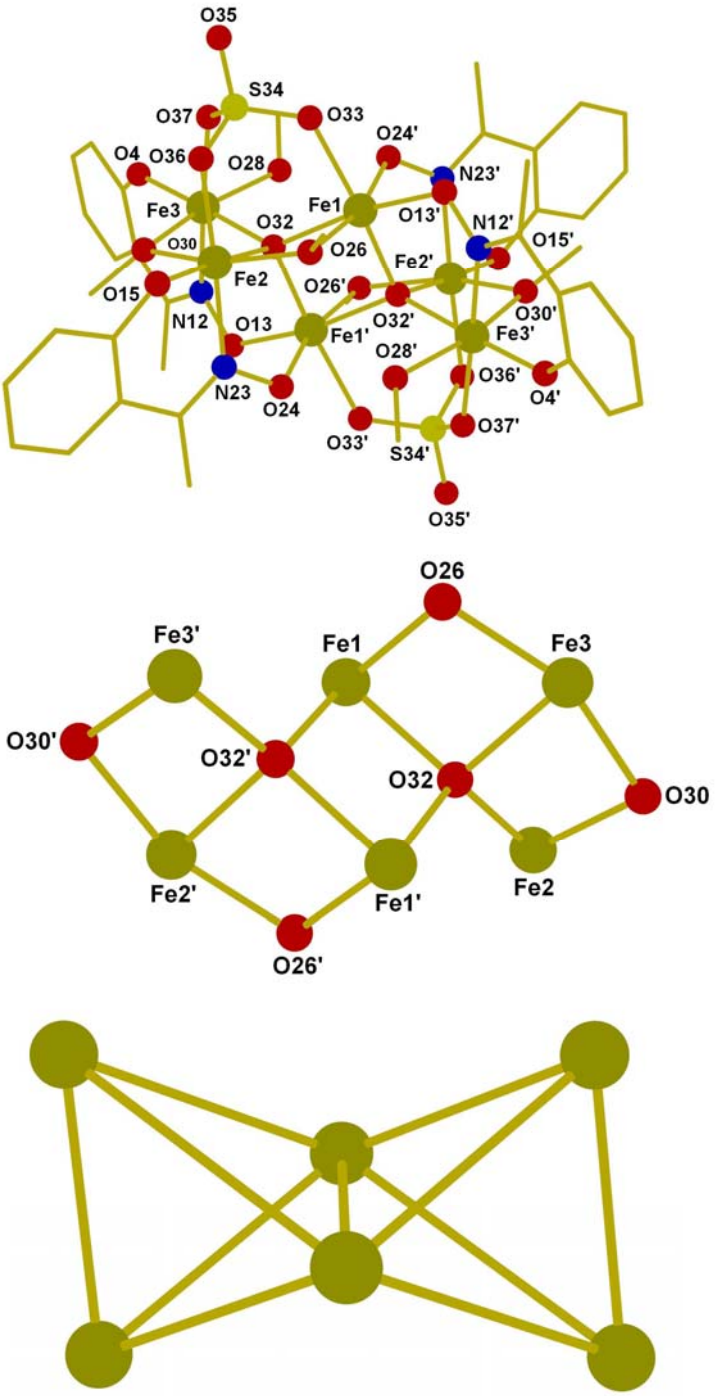

Fig 3.7 The molecular structure (top), Fe-O core (middle) and metallic skeleton (bottom) of **10**. Colour code: Fe = green; O = red; N = blue; C = gold; S = yellow

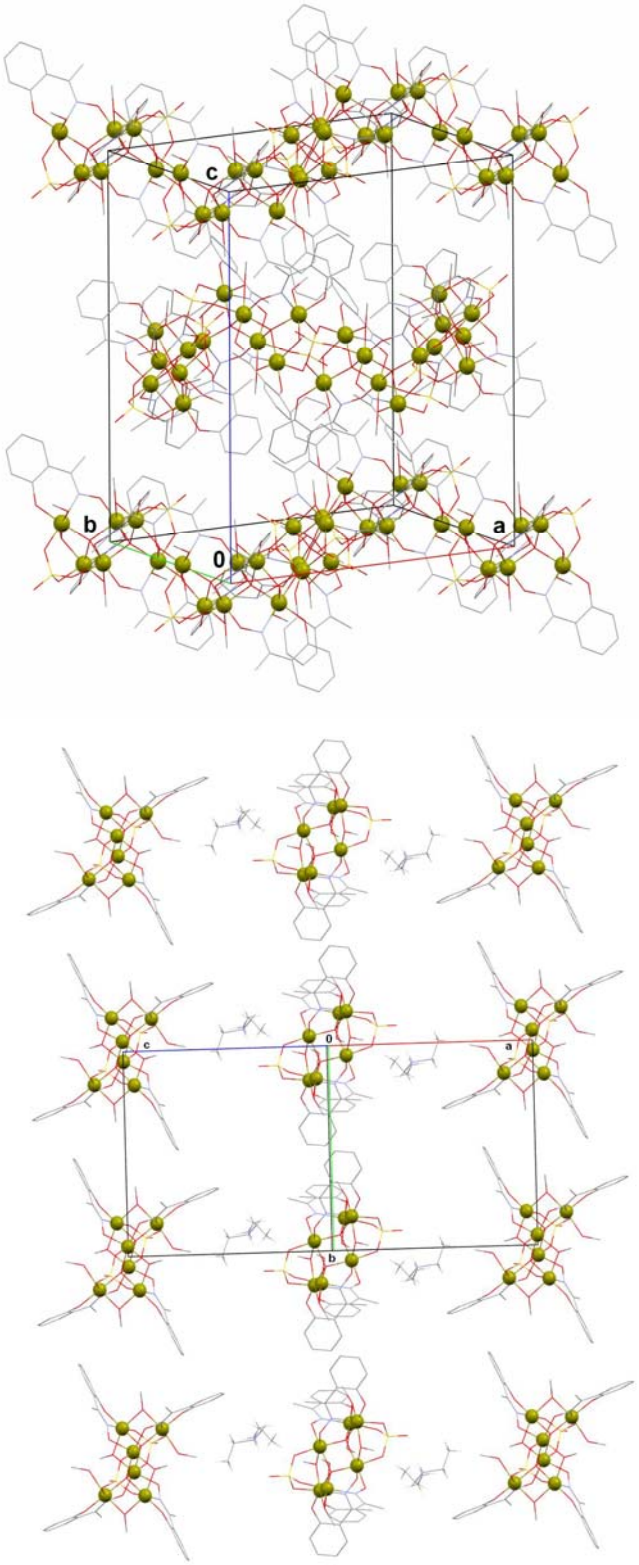

Fig. 3.8 The packing of molecules of **10** in the unit cell (top) and viewed along the ac-plane (bottom).

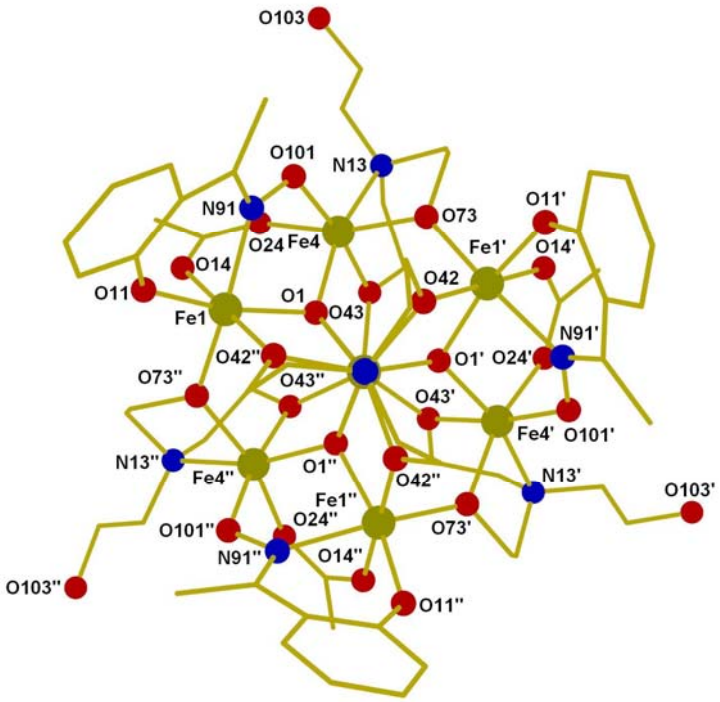

Fig. 3.9 The molecular structure viewed parallel to C_3–axis common to **11-13**

$[Fe^{III}_8O_3(OR)_9]^{9+}$ core. Both the $MeCO_2^{2-}$ ligands (in their familiar *syn*, *syn*, μ-mode) and the Me-sao^{2-} ligands (in η^1: η^1: η^1: μ a -fashion) bridge between vertex Fe^{III} ions of the trigonal prism. Each Fe^{III} ion is in a distorted octahedral geometry (*cis*,77.50(9)–105.54(8)°; *trans*, 154.24(9)–176.52(10)°) with their oxidation states again assigned using charge balance considerations, bond lengths and BVS calculations (Fig. A.3.10). In the crystal the packing arrangement of the molecules (Fig. 3.12) is directed by three O–H· · ·O hydrogen bonds (per molecule) between the unbound OH-group on each arm of the Htea^{2-} ligand and a phenolate O-atom on the Me-sao^{2-} ligand on an adjacent cluster (O. . .O, 2.7520(5) Å). The result is a structurally pleasing hexagonal close packed like arrangement of molecules.

Complex **12** also crystallises in the rhombohedral space group *R*3*c* and is identical to **11** except for the use of the ligand Et-saoH$_2$ instead of Me-saoH$_2$, but complex **13** crystallises in the triclinic space group *P*-1 (selected bond lengths,

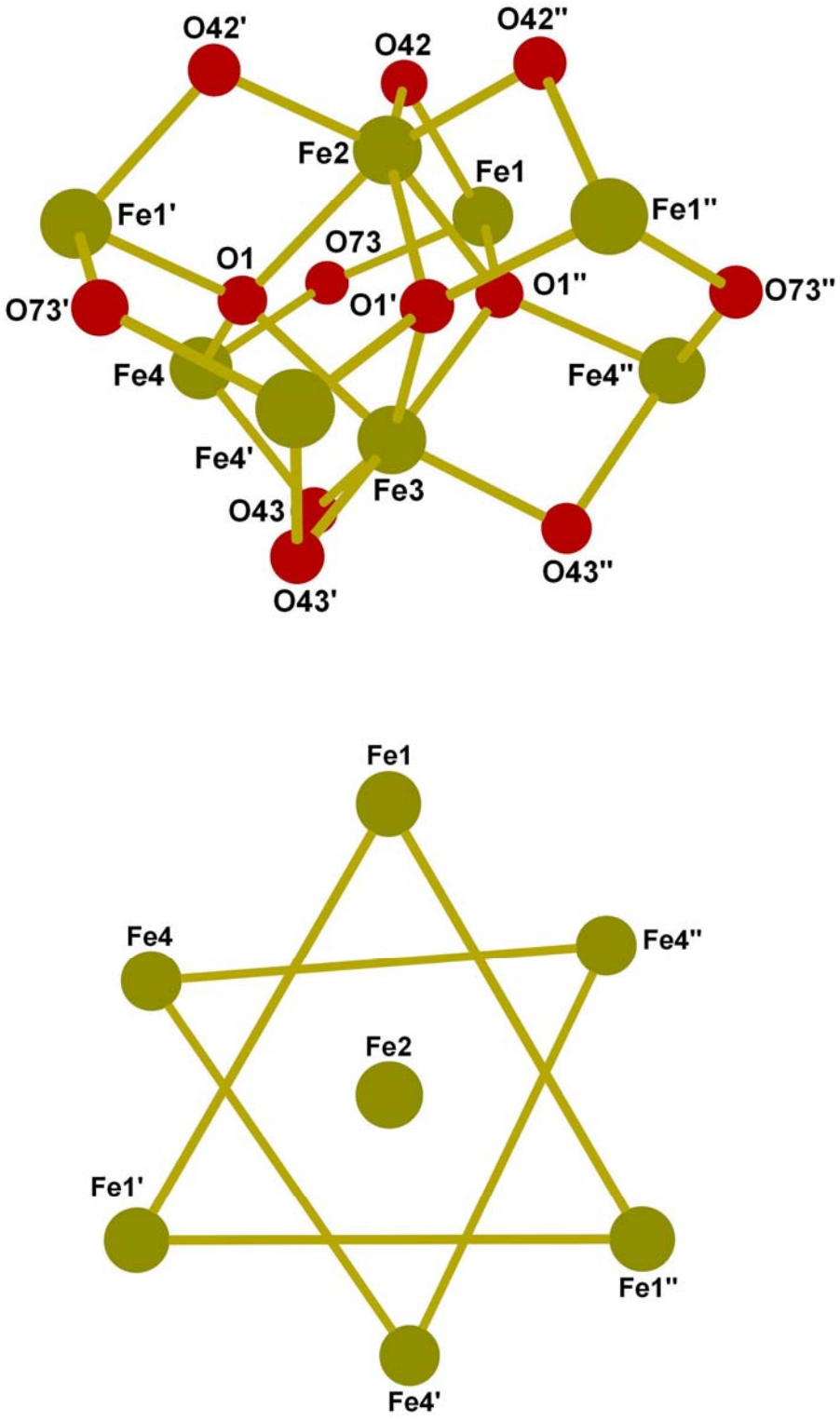

Fig. 3.10 The metal oxygen core (top) and metallic skeleton viewed parallel to C_3 – axis described by the Fe2-Fe3 (bottom) vector common to **11**-**13**.

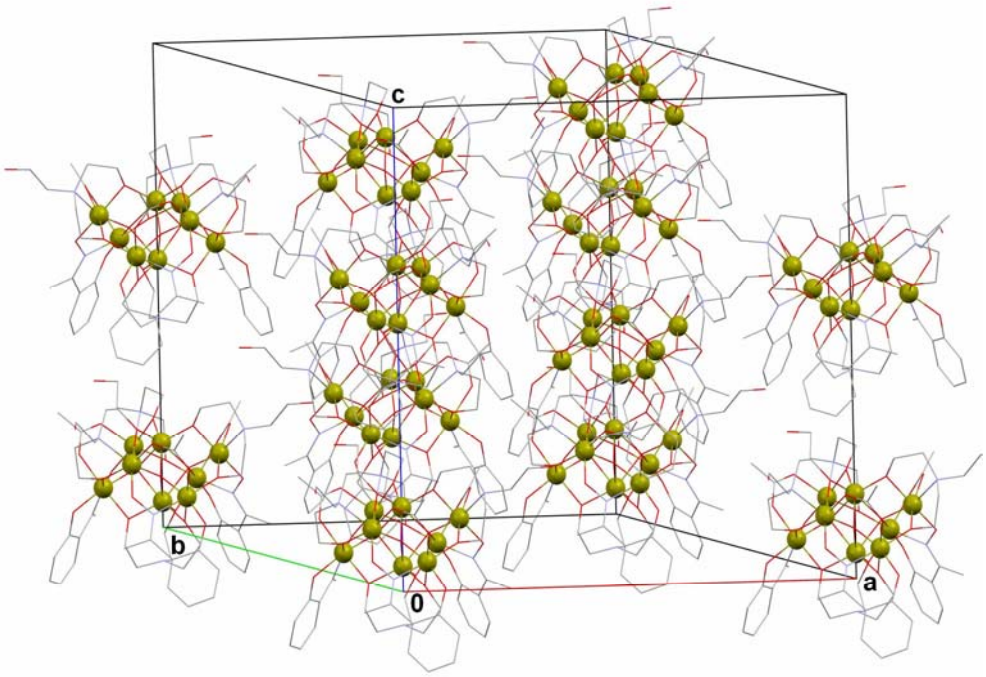

Fig. 3.11 The packing of molecules of **11**.

, angles and BVS calculations are given in Tables A.3.11-A.3.14). **13** contains a single O–H· · ·O intramolecular hydrogen bond between the unbound HO- arm of the $Htea^{2-}$ ligand and the oximate O-atom of a Ph-sao^{2-} ligand, with an O. . .O distance of 2.6941(8) Å . The packing of **13** is dictated by three different intermolecular H-bonds: the first (C · · · O, 3.5807(97) Å)between a Ph-sao^{2-} ligand and the phenolic O atom; the second between a $Htea^{2-}$ ligand and a phenolic O atom (C· · ·O, 3.1630(81) Å and 3.3129(89) Å); and the third between a Ph-sao^{2-} ligand and the uncoordinated HO-arm of $Htea^{2-}$ ligand (C· · ·O, 3.5556(122) Å). The result is a serpentine like packing arrangement, unlike the hexagonal nature of **11** and **12** (Fig. 3.13). The addition of the phenyl group to our ligand has resulted in C–H· · ·O hydrogen bonds which determine the packing in the crystal structure in the absence of the stronger O–H· · ·O hydrogen bonds.

$[Fe_6O_2(OH)_2(Et\text{-}sao)_2(Et\text{-}saoH)_2(O_2CPh)_6]$ (**14**). Complex **14** crystallises in

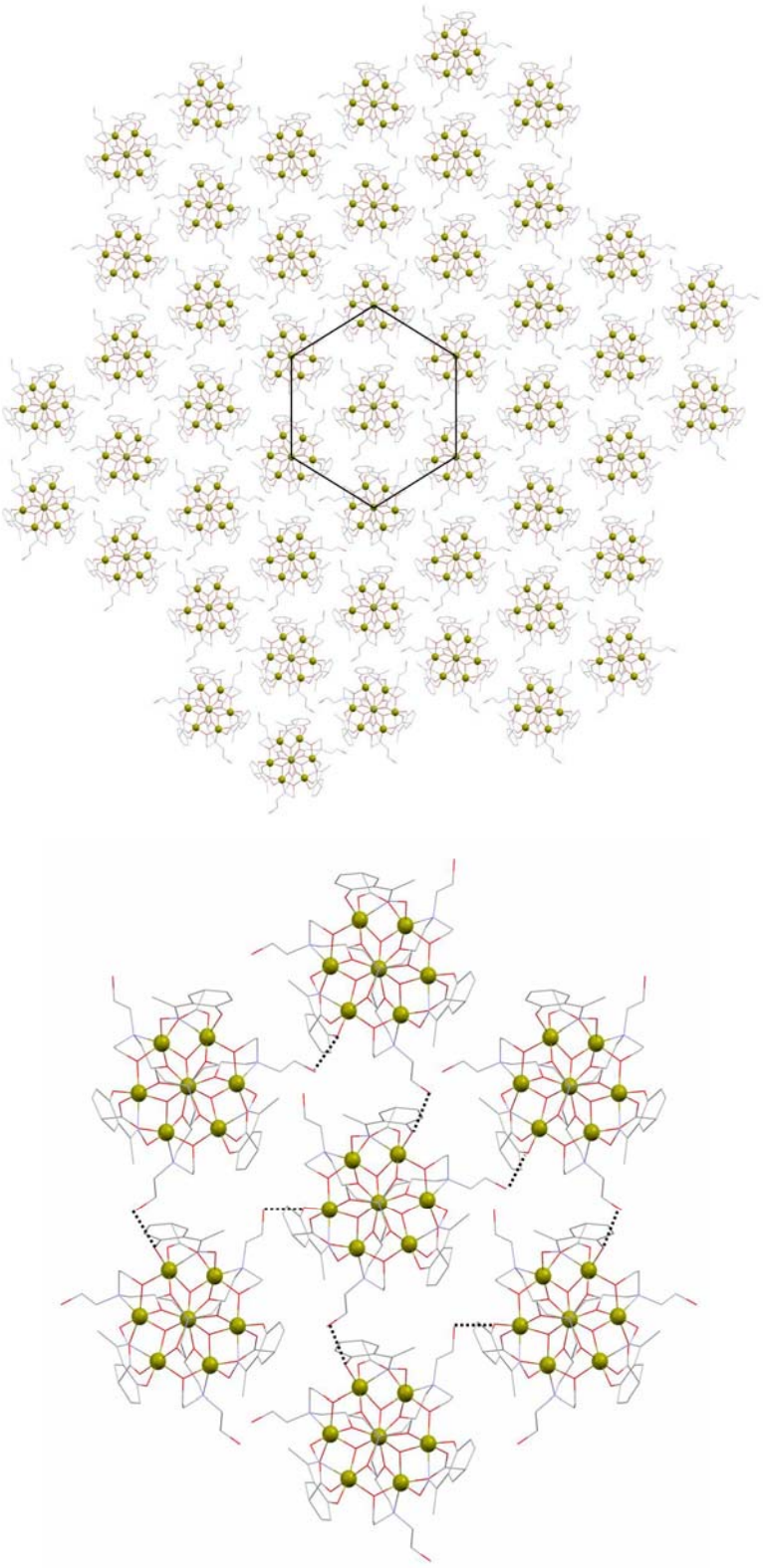

Fig. 3.12 The packing of **11**, **12** in the crystal. The highlighted area on the top is shown in greater detail on the right. H bonding shown as dashed lines.

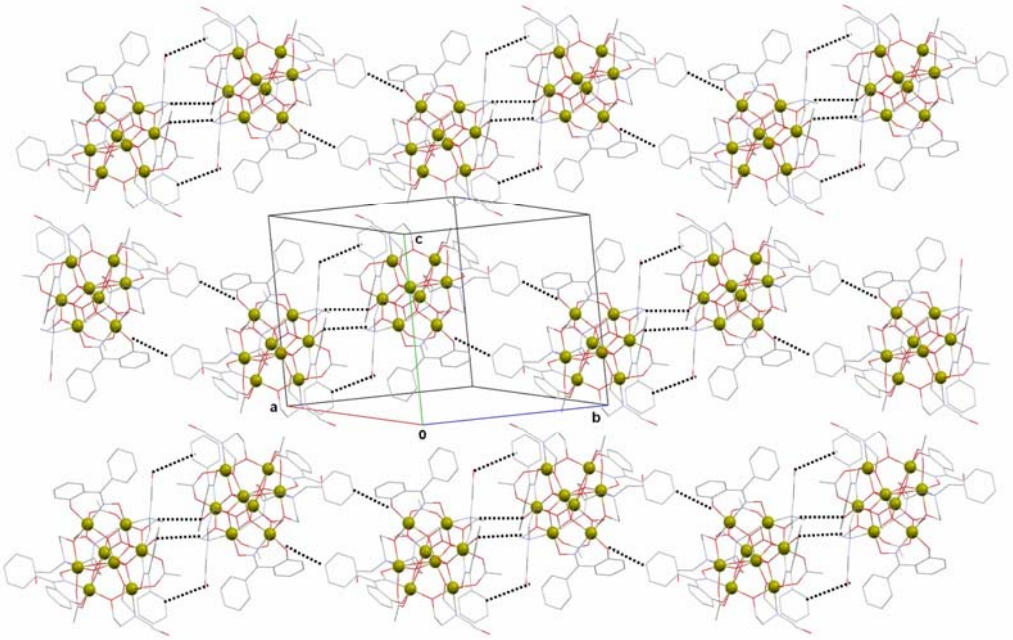

Fig. 3.13 The packing of **13**. H bonding shown as dashed lines.

the triclinic space group *P*-1 with one molecule in the unit cell which lies on an inversion centre (Fig. 3.14, 3.15; selected bond lengths and angles are given in Table A.3.15). The molecule contains the $[Fe^{III}_6(\mu_3\text{-}O_2)(\mu\text{-}OH)_2]^{12+}$ core, whose topology consists of two centrosymmetricaly related off-set, stacked $[Fe^{III}_3(\mu_3\text{-}O_2)]$ triangular units linked at one Fe_2 edge (Fe1-Fe3) by two μ-OH^- ions and two oximate O atoms from two $\eta^1{:}\eta^1{:}\eta^2{:}\mu_3$ Et-saoH$^-$ ligands. Two Fe_2 edges (Fe2-Fe3) are each bridged by one oximate oxygen atom from one $\eta^1{:}\eta^1{:}\eta^1{:}\mu_2$ Et-sao^{2-} and one $PhCO_2^-$ ligand in its familiar *syn, syn, μ-* mode. The remaining two Fe_2 edges (Fe1-Fe2) are bridged by two $PhCO_2^-$ ligands in their familiar *syn, syn, μ-* mode. Each Fe^{III} ion lies in a distorted octahedral geometry (*cis*, 81.47(16)-105.51(17)°; *trans*, 161.79(16)-178.37(18)°) with their oxidation states assigned using charge balance considerations, bond lengths and BVS calculations (Table A.3.16) In the crystal lattice intermolecular hydrogen bond interactions between two Et-sao^{2-} ligands and two phenolic O- atoms (C···O, 3.406(7) Å) direct the formation of 1D chains (Fig. 3.15). The closest intermolecular Fe···Fe distance is 7.758(1) Å.

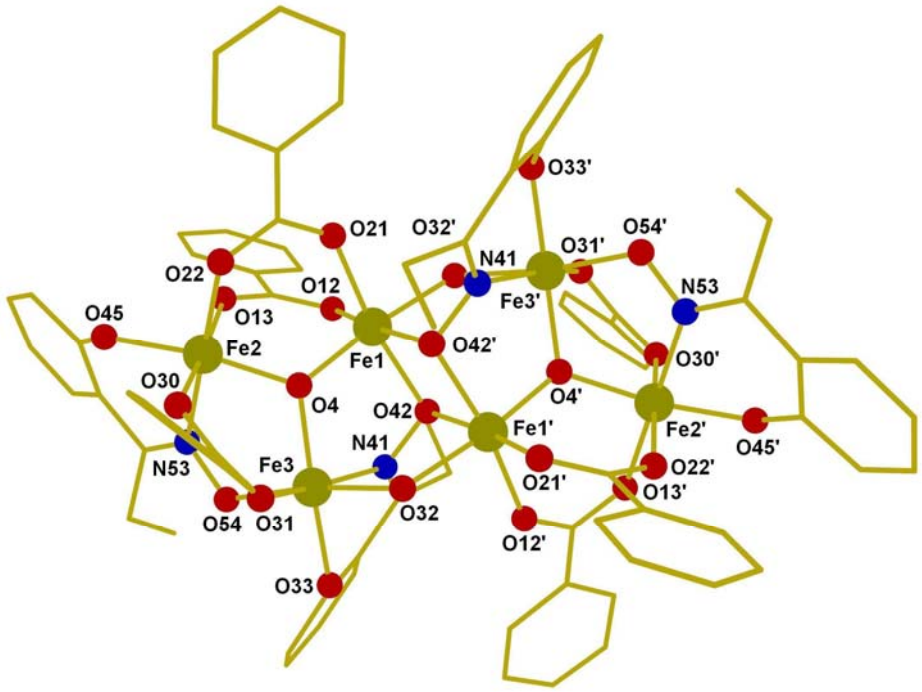

Fig. 3.14 The molecular structure of **14** Colour code: Fe = green; O = red; N = blue; C = gold.

$[HNEt_3]_2[Fe_6O_2(OH)_2(Et\text{-}sao)_4(O_2CPh(Me)_2)_6]$ (**15**) is a similar structure to **14** with the following differences: the two singly deprotonated Et-saoH$^-$ ligands in **14** are replaced by two fully (doubly) deprotonated Et-sao^{2-} ligands, which is sensible given the larger amount of base used in the synthesis of **15** compared to **14**; **15** has six $(Me)_2PhCO_2^-$ ligands compared to six $PhCO_2^-$ ligands in **14** and **15** has two cations per $[Fe_6]$ unit. Each Fe^{III} ion lies in a distorted octahedral geometry (*cis*, 80.46(15)-103.24(15)°; *trans*, 164.76(16)-177.27(15)°) with their oxidation states assigned using charge balance considerations, bond lengths and BVS calculations (Table A.3.18). In the crystal lattice intermolecular hydrogen bond interactions between: two phenolic O- atoms and the two cations (N···O, 2.793(8) Å); a phenolic O- atom and the cation (C···O, 3.533(8) Å) and between a $(Me)_2PhCO_2^-$ ligand and the cation (C···O, 3.271(11) Å) direct the formation of 2D sheets lying in the bc plane (Fig. 3.17). The closest intermolecular Fe···Fe distance is 8.925(0) Å.

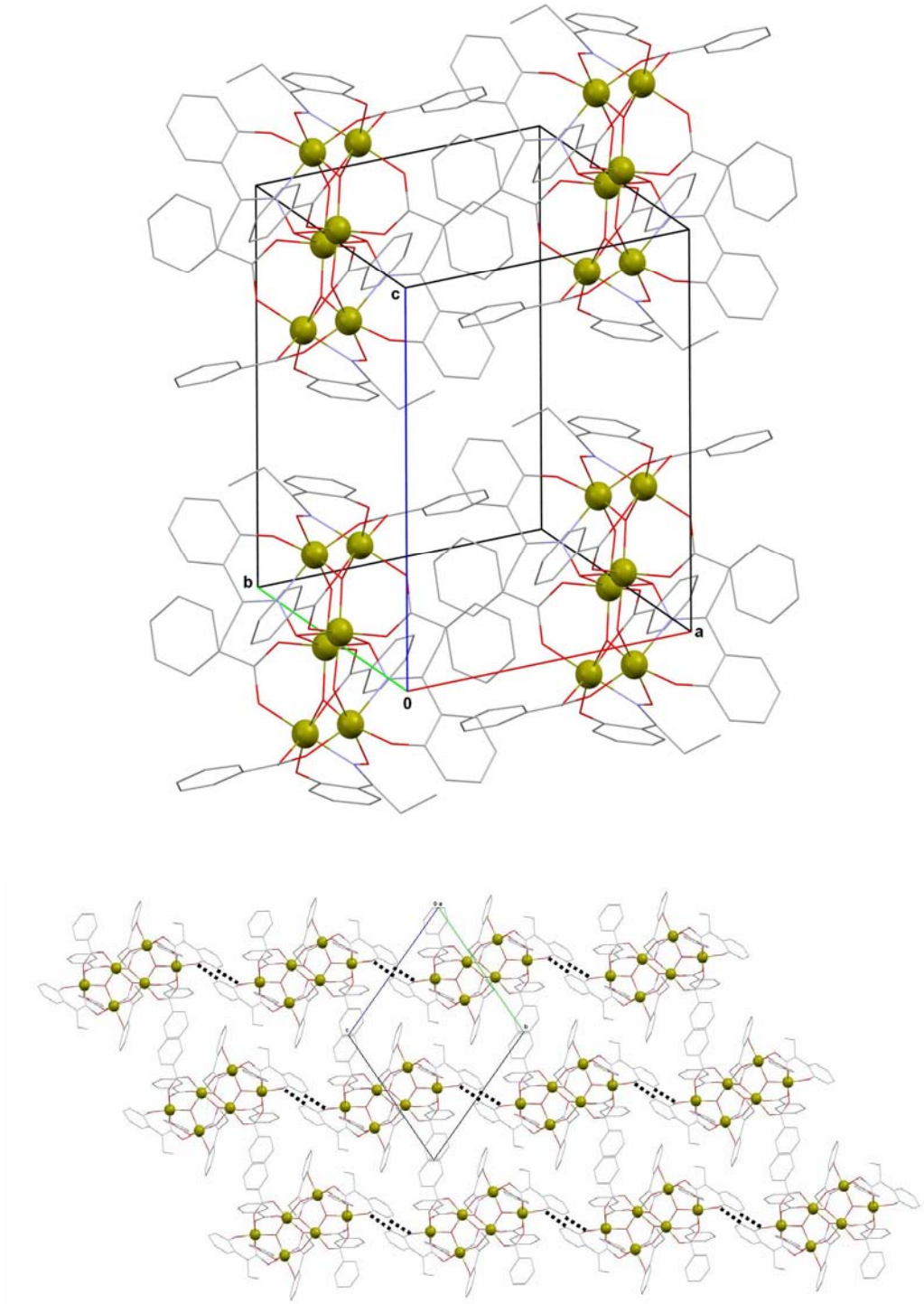

Fig. 3.15 The packing of molecules of **14** in the unit cell (top) and viewed along the a-axis (bottom). H bonding shown as dashed lines.

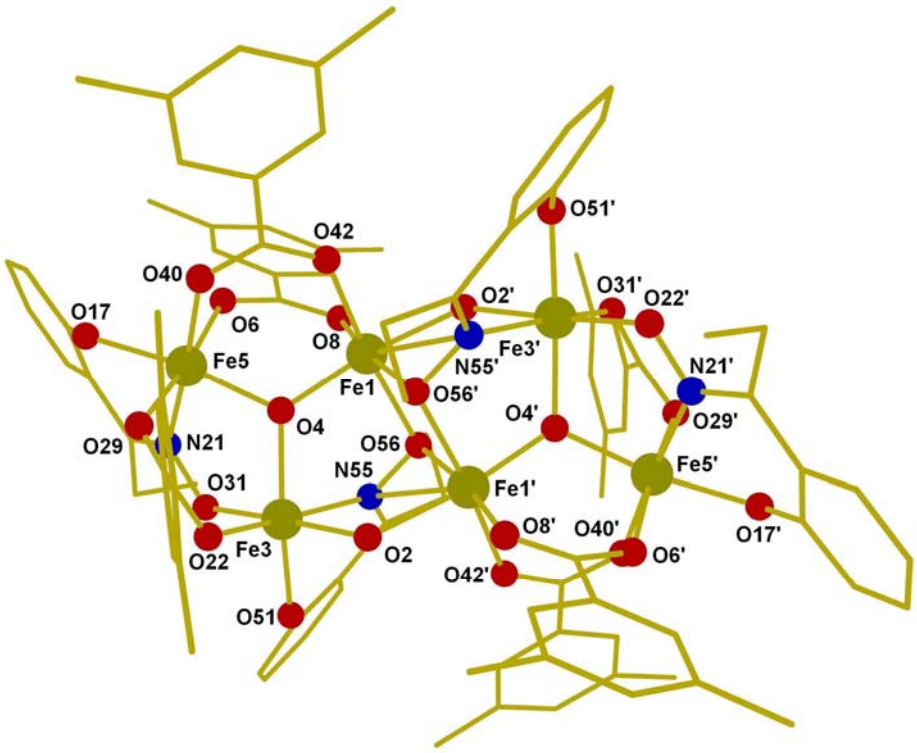

Fig. 3.16 The molecular structure of **15**. Colour code: Fe = green; O = red; N = blue; C = gold.

$([Fe_6Na_3O(OH)_4(Me\text{-}sao)_6(OMe)_3(H_2O)_3(MeOH)_6])_n$ (**16**) crystallises in the hexagonal space group *P*63/m with two molecules in the unit cell and has a 2D framework structure (Fig. 3.18-3.20; selected bond lengths and angles are given in Table A.3.19). The metallic skeleton of the [Fe_6] unit (composed of two linked $[Fe_3(\mu_3\text{-}O)_{0.5}(\mu_3\text{-}OH)_{0.5}]^{+7.5}$ triangles) (Fig. 3.19) within the 2D framework describes a trigonal prism of Fe^{III} ions connected via three μ_3-OH^- ions and three μ-MeO^- ions to form an $[Fe^{III}_6(\mu_3\text{-}O)(\mu_3\text{-}OH)_4(\mu\text{-}OMe)_3]^{9+}$ core. BVS calculations on O3 (Table A.3.20) and s.e of the $[Fe_3(\mu_3\text{-}O)_{0.5}(\mu_3\text{-}OH)_{0.5}]^{+7.5}$ triangles reveal values that lie between the values expected for O^{2-} and OH^- suggesting that a proton is shared between O3 and s.e which is reasonable considering the short O···O distance of 2.472(3) Å between O3 and s.e indicative of such a hydrogen bonding interaction.. The six Fe_2 edges (Fe1-Fe1′ and s.e) of the triangular faces of the trigonal prism are each linked by a fully deprotonated Me-sao^{2-} ligand bridging in a $\eta^1{:}\eta^1{:}\eta^1{:}\mu$ fashion.

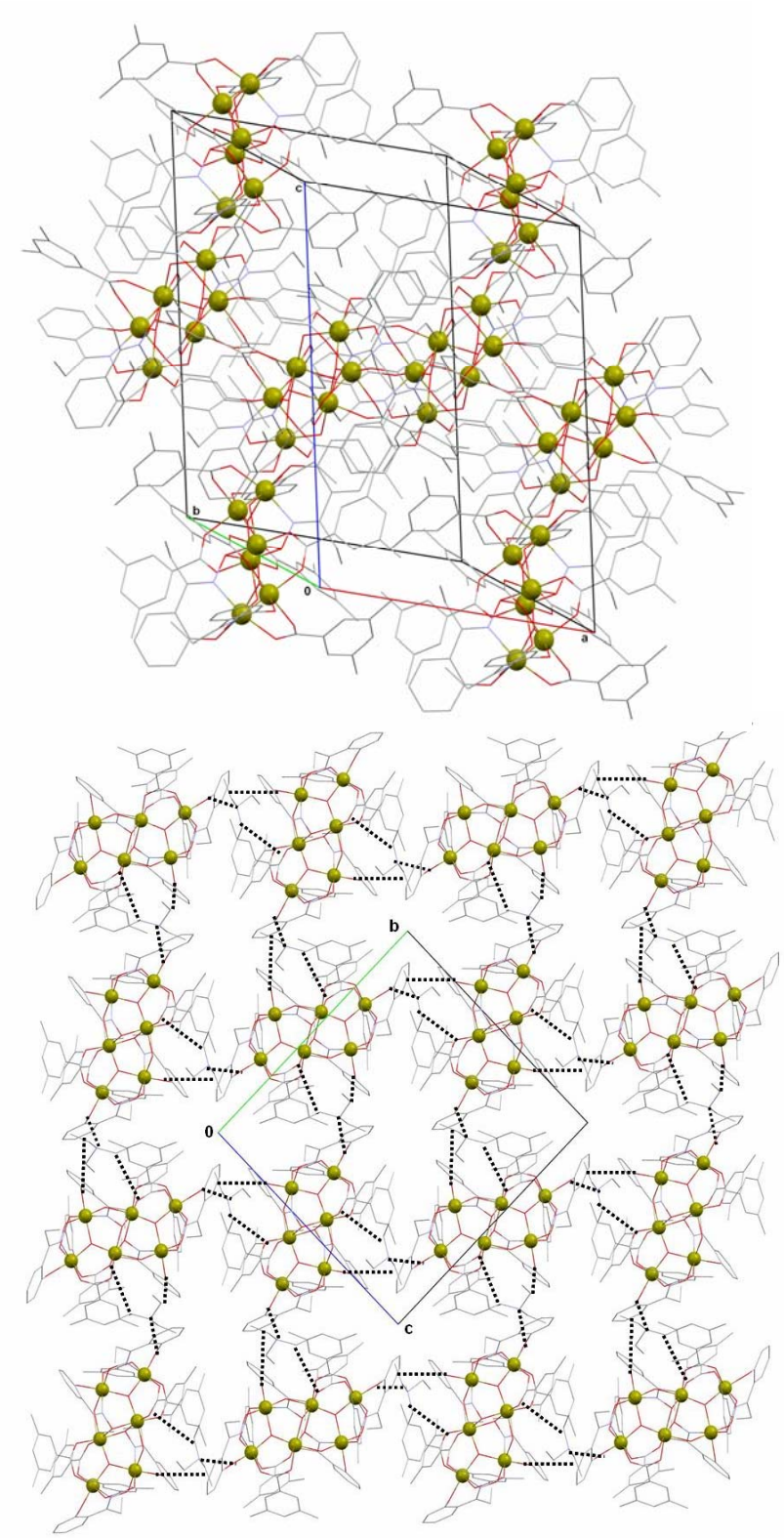

Fig. 3.17 The packing of molecules of **15** in the unit cell (top) and viewed along the a-axis (bottom). H bonding shown as dashed lines.

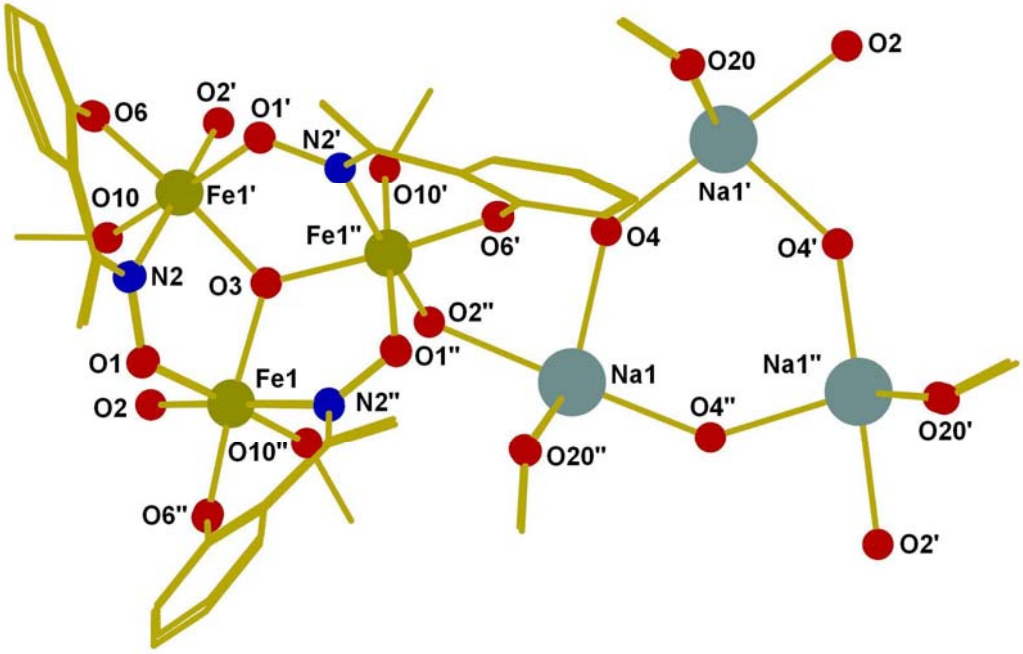

Fig. 3.18 The molecular structure of **16.** Colour code: Fe = green; O = red; N = blue; C = gold.

Each Fe ion lies in a distorted octahedral geometry (*cis*, 76.94(6)-97.07(7)°; *trans*, 169.42(6)-172.01(6)°) with their oxidation states assigned using charge balance considerations, bond lengths and BVS calculations (Table A.3.20) The $[Na_3]$ unit (Fig. 3.19) within the framework describes a triangle of Na^+ ions connected via three μ-H_2O molecules each of which bridges an entire edge of the triangle. Each Na^+ ion is linked to the $[Fe_6]$ unit via a μ_3-OH^- ion; with six terminal methanol molecules completing the coordination sphere. Each Na ion lies in a distorted trigonal bipyramidal geometry with a τ value of 0.955 where $\tau = (\beta-\alpha)/60$.[24] Each $[Fe^{III}_6O(OH)_4(Me\text{-}sao)_6(OMe)_4]$ unit is linked to three $[Na_3(\mu\text{-}H_2O)_3(MeOH)_6]$ units forming a non interpenetrated 2D network with the centroid calculated between O3 and s.e of the $[Fe^{III}_6O(OH)_4(Me\text{-}sao)_6(OMe)_4]$ unit and the centroid calculated

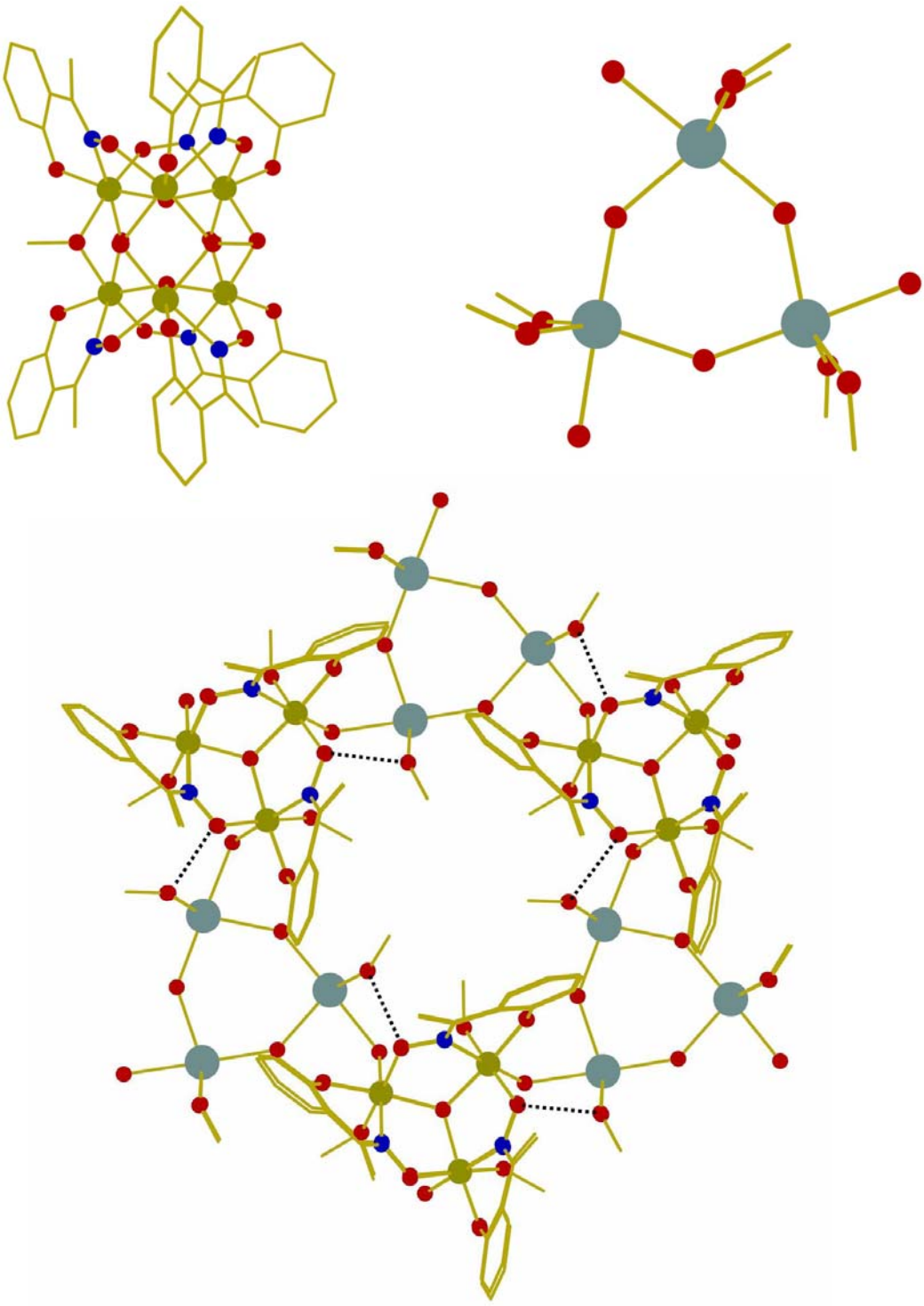

Fig. 3.19 The molecular structure of the [Fe_6] (top left) and [Na_3] (top right) units of **16** and their respective packing in the crystal as viewed through c (bottom). H bonding shown as dashed lines. Colour code: Fe = green; Na = cyan; O = red; N = blue; C = gold.

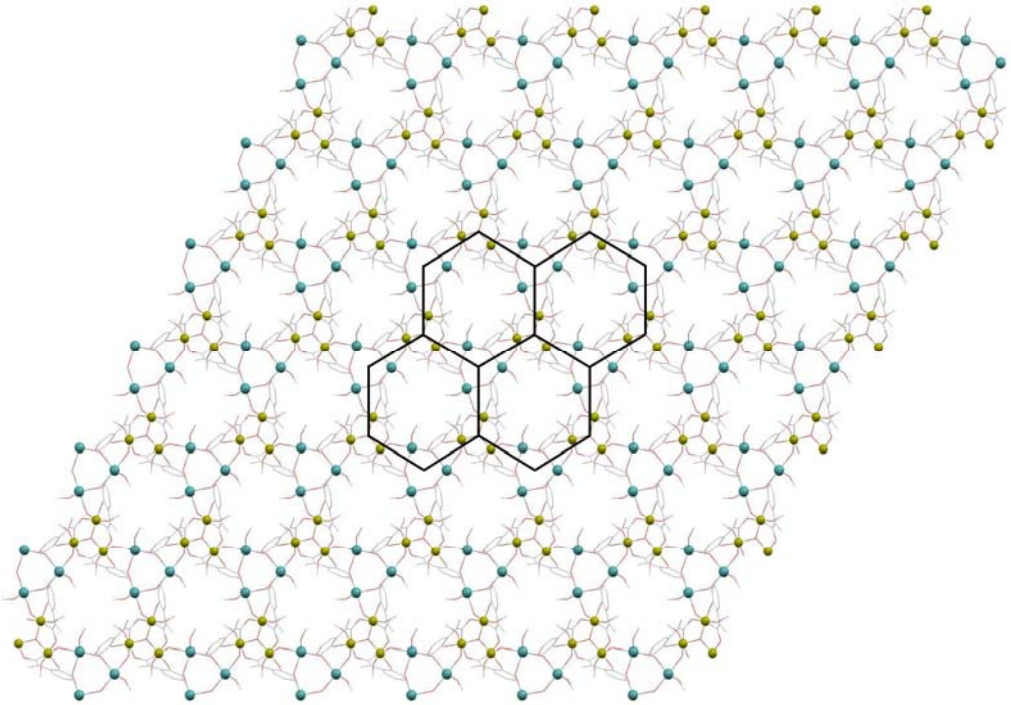

Fig. 3.20 The packing of **16** as viewed through c with the black lines highlighting the (6,3) 2D net.

between the three Na ions of the $[Na_3(\mu\text{-}OH_2)_3(MeOH)_6]$ unit forming two 3-connecting nodes of a (6,3) 2D net in the ab plane (Fig. 3.20). In the crystal lattice there are a significant number of complimentary hydrogen bonds: two between the terminally bound MeOH molecules and the oximato O-atoms (O···O, 2.742(3) Å); two between the phenolic O-atoms and bridging H_2O molecules; and one between a OH^- ion and a bridging OMe^-.

$[HNEt_3]_2[Fe_{12}Na_4O_2(OH)_8(sao)_{12}(OMe)_6(MeOH)_{10}]$ (**17**) crystallises in the monoclinic space group $P2_1/c$ with two molecules in the unit cell (Fig. 3.21-3.24; selected bond lengths and angles are given in Table A.3.21). The molecule contains the $[Fe^{III}_{12}Na_4(\mu_3\text{-}O)_2(\mu_2\text{-}OH)_2(\mu_3\text{-}OH)_6(\mu\text{-}OMe)_6(\mu\text{-}MeOH)_2]^{22+}$ core whose topology consists of two $[Fe_6Na]$ units linked by a single $[Na_2]$ unit forming an S-shaped molecule (Fig. 3.21). This is structurally very similar to **16** except a single Na^+ is connected to one edge of the trigonal prism via one $\mu_3\text{-}OH^-$ and two sao^{2-} ligands bridging in a $\eta^2{:}\eta^1{:}\eta^1{:}\mu_3$ fashion forming the $[Fe_6Na]$ unit. Also three Fe_2

edges (Fe1-Fe2, Fe2-Fe3, Fe5-Fe6) of the triangular faces of the trigonal prism are linked by a fully deprotonated sao^{2-} ligand bridging in a $\eta^1:\eta^1:\eta^1:\mu$ fashion while the remaining three Fe_2 edges (Fe1-Fe3,Fe4-Fe5, Fe4-Fe6) are linked by a fully deprotonated sao^{2-} ligand bridging in a $\eta^2:\eta^1:\eta^1:\mu_3$ fashion. Each Fe^{III} ion lies in a distorted octahedral geometry (*cis*, 76.4(3) – 100.6(3)°; *trans*, 166.4(3)-173.9(3)°) with their oxidation states assigned using charge balance considerations, bond lengths and BVS calculations (Table A.3.22). In **16** the $[Fe_6]$ units were connected by $[Na_3]$ units whereas in **17** the linkers are $[Na_2]$ units. These are connected via two μ-MeOH molecules which are then connected to each of the two $[Fe_6Na]$ units via one μ_3-OH^- ion and the phenolate oxygen of a $\eta^2:\eta^1:\eta^1:\mu_3$ sao^{2-} ligand (Fig. 3.22). Terminal MeOH molecules then complete the coordination of the Na^+ ions in the $[Na_2]$ unit forming a discrete complex in direct comparision to the coordination polymer found in **17**. The Na^+ ion in the $[Fe_6Na]$ unit lies in a distorted octahedral geometry (*cis*, 68.1(3) – 117.7(11)°; *trans*, 147.66(3)-170.57(3)°) The Na^+ ions in the $[Na_2]$ unit lie in a distorted square pyramidal geometry with a τ value of 0.119 where $\tau = (\beta-\alpha)/60$.[24] In the crystal lattice there are a significant number of intra-molecular hydrogen bonds: two between oximic O atoms and bridging MeOH molecules (O···O, 2.615(0) Å); two between phenolate O atoms and terminal MeOH molecules (O···O, 2.814(11) Å); four between μ_3-OH^- ions and bridging OMe^- ions (O···O, 2.693(7), 2.633(0) Å); and two between μ_3-OH^- ions and μ_3-O^{2-} ions (O···O, 2.526(7) Å). The packing of **17** in the crystal can be found in Fig 3.24. The closest intermolecular Fe···Fe distance is 8.751 (2) Å.

Complexes **7** and **13** are the first structurally characterised complexes of any metal that contain Ph-sao^{2-} or Ph-$saoH^-$ as ligands. Complexes **8–12** and **14-16** join a rather small but growing family of complexes containing the anionic forms of Me-$saoH_2$[1e,19,22a-f] and Et-$saoH_2$[1a-e,22g-i] as ligands; however, these are the first Fe^{III} complexes with the Me-$saoH^-$/Me-sao^{2-} and Et-$saoH^-$/Etsao^{2-} ligands. Fe^{III} salicylaldoximate complexes have been characterised; these are $[Fe_4O_2(O_2CMe)_3(sao)_2L_2](PF_6)$,[23a] $(HNEt_3)[Fe_3O(sao)(saoH)L']$,[23b] $[Fe_4(sao)_4(saoH)_4]$,[23c] $[Fe_2(sao)_3L]$,[23d] $[Fe_4O_2L_3''(sao)_2L_2](ClO_4)$,[23e]

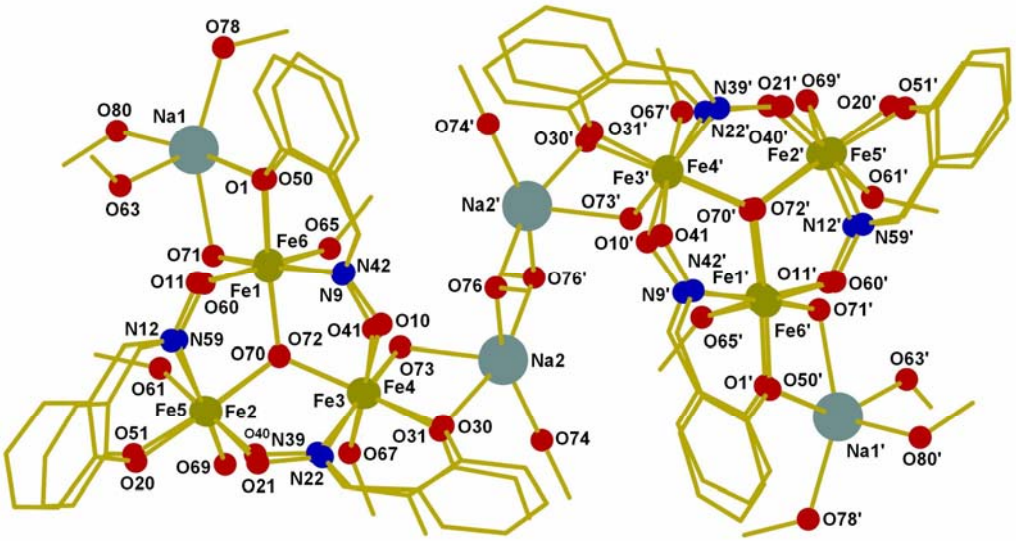

Fig. 3.21 The molecular structure of **17.** Colour code: Fe = green; Na = cyan O = red; N = blue; C = gold.

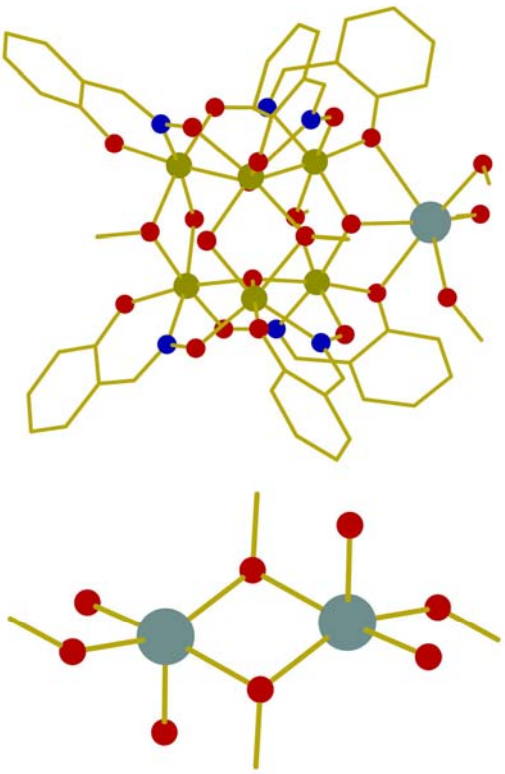

Fig. 3.22 The molecular structure of the [Fe_6Na] and [Na_2] units of **17.** Colour code: Fe = green; Na = cyan O = red; N = blue; C = gold.

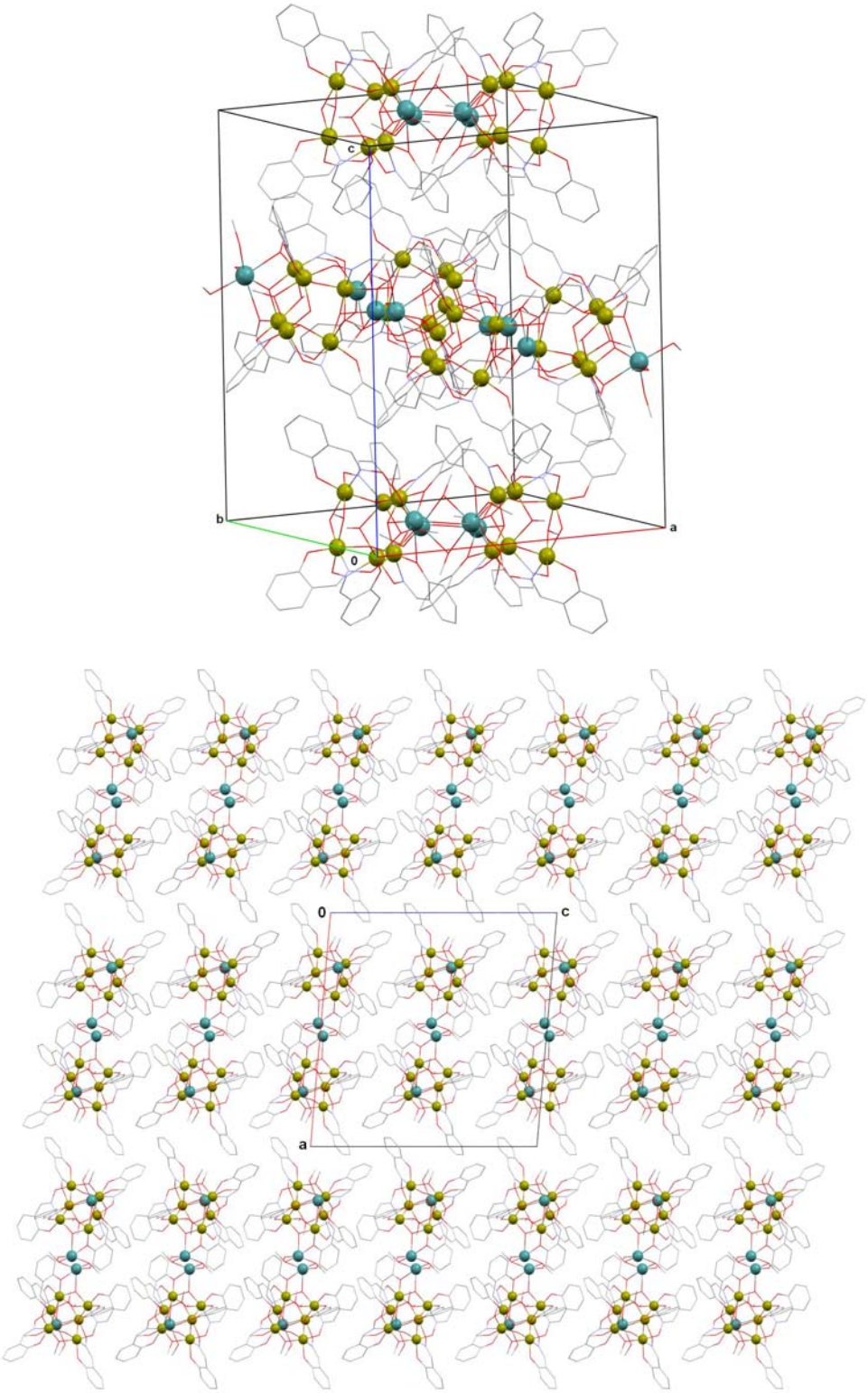

Fig. 3.23 The packing of molecules of **17** in the unit cell (top) and viewed along the b-axis (bottom).

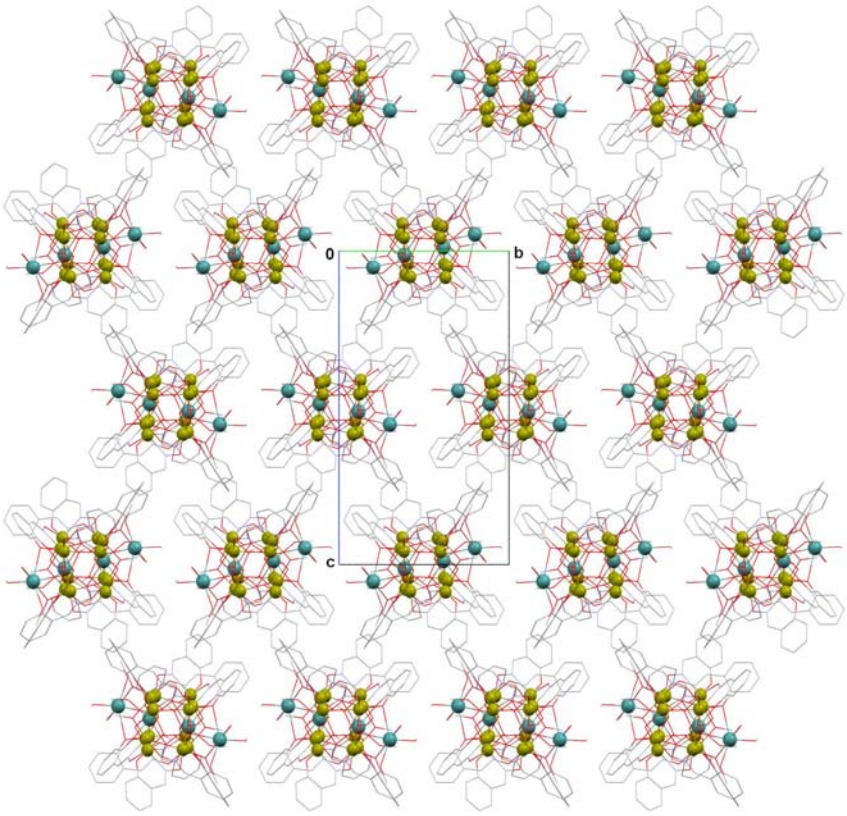

Fig. 3.24 The packing of molecules of **17** viewed along the a-axis.

$[Fe_2Mn_2O_2(O_2CMe)_3(sao)_2L_2](ClO_4)$,[23e] $[Fe_2Mn_2O_2L_3''(sao)_2L_2](ClO_4)$,[23e] $[Fe_2Mn_2O_2(O_2CPh)_3(sao)_2L_2](ClO_4)$,[23e] $[Fe_6O_2(O_2CPh)_{10}(sao)_2(MeCONH_2)_2]$,[23f] $[Fe_6O_2(O_2CPh)_{10}(sao)_2(H_2O)_2]$,[23f] $[Fe_3O(O_2CPh)_5(sao)(MeOH)_2]$,[23g] $[Fe_3O(O_2CPh)_5(sao)(EtOH)(H_2O)]$[23g] and $[Fe_8O_4(sao)_8(py)_4]$,[3q] where L is 1,4,7-trimethyl-1,4,7-triazacyclononane, L′ is the 2(bis(salicylideneamino)methyl)phenolate (-3) produced *in situ* through a reductive deoximation of $saoH_2$ by the Fe^{II} ion and L′′ is the benzilate(−1) ligand. Complex **8** bears a striking structural similarity with $[Fe_3O(O_2CPh)_5(sao)(MeOH)_2]$,[23g]indicating that the nature of the R group (H *vs*. Et) of the R-$saoH_2$ ligand, in an otherwise similar reaction mixture, has little structural effect. It should be mentioned at this point that there is only one structurally characterised iron complex with a derivatised salicylaldoxime – other than R-$saoH_2$ (R = Me, Et, Ph) –ligand. This is the dinuclear

complex $[Fe_2(t\text{Bu-sao})_3L]$,[23d] where *t*Bu-sao^{2-} is 4,6-di-*tert*-butylsalicylaldoximate(−2). Complex **10** joins a handful of structurally characterised sulfato-bridged Fe^{III} clusters,[8-17] the majority of which are dinuclear (Table 3.1). Compounds **11–13** are new additions to the family of octametallic iron(III) clusters with N,O-ligation.[3]

DC Magnetic Studies

Direct current (dc) magnetic susceptibility studies were performed for microcrystalline samples of **7–13** in the 1.8–300 K range and **14-17** in the 5.0-300K range under an applied field of 1 kG and are shown in Fig. 3.25–3.32.

For **7** the room temperature $\chi_M T$ value of approx. 4.8 cm^3 K mol^{-1} (Fig. 3.25) is lower than that expected for two non-interacting Fe^{III} ions (8.75 cm^3 K mol^{-1}). Upon cooling, the value of $\chi_M T$ decreases to approx. 0 cm^3 K mol^{-1} at 1.8 K. This behaviour is indicative of antiferromagnetic exchange between the metal centres and an $S = 0$ ground state. For complex **8**, the room temperature $\chi_M T$ value of approx. 3.5 cm^3 K mol^{-1} (Fig. 3.26) is lower than that expected for three non-interacting Fe^{III} ions (13.125 cm^3 K mol^{-1}). Upon cooling, the value of $\chi_M T$ decreases to approx. 0.5 cm^3 K mol^{-1} at 1.8 K. This behaviour is indicative of antiferromagnetic exchange between the metal centres with the low temperature value suggesting an $S = ½$ ground state for **8**. For complex **9**, the room temperature $\chi_M T$ value of approx. 8.5 cm^3 K mol^{-1} (Fig. 3.26) decreases to approx. 0.1 cm^3 K mol^{-1} at 1.8 K. This behaviour is again indicative of antiferromagnetic exchange between the metal centres, with the low temperature value suggesting an $S = 0$ ground state. Using the program MAGPACK[25] and employing the spin Hamiltonians $\hat{H} = -2J(\hat{S}_1\hat{S}_2)$ (complex **7**), $\hat{H} = -2J_1(\hat{S}_1\hat{S}_2 + \hat{S}_1\hat{S}_3) - 2J_2(\hat{S}_2\hat{S}_3)$ (complex **8**) and $\hat{H} = -2J_1(\hat{S}_1\hat{S}_2 + \hat{S}_1\hat{S}_4 + \hat{S}_2\hat{S}_3 + \hat{S}_3\hat{S}_4) - 2J_2(\hat{S}_1\hat{S}_3 + \hat{S}_2\hat{S}_4)$ (complex **9**) allowed us to satisfactorily simulate the data (Fig. 3.25-3.26) with parameters $J = -18.2$ cm^{-1} and $g = 1.99$ for **7**; $J_1 = -38.0$ cm^{-1}, $J_2 = -29.3$ cm^{-1} and $g = 1.99$ for **8**; and $J_1 = -12.4$ cm^{-1}, $J_2 = -5.5$ cm^{-1} and $g = 2.01$ for **9**.

The value of the exchange parameter in **7** is in the same order of magnitude as the antiferromagnetic coupling constant of −11.8 cm^{-1} found for complex $[Fe_2(sao)_3(tmtacn)]$ which contains three bridging oximate groups (tmtacn=1,4,7-trimethyl-1,4,7-triazacyclononane).[23d] The derived values for the exchange parameters in **8** fall well within the range of values usually found in trinuclear Fe^{III} complexes containing the $[Fe^{III}_3(\mu_3\text{-}O)]^{7+}$ core.[26] In particular, its J_1 and J_2 values (−38.0 cm^{-1} and −29.3 cm^{-1}) are very similar with the corresponding values (−35.9 cm^{-1} and −29.8 cm^{-1}) for the structurally similar complex $[Fe^{III}_3O(sao)(O_2CPh)_5(EtOH)(H_2O)]$.[23g]

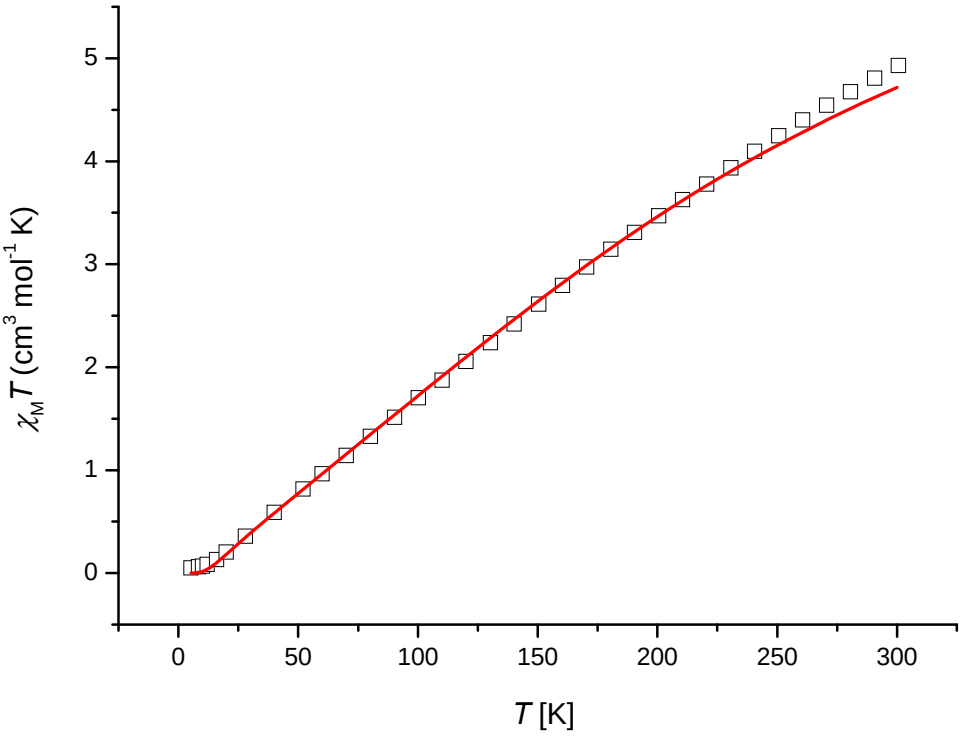

Fig. 3.25 Plot of $\chi_M T$ *vs* T for complex **7.** The solid lines represent simulations of the experimental data in the temperature range 300–5 K.

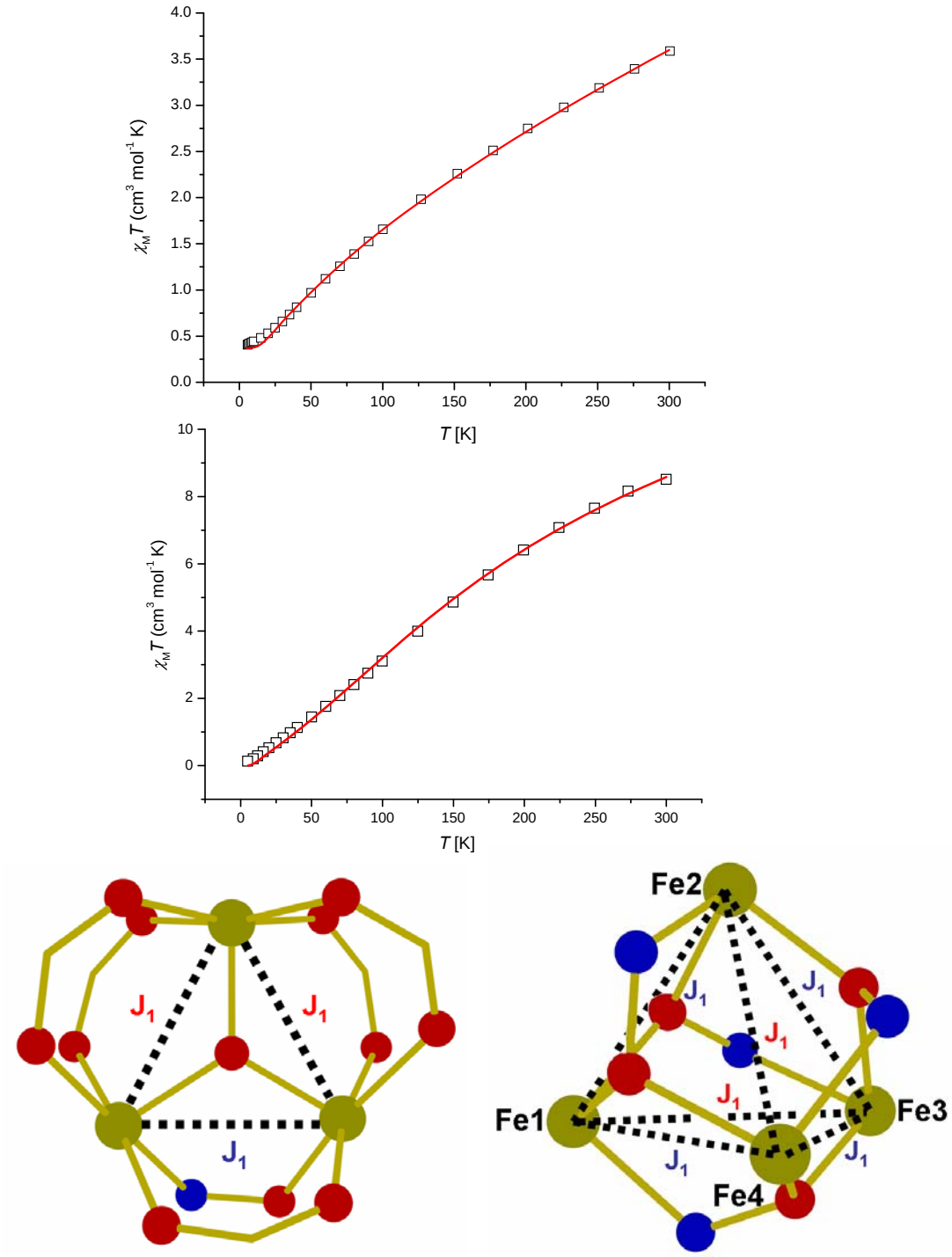

Fig. 3.26 Plot of $\chi_M T$ *vs* T for complexes **8** (top) and **9** (middle)**.** The solid lines represent simulations of the experimental data in the temperature range 300–5 K. Exchange interaction model used for **8** (bottom left) and **9** (bottom right).

It is not possible to discuss the correlation between the bridging units and the derived *J* values in **7–9**, because the bridging is different in the three cases. No strict theoretical concept for the interpretation of the magnetostructural correlation in dinuclear and polynuclear Fe^{III} complexes has been developed so far. The main reason is the large number of magnetic orbitals which have to be taken into account. Thus, with the exception of tetranuclear Fe^{III} complexes of the "butterfly" type,[27] only empirical[28] or semi-empirical[29,30] magnetostructural correlations for exchange coupled Fe^{III} centres have been established. The *J* value for complex **7** is approximately as expected from the empirical *J vs. P* relationship reported by Gorun and Lippard,[28] where *P* is defined as half the shortest superexchange pathway between the Fe^{III} ions. The *J vs P* relationship is described by the equation $-J = A\exp(BP)$, where $A = 8.763 \times 10^{11}$ cm^{-1} and $B = -12.663$ $Å^{-1}$, and *J* is based on the $\hat{H} = -2J\hat{S}_1\hat{S}_2$ spin Hamiltonian. For **7**, half the Fe(1)–O(15)–Fe(2) pathway distance is 1.981 Å , giving a predicted *J* of -11.2 cm^{-1}. The agreement with the experimental value obtained from fitting the susceptibility data (-18.2 cm^{-1}) is becoming better (the predicted value of *J* is -14.1 cm^{-1}) if we apply the relationship $J = -A\exp(Bd)$, where $A = -107$ cm^{-1}, $B = -6.8$ $Å^{-1}$ and *d* is the mean Fe^{III}–O distance of the Fe^{III}–O(R)–Fe^{III} bridge (R = H, Me, Ph). This expression was derived for an extensive group of hydroxide-, alkoxide- and phenoxide-bridged Fe^{III} dimers by Haase and coworkers,[30] who employed both the exponential model of Gorun and Lippard[28] and the quantum mechanical (based on the Angular OverlapModel, AOM) Weihe–Güdel expression $J = A(B + C\cos\varphi + \cos^2\varphi)\exp(Dr)$, where φ is the Fe^{III}–O–Fe^{III} angle and *r* is the Fe^{III}–O distance.[29] Haase and coworkers[30] took into account only the hydroxo-, alkoxo- and phenoxo-bridges, which provide a much more efficient superexchange pathway than other polyatomic bridges, and concluded that angular dependence is small. Applying the Gorun–Lippard relationship to complex **8** (their correlation applies not only to dinuclear but also to complexes of higher nuclearity[28]

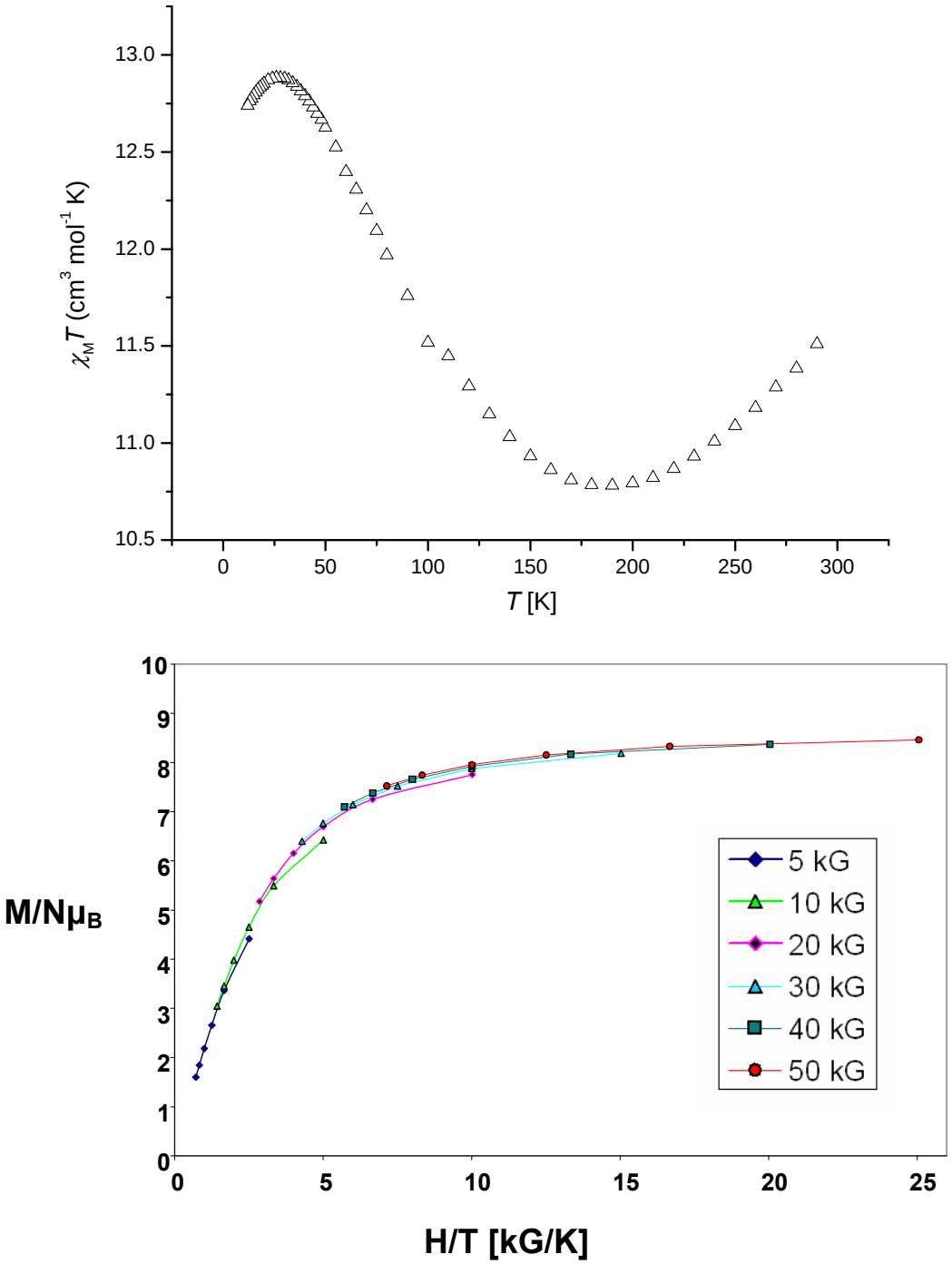

Fig. 3.27 Plot of $\chi_M T$ *vs* T (top) and reduced magnetisation ($M/N\mu_B$) *vs* H/T for **10** (bottom).

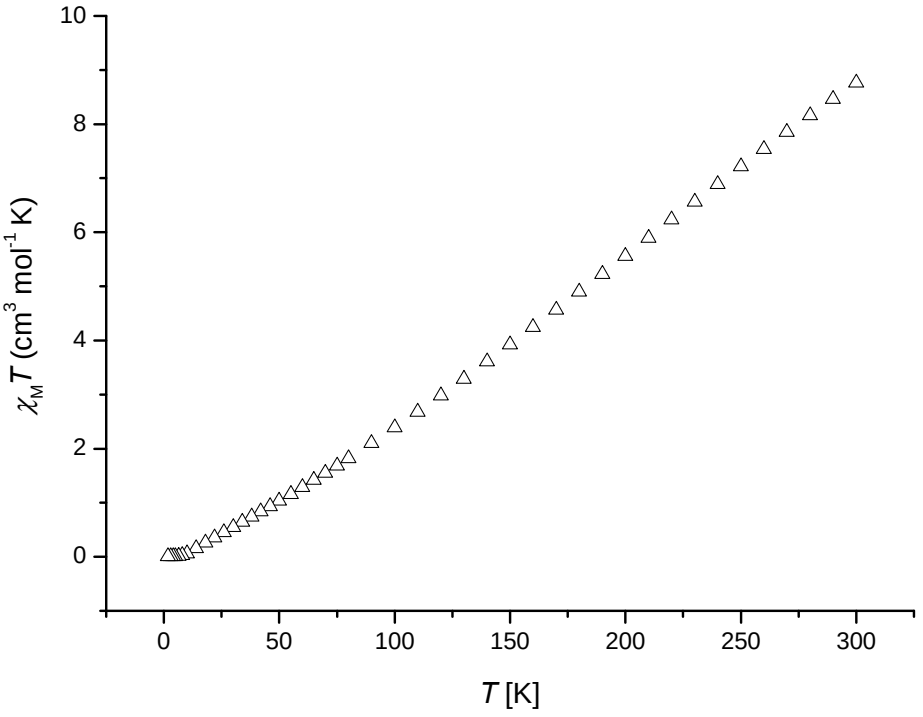

Fig. 3.28 Plot of $\chi_M T$ *vs* T for complexes **11**-**13**.

), gives $J_1 = -33.2$ and -41.7 cm^{-1} (average -37.5 cm^{-1}) for the Fe1· · · Fe3 and Fe2 · · ·Fe3 interactions (see Fig. 3.3, middle), respectively, and $J_2 = -28.9$ cm^{-1}, which are in good overall agreement with the experimental J values ($J_1 = -38.0$ cm^{-1} and $J_2 = -29.3$ cm^{-1}) obtained from fitting the susceptibility data.

For complex **10** the room temperature $\chi_M T$ value of 11.5 cm^3 K mol^{-1}(Fig. 3.27) is lower than the spin only ($g = 2$) value of 26.25 cm^3 K mol^{-1} expected for six non interacting Fe^{III} ions. The value decreases gradually as the temperature is decreased until *ca* 190 K where it begins to increase to a maximum value of 12.75 cm^3 K mol^{-1} at 26 K, below which it decreases to a value of 11.55 cm^3 K mol^{-1} at 1.8 K This behaviour is consistent with the presence of both antiferromagnetic and ferromagnetic interactions between the metal centres with the low temperature maximum indicating an $S = 4$ spin ground state. In-phase (as $\chi_M' T$) ac susceptibility data collected on **10** below 10 K in an oscillating field of 3.5 G are superimposable

on the dc $\chi_M T$ data, confirming the S = 4 spin ground state. The complexity of the structure precludes fitting of the susceptibility data by standard procedures. Variable temperature and variable field dc magnetisation data collected in the temperature and field ranges 2–7 K and 5–50 kG, are shown in Fig. 3.27 as $M/N\mu_B$ *vs* H/T. However, attempts to fit the data using a matrix-diagonalisation method to a model that assumes only the ground state is populated resulted in fits of rather poor quality. This presumably arises from the population of low-lying excited states. The combination of the maximum in $\chi_M T$, the ac data and the saturation of $M/N\mu_B$ at~8 implies a best "guess" of S =4 ±1.

For complexes **11–13** the room temperature $\chi_M T$ value of approximately 8.8 cm^3 K mol^{-1} (Fig. 3.28) is much lower than the spin-only value expected for a $\{Fe^{III}_8\}$ unit (35 cm^3 K mol^{-1}), suggesting the presence of relatively strong antiferromagnetic exchange, even at 300 K. As the temperature is decreased, $\chi_M T$ continually drops to a value of 0.01 cm^3 K mol^{-1} at 1.8 K indicating an S = 0 spin ground state.

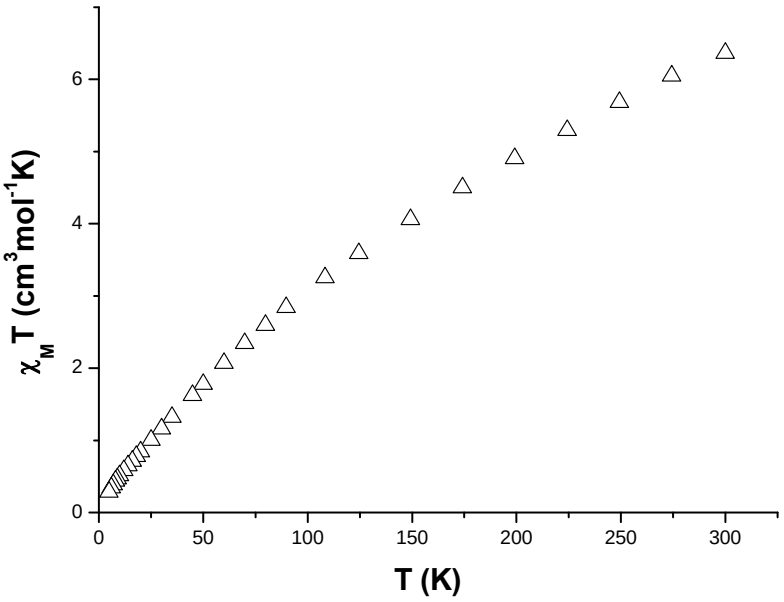

Fig. 3.29 Plot of $\chi_M T$ *vs* T for complex **14**

For complexes **14-17** the room temperature $\chi_M T$ value of approx. 6.4, 6.1, 11.0 and 10.2 cm^3 K mol^{-1} respectively (Fig. 3.29-3.32) is lower than that expected for six non-interacting Fe^{III} ions (26.25 cm^3 K mol^{-1}). Upon cooling, the value of $\chi_M T$ decreases to approx. 0, 1.1, 0.25, 0.22 cm^3 K mol^{-1} at 5 K respectively. This behaviour is indicative of antiferromagnetic exchange between the metal centres and an $S = 0$ ground state. The complexity of structures **14-17** precludes the fitting of the susceptibility data by standard procedures.

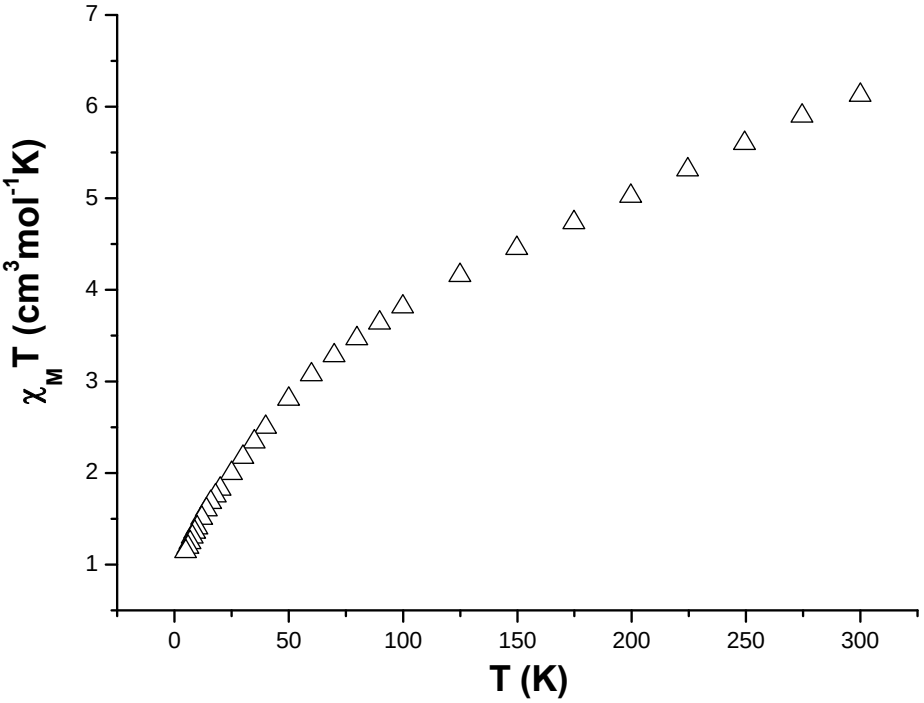

Fig. 3.30 Plot of $\chi_M T$ *vs* T for complex **15**

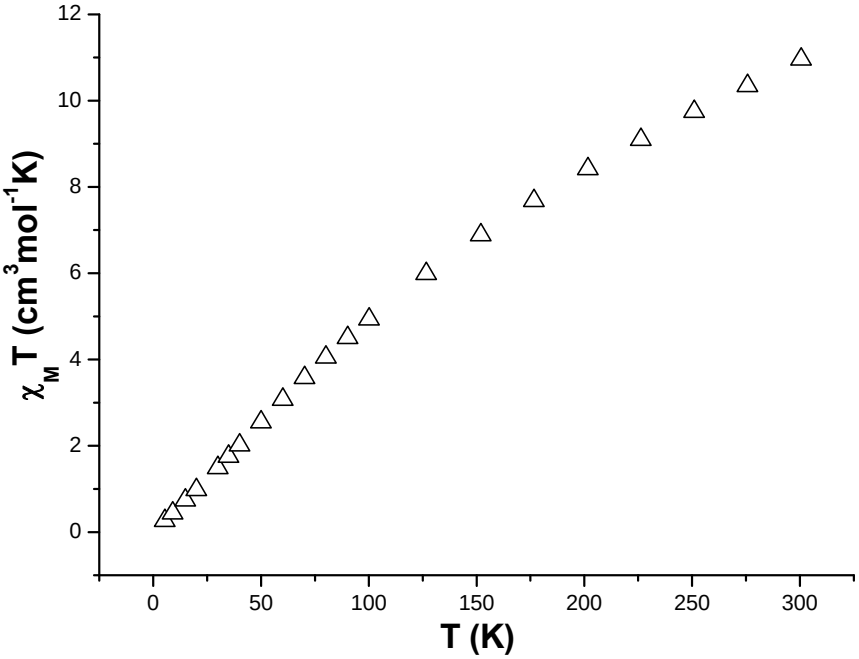

Fig. 3.31 Plot of $\chi_M T$ *vs T* for complex **16**

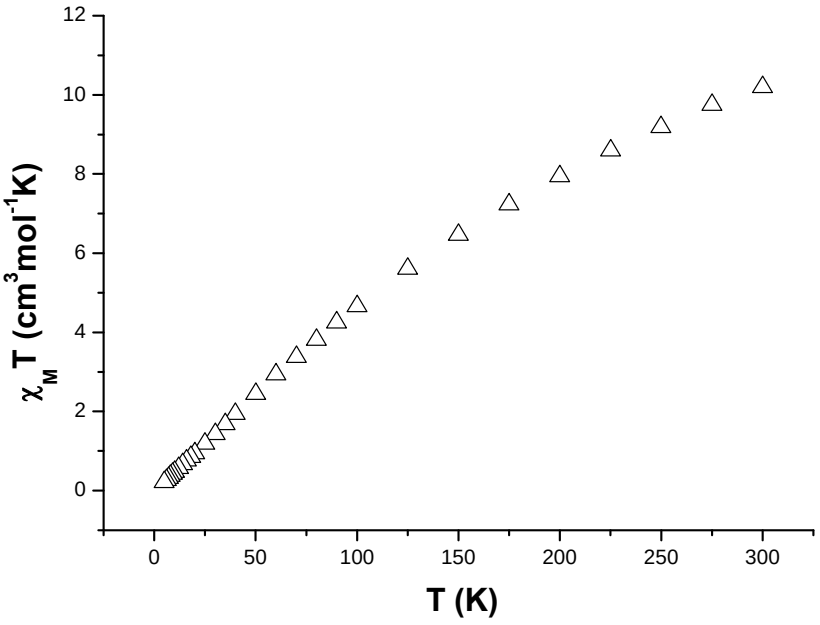

Fig. 3.32 Plot of $\chi_M T$ *vs T* for complex **17**

Conclusions

We have presented the first ten structurally characterised Fe^{III} compounds synthesised using the derivatised salicylaldoxime ligands, R-saoH_2. Four are the largest examples of polynuclear iron clusters reported using salicylaldoxime ligands, derivatised or otherwise. A combination of R-saoH_2 with the sulfate ligand, SO_4^{2-}, has resulted in the only example of a hexanuclear iron complex bearing a coordinated sulfate ligand; while combination with the tripodal ligand H_3tea, resulted in the formation of a family of novel octametallic clusters. By simply replacing the Me-saoH_2 ligand employed in **16** to the saoH_2 ligand employed in **17** results in a drastic change in structure from an extended network (**16**) to a discrete polynuclear complex (**17**). This collection of rather unusual polymetallic clusters demonstrates the flexibility, versatility and potential of combining R-saoH_2 ligands with other flexible bridging ligands.

References

1 (*a*) C. J. Milios, I. A. Gass, A. Vinslava, L. Budd, S. Parsons, W. Wernsdorfer, G. Christou, S. P. Perlepes, E. K. Brechin, *Inorg. Chem.*, 2007, **46**, 6215; (*b*) C. J. Milios, A. Vinslava, P. A. Wood, S. Parsons, W. Wernsdorfer, G. Christou, S. P. Perlepes, E. K. Brechin, *J. Am. Chem. Soc.*, 2007, **129**, 8; (*c*) C. J. Milios, A. Vinslava, W.Wernsdorfer, S.Moggach, S. Parsons, S. P. Perlepes,G. Christou, E. K. Brechin, *J. Am. Chem. Soc.*, 2007, **129**, 2754; (*d*) C. J. Milios, A. Vinslava,W.Wernsdorfer, A. Prescimone, P. A.Wood, S. Parsons, S. P. Perlepes, G. Christou, E. K. Brechin, *J. Am. Chem. Soc.*, 2007, **129**, 6547; (*e*) C. J.Milios, R. Inglis, A. Vinslava, R. Bagai,W.Wernsdorfer, S. Parsons, S. P. Perlepes, G. Christou, E. K. Brechin, *J. Am. Chem. Soc.*, 2007, **129**, 12511.

2 (*a*) A. G. Smith, P. A. Tasker, D. J.White, *Coord. Chem. Rev.*, 2003, **241**, 61; (*b*) P. Chaudhuri, *Coord. Chem. Rev.*, 2003, **243**, 143; (*c*) C. J. Milios, C. P.

Raptopoulou, A. Terzis, F. Lloret, R. Vicente, S. P. Perlepes, A. Escuer, *Angew. Chem., Int. Ed.*, 2004, **43**, 210.

3 (*a*) A. L. Barra, F. Bencini, A. Caneschi, D. Gatteschi, C. Paulsen, C. Sangregorio, R. Sessoli, L. Sorace, *ChemPhysChem*, 2001, **2**, 523; (*b*) K.Weighardt, K. Pohl, I. Jibril, G. Huttner, *Angew. Chem., Int. Ed. Engl.*, 1984, **23**, 77; (*c*) C. C. Vilalta, M. Pink, G. Christou, *Chem. Commun.*, 2003, 1240; (*d*) C. C. Vilalta, T. A. O'Brien, M. Pink, E. R. Davidson, G. Christou, *Inorg. Chem.*, 2003, **42**, 7819; (*e*) R. G. Raptis, I. P.Georgakaki, D. C. R. Hockless, *Angew. Chem., Int. Ed.*, 1999, **38**, 1633; (*f*) J. H. Satcher, Jr, M. M. Olmstead, M. W. Droege, S. R. Parkin, B. C. Noll, L. May and A. L. Balch, *Inorg. Chem.*, 1998, **37**, 6751; (*g*) E. K. Brechin, M. J. Knapp, J.C. Huffman, D. N. Hendrickson, G. Christou, *Inorg. Chim. Acta*, 2000, **297**, 389; (*h*) L. F. Jones, A. Batsanov, E. K. Brechin, D. Collison, M. Helliwell, T. Mallah, E. J. L. McInnes, S. Piligkos, *Angew. Chem., Int. Ed.*, 2002, **41**, 4319; (*i*) P. Ammala, J. D. Cashion, C. M. Kepert, B. Moubaraki,K. S.Murray, L. Spiccia, B. O. West, *Angew. Chem., Int. Ed.*, 2000, **39**, 1688; (*j*) W. Schmitt, M. Murugesu, J. C. Goodwin, J. P. Hill, A. Mandel, R. Bhalla, C. E. Anson, S. L. Heath, A. K. Powell, *Polyhedron*, 2001, 1687; (*k*) D. B. Dell'Amico, F. Calderazzo, L. Labella, C. Maichle-Mössmer, J. Strahle, *J. Chem. Soc., Chem. Commun.*, 1994, 1555; (*l*) I. Lorenz, W. Pohl, H. Nöth, *Angew. Chem., Int. Ed. Engl.*, 1997, **36**, 55; (*m*) M. Murugesu, K. A. Abboud, G. Christou, *Dalton Trans.*, 2003, 4552; (*n*) I.Gautier-Luneau, C. Fouquard, C. Merle, J. Pierre, D. Luneau, *J. Chem. Soc., Dalton Trans.*, 2001, 2127; (*o*) L. F. Jones, P. Jensen, B. Moubaraki, K. J. Berry, J. F. Boas, J. R. Pilbrow, K. S. Murray, *J. Mater. Chem.*, 2006, **16**, 2690; (*p*) A. M. Ako, O. Waldmann, V. Mereacre, F. Klower, I. J. Hewitt, C. E. Anson, H. U. Güdel, A. K. Powell, *Inorg. Chem.*, 2007, **46**, 756; (*q*) I. A. Gass, C. J. Milios, A. G. Whittaker, F. P. A. Fabiani, S. Parsons, M. Murrie, S. P. Perlepes, E. K. Brechin, *Inorg. Chem.*, 2006, **45**, 5281.

4 C. Papatriantafyllopoulou, G. Aromi, A. J. Tasiopoulos, V. Nastopoulos, C. P. Raptopoulou, S. J. Teat, A. Escuer, S. P. Perlepes, *Eur. J. Inorg. Chem.*, 2007, 2761.

5 (*a*) Y.-L. Fu, Z.-W. Xu, J.-L. Ren, S. W. Ng, *Acta Crystallogr., Sect. E: Struct. Rep. Online*, 2005, **61**, m1478; (*b*) R. K.Murmann, C. L. Barnes, *Acta Crystallogr., Sect. C: Cryst. Struct. Commun.*, 1999, **55**, 2004; (*c*) L. Carlucci, G. Ciani, D. M. Prosperio, S. Rizzato, *CrystEngComm*, 2003, **5**, 190; (*d*) Y.-L. Fu, Z.-W. Xu, J.-L. Ren, S. W. Ng, *Acta Crystallogr., Sect. E: Struct. Rep. Online*, 2005, **61**, m593; (*e*) Y.-L.Fu, Z.W. Xu, J.-L. Ren, S.W. Ng, *Acta Crystallogr., Sect. E: Struct. Rep. Online*, 2005, **61**, m596; (*f*) Y.-L. Fu, Z.-W. Xu, J.-L. Ren, S.W. Ng, *Acta Crystallogr., Sect. E: Struct. Rep. Online*, 2005, **61**, m1831; (*g*) S. Noro, M. Kondo, S. Kitagawa, T. Ishii, H. Matsuzaka, *Chem. Lett.*, 1999, 727; (*h*) Y.-L. Fu, Z.-W. Xu, J.-L. Ren, S.W. Ng, *Acta Crystallogr., Sect. E: Struct. Rep. Online*, 2005, **61**, m1641; (*i*) M. Shatruk, A. Chouai, A. V. Prosvirin, K. R. Dunbar, *Dalton Trans.*, 2005, 1897; (*j*) G. Paul, A. Choudhury, C.N. R.Rao, *Chem. Mater.*, 2003, **15**, 1174; (*k*) H.-Y. Guo, Z.-H. Li, X.-Y. Li, C.-Y. Zhang, R.-J.Wang, *Chin. J. Chem.*, 2003, **21**, 466; (*l*) D. V. Naik, G. J. Palenik, *Chem. Phys. Lett.*, 1974, **24**, 260; (*m*) G. F. Volodina, L. I. Petukhov, A. V. Ablov, N. V. Gerbeleu, *Dokl. Acad. Nauk SSSR*, 1974, **218**, 1351; (*n*) H. Z. Shi, Z.-L. Li, Y.-K. Shan, *Z. Kristallogr. -New Cryst. Struct.*, 2005, **220**, 245; (*o*) H. Dittmar, K. Bohn, N. Walker, *Z. Kristallogr. - New Cryst. Struct.*, 2000, **215**, 189.

6 (*a*) C. N. Rao, E. V. Sampathkumaran, R. Nagarajan, G. Paul, J. N. Behera A. Choudhury, *Chem. Mater.*, 2004, **16**, 1441; (*b*) G. Paul, A. Choudhury, E. V. Sampathkumuran, C. N. R. Rao, *Angew. Chem., Int. Ed.*, 2002, **41**, 4297; (*c*) G. Paul, A. Choudhury, C. N. R. Rao, *Chem. Commun.*, 2002, 1904; (*d*) J. N. Behera, C. N. R. Rao, *Inorg. Chem.*, 2006, **45**, 9475.

7 (*a*) W. K. Miller, J. D. Gilbertson, C. Leiva-Paredes, P. R. Bernatis, T. J. R. Weakley, D. K. Lyon, D. R. Tyler, *Inorg. Chem.*, 2002, **41**, 5453; (*b*) W. R. Scheidt, Y. J. Lee, M. G. Finnegan, *Inorg. Chem.*, 1988, **27**, 4725; (*c*) H. Borzel, P. Comba, K. S.Hagen, Y. D. Lampeka, A. Lienke, G. Linti, M. Merz, H.

Pritzkow, L.V. Tsymbal, *Inorg. Chim. Acta*, 2002, **337**, 407; (*d*) P. Held, *Acta Crystallogr., Sect. E: Struct. Rep. Online*, 2003, **59**, m197; (*e*) T. Hirano, M. Hirobe, K. Kobayashi, A. Odani, O. Yamauchi, M. Ohsawa, Y. Satow, T. Nagano, *Chem. Pharm. Bull.*, **48**, 223.

8 (*a*) W. R. Scheidt, Y. J. Lee, T. Bartzcak, K. Hatano, *Inorg. Chem.*, 1984, **23**, 2552; (*b*) M.A. Phillippi, N. Baenziger, H. M.Goff, *Inorg. Chem.*, 1981, **20**, 3904; (*c*) M. S.Reynolds, R.H. Holm, *Inorg. Chim. Acta*, 1989, **155**, 113.

9 M. Odoko, N. Okabe, *Acta Crystallogr., Sect. E: Struct.Rep. Online*, 2005, **61**, 587.

10 A. C. Sudik, A. R. Milliward, N. W. Ockwig, A. P. Cote, J. Kim, O. M. Yaghi, *J. Am. Chem. Soc.*, 2005, **127**, 7110.

11 P. L. Jones, J. C. Jeffrey, J. A. McCleverty, M. D. Ward, *Polyhedron*, 1997, **16**, 1567.

12 M. A. De Brito, A. Neves, I. Vencato, C. Zucco, V. Drago, K. Griesar, W. Haase, *J. Braz. Chem. Soc.*, 1997, **8**, 443.

13 E. Andres, G. De Munno, M. Julve, J. A. Real, F. Lloret, *J. Chem. Soc., Dalton Trans.*, 1993, 2169.

14 N. Arulsamy, P. A. Goodson, D. J. Hodgson, J. Glerup, K. Michelsen, *Inorg. Chim. Acta*, 1994, **216**, 21.

15 Y. T. Struchkov, G. G. Aleksandrov, V. S. Kaganovich, M. I. Rybinskaya, *Koord. Khim.*, 1981, **7**, 949.

16 K. Weighardt, S. Drueke, P. Chaudhuri, U. Florke, H.-J. Haupt, B. Nuber, J. Weiss, *Z. Naturforsch. B: Chem. Sci.*, 1989, **44**, 1093.

17 A. Neels, H. Stoeckli-Evans, *Chimia*, 1993, **47**, 198.

18 R. Dunsten, T. A. Henry, *J. Chem. Soc. Trans.*, 1899, **75**, 66.

19 C. J. Milios, A. Prescimone, A.Mishra, S. Parsons,W.Wernsdorfer, G. Christou, S. P. Perlepes, E. K. Brechin, *Chem. Commun.*, 2007, 153.

20 E. K. Brechin, *Chem. Commun.*, 2005, 5141.

21 (*a*) I. D. Brown, D. Altermatt, *Acta Crystallogr., Sect. B: Struct. Sci.*, 1985, **B41**, 244; (*b*) H. H. Thorp, *Inorg. Chem.*, 1992, **31**, 1585.

22 (*a*) C. J. Milios, P. A. Wood, S. Parsons, D. Foguet-Albiol, C. Lampropoulos, G. Christou, S. P. Perlepes, E. K. Brechin, *Inorg. Chim. Acta*, 2007, **360**, 3932; (*b*) L. F. Larkworthy and D. C. Povey, *J. Crystallogr. Spectrosc. Res.*, 1983, **13**, 413; (*c*) Z. Kangjing, Z. Chengming, C. Xing, Y. Chengye, *Kexue Tongbao (Chin. Ed.)*, 1985, **30**, 266, (*Chin. Sci. Bull.*, 1983, **30**, 1484); (*d*) R. Acharyya, F. Basuli, G. Rosair, S. Bhattacharya, *New J. Chem.*, 2004, **28**, 115; (*e*) A. G. Hatzidimitriou, M. Uddin, M. Lalia-Kantouri, *Z. Anorg. Allg.Chem.*, 1997, **623**, 627; (*f*) H.-L. Xiao, F. F. Jian, *Acta Crystallogr., Sect. E: Struct.Rep. Online*, 2006, **62**,m1512; (*g*) M. Lalia-Kantouri, M. Uddin, C. C. Hadjikostas, H. Papanikolas, G. Palios, S. Anagnostis, V. Anesti, *Z. Anorg. Allg. Chem.*, 1997, **623**, 1983; (*h*) M. Lalia-Kantouri, M. Hartophylles, P. D. Jannakoudakis, G. P. Voutsas, *Z. Anorg. Allg. Chem.*, 1995, **621**, 645; (*i*) G. P. Voutsas, K. G. Keramidas, M. Lalia-Kantouri, *Polyhedron*, 1996, **15**, 147.

23 (*a*) P. Chaudhuri, M. Vinter, P. Fleischhauer, W. Haase, U. Flörke, H.-J. Haupt, *Inorg. Chim. Acta*, 1993, **212**, 241; (*b*) E. Bill, C. Krebs, M.Winter,M. Gerdan, A. X. Trautwein, U. Flörke, H.-J. Haupt, P. Chaudhuri, *Chem.–Eur. J.*, 1997, **3**, 193; (*c*) J. M. Thorpe, R. L. Beddoes, D. Collison, C.D. Garner, M.Helliwell, J. M. Holmes, P. A. Tasker, *Angew. Chem., Int. Ed.*, 1999, **38**, 1119; (*d*) G. N. Verani, E. Bothe, D. Burdinski, T.Weyhermüller, U. Flörke, P. Chaudhuri, *Eur. J. Inorg.Chem.*, 2001, 2161; (*e*) P. Chaudhuri, E. Rentschler, F. Birkelbach, C. Krebs, E. Bill, T. Weyhermüller, U. Flörke, *Eur. J. Inorg. Chem.*, 2003, 541; (*f*) C. P. Raptopoulou, A. K. Boudalis, Y. Sanakis, V. Psycharis, J. M. Clemente-Juan, M. Fardis, G. Diamantopoulos, G. Papavassiliou, *Inorg. Chem.*, 2006, **45**, 2317; (*g*) C. P. Raptopoulou, Y. Sanakis, A. K. Boudalis, V. Psycharis, *Polyhedron*, 2005, **24**, 711.

24 A. W. Addison, T. N. Rao, J. Reedijk, J. van Rijn, G. C. Verschoor, *J. Chem. Soc. Dalton Trans.*, 1984, 1349.

25 J. J. Borras-Almenar, J. M. Clemente-Juan, E. Coronado and B. S. Tsukerblat, *J. Comput. Chem.*, 2001, **22**, 985.

26 (*a*) R. D. Cannon and R. P. White, *Prog. Inorg. Chem.*, 1988, **36**, 195; (*b*) F. E. Sowrey, C. Tilford, S. Wocadlo, C. E. Anson, A. K. Powell, S. M. Bennington,W. Montfrooij,U. A. Jayasooriya and R.D. Cannon, *J. Chem. Soc., Dalton Trans.*, 2001, 862; (*c*) G. J. Long,W. T. Robinson, W. P. Tappmeyer and D. L. J. Bridges, *J. Chem. Soc., Dalton Trans.*, 1973, 573.

27 T. Cauchy, E. Ruiz and S. Alvarez, *J. Am. Chem. Soc.*, 2006, **128**, 15722.

28 S. M. Gorun and S. J. Lippard, *Inorg. Chem.*, 1991, **30**, 1625.

29 H. Weihe and H. U. Güdel, *J. Am. Chem. Soc.*, 1997, **119**, 6539.

30 R. Werner, S. Ostrovsky, K. Griesar and W. Haase, *Inorg. Chim. Acta*, 2001, **326**, 78.

Chapter 4
Microwave-Assisted Synthesis of an Octametallic Fe^{III} Cluster

Introduction

Coordination chemists attempting to make large polymetallic clusters of paramagnetic transition metals rarely perform syntheses in conditions other than ambient temperature and pressure. The reason is simple: it is not necessary because the overwhelming majority of polynuclear complexes have been made via simple benchtop methods.[1] Only when making complexes of inert ions such as Cr^{3+} have alternative techniques been pursued.[2] Indeed, the use of solvothermal synthesis has only recently become "standard practice" for metal clusters of, for example, Fe, Ni, and Mn.[3] There is no reason why synthetic inorganic chemists should confine their experiments to a limited temperature and pressure regime, whether that be for the purposes of making completely new complexes or known species in higher yields and in faster reaction times. Given recent successes in the solvothermal synthesis of large metal clusters,[3] we decided to examine whether microwave heating could be used for a similar purpose.

Microwave heating is now used routinely in many areas of chemistry such as homogeneous organic reactions[4,5] where superheating effects are primarily believed to be responsible for the improvement in reaction rates and yields.[6,7] Microwaves are also used in analytical chemistry,[8] intercalation reactions,[9] solid-state reactions,[10] liquid-phase organic syntheses, organic dry-media reactions,[11] and in cross-coupling methods of C-C bond formation, such as the Pd-catalysed Heck,[12] Suzuki[13] and Stille[14] reactions with the dramatic rate enhancement over conventional methods achieved through the use of microwave heating.

Surprisingly reactions involving liquid-phase inorganic syntheses have received no attention. In our experience, microwave heating not only provides an alternative synthetic tool but also may help to improve the yield and reproducibility of large polymetallic complexes. Moreover, it may also lead to novel products, by permitting

access to alternative kinetic pathways. This is especially possible when it effects exceptionally rapid heating of the reaction components.[15] Irrespective of the nature of the product, the reduction of the reaction times through microwave heating permits a larger number of reaction conditions to be explored more quickly, making exploratory synthetic programs more efficient. Here we report the microwave-assisted synthesis of an $\{Fe^{III}_8\}$ cluster that cannot be synthesised under ambient reaction conditions.

The ligand used for the preparation of the $\{Fe^{III}_8\}$ cluster is salicylaldoxime (IUPAC name: 2-hydroxybenzaldehyde oxime, $saoH_2$). This ligand belongs to the family of phenolic oximes[16] introduced in chapter 3; while their classical mode of coordination via deprotonation of the phenol to bind to a metal centre as a monoanionic bidentate ligand is frequently observed, a literature survey reveals a plethora of less common coordination modes that can be attained via deprotonation of both the phenolic and oximic groups, resulting in the formation of tridentate ligands and polynuclear metal complexes.[16-18] The formation of such polynuclear complexes (clusters) at lightly oxidised metal surfaces also accounts for the efficacy of $saoH_2$ derivatives as corrosion inhibitors.[19] Another point of interest in the coordination chemistry of $saoH_2$ is its activation by 3d metal centres toward further reactions,[20] which seems to be an emergent area of synthetic chemistry.[21]

Experimental Section

All manipulations were performed under aerobic conditions using chemicals as received, unless otherwise stated.

Synthetic Procedures

$[Fe_8O_4(sao)_8(py)_4]\cdot 4py$ (18·4py)

$Fe(O_2CMe)_2$ (229 mg, 1.32 mmol), $saoH_2$ (179 mg, 1.32 mmol), and pyridine (6 mL) were placed in a sealed glass tube, which was then inserted into the cavity of

a microwave reactor. The reaction mixture was maintained at T = 120°C, power = 200 W, and pressure = 130 psi for a total of 2 min. After cooling (ca. 1 min), the solution was filtered and allowed to stand. Large red-brown needlelike crystals of **18**·4py started to form immediately. The dried sample analysed as **18**·3py. Found (calc.%) $C_{91}H_{75}Fe_8O_{20}N_{15}$ C, 51.31 (50.94), H, 3.36 (3.52), N 9.86 (9.79). IR data (KBr pellet; cm^{-1}): 1596s, 1577m, 1469m, 1438s, 1326m, 1300m, 1267m, 1243m, 1040m, 1022s, 916m, 755m, 696m, 669s, 605m, 544m, 526m, 436m.

Results and Discussion

Synthesis

Complex **18** cannot be made under ambient reaction conditions or by refluxing of a pyridine solution of $Fe(O_2CMe)_2$ and $saoH_2$. Employing different $Fe^{II/III}$ salts, different solvents or combinations of solvents, and different reaction times also does not produce complex **18**. A microcrystalline powder with an IR spectrum similar to that of complex **18** can be isolated under solvothermal reaction conditions (sealed Teflon container; 120 °C) but requires a minimum heating/cooling period of 24 h and forms in yields of less than ~10%; this equates to an approximately 7-fold decrease in comparison to the microwave reaction. This perhaps suggests that the rapid heating and cooling employed by the microwave plays an important synthetic role.

Description of Structures

$[Fe_8O_4(sao)_8(py)_4]$ (18) Selected bond lengths and angles are given in Table 4.2. The complex crystallises in the tetragonal space group $I4_1/a$ (Table 4.1). The core of the complex (Fig. 4.1, 4.2) contains a central $[Fe^{III}_4O_4]^{4+}$ cubane, with each of the four distorted tetrahedral μ_4-O^{2-} ions further bridged to a peripheral Fe^{III} ion (Fe2

and symmetry equivalents). The peripheral metal ions themselves form a tetrahedron, encapsulating the cube such that each face of the tetrahedron is capped (Fig. 4.3). The eight sao^{2-} ligands bridge in two ways: four in a η^2: η^1: η^1:μ_3 fashion along one complete edge of the tetrahedron, with the phenolate O atom bridging one Fe^{III} ion of the cube and one Fe^{III} ion of the tetrahedron, and four in a η^1: η^1: η^1:μ fashion along half an edge, between an Fe^{III} ion in the tetrahedron and a face-capping Fe^{III} ion of the central cube. The observed η^2: η^1: η^1:μ_3 coordination mode is unique among the structurally characterised metal complexes containing the sao^{2-} ligand.[16,17] A μ_3 behaviour has been observed in sao^{2-} complexes, but with the oximate O providing the bridge between metal ions. The coordination sphere of each of the four Fe^{III} ions in the outer tetrahedron is completed by a terminal pyridine molecule. Each Fe^{III} ion is in a distorted octahedral geometry, with the Fe^{III} ions of the cubane [cis, 73.95(7)-113.22(7)°; trans, 147.88(7)-163.93(7)°] more distorted than those in the outer tetrahedron [cis, 77.56(7)-96.47(7)°; trans, 170.09(7)-174.51(7)°]. Within the $[Fe_4O_4]^{4+}$ cubane, there are two small (93.55° and 95.68°) and one large Fe-O-Fe [105.66(7)°] angles, suggesting a rather "twisted" metal cubane. There are no hydrogen bond interactions in **18** leading to the packing in the crystal seen in Fig. 4.4

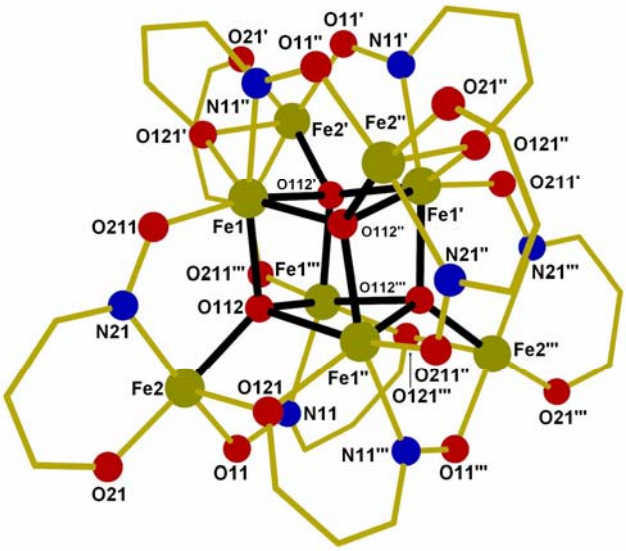

Fig. 4.1 Molecular structure of complex **18** (top). The pyridine rings and most C atoms of the phenyl groups of the oximato ligands have been omitted for clarity.

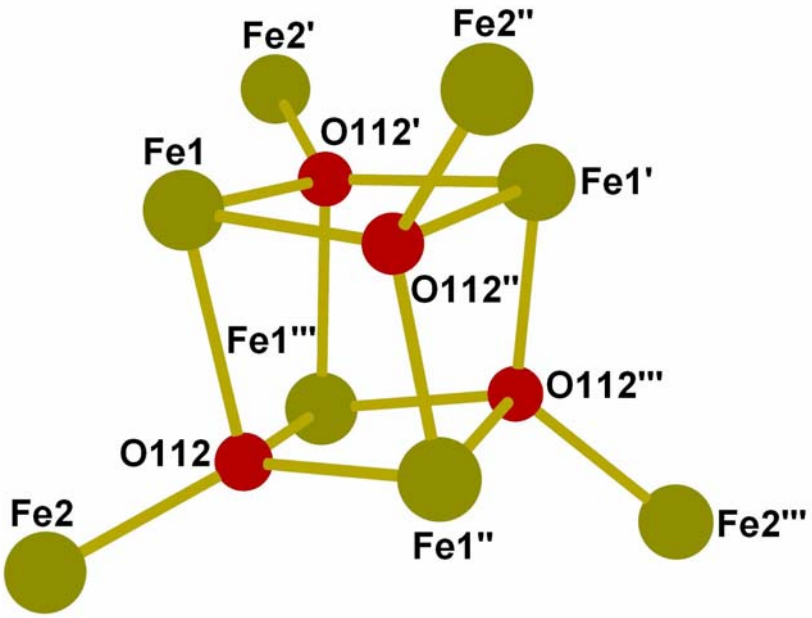

Fig. 4.2 Structure of the metal-oxygen core of complex **18**.

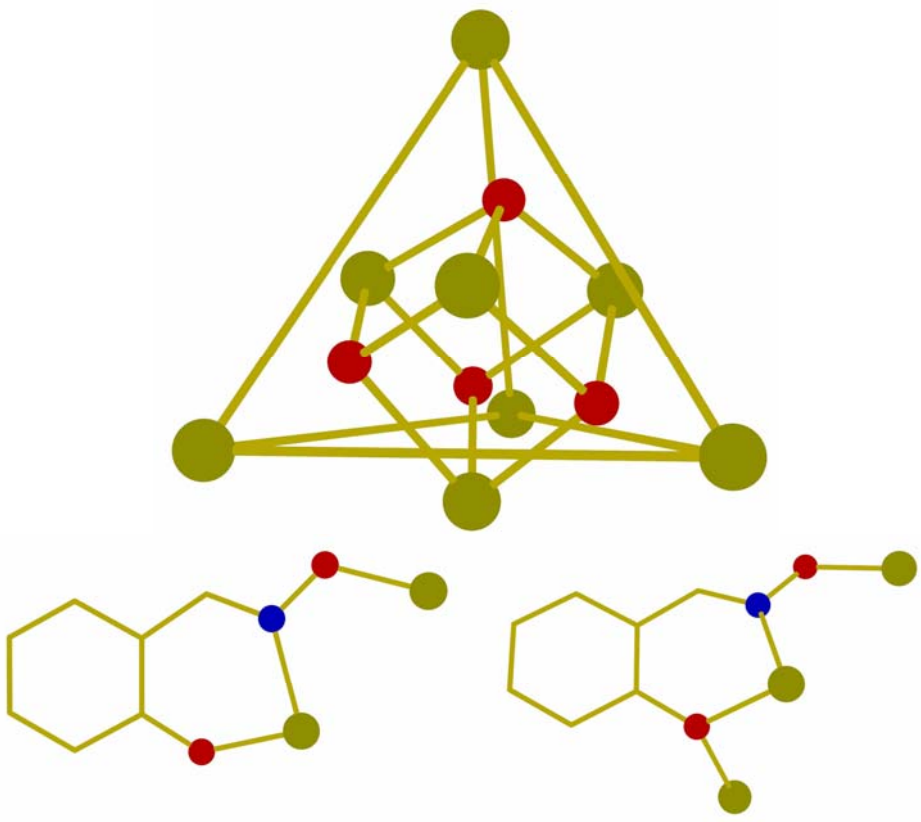

Fig. 4.3 "Metallic skeleton" of complex **18** (top) showing the $\{Fe_4O_4\}$ cubane within the $\{Fe_4\}$ tetrahedron.The bridging modes of the sao^{2-} ligands (bottom).

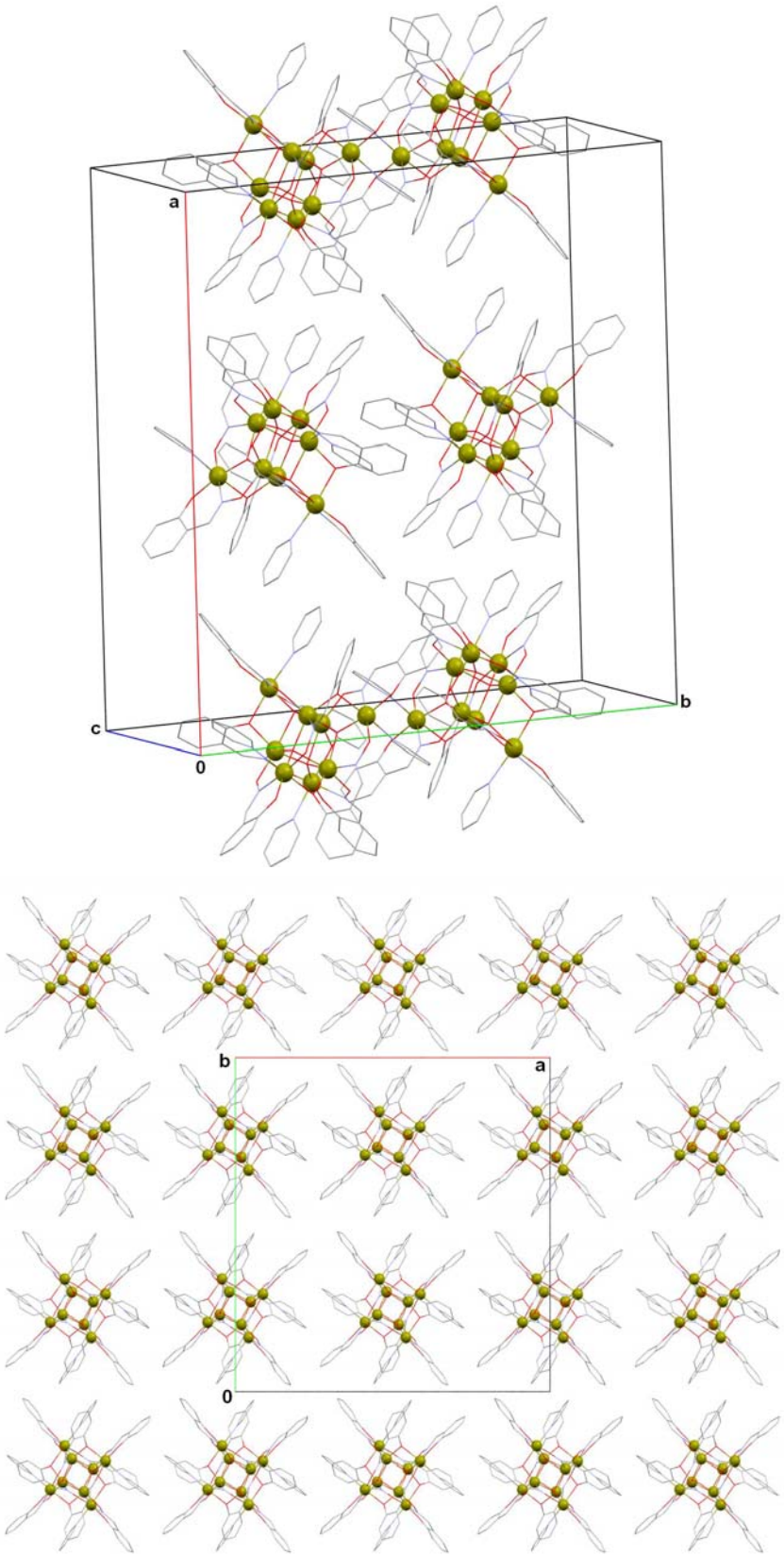

Fig. 4.4 Packing of **18** in the crystal.

Table 4.1 Crystallographic details for complex **18**

	18·4py
M, gmol^{-1}	2224.56
crystal system	Tetragonal
space group	I 41/a
a, Å	28.9096(3)
b, Å	28.9096(3)
c , Å	11.1722(3)
α, deg	90
β, deg	90
γ, deg	90
V , Å^3	9337.3(3)
Z	4
$\rho_{, calc}$ [g cm^{-3}]	1.582
T , K	150
λ (Å)	0.71073
μ, [mm^{-1}]	1.287
Measd/independant (R_{int})	56039/5891 (0.048)
Obsd reflns [I>2σ (*I*)]	3808
*R*1[b]	0.0384
*wR*2[c]	0.0867
GOF on F^2	0.6355
Δ $\rho_{max,min,}$ e Å^{-3}	1.06, -0.80

[a]*R*1) Σ(j*F*oj - j*F*cj)/Σ(j*F*oj) for observed reflections. [b] $_b$*wR*2) {Σ[*w*(F_{o2} - F_{c2})$_2$]/Σ[*w*($F_{o\ 2}$)$_2$]}$_{1/2}$ for all data.

The $[Fe_8O_4]^{4+}$ core is uncommon, observed only in one other complex: $[Fe_8O_4(pz)_{12}Cl_4]$ (pz) pyrazolate anion, $C_3H_3N_2^-$) reported in 1999.[22] Similar $[M_8O_4]^{n+}$ cores have been seen in three other complexes: $[VZnO(O_2CPh)_3(THF)]_4$, in which the four V^{III} ions form the central cubane and the four Zn^{II} ions the outer tetrahedron;[23] $[Co^{III}_4Co^{II}_4O_4(O_2CPh)_{12}(MeCN)_3(H_2O)]$, where the four Co^{III} ions

form the cubane;[24] and $[Cr^{III}_8O_4(O_2CPh)_{16}]$.[25] The central $Fe^{III}_4O_4$ cubane is an extremely rare unit at this oxidation level. Some Fe/O cubanes with Fe^{II} or mixed $Fe^{II/III}$ cores are known, but there are only two $Fe^{III}_4O_4$ cubane units (both inside larger clusters) in the literature.[22,26] Complex **18**·4py joins a rather small family of octanuclear Fe^{III} clusters[27] with O and/or N ligation and a handful of structurally characterised $saoH^-$ and/or sao^{2-}-Fe^{III} complexes.[17, 19-21, 28]

Table 4.2 Selected bond length ranges (Å) and angles (°) for complex **18**

	18
Fe-O (oxide)	1.904(2) – 1.990(2)
Fe-O (oxime)	1.902(2) – 2.231(2)
Fe-N (oxime)	2.145(2) – 2.183(2)
Fe-N (pyridine)	2.216(2) – 2.216(2)
Fe1-O112-Fe1	93.55(7) – 105.66(8)
Fe1-O112-Fe2	102.86(8) – 124.76(10)

DC Magnetic Studies

The following work was in collaboration with L. Engelhardt and M. Luban. Our measurements on **18** of the weak-field molar susceptibility, $\chi = M / H$, were made using a superconducting quantum interference device (SQUID) magnetometer in the temperature range 1.8–300 K in a fixed magnetic field H=0.1 T. These data are shown in Fig. 4.5, where the most noteworthy features are a shallow minimum at approximately 7 K and a monotonic increase with increasing T to the highest measured temperature. Two important inferences follow from an inspection of Fig. 4.6, where the corresponding values of $\chi_M T$ are shown. First, we note that, on the low-temperature side, the very small limiting value, $\chi_M T < 0.01$ cm^3 K mol^{-1}, strongly suggests that the total angular momentum quantum number of the ground

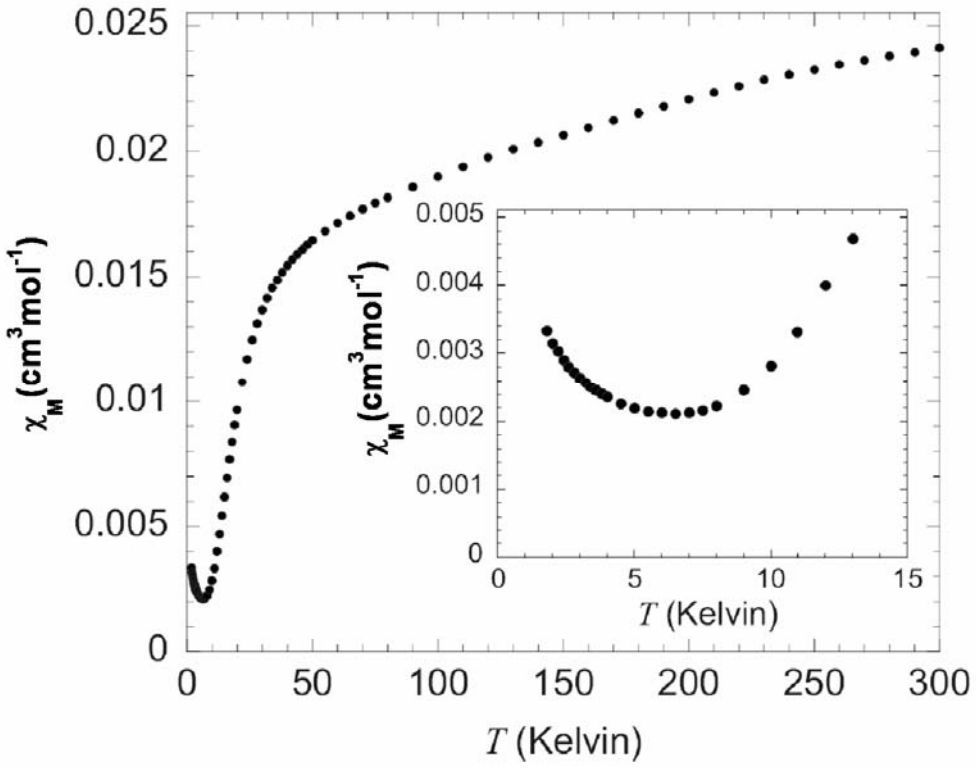

Fig. 4.5 Experimental values of the molar susceptibility χ vs temperature T for H=0.1 T. The low-temperature data are shown in the inset.

state is given by S=0. This follows from the fact that the value of $\chi_M T$ in the limit $T \rightarrow 0$ is given by $N_A g^2 \mu_B^2 S(S+1) / (3k_B)$ for a ground state that has total angular momentum S, where N_A is Avogadro's number, g is the spectroscopic splitting factor, μ_B is the Bohr magneton, and k_B is Boltzmann's constant. In particular, for an S=1 ground state and with g=2,[29] the limiting low-temperature value is $\chi_M T \approx 1$ cm^3 K mol^{-1}, which is larger than the observed value by more than 2 orders of magnitude. The second inference from Fig. 4.6 is that, on the high-temperature side, $\chi_M T$ has only reached the value of 7.2 cm^3 K mol^{-1} K by 300 K, compared to 8 $N_A g^2 \mu_B^2 s(s+1) / (3k_B) \approx 35$ cm^3 K mol^{-1}, which is the limiting (Curie law) high-temperature value for eight s =5/2 Fe^{III} ions. This strongly suggests that the dominant interaction strength (all energies henceforth are stated in units of Kelvin) in this system is considerably larger than 10 K. It is thus reasonable to expect that the energy gap

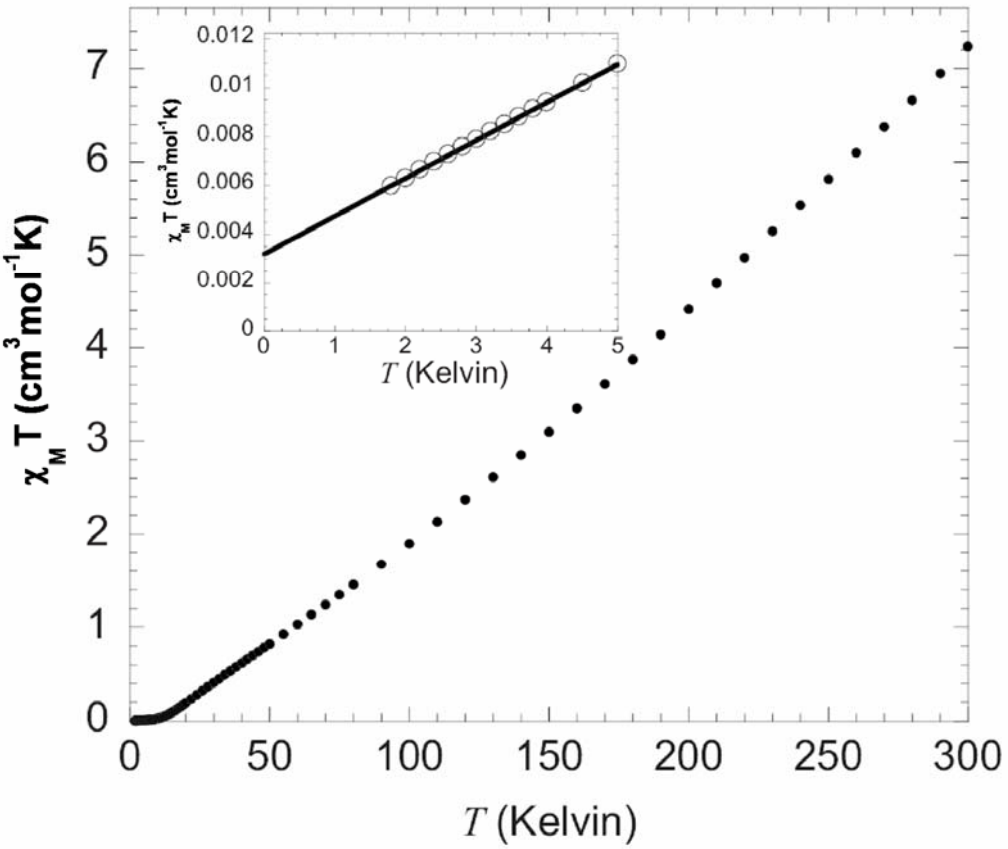

Fig. 4.6 Temperature dependence of χT for the data shown in Fig. 4.5. The low-temperature data are shown in the inset (symbols), along with the function (solid line) that describes the extrinsic contribution to χ, as described in the text.

between the ground state and the lowest S=1 level is of the same order of magnitude, with the consequence that the intrinsic contribution to $\chi_M T$ —provided by the molecules of **18**—can be expected to be negligible below about 10 K.

Given an S=0 ground state, the simplest explanation for the weak rise in the experimental $\chi_M T$ data upon cooling below 7 K is that a small concentration of detached individual Fe^{III} ions is present in the sample. Such detached ions would provide a contribution to the magnetisation M that is proportional to the Brillouin function $B_{5/2}(gs\mu_B H/k_B T)$, which, in turn, is proportional to its argument in the regime $gs\mu_B H/k_B T \leq 1$. In particular, with the weak measuring field of H=0.1 T and for the temperature range $T > 2$ K, this inequality is satisfied well. Thus, this contribution to

the magnetisation can be accurately described by the simpler function cH/T, where c is proportional to the concentration of detached Fe^{III} ions. The resulting contribution to χ_M is therefore given by c/T, so the value of c can be inferred by simply extrapolating the experimental $\chi_M T$ data to the T=0 limit. This is shown in the inset of Fig. 4.6 and yields the value c=0.0032 cm^3 K mol^{-1}, which corresponds to approximately seven detached Fe^{III} ions per 10^4 molecules of **18**.

There is another expected extrinsic contribution to χ (due to diamagnetism and Van Vleck paramagnetism) that is temperature independent, to be denoted by χ_{TI}. In fact, we suggest that this is the source of the linear behaviour of $\chi_M T$ that is visible for T <5 K (see the inset of Fig. 4.6) where, as remarked above, the intrinsic contribution to $\chi_M T$ — provided by the molecules of **18** — is expected to be vanishingly small. Using the slope of the low-temperature $\chi_M T$ versus T data provides the value χ_{MTI}= 0.00155 cm^3 mol^{-1}. The diamagnetic correction from Pascal's constants is of the order -10^{-3} cm^3 mol^{-1}, implying that the Van Vleck paramagnetism is approximately 2.5 x 10^{-3} cm^3 mol^{-1}, which is consistent with the values that have been employed for similar clusters.

Having determined the values of c and χ_{MTI}, which are the two parameters that define the extrinsic contributions to χ_M, we assume in the following that the experimental susceptibility over the complete temperature range 1.8–300 K is given by

$$\chi_M T = \chi_{Mi} T + \chi_{MTI} + (c/T) \qquad (4.1)$$

where $\chi_{Mi} T$ is the intrinsic contribution of the interacting spin system of **18**. The function $\chi_{Mi} T$ is calculated in the following section using an isotropic Heisenberg model after we introduce a specific scenario for the couplings between the spins. The parameters of the model Hamiltonian will be determined by optimising the fit between the results for $\chi_M T$ obtained by theory and experiment.

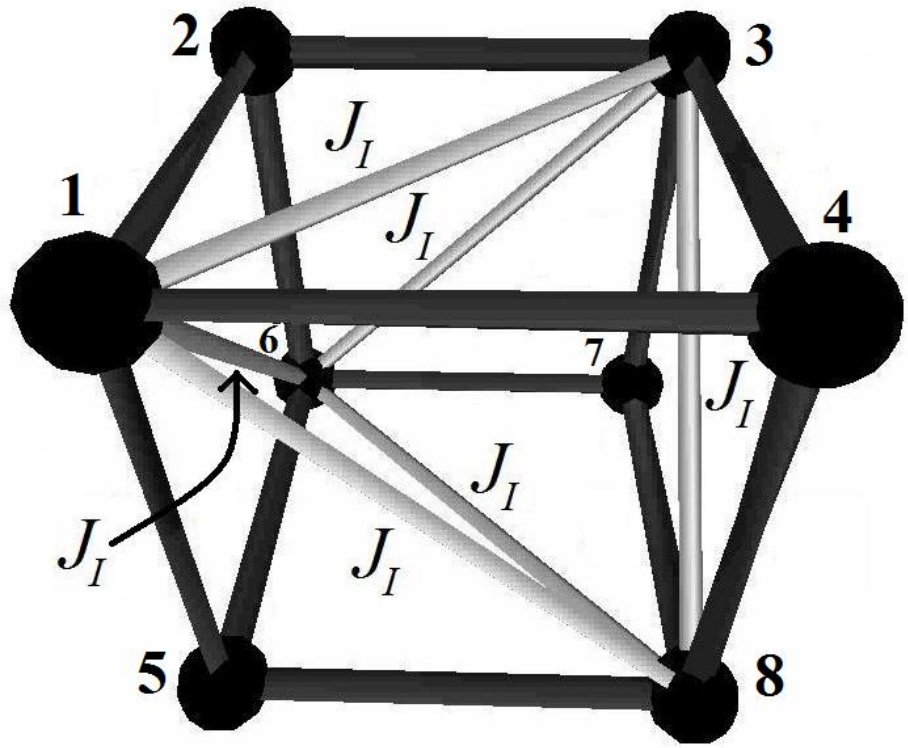

Fig. 4.6 Structure of the magnetic interactions for **18**. The black spheres labeled 1–8 correspond to the Fe^{III} ions of Fig. 4.2 labelled Fe1, Fe2, Fe1''', Fe2', Fe2'', Fe1'', Fe2''', Fe1', respectively. The 12 unlabeled black lines [forming the cube in (b)] represent the outer bonds, J_O. The six light grey lines, labeled J_I, represent the inner bonds.

The geometrical structure of the eight Fe^{III} ions of **18** is as shown in Fig. 4.2. The interior ions (labeled Fe1, Fe1', Fe1'', Fe1''') occupy alternate sites of a cube. Each of these interior ions is coordinated to the three other interior Fe^{III} ions, and in each case there are two distinct but presumably identical pathways via intervening oxygen ions. We suppose that each such coordination may be described by isotropic Heisenberg exchange, and we denote the strength of this interaction by J_I. Additionally, each of the four exterior Fe^{III} ions (labeled Fe2, Fe2', Fe2'', Fe2''') are coordinated to three of the four interior Fe^{III} ions via a single oxygen ion. This coordination will also be assumed to be described by isotropic Heisenberg exchange

and the strength of this interaction will be denoted by J_O. A more convenient way to graphically highlight the various exchange bonds is shown in Fig. 4.6, where the 8 Fe^{III} ions occupy the vertices of a cube and the 12 black edges correspond to interactions of strength J_O, while the 6 grey edges correspond to interactions of strength J_I. The transcription of the labeling of the Fe^{III} ions from Figs. 4.2 and 4.6 is given in the caption.

Based on the notation of Fig. 4.6, we are, in summary, adopting an isotropic Heisenberg Hamiltonian of the form:

$$\begin{aligned} \mathrm{H} = J_O(&\vec{s}_1\cdot\vec{s}_2+\vec{s}_2\cdot\vec{s}_3+\vec{s}_3\cdot\vec{s}_4+\vec{s}_4\cdot\vec{s}_1+\vec{s}_5\cdot\vec{s}_6+\vec{s}_6\cdot\vec{s}_7+\vec{s}_7\cdot\vec{s}_8+\vec{s}_8\cdot\vec{s}_5+ \\ &\vec{s}_1\cdot\vec{s}_5+\vec{s}_2\cdot\vec{s}_6+\vec{s}_3\cdot\vec{s}_7+\vec{s}_4\cdot\vec{s}_8) \quad + \\ J_I(&\vec{s}_1\cdot\vec{s}_3+\vec{s}_1\cdot\vec{s}_6+\vec{s}_1\cdot\vec{s}_8+\vec{s}_3\cdot\vec{s}_6+\vec{s}_3\cdot\vec{s}_8+\vec{s}_6\cdot\vec{s}_8) \quad + \quad g\mu_B\vec{H}\cdot\sum_{i=1}^{8}\vec{s}_i \end{aligned} \tag{4.2}$$

where each spin operator $\vec{s}_i$ ($1 \le i \le 8$) is in units of $\hbar$. In Fig. 4.6 we show each of these bonds, as well as the numbering scheme for the ions. The dimensionality of this matrix is fairly large ($6^8 > 10^6$), but using modern matrix diagonalisation methods,[30] we have calculated the intrinsic magnetic susceptibility $\chi_{Mi}T$ for the Heisenberg Hamiltonian given in Eq. (4.2) in the weak-field limit as a function of temperature. This calculation was repeated for a very large and representative selection of choices of the two exchange constants, J_O and J_I. This process yielded an optimal pair of exchange constants by minimising the square of the deviation between the experimental $\chi_M T$ data and the theoretical $\chi_M T$ data [calculated from Eqs. 4.1 and 4.2]. As a result, an excellent simulation has been achieved over the entire measured temperature range for the values J_I/k_B=22±2 K and J_O/k_B=71.5±2 K, which corresponds to the ratio J_O/J_I=3.25. The intrinsic susceptibility is shown in Fig. 4.7, where the individual data points represent the inferred experimental data, as obtained by subtracting the extrinsic contributions (diamagnetism, Van Vleck paramagnetism, and detached magnetic ions) from the raw experimental data. The very small values of $\chi_{Mi}T$ below 10 K is a direct consequence of the relatively large energy gaps, summarised below, of the energy levels with $S>0$ above the ground state level.

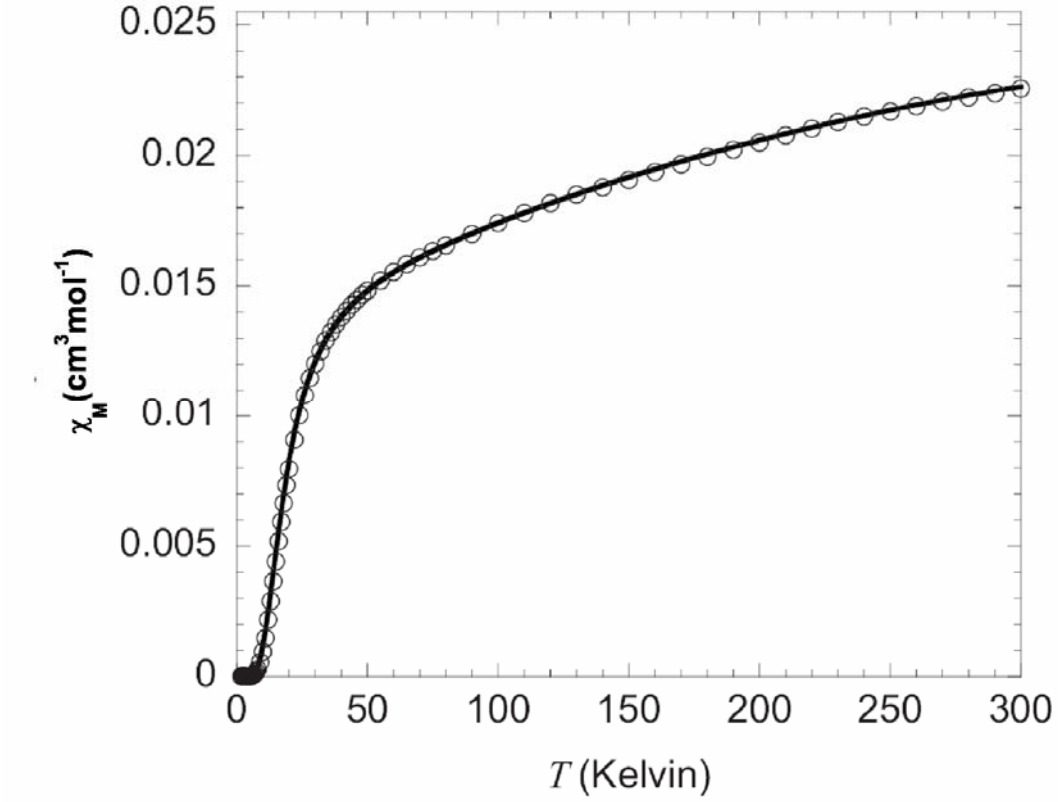

Fig. 4.7 The intrinsic susceptibility, $\chi_{Mi}T$, inferred from experiment (circles) and theory (solid curve). The theoretical curve was calculated using the Heisenberg Hamiltonian of Eq. 4.2, where the numerical values of the exchange constants (given in the text) were chosen so as to provide the best fit to the experimental data.

As part of the matrix diagonalisation procedure, we have obtained the full set of energy levels for **18**. The lowest-lying levels (energies measured from the S=0 ground state level, in Kelvin) are 55 K (lowest S=1 level, multiplicity=1), 164 K (lowest S=2 level, multiplicity=1), and 340 K (first excited S=1 level, multiplicity=3). The first excited S=0 level has an energy that is higher still: 757 K, with multiplicity=5.

The most significant remaining open question is whether additional, independent experimental tests of the theoretical model can be provided. In our opinion, successful reproduction of the temperature dependence of the measured

susceptibility by a theoretical model is a necessary but perhaps insufficient test of the model. Indeed, we have provided detailed quantitative information on the spectrum of low-lying energy levels in **18.** The large value of the energy gap between the ground state and the lowest S=1 level translates to the prediction that the lowest level crossing field is given by H_c=41 T. That is, a measurement at low temperatures of the differential susceptibility, dM/dH, should not show the characteristic peak associated with a level crossing for fields below *Hc*. Use of a pulsed-field set up in the range 0-60T has provided dramatic confirmation of the calculated spectrum of low-lying energy levels and the theoretical model proposed (Fig. 4.8).

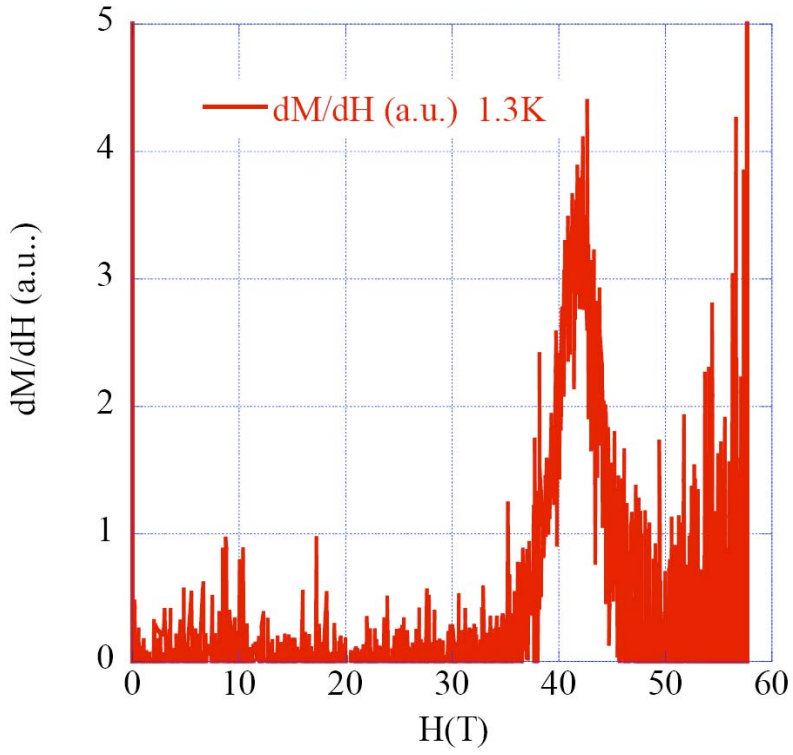

Fig. 4.8 Differential susceptibility measurements in the range 0-60T on **18**.

Conclusions

We have demonstrated that the use of microwave heating is a new appealing approach for the synthesis of large polymetallic transition-metal cluster compounds. In this instance, it has not only led to the isolation of a beautiful and unusual $\{Fe_8\}$

cluster, impossible to produce under ambient reaction conditions, and to a novel coordination mode of the ligand involved but has also greatly improved the reaction rate and enhanced the yield in comparison to solvothermal methods. The use of microwave heating thus has enormous potential for inorganic cluster chemists, and we hope this acts as a stimulus for others in the field. A secondary, but also important, chemical message of this preliminary work is that the coordinative flexibility and versatility of the doubly deprotonated salicylaldoximate ligand make it useful for a variety of synthetic objectives in the field of cluster chemistry. We have, first, presented our susceptibility data for **18** and, second, provided a quantitative theoretical analysis based on the isotropic Heisenberg model utilising two relatively large exchange constants. For the optimal choices of the exchange constants, we have achieved excellent agreement between theory and experiment over the full range of measured temperatures (1.8–300 K). In this regard, the present system provides a striking example of where a magnetic molecule is accurately described by the isotropic Heisenberg model. The ground state of the system has total angular momentum S=0 and thus the intrinsic susceptibility plummets to zero below approximately 10 K. In addition to the intrinsic contribution to the susceptibility, we have found that there is a small extrinsic contribution which is of some significance below 5 K. Our analysis suggests, apart from standard diamagnetic and temperature-independent Van Vleck contributions, the presence of a small concentration of detached Fe^{III} ions.

References

1 For reviews, see: (a) R. E. P. Winpenny, *Dalton Trans.*, 2004, 1; (b) S. Parsons, R. E. P. Winpenny, *Acc. Chem. Res.*, 1997, **30**, 89; (c) R. E. P. Winpenny, *Adv. Inorg. Chem.*, 2001, **52**, 1; (d) E. K. Brechin, A. Graham, P. E. Y. Milne, M. Murrie, S. Parsons, R. E. P. Winpenny, *Philos. Trans. R. Soc. London, Ser. A.*, 1999, **357**, 3119; (e) E. K. Brechin, *Chem. Commun.*, 2005, 5141; (f) G. S. Papaefstathiou, S. P. Perlepes, *Comments. Inorg. Chem.*, 2002, **23**, 249.

2 E. J. L. McInnes, S. Piligkos, G. A. Timco, R. E. P. Winpenny, *Coord. Chem. Rev*., 2005, **249**, 2577.

3 (a) R. H. Laye, E. J. L. McInnes, *Eur. J. Inorg. Chem*., 2004, 2811 and references cited therein; (b) L. F. Jones, D. M. Low, M. Helliwell, J. Raftery, D. Collison, G. Aromı´, J. Cano, T. Mallah, W. Wernsdorfer, E. K. Brechin, E. J. L. McInnes, *Polyhedron,* 2006, **25**, 325; (c) R. Shaw, I. S. Tidmarsh, R. H. Laye, B. Breeze, M. Helliwell, E. K. Brechin, S. L. Heath, M. Murrie, S. Ochsenbein, H.-U. Güdel, E. J. L. McInnes, *Chem. Commun.*, 2004, 1418; (d) D. M. Low, E. K. Brechin, M. Helliwell, T. Mallah, E. Rivie`re, E. J. L. McInnes, *Chem. Commun.*, 2003, 2330; (e) D. M. Low, L. F. Jones, A. Bell, E. K. Brechin, T.Mallah,E. Rivie`re, S. J. Teat, E. J. L. McInnes, *Angew. Chem., Int. Ed.* 2003, **42**, 3781.

4 S. Toma, *Chemicke Listy*, 1993, **87**, 888.

5 S. Toma, *Chemicke Listy,* 1993, **87**, 627.

6 D. R. Baghurst, D. M. P. Mingos, *J. Chem. Soc. Chem. Commun.,* 1992, 674.

7 G. Bond, R. B. Moyes, S. D. Pollington, D. A. Whan, *Chemistry & Industry*., 1991 686.

8 A. Zlotorzynski, *Critical Reviews In Analytical Chemistry*, 1995, **25**, 43.

9 K. Chatakondu, M. Green, D. Mingos, S. M. Reynolds, *J. Chem. Soc. Chem. Commun*., 1989, 1515.

10 K. J. Rao, B. Vaidhyanathan, M. Ganguli, P. A. Ramakrishnan, *Chemistry of Materials*, 1999, **11**, 882.

11 A. De La Hoz, A. Diaz-Ortis, A. Moreno, F. Langa, *Eur. J. Org. Chem*., 2000 3659.

12 Olofsson, M. Larhed, A. Hallberg, *J. Org. Chem*., 1998, **63**, 5076.

13 M. Larhed, G. Lindeberg, A. Hallberg, *Tetrahedron Lett*., 1996, **37**, 8219.

14 M. Larhed, M. Hoshino, S. Hadida, D. P. Curran, A. Hallberg, *J. Org. Chem.*, 1997, **62,** 5583.

15 D. Stuerga, K. Gonon, M. Lallemant, *Tetrahedron,* 1993, **49**, 6229.

16 For a review, see: A. G. Smith, P. A. Tasker, D. J. White, *Coord. Chem. Rev*., 2003, **241**, 61.

17 P. Chaudhuri, *Coord. Chem. Rev.,* 2003, **243**, 143.

18 For example, see: C. J. Milios, C. P. Raptopoulou, A. Terzis, F. Lloret, R. Vicente, S. P. Perlepes, A. Escuer, *Angew. Chem., Int. Ed.*, 2004, **43**, 210.

19 J. M. Thorpe, R. L. Beddoes, D. Collison, C. D. Garner, M. Helliwell, J. M. Holmes, P. A. Tasker, *Angew. Chem., Int. Ed.*, 1999, **38**, 1119.

20 E. Bill, C. Krebs, M. Winter, M. Gerdan, A. X. Trautwein, U. Flörke, H.-J. Haupt, P. Chaudhuri, *Chem.-Eur. J.*, 1997, **3**, 193.

21 A. J. L. Pombeiro, V. Yu. Kukushkin, *Comprehensive Coordinate Chemistry II*; J. A. McCleverty, T. C. Meyer, Eds., Elsevier: Amsterdam, The Netherlands, 2004, **1**, 631.

22 R. G. Raptis, I. P. Georgakaki, D. C. R. Hockless, *Angew. Chem., Int. Ed*. 1999, **38**, 1632.

23 F. A. Cotton, S. A. Duraj, W. J. Roth, *Inorg. Chem*., 1984, **23**, 4042.

24 K. Dimitrou, J.-S Sun, K. Folting, G. Christou, *Inorg. Chem.*, 1995, **34**, 4160.

25 I. M. Atkinson, C. Benelli, M. Murrie, S. Parsons, R. E. P. Winpenny, *Chem. Commun*., 1999, 285.

26 D. Foguet-Albiol, K. A. Abboud, G. Christou, *Chem. Commun.,* 2005, 4282.

27 Representative papers: (a) K. Wieghardt, K. Pohl, I. Jibril, G. Huttner, *Angew. Chem., Int. Ed. Engl.*, 1984, **23**, 77; (b) P. Ammala, J. D. Cashion, C. M. Kepert, B. Moubaraki, K. S. Murray, L. Spiccia, B. O. West, *Angew. Chem., Int. Ed.*, 2000, **39**, 1688 and references cited therein; (c) C. Canada-Vilalta, T. A. O'Brien, M. Pink, E. R. Davidson, G. Christou, *Inorg. Chem.*, 2003, **42**, 7819.

28 (a) C. P. Raptopoulou, Y. Sanakis, A. K. Boudalis, V. Psycharis, *Polyhedron*, 2005, **24**, 711. (b) C. P. Raptopoulou, A. K. Boudalis, Y. Sanakis, V. Psycharis, J. M. Clemente-Juan, M. Fardis, G. Diamantopoulos, G. Papavassiliou, *Inorg. Chem.*, 2006, **45**, 2317. (c) P. Chaudhuri, M. Winter, P. Fleischhauer, W. Haase, U. Flörke, H.-J. Haupt, *Inorg. Chim. Acta*., 1993, **212**, 241.

29 The spectroscopic splitting factor is chosen as g=2 in this work, as this value is very close to experimentally derived values for Fe^{III} compounds.

30 We have used the MAGPACK matrix diagonalization package. J. J. Borrás-Almenar, J. M. Clemente-Juan, E. Coronado, B. S. Tsukerblat, *Inorg. Chem*., 1999, **38**, 6088 ; *J. Comput. Chem*., 2001, **22**, 985.

Publications

Simple Synthetic Routes to Molecular Magnetite

I. A. Gass, S. Parsons, A. Collins, W. Wernsdorfer, D. Collison, M. Evangelesti, E. K. Brechin, *Dalton Trans.*, 2008, submitted.

Polymetallic clusters of iron(III) with derivatised salicylaldoximes

I. A. Gass, C. J. Milios, A. Collins, F. J. White, L. Budd, S. Parsons, M. Murrie, S. P. Perlepes, E. K. Brechin, *Dalton Trans*., 2008, 2043.

From single-molecule magnetism to long-range ferromagnetism

C. Vecchini, D. H. Ryan, L. M. D. Cranswick, M. Evangelisti, W. Kockelmann, P. G. Radaelli, A. Candini, M. Affronte, I. A. Gass, E. K. Brechin, O. Moze, *Phys. Rev. B.*, 2008, **77**, 224403.

Heisenberg model of an {Fe8}-cubane cluster

L. Engelhardt, I. A. Gass, C. J. Milios, E. K. Brechin, M. Murrie, R. Prozorov, M. Vanette, M. Luban, *Phys. Rev. B.*, 2007, **76**, 172406.

Synthesis and magnetic properties of heptadecametallic Fe(III) clusters

I. A. Gass, C. J. Milios, M. Evangelisti, S. Heath, D. Collison, S. Parsons, E. K. Brechin, *Polyhedron*, 2007, **26**, 1835.

Tunable Dipolar Magnetism in High-Spin Molecular Clusters

M. Evangelisti, A. Candini, A. Ghirri, M. Affronte, G. W. Powell, I. A. Gass, P. A. Wood, S. Parsons, E. K. Brechin, D. Collison, S. L. Heath, *Phys. Rev. Lett*., 2006, **97**, 167202.

A Cube in a Tetrahedron: Microwave-Assisted Synthesis of an Octametallic FeIII Cluster

I. A. Gass, C. J. Milios, A. G. Whittaker, F. P. A. Fabiani, S. Parsons, M. Murrie, S. P. Perlepes, E. K. Brechin, *Inorg. Chem.*, 2006, **45**, 5281.

Conferences attended

"MAG-NET Magnetism Workshop", Cambridge, U.K, September 2005 (poster presentation)

"**EastChem Symposium"**, St Andrews and University of Edinburgh, June 2006 (five minutes presentations)

"**10th ICMM Conference: International Conference on Molecule-based Magnets"**, Victoria, Vancouver Island, British Columbia, August 2006 (poster presentation)

"MAG-NET Magnetism Workshop", Edinburgh, U.K, August 2006 (poster presentation).

"**Royal Society of Chemistry Discussion Group Meetings: Inorganic Reaction Mechanisms Coordination Chemistry"**, University of Edinburgh, June 2008 (poster presentation).